Novel GEM detectors for CMS and exotic physics searches at the HL-LHC

Von der Fakultät für Mathematik, Informatik und Naturwissenschaften der RWTH Aachen University zur Erlangung des akademischen Grades eines Doktors der Naturwissenschaften genehmigte Dissertation

vorgelegt von

Master of Science RWTH Aachen University

Henning Christoph Keller

aus

Würzburg

Berichter: Univ.-Prof. Dr. rer. nat. Thomas Hebbeker
apl. Prof. Dr. rer. nat. Oliver Pooth

Tag der mündlichen Prüfung: 19.06.2020

Diese Dissertation ist auf den Internetseiten der Universitätsbibliothek verfügbar.

To my wife Inga

Abstract

The LHC at CERN will be upgraded to become the HL-LHC during the first half of the 2020s. The significant increase in instantaneous luminosity allows probing particle physics with even greater sensitivity. At the same time, the physics environment will become even harsher, compared to the present LHC conditions. To cope with these conditions, the CMS detector at the LHC needs to be upgraded. This thesis focuses on the transition of CMS to the HL-LHC era. Two main topics will be discussed: 1) novel GEM detectors for the CMS detector upgrades and 2) innovative strategies for displaced muon searches at the HL-LHC.

For the installation in the first endcap stations of CMS (GE1/1), large-size triple-GEM detectors have been mass-produced for the first time in high-energy physics. The CMS GEM group was able to assemble, test, and qualify the needed 144 chambers. The integration of GE1/1 detectors in CMS is currently taking place. The GE1/1 GEM chambers show acceptable behavior in terms of gas tightness and high-voltage integrity. The gas gain variations across the large detector area are found to be non-negligible. However, they do not exceed acceptable levels. To understand the origin of these variations, additional gas gain measurements with X-rays were performed while varying environmental and design parameters. Different sources of gain variations have been identified, listed in decreasing importance for the GE1/1 GEM chambers: induction field, drift field, thickness of GEM foil, contamination to nominal gas mixture. For the production of large-size GEM foils, the single-mask etching technique is used, as opposed to the double-mask technique. The influence of the etching technique on the gas gain is found to be non-negligible. The double-mask foils show the highest gain. The orientation of the single-mask foils with respect to the drift and induction fields matters for the gas gain of the detector. To deepen the understanding of signal formation in a triple-GEM detector, microscopic simulations of the electron avalanches inside the complex, active volume were performed. The best configuration of hole pitch and diameter on the GEM foil with respect to the effective gas gain is the symmetric double-mask foil.

In addition, the sensitivity of a physics study for displaced muons at the HL-LHC is discussed in this thesis. The HL-LHC offers a unique possibility to search for exotic, rare signatures. A possible search would significantly profit from the usage of dedicated tools for triggering, reconstruction, and analysis techniques. The study is constructed in a signature-driven and model-independent way to be sensitive to long-lived particles decaying to muons from different beyond the standard model physics. For the smuon interpretation within GMSB SUSY models, a search is sensitive to masses around 100 GeV. In the case of Dark SUSY models, the study is sensitive to the discovery of a hypothetical dark photon with $10 \leq m_{\gamma_D}/\mathrm{GeV} \leq 45$ and $10^{-8} < \epsilon < 10^{-7}$, where ϵ gives the strength of the kinetic mixing between the standard model photon and the dark photon. This addresses a phase-space of dark photon models not yet covered by existing searches.

Zusammenfassung

Bis zur Mitte der 2020er Jahre wird der LHC am CERN zum HL-LHC aufgerüstet. Die signifikante Erhöhung der instantanen Luminosität ermöglicht die Untersuchung der Teilchenphysik mit einer noch größeren Empfindlichkeit. Gleichzeitig wird die Umgebung für Physiksuchen noch rauer als am LHC. Um mit den neuen, härteren Bedingungen zurecht zu kommen, muss der CMS-Detektor am LHC erneuert und erweitert werden. Diese Arbeit beschäftigt sich mit dem Übergang des CMS-Detektors in die neue HL-LHC Ära. Die zwei Hauptthemen dieser Arbeit sind, einerseits, neuartige GEM-Detektoren für die CMS-Detektor-Upgrades und, andererseits, innovative Strategien für Suchen nach räumlich versetzten Myonen am HL-LHC.

Für die Installation in die inneren CMS-Endkappenstationen (GE1/1) wurden, zum ersten Mal in der Geschichte der Hochenergiephysik, triple-GEM-Detektoren im Großformat mittels Massenproduktion hergestellt. Der CMS-GEM-Arbeitsgruppe war es möglich, die notwendigen 144 Kammern zu montieren, zu testen und erfolgreich zu validieren. In 2019 und 2020 findet die Integration der GE1/1-Detektoren in CMS statt. Die GEM-Kammern zeigen ein anständiges Verhalten in Bezug auf Gasdichtigkeit und Hochspannungsintegrität. Die Schwankungen der Gasverstärkung über den großen Detektorbereich sind nicht zu vernachlässigen. Sie überschreiten jedoch nicht die zulässigen Werte. Um den Ursprung dieser Schwankungen zu verstehen, wurden zusätzliche Studien und Messungen mit Röntgenstrahlen durchgeführt, wobei die Umgebungs- und Konstruktionsparameter des untersuchten GEM Detektors geändert wurden. Es wurden verschiedene Ursachen für Verstärkungsschwankungen identifiziert, die hier in abnehmender Bedeutung für die GE1/1 GEM-Kammern aufgeführt sind: Induktionsfeld, Driftfeld, Dicke der GEM-Folien, Verunreinigungen der nominalen Gasmischung. Bei der Herstellung von großformatigen GEM-Folien wird im Gegensatz zur standardmäßigen Doppelmaskentechnik die Einmaskentechnik für das Ätzen der Löcher in den GEM-Folien verwendet. Es wurde herausgefunden, dass der Einfluss der Ätztechnik auf die Gasverstärkung nicht zu vernachlässigen ist. Die Doppelmaskenfolien zeigen die größte effektive Gasverstärkung. Die Ausrichtung der Einzelmaskenfolien in Bezug auf die Drift- und Induktionsfelder ist für die Gasverstärkung des Detektors von Bedeutung. Um das Verständnis der Signalbildung in einem triple-GEM Detektor weiter zu vertiefen, wurden mikroskopische Simulationen der Elektronenlawinen innerhalb des komplexen aktiven Detektorvolumens durchgeführt. Die beste Konfiguration für Lochabstand und Durchmesser in Bezug auf die effektive Gasverstärkung scheint die symmetrische Doppelmaskenfolie zu sein.

Die Sensitivität einer physikalischen Suche nach räumlich versetzten Myonen am HL-LHC wird ebenfalls in dieser Arbeit diskutiert. Der HL-LHC bietet eine einzigartige Möglichkeit, nach exotischen, seltenen Signaturen zu suchen. Eine mögliche Suche würde erheblich von der Verwendung dedizierter Tools für Trigger- und Rekonstruktionstechniken als auch für Analysestrategien profitieren. Die Studie ist signaturbasiert und modellunabhängig aufgebaut. Somit ist man empfindlich auf verschiedenartige langlebige Teilchen, die in Myonen zerfallen und die nicht der Standardmodellphysik entsprechen. Für Smuonen aus GMSB-SUSY-Modellen wäre eine Suche empfindlich auf Massen um 100 GeV. Im Falle von Dark-SUSY-Modellen ist die Studie empfindlich auf die Entdeckung eines hypothetischen Dark-Photons mit $10 \leq m_{\gamma_D}/\mathrm{GeV} \leq 45$ und $10^{-8} < \epsilon < 10^{-7}$. Dabei gibt ϵ die Stärke der kinetischen Mischung zwischen dem Standardmodell-Photon und dem Dark-Photon an. Dies adressiert einen Phasenraum von Dark-Photon-Modellen, der noch nicht durch bestehende Physiksuchen abgedeckt ist.

Contents

1 Introduction **1**

2 Basics of particle physics **5**
2.1 Standard model of particle physics 5
2.1.1 Electroweak sector 6
2.1.2 Higgs mechanism 6
2.1.3 Quantum chromodynamics 6
2.2 Beyond the standard model 6
2.2.1 Theoretical limitations 7
2.2.2 Experimental evidence 7
2.3 Long-lived particles 8
2.3.1 Decay and lifetime 9
2.3.2 Long-lived particles in the standard model 10

3 Gaseous detectors **11**
3.1 Interactions of charged particles with matter 11
3.1.1 Contributions to energy loss 11
3.1.2 Multiple scattering 13
3.2 Interactions of electrons and photons with matter 14
3.2.1 Photoelectric effect 15
3.2.2 Compton effect 16
3.2.3 Pair production 16
3.3 Processes in gaseous detectors 17
3.3.1 Ionization 17
3.3.2 Quenching gas and Penning transfer 17
3.3.3 Electron motion in gas 18
3.3.4 Recombination 20
3.3.5 Electron attachment 20
3.3.6 Gas amplification and operational modes 20
3.3.7 Signal generation 23
3.4 Evolution of gaseous detectors 23
3.4.1 Proportional counter 23
3.4.2 Multi-wire proportional chamber 24
3.4.3 Micro-pattern gaseous detector 24

4 The CMS detector at the LHC and beyond **31**
4.1 The LHC 31
4.1.1 The LHC and accelerator basics 31
4.2 The CMS detector 34
4.2.1 General information 34
4.2.2 Coordinate system 34
4.2.3 Solenoid magnet 35
4.2.4 Tracker 36
4.2.5 Calorimeter system 38
4.2.6 Muon system 39
4.2.7 Trigger system 42
4.2.8 Event processing 43

4.2.9 Muon reconstruction . . . 43
4.3 The HL-LHC and CMS Phase-2 upgrades . . . 44
4.3.1 Current limitations of the LHC . . . 44
4.3.2 The LHC towards Phase-2 . . . 45
4.3.3 Overview of CMS Phase-2 upgrades . . . 47

5 CMS GEM projects **49**
5.1 Overview . . . 49
5.2 GE1/1 project . . . 50
5.2.1 Motivation . . . 50
5.2.2 Detector design . . . 52
5.3 GE1/1 detector production . . . 59
5.3.1 Production community . . . 59
5.3.2 Overview of assembly and quality control tests . . . 59
5.3.3 Assembly and first quality control tests . . . 60
5.3.4 Gas tightness . . . 62
5.3.5 HV integrity . . . 64
5.3.6 Gas gain measurements . . . 66
5.3.7 Statistics of GE1/1 production . . . 77
5.3.8 Superchamber assembly . . . 78
5.3.9 Efficiency measurement with final electronics . . . 81
5.4 Status and outlook . . . 81

6 Characterization of GEM detectors **83**
6.1 Notation and conventions . . . 83
6.2 Gas gain measurements . . . 83
6.2.1 Gas mixtures . . . 87
6.2.2 Electric field variations . . . 87
6.2.3 GEM hole shape . . . 91
6.3 GEM simulation studies . . . 93
6.3.1 Simulation basics . . . 93
6.3.2 HV distribution and simulation scenarios . . . 97
6.3.3 Definition of quantities . . . 98
6.3.4 Gas mixtures . . . 99
6.3.5 Electric fields . . . 99
6.3.6 Hole shape and pitch . . . 100
6.3.7 Conclusive statements . . . 103
6.4 Comparison of simulation and measurements . . . 104
6.4.1 Discrepancy between measurements and simulations . . . 104
6.4.2 Conclusive statements . . . 105
6.5 Comparison with literature and summary . . . 105

7 Sensitivity study on displaced muons at the HL-LHC **107**
7.1 Introduction and motivation . . . 107
7.1.1 Detector signature . . . 107
7.1.2 Identification variables . . . 107
7.2 BSM models with long-lived signatures . . . 109
7.2.1 General aspects of SUSY . . . 109
7.2.2 Dark photons in Dark SUSY . . . 109
7.2.3 Smuons in GMSB SUSY . . . 113

7.3 Search for displaced muons . . . 116
7.3.1 Triggering on displaced muons . . . 116
7.3.2 Displaced muon reconstruction . . . 117
7.3.3 Backgrounds . . . 120
7.3.4 Generators and event simulation . . . 122
7.3.5 Selection criteria . . . 123
7.3.6 Search regions . . . 124
7.3.7 Systematic uncertainties . . . 124
7.4 Statistical interpretation . . . 126
7.4.1 Basics . . . 126
7.4.2 Results . . . 128
7.4.3 Comparison with recent studies . . . 133
7.5 Summary . . . 134

8 Conclusion **135**

A Appendix **137**
A.1 Details on GE1/1 quality control tests . . . 137
A.2 Inventory of Aachen GEM laboratory . . . 138
A.3 Measurements of GEM hole openings . . . 139
A.4 Microscopic simulation step in Garfield++ . . . 140
A.5 HV distributions in Garfield++ simulations . . . 140
A.6 Kinematic distributions of simulated signal processes . . . 141
A.7 Determination of search regions and signal efficiencies . . . 142
A.8 List of event samples for sensitivity study . . . 144
A.9 Collection of quality control plots . . . 147

B Glossary **151**

Bibliography **155**

1 Introduction

The guiding question in the field of particle physics for many decades and even centuries has been, and still is:

What are the elementary particles and forces, that build up everything around us?

On the quest for answers, experimental and theoretical particle physicists have developed the standard model (SM) of particle physics, which describes very accurately the currently known elementary particles and forces. In the last decades, enormous and stringent efforts led to the discovery of the Higgs boson; the last piece of the SM puzzle. The discovery was, among others, reported by the Compact Muon Solenoid (CMS) experiment at the Large Hadron Collider (LHC) in 2012 [1]. This constituted a major milestone in the history of particle physics and the experiments at the LHC.

Despite the enormous success, theoretical shortcomings of the SM, as well as experimental evidence, in particular from astroparticle physics observations, suggest that the SM is not the ultimate theory of particle physics. Theories beyond the standard model (BSM) - often called new physics - extend the SM trying to solve the apparent issues. However, so far, no significant signs of new physics have shown up in the data from the LHC experiments.

By the mid-2020s, the LHC will be upgraded to the high-luminosity LHC (HL-LHC). The HL-LHC, or Phase-2 period, is expected to provide about 10 times the amount of data taken so far by the experiments at the LHC, substantially increasing the sensitivity to (very) rare processes. With its higher luminosity, the physics environment for the experiments at the HL-LHC will be even harsher than before. Among other things, the experiments will be exposed to a larger radiation dose, more pileup interactions, and background rates. To cope with the new challenges, the CMS experiment at the LHC needs to be upgraded for Phase-2. This begs the following questions, that also direct the work of this thesis:

What detector technologies are suitable for particle detection at the HL-LHC and how do these technologies behave for the use case of the CMS experiment?

How will the large amount of data be used? Where should one look for new physics?

How can the sensitivity for exotic signatures at the HL-LHC be increased?

Possible answers to these questions include modern and novel detector technologies and innovative search strategies. The following two paragraphs fill these catchwords with life by introducing the main topics of this thesis[1].

Modern gaseous detector - GEM detectors for the CMS Phase-2 detector at the HL-LHC
Gaseous detectors have paved the road for particle physics for many decades. The detectors have proved to be stable, flexible, and cost-effective solutions for high-energy particle detection. One of the most modern technologies is the gas electron multiplier (GEM) introduced by F. Sauli [2]. GEM detectors belong to the class of micro-pattern gaseous detectors (MPGDs). They are based on polyimide foils, covered with a thin copper layer on top and bottom. The foils are perforated with a pattern of holes. The detection principle relies on electron multiplication in the holes of the foils, where a large electric field is present. Detectors based on GEM technology are used in high-energy physics as well as in several nuclear physics experiments, i.e. COMPASS [3], PHENIX [4], STAR [5], TOTEM [6], LHCb [7] and the CMS Phase-2 detector. With an excellent performance in high rate environments [8],

[1] In general, there is a manifold of answers to the questions, which go far beyond the scope of this thesis.

resistance to aging [9], and a flexible geometry, GEM detectors fulfill the high demands for a detector system in CMS at the HL-LHC. With the addition of GEM detectors, the CMS trigger and reconstruction capabilities can be maintained, likely, even improved for Phase-2 [10, 11].

During 2019 and 2020, 144 GEM chambers are in process of being installed in the first endcap stations of the CMS detector (GE1/1). For the first time, large-area ($\mathcal{O}(1\ \mathrm{m}^2)$) GEM detectors are being mass-produced for a high-energy physics experiment. A dedicated and robust quality control procedure is needed for production. This thesis discusses the quality control steps for the GE1/1 detectors. With their large area, special attention is paid to the check of uniform performance across the detector area. Non-uniformities can cause severe performance degradations. New etching techniques are applied to produce large-area GEM foils. The influence of those and other parameters on the gas gain of GEM detectors is studied. Other recent studies on the performance parameters of GEM chambers can be found in Refs. [12, 13].

Innovative search strategy - sensitivity study for displaced muons at the HL-LHC For the HL-LHC, not only new detector technologies are needed but also innovative strategies for physics searches should be considered. This includes new, or improved, techniques in triggering, reconstruction, and analysis. This thesis presents a sensitivity study for the exotic signature of displaced muons at the HL-LHC using the upgraded CMS Phase-2 detector. At the HL-LHC, with the large amount of data provided to the experiments, it is promising to look for exotic signatures from rare processes, such as displaced muons emerging from the decay of long-lived particles (LLPs) from BSM models. A large fraction of the possible phase-space is currently not covered by existing searches. The expected sensitivity at the HL-LHC of a possible search for displaced muons from BSM physics is determined in this work. Two examples of BSM models predicting LLPs are considered: a lighter ($\mathcal{O}(10\ \mathrm{GeV})$) dark photon from so-called Dark SUSY models, and a heavier ($\mathcal{O}(1\ \mathrm{TeV})$) smuon from GMSB SUSY models. Expected exclusion limits and discovery significances are calculated for the two interpretations assuming the foreseen amount of data provided by the HL-LHC. Recent searches at the LHC from CMS [14] and ATLAS [15] at $\sqrt{s} = 8\ \mathrm{TeV}$, as well as $\sqrt{s} = 13\ \mathrm{TeV}$, looking for dark photons have shown no signs of new physics. Existing constraints from those LHC searches, as well as heavy-ion colliders (PHENIX [16]), cosmological observations [17], and low-energy electron-positron colliders (KLOE [18], BaBar [19]) are compared with this sensitivity study. Furthermore, the influence of dedicated displaced trigger, reconstruction, and analysis techniques on the sensitivity is investigated.

Structure of this thesis This thesis is divided into introductory sections (Sec. 2, 3 and 4) and those sections that contain - among other things - the work performed by the author (Sec. 5, 6 and 7). The introductory sections should be regarded as a collection of the essential information necessary for the work presented afterwards.

- In Sec. 2, the standard model of particle physics is briefly introduced. Its theoretical limitations and experimental evidence, that is contradictory to the predictions of the standard model, are discussed. Additionally, mathematical descriptions of particle decays are given. This section can be regarded as a prerequisite for the HL-LHC sensitivity study presented in Sec. 7.

- Sec. 3 provides an introduction to gaseous detectors with a clear focus on modern technologies, such as GEM detectors. The fundamental principles of particle detection, from the interaction of charged particles with matter to the signal generation inside

gaseous detectors, are scrutinized. Finally, the development of gaseous detectors over the last decades is considered with a strong emphasis on the GEM technology. The information sets the ground for the discussion of the CMS GEM projects in Sec. 5 and the characterization of GEM detectors in Sec. 6.

- In Sec. 4, the CMS experiment and the LHC are presented. In addition to a description of the current status of the detector and its subdetectors, the foreseen upgrades towards the high-luminosity era of the LHC are discussed. This is important to motivate and understand the requirements for the CMS GEM projects in Sec. 5. The work presented in Sec. 6 is also guided by the ideas presented in this section.

- In Sec. 5, an overview of the foreseen CMS GEM projects is given in the beginning. The GE1/1 project is motivated and the requirements, design, and performance are discussed in detail. Special attention is paid to the production of the GE1/1 GEM detectors. The huge effort of planning, constructing, and testing of the chambers is shared among the CMS GEM group. The author of this thesis contributed to a great extent to the construction and commissioning of the Aachen setup. This effort led to the approval of the setup by the CMS GEM group. The measurements and analyses within the GE1/1 quality control, that were performed by the author of this thesis, are highlighted in this section.

- Sec. 6 consists of a collection of measurements and simulations for the characterization of GEM detectors. Various design and environmental parameters are studied to get a deeper understanding of the behavior of the gas gain in GEM detectors. The studies presented in this section have been planned, executed and analyzed by the author of this thesis.

- In Sec. 7, a sensitivity study on displaced muons at the HL-LHC is presented. In the beginning, the general strategy of the study is discussed. BSM models predicting long-lived particles, that decay into muons inside the active volume of the CMS detector, are discussed. The analysis is considered with a particular emphasis on novel trigger and reconstruction techniques for displaced signatures. This study comes from the pen of the author.

Contributions to publications related to this thesis Parts of the results of the HL-LHC sensitivity study on displaced muons have been published before in a Physics Analysis Summary (PAS) [20] by the CMS collaboration.

- CMS collaboration, *Search sensitivity for dark photons decaying to displaced muons with CMS at the high-luminosity LHC*, CMS-PAS-FTR-18-002, 2018

The author of this thesis has been the leading author of this publication. Additionally, comprehensive summaries of the study are included in documents with a larger scope than this thesis. The study can be found, on the one hand, in the HL-LHC Yellow Report [21] and, on the other hand, in the LHC LLP white paper [22]. The study was presented - together with other results from the ATLAS and CMS collaborations - by the author at the following international conference and workshop.

- SUSY2018: 26th International Conference on Supersymmetry and Unification of Fundamental Interactions, 23-27 Jul 2018, Barcelona (Spain),
  Beyond-Standard-Model Physics at the High-Luminosity LHC (ATLAS+CMS)

- LLP2-2017: Searches for long-lived particles at the LHC: Second workshop of the LHC LLP Community, 18-20 Oct 2017, Trieste (Italy),
  Upgrade studies at CMS in the context of LLPs

An overview of the outcome of the GE1/1 quality control tests performed in Aachen, as well as parts of the additional studies on GEM detectors, have been presented by the author on two occasions in the form of a poster.

- Posters@LHCC: Students' Poster Session at the 2019 Winter LHCC meeting, 27 Feb 2019, CERN, Geneva (Switzerland)
  Present and future CMS GEM activities in Aachen

- INSTR'20: Instrumentation for Colliding Beam Physics, 24-28 Feb 2020, Novosibirsk (Russian Federation)
  Influence of hole geometry on gas gain in GEM detectors

2 Basics of particle physics

This section builds up the theoretical base for the HL-LHC sensitivity study, described in Sec. 7. In Sec. 2.1, an overview of the standard model (SM), which is the best current description of particle physics, is given. Theoretical arguments and experimental evidence suggest that the standard model is not the ultimate theory of particle physics (Sec. 2.2). Models addressing these topics and extending the SM are subsumed under the term beyond the standard model (BSM) physics. A subset of BSM models predicting long-lived particles (LLPs) is discussed in Sec. 7.2. For the HL-LHC sensitivity study, the processes predicted by those BSM models are considered as signals. Sec. 2.3 explicitly states some of the formalisms used for long-lived particles. The theoretical parts of this section are based on Refs. [23–25]. Experimental considerations rely on Refs. [26–28].

2.1 Standard model of particle physics

The standard model of particle physics is the product of decades of theoretical and experimental work. The standard model offers a unification of special relativity and quantum mechanics. It describes all known elementary particles and their interactions, expect gravity. The particle content is shown in Fig. 2.1. For each of the particles listed in Fig. 2.1, an

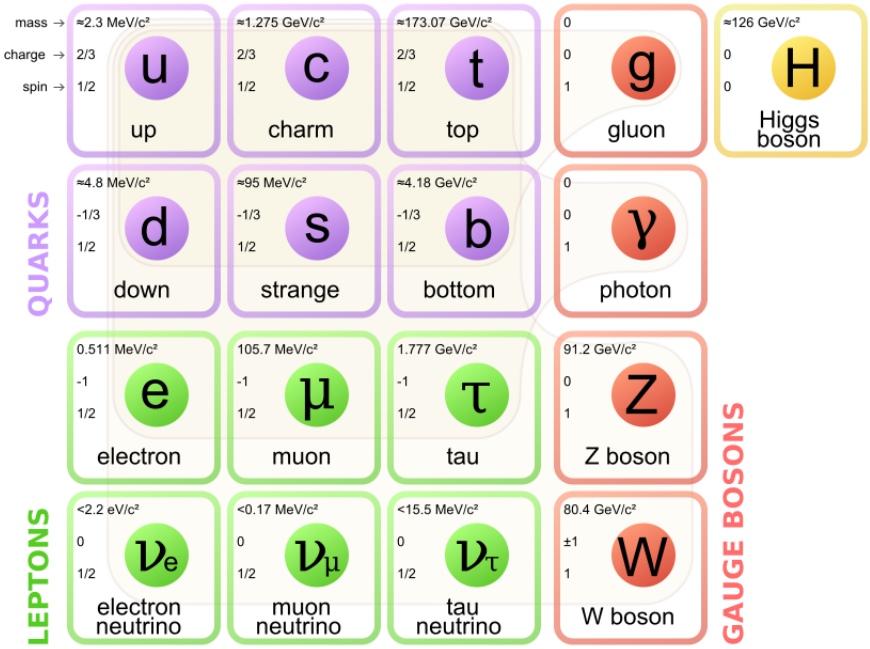

Figure 2.1: Particle content of the standard model showing the matter particles with spin 1/2, called fermions, the gauge bosons with spin 1 and the Higgs boson with spin 0. The fermions are divided into leptons and quarks. Properties such as mass, spin, and charge of the standard model particles are listed. The figure is taken from Ref. [29].

antiparticle exists with the same quantities but opposite-sign charges. There are two categories of particles: fermions with half-integer spin and bosons with integer spin. The matter particles have spin $\frac{1}{2}$ and are called fermions. The fundamental interactions, i.e. electromagnetic, weak and strong interaction, are mediated by the force carriers having spin 1 and being called bosons. The Higgs boson with spin 0 completes the theory.

From a theoretical point of view, general concepts need to be imposed to construct a meaningful theory. In the following, the perturbative structure of a theory and renormalizability are discussed. The perturbative structure of a theory relies on the assumption that the theory can be written as an expansion in a given coupling parameter α. In this case, the full theory is described by the (infinite) power series in α. The term of the power series at leading order (LO) can be used to obtain an approximation of the full theory. To get an even better approximation, one can determine the higher-order terms, called next-to-leading order (NLO, NNLO,...). This technique can be visualized by Feynman graphs. Each term of the power series is associated with a set of Feynman diagrams. The theoretical prediction of a process consists of the sum of all Feynman graphs. Phenomenologically spoken, a theory is said to be renormalizable if the divergences can be handled. If the power series, discussed above, contains divergent terms, they can be compensated by divergent bare quantities. These bare quantities are not measurable. An example of this procedure is given by the calculation of the Higgs mass (Sec. 2.2.1). Besides the standard model, also BSM models are constructed in a way that they obey these concepts. Further information on renormalizability and the perturbative structure of a theory, as well as Feynman graphs and rules, can be found in Ref. [23].

2.1.1 Electroweak sector

The electroweak sector is a unification of the electromagnetic force, mediated by the photon γ, and the weak force, mediated by the $W^{\pm}$ and Z bosons. The theoretical work goes back to the physicists Glashow, Weinberg, and Salam [30, 31]. All fermions with an electric charge interact with the photon. Those fermions with a weak charge interact with the $W^{\pm}$ and Z bosons. Additionally, self-interactions of the gauge[1] bosons are present.

2.1.2 Higgs mechanism

The Higgs mechanism denotes a theoretical concept of spontaneous symmetry breaking of the electroweak gauge group[2]. This idea allows integrating mass terms for the fermions, as well as for the W and Z bosons, in the standard model. The concept was proposed by Brout, Englert, and Higgs [32, 33] in the 1960s, long before the Higgs boson was discovered in 2012 [1]. According to today's knowledge, the Higgs boson is the only elementary particle in the standard model with spin 0 [34].

2.1.3 Quantum chromodynamics

Quantum chromodynamics (QCD) describes the strong interaction of gluons (gauge bosons of the strong force) and quarks (matter particles with a color charge). The gluons are massless and carry a color charge themselves, as opposed to, e.g. the electrically neutral photon in the electromagnetic case. In total, there are 8 gluons. The gluons do not couple to leptons.

2.2 Beyond the standard model

The standard model is supposed to be one of the best-tested theories in the history of physics. The agreement of measurements and theoretical predictions of the standard model is remarkable[3]. However, there are several theoretical limitations evident in the standard

[1] This name goes back to the close connection of gauge symmetries and force carriers, which is discussed in the given literature.

[2] The concepts of symmetry breaking are discussed in Ref. [24]

[3] To convince yourself, consult e.g. Ref. [35].

model and there is experimental evidence, showing that the particle content of the standard model is not enough to explain certain phenomena. This leads to the conclusion that the standard model is not the ultimate theory of particle physics. There is a wide range of proposed BSM models extending the standard model and trying to solve the apparent issues.

2.2.1 Theoretical limitations

One of the theoretical issues of the standard model is that gravity, one of the fundamental forces, is not included. General relativity offers a precise description of gravity. Unifying the concepts of general relativity and quantum field theory has not been achieved. At the Planck scale, corresponding to the Planck mass of $M_{\text{Pl}} = 1.22 \cdot 10^{19}$ GeV, quantum effects of gravity start to play a role - similar to the TeV-scale for the electroweak force. Thus, BSM physics must appear somewhere between the electroweak scale ($\sim$ TeV), where current particle physics experiments perform measurements, and the Planck scale.

In the standard model, the value of the Higgs mass, m_h, can be calculated by adding two contributions: the bare mass m_h^0 and the quantum corrections to the mass by loop corrections δm_h. With the approach of an effective field theory, the loop corrections have been determined to be

$$(\delta m_h)^2 \propto G_F^2 \left[\Lambda_{UV}^2 + ...\right]. \tag{2.1}$$

G_F^2 is the coupling constant of the Higgs to the fermions and Λ_{UV} denotes the fundamental scale of new physics. Depending on the scale of new physics, the quantum corrections could be very large compared to the measured Higgs mass of 125 GeV. If the scale of new physics is, e.g. the Planck scale of $\approx 10^{19}$ GeV, one would need a huge bare mass $m_h^0 \gg m_h$. It is seen as highly unnatural, that the Higgs mass is the result of quantities that are several orders of magnitude larger. This is called the hierarchy or fine-tuning problem of the Higgs mass [36].

2.2.2 Experimental evidence

Observations by astrophysical experiments show, that, in our universe, there is a type of matter called dark matter, which cannot be described by the standard model. A selection of dark matter observations is given in the following. In Ref. [37], a more extensive list can be found.

WIMPs and freeze-out Weakly interacting massive particles (WIMPs) denote a concept that proposes a massive elementary particle χ that is stable, electrically neutral and yet undiscovered. In the early universe, the χ's are in thermal equilibrium with the SM particles. The back-and-forth processes $\chi\bar{\chi} \leftrightarrow f\bar{f}$, where f denotes a given SM particle, ensure this equilibrium. As time passes by, the universe expands and the temperature drops. The particles get less kinetic energy and one direction of $\chi\bar{\chi} \leftrightarrow f\bar{f}$ is suppressed due to the high mass of the χ's. From exclusion limits of collider searches, $m_\chi \geq 100$ GeV can be imposed [38]. As a consequence, the WIMPs decouple from the standard model particles and the number of WIMPs in the universe becomes more or less constant. In astroparticle physics, this phenomenon is called freeze-out of the WIMPs. The remaining cosmological abundance can be estimated by

$$\Omega_\chi = \frac{10^{-37}\ \text{cm}^2 \cdot c}{\langle v \cdot \sigma_{\chi\bar{\chi}\to f\bar{f}} \rangle_{\text{freeze}}}. \tag{2.2}$$

$\sigma_{\chi\bar{\chi}\to f\bar{f}}$ denotes the annihilation cross section. c is the speed of light and v the velocity of the χ's. The brackets in the denominator indicate that the average of the quantities at the freeze-out is taken into account. The velocity of the χ's can be estimated to be $v \approx \frac{1}{3}c$, based

on freeze-out calculations of heavy particles [39]. By inserting the abundance of dark matter in the universe Ω_χ,

$$\sigma_{\chi\bar{\chi}\to f\bar{f}} \approx 10^{-36}\ \mathrm{cm}^2 = 1\ \mathrm{pbarn} \tag{2.3}$$

is obtained [39]. The annihilation cross section happens to be of the same order of magnitude as typical cross sections of the weak interaction in the standard model. This coincidence of orders of magnitude in cross section is called the WIMP miracle. Thus, it makes sense to search for dark matter particles in collider experiments at the LHC.

Observation of cluster merger The cluster merger 1E0657558 provides strong evidence of dark matter [40]. It is observed with X-ray detection and, at the same time, with gravitational lensing. The detection via X-rays creates an image of the ordinary matter. With gravitational lensing, the distribution of all the matter interacting via gravity can be seen. The resulting matter distributions of the two detection methods differ significantly (see Fig. 2.2). Introducing dark matter could explain the observation.

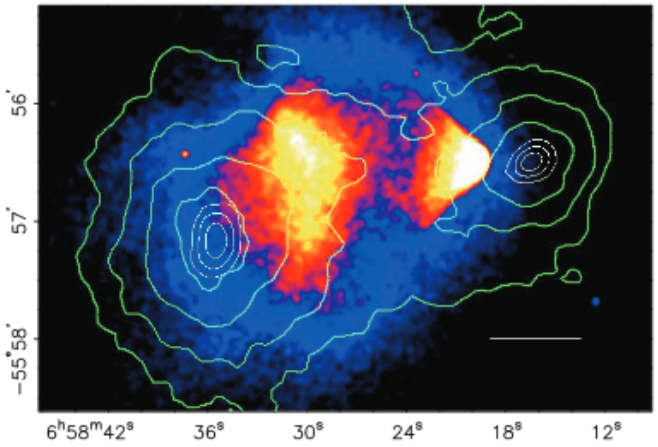

Figure 2.2: Observation of cluster merger 1E0657558. The colored contour shows the result of the X-ray detection. In green contours, the result of the measurement using gravitational lensing is depicted. The figure is taken from Ref. [40].

Matter-antimatter asymmetry The universe is full of matter but there is almost no antimatter (matter-antimatter asymmetry). A priori, matter and antimatter should have been equally abundant during the Big Bang. In the literature, one idea to explain the observed matter-antimatter asymmetry is CP violation at the electroweak energy scale [41]. CP violation is present in the electroweak sector of the standard model. In QCD, experiments do not indicate any CP violation. However, the amount of CP violation in the standard model is not large enough to describe the matter-antimatter asymmetry in the universe. Any extension of the standard model should contain more CP-violating terms than the standard model.

2.3 Long-lived particles

The phenomenology of long-lived particles deserves some dedicated considerations. A short introduction into the basic concepts of particle decays is presented, followed by a discussion of the LLPs in the standard model. The section is based on Ref. [42].

2.3.1 Decay and lifetime

Fermi's golden rule The decay rate of a particle with mass M into n daughter particles is given by

$$\mathrm{d}\Gamma = \frac{(2\pi)^4}{2M}|\mathcal{M}|^2 \mathrm{d}\Phi_n(P; p_1, .., p_n), \tag{2.4}$$

where $\mathcal{M}$ denotes the matrix element. $\mathrm{d}\Phi_n$ is the n-body phase-space. The physics of the decay, e.g. coupling constants, is contained in the matrix element, while the kinematic behavior of the decay is described by the phase-space. Eq. 2.4 is valid in the rest frame of the mother particle and is often referred to as Fermi's golden rule. The total decay rate of a particle is the sum of the individual decay rates for all possible decays.

Lifetime and survival probability The decay of a particle is a Poisson process. The survival probability P of a particle with the 4-momentum $(E, \vec{p})$ after a time t can be written as

$$P(t) = \exp(-\frac{\Gamma}{\gamma}t) = \exp(-\frac{M}{E}\Gamma t). \tag{2.5}$$

Γ is the decay rate. γ denotes the relativistic kinematic factor. A similar equation can be established for the probability that a particle travels the distance d or greater before it decays.

$$P(d) = \exp(-\frac{M}{|\vec{p}|}\Gamma d). \tag{2.6}$$

The lifetime τ is defined as $\tau = \frac{1}{\Gamma}$. The quantity $c\tau$ is also called lifetime. In natural units with $c = 1$, it is indeed the same. However, in classical units, $c\tau$ describes a distance and not a time.

The factorization of Eq. 2.4 in matrix element and phase-space allows drawing some conclusions for the lifetime. A small matrix element or a small available phase-space can cause a small decay rate and, thus, a long lifetime. The magnitude of the matrix element depends on the coupling constants of the process responsible for the decay. A small coupling would cause a large lifetime. The matrix element can also be small due to tiny violations of quantum numbers, e.g. lepton flavor violations in the neutrino sector of the SM. The degeneracy of the masses of mother and one of the daughter particles would limit the available phase-space for the decay and would lead to a larger lifetime. Mass degeneracies can be caused by approximate symmetries. An example is given by the isospin which leads to almost degenerate masses of the proton and neutron.

Two-body decay The kinematically most simple case is the particle decay into two daughter particles. Fig. 2.3 defines the variables used for the description of the two-body decay. In

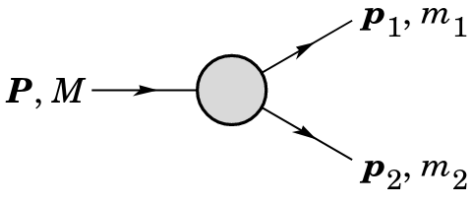

Figure 2.3: Illustration of the variables of the two-body decay. Uppercase letters denote the momentum and mass of the mother particle. The lowercase letters denote the momentum and mass of the daughter particles. The figure is taken from Ref. [42].

case of a two-body decay, the general form of the decay rate shown in Eq. 2.4 boils down to

$$\mathrm{d}\Gamma = \frac{1}{32\pi^2}|\mathcal{M}|^2\frac{|p_1|}{M^2}\mathrm{d}\Omega, \tag{2.7}$$

with $\mathrm{d}\Omega = \mathrm{d}\phi_1\mathrm{d}(\cos\theta_1)$ being the solid angle of particle 1.

Definition of long-lived particles for collider searches Before long-lived particles in the standard model and in BSM theories are discussed further, it has to be defined what is meant by long-lived in the context of collider searches with the CMS detector (see Sec. 4.2) at the LHC. In this thesis, the LLPs of the BSM models do not leave any signal in the detector. However, if they decay to detectable SM particles inside the detector volume, a measurable signal can be analyzed. If the LLP lifetime is short, it might not be possible to separate the decay vertex from the primary vertex. If the LLP lifetime is too long, the probability that it leaves the detector without any signal is too high. The former case can be covered by prompt searches and the latter case can be addressed by searches for missing transverse momentum in the detector.

2.3.2 Long-lived particles in the standard model

In the standard model, there are several examples of long-lived particles. Fig. 2.4 gives a comprehensive summary of the currently known lifetimes of elementary particles and several bound states. The figure illustrates the fact, that SM physics is full of long-lived

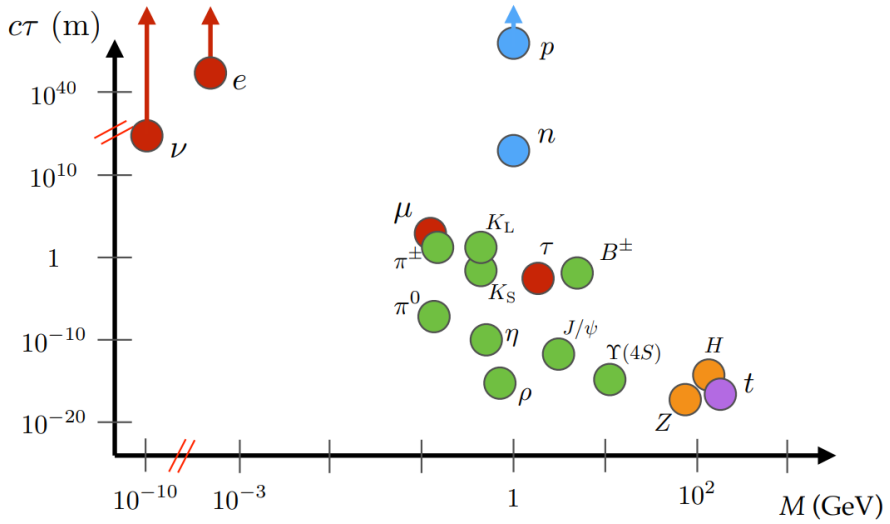

Figure 2.4: Overview of lifetimes of elementary SM particles and several bound states. Leptons are shown in red, baryons in blue, mesons in green, gauge bosons in orange and the top quark in violet. An arrow attached to the circle indicates that only a lower limit on the lifetime of the particle exists. The figure is taken from Ref. [43].

particles. The range of lifetimes of elementary particles can vary from a few microns, e.g. the τ lepton, to several hundred meters, e.g. the muon.

3 Gaseous detectors

In the beginning of this section, the basics of particle detection are introduced (Sec. 3.1 and 3.2). In Sec. 3.3, relevant processes in gaseous particle detectors are discussed. A description of the most modern technologies of gaseous detectors, among them the GEM technology, can be found in Sec. 3.4. A large fraction of the content is based on Refs. [42, 44–48].

3.1 Interactions of charged particles with matter

Charged particles traversing a material interact with the matter via forces. The gravitational force is by far negligible compared to the other forces on the scale of elementary particles. For the processes, which are relevant for particle detection with gaseous detectors, the strong force can be neglected[1]. The electromagnetic and weak force must be considered. Except for neutral particles, e.g. neutrinos, the electromagnetic force plays the most dominant role. The interaction between the electromagnetic field of the charged particle and of the matter leads predominantly to excitations and/or ionizations of the matter. Free charges are released in these processes, which can be used to generate a detectable electric signal. In the following, heavy charged particles, i.e. with a mass much greater than the electron, traversing matter are discussed. Sec. 3.2 provides information about interactions of electrons and photons with matter.

3.1.1 Contributions to energy loss

Interactions of heavy charged particles traversing matter are predominantly leading to ionization and/or excitations of the atoms inside the medium. For the ionization process, an electron in an atomic shell acquires enough energy to escape the binding potential of the nucleus. This creates electron-ion pairs in the medium. The electrons can interact further with the surrounding matter. The interaction with the incident particle can also cause an excitation of the atoms. When the atoms de-excite, photons are emitted. The energy of the incident charged particle is reduced after each collision.

The mean rate of energy loss (or mass stopping power), $\langle -\frac{\mathrm{d}E}{\mathrm{d}x} \rangle$, for an anti-muon in copper is shown in Fig. 3.1. The function of the mass stopping power can be divided into three regions: low ($\beta\gamma < 0.1$), intermediate ($0.1 < \beta\gamma < 1000$) and high ($\beta\gamma > 1000$) momenta of the incident particle. β and γ are the relativistic kinematic factors of the incident particle.

Bethe-Bloch regime For the stopping power at intermediate momenta and for materials with low and intermediate atomic numbers, the mean energy loss is well-described by the Bethe-Bloch formula

$$\langle -\frac{\mathrm{d}E}{\mathrm{d}x} \rangle = K z^2 \frac{Z}{A} \frac{1}{\beta^2} \left(\frac{1}{2} \ln \frac{2 m_e \beta^2 \gamma^2 W_{max}}{I^2} - \beta^2 - \frac{\delta(\beta\gamma)}{2} \right), \tag{3.1}$$

where $K = 4\pi N_A r_e^2 m_e$ with N_A denoting the Avogadro constant, with r_e and m_e being the classical electron radius and the electron mass, respectively. z is the charge number of the incident particle. Z and A denote the atomic number and atomic mass of the absorber material. The δ term denotes the contribution due to the density correction for higher energies [45]. I denotes the mean excitation energy of the medium. W_{max} is the maximum

[1] In multiple scattering processes of hadronic particles, the strong force must be taken into account.

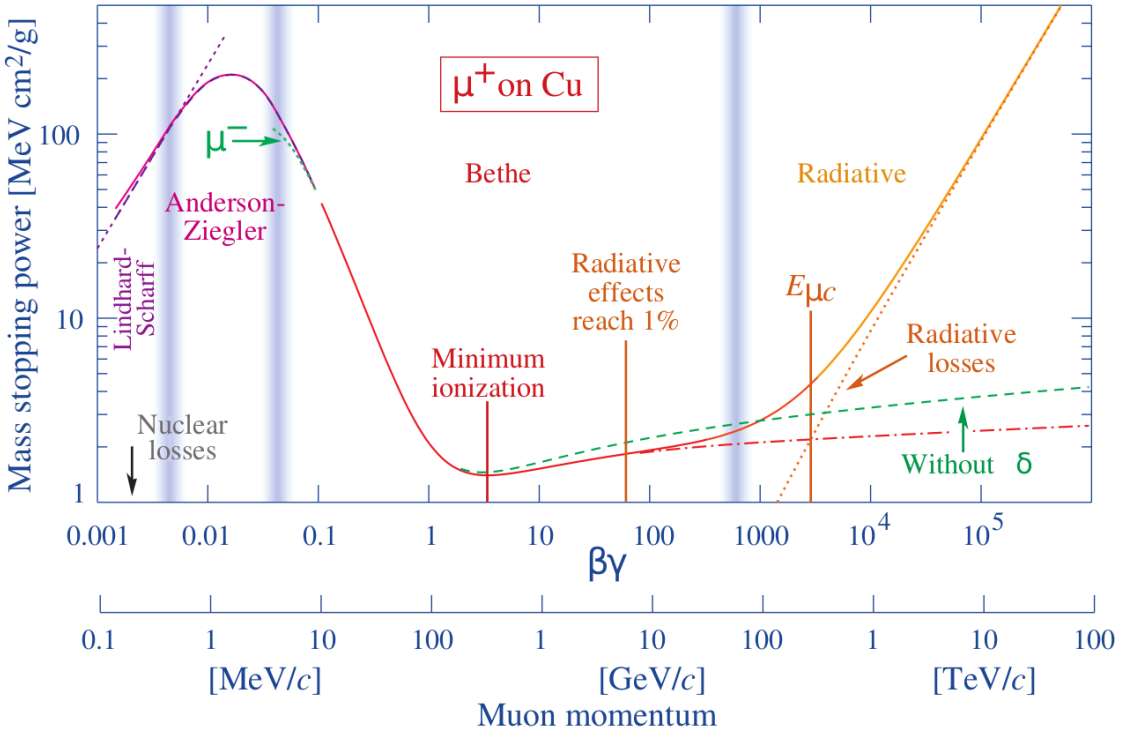

Figure 3.1: Mass stopping power (or mean energy loss) for an anti-muon in copper. $\langle -\frac{\mathrm{d}E}{\mathrm{d}x} \rangle$ is shown as a function of the relativistic expression $\beta\gamma$ and as a function of the muon momentum. The solid curves indicate the total stopping power. The validity regions of the different approximations are indicated by the vertical blurred lines. For intermediate energies, the Bethe-Bloch formula is valid. The red and green lines show the Bethe-Bloch energy loss with and without the δ correction, respectively. At higher energies, radiative losses (dashed yellow line) dominate. At lower energies, called the Anderson-Ziegler region, the stopping power is given by a parametrization of data. The Lindhard-Scharff region is a theoretical model, where the energy loss is proportional to β (pink dashed line). The figure is taken from Ref. [42], where the reader can find more details and explanations.

energy transfer possible in a single collision and is given by

$$W_{max} = \frac{2m_e\beta^2\gamma^2}{1 + 2\gamma m_e/M + (m_e/M)^2} \tag{3.2}$$

for an incident particle with mass M. Although $\langle -\frac{\mathrm{d}E}{\mathrm{d}x} \rangle$ forms a good general understanding of the energy loss in a material, this quantity must be taken with caution because the mean is pushed to higher values by a few collisions with large amounts of energy loss. In some studies, instead of the mean energy loss, the most probable energy loss is preferred. At low energies ($\beta\gamma < 0.1$), several corrections must be applied to Eq. 3.1, e.g. corrections for atomic binding effects. A detailed discussion of all the corrections needed for the low energy region can be found in Ref. [42].

Radiative effects For $\beta\gamma > 4$, radiative effects, i.e. e^+e^- pair production, bremsstrahlung and photonuclear effects, start to play a role. The stopping power at higher energies ($\beta\gamma > 1000$) is fully driven by radiative effects. For high-Z materials, the radiative effects become important even at lower energies. A convenient way to describe the energy loss at high energies is

$$\langle -\frac{\mathrm{d}E}{\mathrm{d}x} \rangle = a(E) + b(E)E, \tag{3.3}$$

where $a(E)$ and $b(E)$ denote the contributions to the energy loss by ionization and radiative effects, respectively. $a(E)$ is given by Eq. 3.1. In Fig. 3.2, the components of $b(E)$ are presented, exemplary for muons in iron.

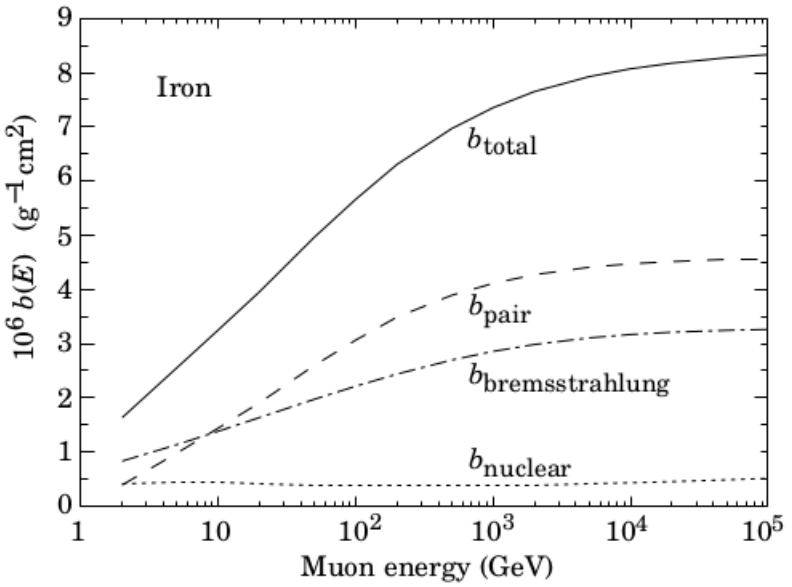

Figure 3.2: Contributions to the fractional energy loss $b(E)$ of muons in iron due to pair production, bremsstrahlung and photonuclear effects. The figure is obtained from Ref. [49].

Applications For several use cases, relativistic particles, e.g. cosmic ray muons, fall into the category of minimum ionizing particles (MIPs), which means that the energy loss is close to the characteristic minimum of the mean energy loss at around $\beta\gamma \approx 3-4$ (see Fig. 3.1). For muon detection with gaseous detectors at the LHC, radiative effects of high-energy muons ($\mathcal{O}$(100 GeV - 1 TeV)) are essential for a precise muon reconstruction. Another use case of $\langle -\frac{\mathrm{d}E}{\mathrm{d}x} \rangle$ is directly related to the detection principle of muon detectors in CMS. Most gas mixtures of the CMS muon detectors are based on argon. With the argon density at hand, the mean energy loss per cm of a MIP, e.g. a muon coming from the center of the detector, can be calculated. Knowing the dimensions of the detector, the expected number of ionizations happening inside the gas volume of a detector can be estimated.

3.1.2 Multiple scattering

When traversing matter, a charged particle is deflected by small-angle scatters mostly due to Coulomb scattering from a nucleus. The theory of Molière [50] provides a good description of the Coulomb scattering distribution. For many small-angle scatters, the distribution of deflection is Gaussian via the central limit theorem. A Gaussian distribution can be used to describe the central 98% of the projected angular distribution with

$$\theta_0 = \frac{13.6\ \text{MeV}}{\beta p} z \sqrt{\frac{x}{X_0}} \left(1 + 0.038 \ln(\frac{x z^2}{X_0 \beta^2}) \right), \tag{3.4}$$

if one assumes $\theta_0 = \theta^{rms}_{plane} = \frac{1}{\sqrt{2}} \theta^{rms}_{space}$, where θ^{rms}_{plane} and θ^{rms}_{space} denote the width of the angular distribution in the projected plane and in the three-dimensional space, respectively. The thickness of the material in radiation lengths is given by $\frac{x}{X_0}$. β, p and z denote the velocity, momentum and charge number of the incident particle. Eq. 3.4 is well-describing

the p and z dependence at small Z (atomic number of absorber). At large Z and with a thin material layer, the velocity dependence of Eq. 3.4 is not accurate anymore. Multiple scattering happens in CMS, when particles travel through the detector material or the iron yoke. It is essential to consider multiple scattering, when reconstructing the trajectory of a particle.

3.2 Interactions of electrons and photons with matter

Electrons lose their energy when traveling through matter primarily either by ionization processes or bremsstrahlung depending on their energy. At low energies, ionization processes cause a higher energy loss. For higher energies, the loss due to bremsstrahlung becomes the dominant effect. These two dominant processes as a function of the electron energy together with the sub-dominant processes can be seen in Fig. 3.3.

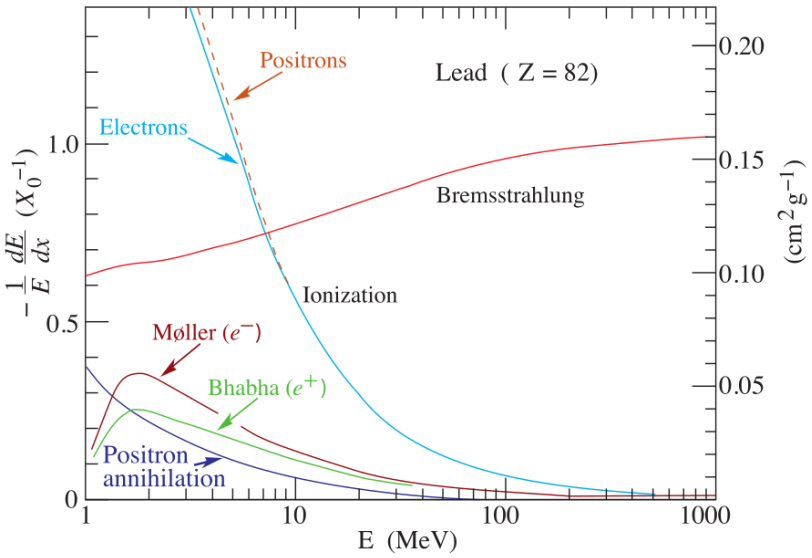

Figure 3.3: Different contributions to the fractional energy loss of electrons or positrons in lead. At low energies, energy losses due to ionizations are dominant. Contributions of subdominant effects, such as Møller scattering, Babha scattering, and e^+ annihilation are shown in this figure. At high energies, losses due to bremsstrahlung are dominant. The figure is taken from Ref. [42].

The behavior of photons going through matter can be accurately described by the following processes: photoelectric effect, Compton effect, and e^+e^-pair production[2]. Due to the nature of the processes, beams of photons are attenuated when going through matter. In contrast to the interaction of charged particles with matter, the photoelectric effect and pair production, which are the dominant processes over a large range of photon energies, "absorb" the photon. The attenuation can be described by the intensity of an incoming photon beam I decreasing with the mass thickness x of the material via

$$I(x) = I_0 \exp(-(\mu/\rho)x). \tag{3.5}$$

Here, μ is the attenuation coefficient and ρ is the material density of the target. In the literature, the mass attenuation coefficient $\left(\frac{\mu}{\rho}\right)$ is often used. μ depends on the cross section of the

[2]For simplicity reasons, the Rayleigh scattering is ignored being a subdominant effect at low photon energies.

photon-matter interactions. Analog to a total cross section, the total attenuation coefficient is simply the sum of the attenuation coefficients of the different processes:

$$\mu_{tot}/\rho = 1/\rho \left(\mu_{\text{photo effect}} + \mu_{\text{Compton}} + \mu_{\text{pair production}}\right). \tag{3.6}$$

Fig. 3.4 presents the total mass attenuation coefficient in Carbon, together with the contributions from different processes. With rising photon energy, first the photoelectric effect, then

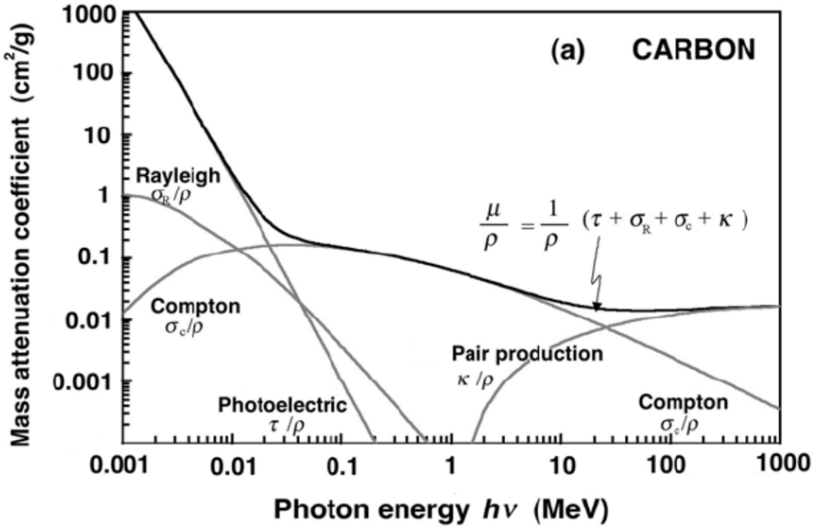

Figure 3.4: Mass attenuation coefficient in Carbon as a function of the photon energy. In this figure, the subdominant process of Rayleigh scattering is shown together with the dominant contributions of the photoelectric effect, Compton scattering, and pair production. The figure is taken from Ref. [51].

the Compton effect and finally the pair production is dominant. The photon/electron processes in matter are worth considering. The CMS muon chambers are subject to, both, electrons and photons coming from radiative effects of high-energy muons. Furthermore, several R&D studies on GEM detectors and the GE1/1 quality control measurements (Sec. 5.3.6) rely on the interactions of photons with matter.

3.2.1 Photoelectric effect

The photoelectric effect denotes a process where the incident photon is interacting with an atom of the medium. In this interaction, the photon is absorbed and gives its energy to a bound electron of an atom. If the photon energy is greater than the binding energy of the electron, the electron is kicked out of the atom and obtains the kinetic energy of $E_{kin} = E_\gamma - E_{bind}$. After the interaction, the medium is in an excited state. The medium de-excites to the ground state via two mechanisms. The first mechanism is called Auger effect. The inner-shell vacancy left by the kicked-out electron is filled with an outer-shell electron. The released energy is transferred to another outer-shell electron which leaves the atom. This second ejected electron is called Auger electron. The other mechanism, called fluorescence, describes a similar process where the released energy is escaping in the form of a photon. This is the fluorescence light with the energy of $E_{X-ray} = E_j - E_i$, where E_i and E_j are the binding energies of the i- and j-shell, respectively. The cross section of the photoeffect strongly depends on the charge number of the material and steeply falls with the photon energy: $\sigma \propto \frac{Z^5}{E_\gamma^3}$ [52].

3.2.2 Compton effect

The Compton effect becomes the dominant effect at intermediate photon energies. It is an interaction of the photon with an electron of the absorber material. The photon is deflected and part of the photon energy is transferred to the electron. The process is illustrated in Fig. 3.5 In the calculations, the electron is assumed to be at rest and quasi-free. The rela-

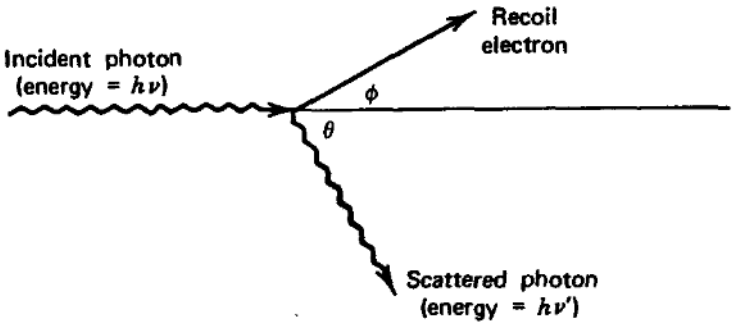

Figure 3.5: Illustration of the Compton scattering process. The incoming photon with the energy $E_\gamma = h\nu$ is scattering off the recoil electron. The scattered photon has the energy $E'_\gamma = h\nu'$. θ and ϕ are the deflection angles of the photon and electron, respectively. The figure is taken from Ref. [52].

tion between the photon energy before the Compton scattering, E_γ, and after the Compton scattering, E'_γ, can be written as

$$E'_\gamma = \frac{E_\gamma}{1 + \frac{E_\gamma}{m_e}(1 - \cos(\theta))}, \tag{3.7}$$

where m_e is the mass of the electron. For the energy transfer to the electron with $E_{e,kin} = 0$, one can write

$$E'_{e,kin} = \Delta E = E'_\gamma - E_\gamma = \frac{E_\gamma \frac{E_\gamma}{m_e}(1 - \cos(\theta))}{1 + \frac{E_\gamma}{m_e}(1 - \cos(\theta))} \tag{3.8}$$

The energy transfer depends on the deflection angle of the photon, called θ. The deposited energy spectrum is a continuum. For small θ, very little energy is transferred and, thus, $E'_\gamma \approx E_\gamma$ and $E'_{e,kin} \approx 0$. At $\theta = 180°$, the energy loss of the photon reaches its maximum and one can write $E'_\gamma = E_\gamma/(1 + \frac{2E_\gamma}{m_e})$ and $E'_{e,kin} = E_\gamma/(1 + \frac{m_e}{2E_\gamma})$. The back scattering marks the end of the continuous spectrum, which is called the Compton edge.

With a higher number of electrons per atom in the material or - in other words - with higher Z, the Compton scattering process becomes more probable. The angular distribution of the scattered photons is described by the Klein-Nishina formula (see Ref. [52]). High energy photons tend to scatter in the forward direction.

3.2.3 Pair production

The process of e^+e^- pair production is energetically possible if $E_\gamma \geq 2m_e$, where m_e denotes the electron mass. Due to momentum conservation, pair production can only take place in the vicinity of an electric field. In matter, this electric field is given by a nucleus or an electron of the medium. At high photon energies, pair production is the dominant effect. The kinetic energies of the produced electron and positron are given by

$$E_{kin}^{electron} + E_{kin}^{positron} = E_\gamma - 2m_e. \tag{3.9}$$

The electron traverses the material as described earlier in the section and the positron is (most probably) annihilated by another electron of the material producing two annihilation photons. If those secondary photons have high enough energy, another secondary pair production is possible. Repeating this procedure creates electromagnetic showers, which are used for particle detection and identification.

3.3 Processes in gaseous detectors

To understand how to detect particles with gaseous detectors, the principles mentioned above are fundamental. First, charged particles traveling through the gas volume of the detector ionize the gas atoms. The extracted electrons drift towards the amplification region, guided by an electric field. In the amplification region, the electric field is large enough that the electrons gain enough kinetic energy to ionize other gas atoms causing an electron avalanche. Depending on the detector type, there are one or several amplification regions. The created negative charge inside the gas volume is collected and registered at the anode of the detector to obtain electrical signals[3].

3.3.1 Ionization

When ionizing particles travel through matter, electron-ion pairs are created in the medium. This is called primary ionization and the electrons are called primary electrons. The primary electrons can have enough energy to cause secondary ionization in the medium. The sum of the two processes (primary and secondary ionization) is called total ionization. The total number of electron-ion pairs is called N_t and can be determined via

$$N_t = \frac{\Delta E}{W_i}, \tag{3.10}$$

where ΔE is the energy loss of the incident particle in a given detector volume. W_i denotes the effective average energy needed to create an electron-ion pair. In gaseous detectors, the medium consists typically of a mixture of different gases. In these cases, W_i can be calculated by a weighted sum. A commonly used gas mixture in gaseous detectors is $\mathrm{Ar/CO_2}$. Noble gases, such as argon, are used as the counting gas due to the absence of rotation and vibration states. Thus, ionization processes dominate. Polyatomic gases, such as $\mathrm{CO_2}$, are added to the counting gas acting as quenchers (see Sec. 3.3.2). For a MIP passing through a gaseous detector filled with $\mathrm{Ar/CO_2}$ (70/30)[4], one can determine N_t for a length of 3 mm (typical length of the drift gap in a CMS GEM detector):

$$N_t = \Delta E \times \left(\frac{0.7}{W_i(\mathrm{Ar})} + \frac{0.3}{W_i(\mathrm{CO_2})} \right) \approx 30 \text{ pairs}. \tag{3.11}$$

ΔE can be determined by using Eq. 3.1. $W_i(\mathrm{Ar}) = 26$ eV and $W_i(\mathrm{CO_2}) = 33$ eV are values taken from Ref. [48].

3.3.2 Quenching gas and Penning transfer

Instead of an ionization, the incident particle can excite a gas atom. The excited atom can emit the de-excitation energy via a photon presumably causing an ionization elsewhere in

[3] In general, the positive charge of the ions at the cathode can also be processed and used as a signal.

[4] In the following, the percentages of the components in gas mixtures are given in parenthesis, i.e. omitting the % symbol.

the gas. In some applications, such photon-induced events are unwanted, since they introduce a spatial and temporal spread of the avalanche. With the addition of a polyatomic gas, e.g. CO_2, these photons can be absorbed. This component is called quenching gas. In mixtures of gases, the excited atom of one component can also transfer the energy via collisions to the other gas component. If the excitation energy exceeds the ionization energy of the collision partner, another avalanche can be induced. This process is called Penning transfer.

3.3.3 Electron motion in gas

The electron motion in gas is complicated to describe due to the energy-dependent interaction cross sections with the gas atoms and the inelastic scattering given by the numerous excitation levels of the atoms. The cross sections of the different interactions in argon and CO_2 are presented in Fig. 3.6.

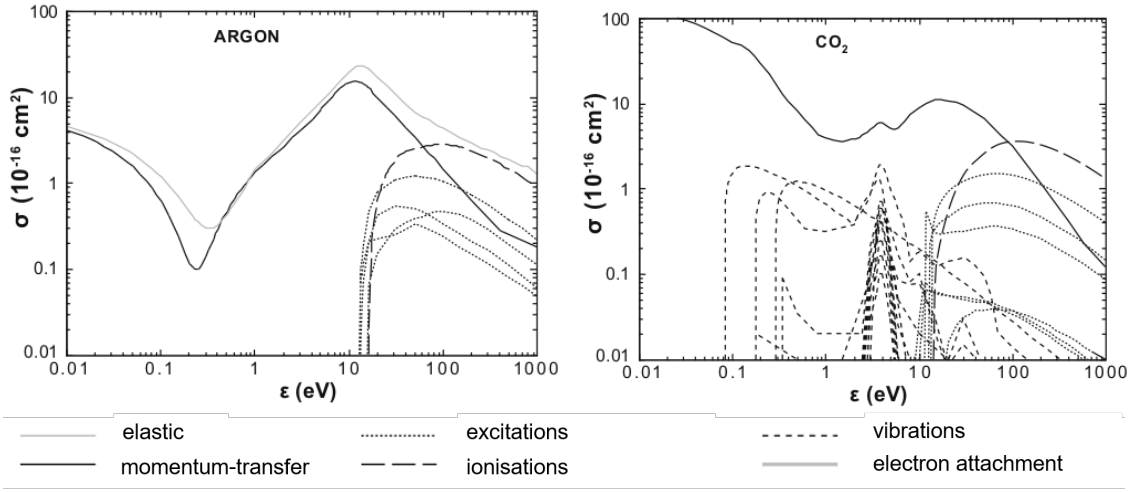

Figure 3.6: Cross sections of elastic and inelastic electron scattering as a function of the electron energy in argon (left) and CO_2 (right). The legend shows which line corresponds to which type of interaction. The figure is taken from Ref. [45].

In general, the evolution of a localized distribution of charges, e.g. electrons, in a gas can be described by the Boltzmann transport equation [45]. Phenomenologically spoken, two terms are contributing to the evolution of a distribution of charges. The first contribution describes the diffusion of the charged particles over time. This happens to all inhomogeneous distributions of charges. The second contribution is induced by an external field, i.e. electric and magnetic field, and is called drift. To obtain the evolution of the charge distribution, the Boltzmann equation has to be solved. Naturally, the solution is highly depending on the interaction cross section (see Fig. 3.6). Before discussing diffusion and drift, commonly used parameters to describe electron motion in gases are introduced:

- $\lambda(\epsilon) = \frac{1}{n\sigma(\epsilon)}$ is the mean free path, where ϵ denotes the electron energy and σ denotes the interaction cross section. The number of gas atoms per volume is given by n.

- $\tau(\epsilon) = \frac{\lambda(\epsilon)}{v}$ is the mean time between two collisions. v is the electron velocity.

Diffusion Without an external field, a localized distribution of electrons in a gas diffuses over time t. Using simple kinetic theory of gases [53] and assuming the number of electrons

N to be constant over time, the evolution of the charge distribution can be described by

$$\rho(\vec{r},t) = \frac{N}{(4\pi Dt)^{3/2}} \exp\left(-\frac{\vec{r}^2}{4Dt}\right), \tag{3.12}$$

where $\vec{r}$ is the position vector and D the diffusion coefficient. The standard deviation of this distribution is a measure for the diffusion of the charges over time

$$\sigma_x = \sqrt{2Dt} \qquad \text{and} \qquad \sigma_V = \sqrt{6Dt}, \tag{3.13}$$

for a linear and a volume diffusion assuming an isotropic diffusion. Thus, a point-like distribution of charges diffuses proportional to $\sqrt{t}$. The diffusion coefficient can be written as $D = \lambda v/3$. In the general case, the diffusion depends on the electric and magnetic field inside the gas volume of the detector and, depending on their orientation, the diffusion can be non-isotropic. Fig. 3.7 shows the dependence of the longitudinal and transverse[5] diffusion coefficient on the electric field strength in Ar/CO_2 (70/30) with a constant magnetic field of 3 T. The results are obtained with the Garfield simulation toolkit [54].

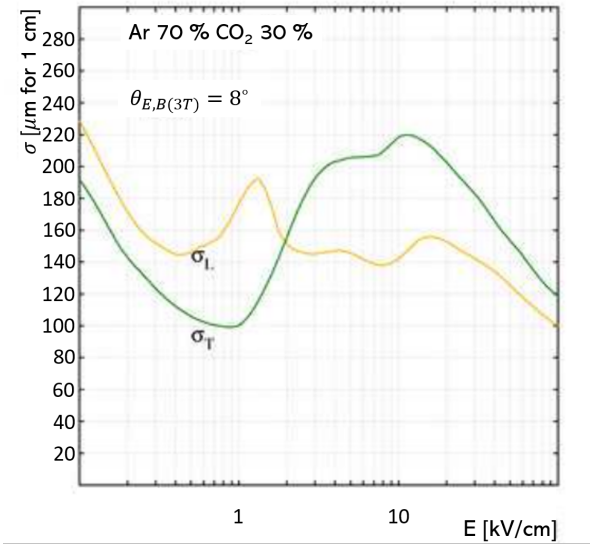

Figure 3.7: Longitudinal (σ_L) and transverse (σ_T) diffusion coefficient for Ar/CO_2 (70/30) with $B = 3$ T and with an angle between the electric and magnetic field of $\angle(\vec{E},\vec{B}) = 8°$. These values correspond to the electric and magnetic fields present at the GE1/1 position in the CMS detector. The figure is taken from Ref. [10].

Drift The drift of electrons is induced by external fields. In the presence of a uniform electric field E, electrons are accelerated along the electric field lines until reaching their drift velocity v_D, which can be expressed by

$$v_D \propto \mu E \propto \frac{q_e}{m_e}\tau E, \tag{3.14}$$

with the definition $\mu \propto \frac{q_e}{m_e}\tau$, which is called electron mobility[6]. q_e and m_e denote the electron charge and mass, respectively. The mean time between collisions, τ, is in general a

[5] Longitudinal and transverse means here along and perpendicular to the electric field lines, respectively.

[6] The formulae are given as proportionalities, because the numerical factor in front of the physical quantities depends on the assumptions made during the calculations.

function of the electric field E. In the ideal gas approximations, the mobility is related to the temperature T and pressure P of the gas via

$$\mu \propto \frac{T^{1/2}}{P}. \tag{3.15}$$

In the presence of an electric and magnetic field, the electron drift is not simply following the electric field lines. If the magnetic field has a component perpendicular to the electric field, called B_T, the direction of the drift velocity and the electric field lines are rotated with respect to each other by the so-called Lorentz angle α_L. The Lorentz angle is given by

$$\tan \alpha_L = \omega\tau, \tag{3.16}$$

with the cyclotron frequency $\omega = \frac{q_e}{m_e} B_T$. Investigations on drift and diffusion of electrons are essential to understand the performance of gaseous detectors. For example, the electron diffusion should be well understood for a good time and spatial resolution.

3.3.4 Recombination

While drifting through the gas volume, electrons can recombine with the positive ions. The recombination process often leads to radiation:

$$X^+ + e^- \rightarrow X + \gamma. \tag{3.17}$$

Recombination is not negligible for those detector geometries, where large parts of the electron drift path go through the volume where the ionizations happen. The process can be critical for the detector performance if the radiated photon induces another electron avalanche disturbing the original signal.

3.3.5 Electron attachment

Electronegative atoms or molecules, e.g. O_2, can capture electrons in their shells. After the electron attachment, the excess of the binding energy and the kinetic energy of the electron can be emitted via radiation, dissociation or collision (see Tab. 3.1). A priori, electronegative

Type	Process	Example
Radiation	$e^- + X \rightarrow X^- + \gamma$	$e^- + O_2 \rightarrow O_2^- + \gamma$
Dissociation	$e^- + XY \rightarrow X^- + Y$	$e^- + O_2 \rightarrow O^- + O$
Collision	$e^- + X + Y \rightarrow X^- + Y$	$e^- + Ne + O_2 \rightarrow Ne + O_2^-$

Table 3.1: Different types of electron attachment. Exemplary, processes with oxygen are shown. The table is extracted from Ref. [45].

atoms, leading to smaller signals, are not desired in a gaseous detector. However, in gas mixtures, the electronegative gas components can be used to absorb unwanted signals and, thus, these components might contribute to a better detector performance.

3.3.6 Gas amplification and operational modes

In regions of high electric field, typically around 10-50 kV/cm, electrons can obtain enough kinetic energy between two collisions to ionize another atom. It comes to the formation of an electron avalanche. The number of created electron-ion pairs in the gas volume increases

dramatically over a small distance. This is essential to create a signal that can be read out. The region is called the amplification region.

The number of produced electron-ion pairs per unit length, the so-called first Townsend coefficient, is given by

$$\alpha = \sigma_{\text{ion}} n = \frac{1}{\lambda_{\text{ion}}}, \tag{3.18}$$

where σ_{ion} and λ_{ion} denote the ionization cross section and the mean free path between ionizing collisions. n is the particle density. The increase of electron-ion pairs $\mathrm{d}N$ per path length $\mathrm{d}s$ is

$$\mathrm{d}N = \alpha(E) N \mathrm{d}s. \tag{3.19}$$

It follows

$$N(s_a) = N_0 \exp\left(\int_{s_0}^{s_a} \alpha(E(s))\mathrm{d}s\right), \tag{3.20}$$

where N_0 and $N(s_a)$ are the numbers of electrons before amplification and at the anode, respectively. The gas gain is defined as

$$G := \frac{N(s_a)}{N_0} = \exp\left(\int_{s_0}^{s_a} \alpha(E(s))\mathrm{d}s\right). \tag{3.21}$$

This is also called effective gas gain. The total gas gain is defined as $G_{tot} := \frac{N_{tot}}{N_0}$, where N_{tot} is the total number of electron-ion pairs including those pairs, where the electron does not reach the anode. In general, the Townsend coefficient α is a function of the energy, which depends on the position-dependent electric field. Assuming α is independent of s, one can write

$$G = \exp(\alpha(s_a - s_0)), \tag{3.22}$$

where the exponential dependency of the gas gain on the Townsend coefficient becomes apparent.

Gaseous detectors operate in different modes according to the value of the gas gain G. Fig. 3.8 shows the signal pulse height as a function of the applied voltage. In the region, where $G \approx 10^3 - 10^6$, the signal is proportional to the initial charge before the amplification. Assuming that in every collision the number of electron-ion pairs is doubled, the number of collisions can be estimated to $13-20$. In this simplified view, half of the charge is produced in the last step, i.e. close to the "boundary" of the amplification region. The gas gain cannot rise above a certain limit due to positive space charges counteracting the external electric field. The limit is called the Raether limit, which is empirically determined to be $G_{max} \approx 10^7 - 10^8$. In the following, the different operational modes are discussed.

Recombination ($G < 1$) For low electric fields, the charges from primary ionizations dominantly recombine. Only if the electric field is strong enough in order to separate them, the output signal starts to rise proportional to the electric field. With a higher electric field, the effect saturates, once all primary charges reach the electrodes.

Ionization mode ($G \approx 1$) The ionization mode is defined by the region where the signal height is saturating in the absence of gas amplification. This mode is useful to measure particle fluxes, e.g. with dosimeters. Measuring a single incident particle is not possible due to the low electric output signal.

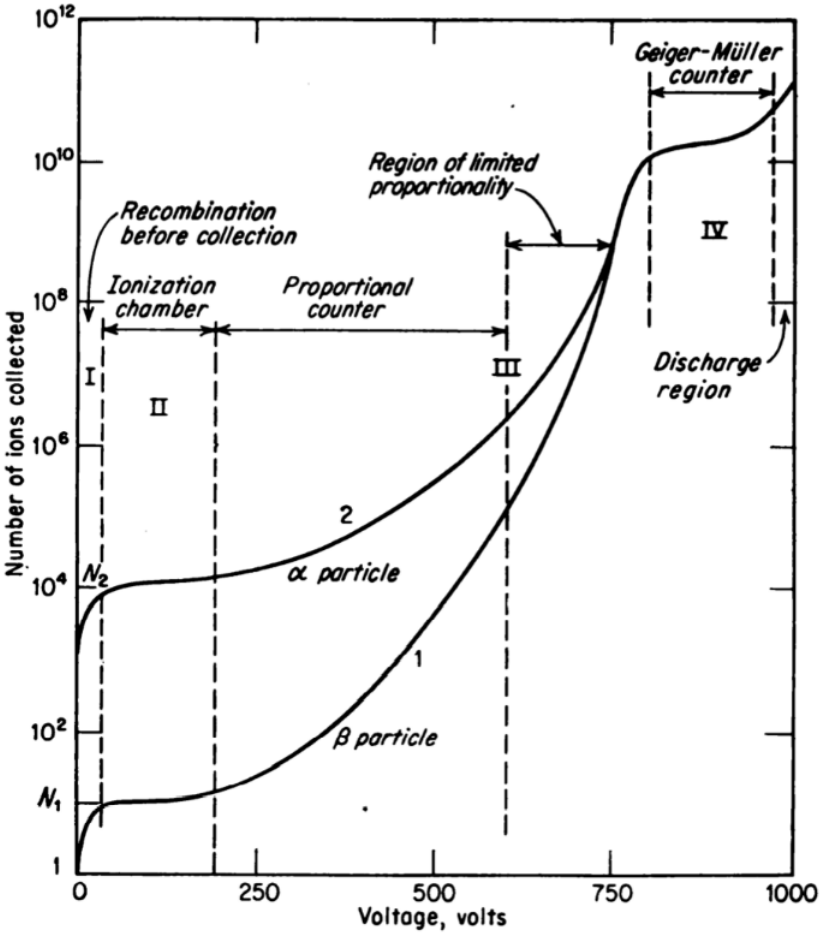

Figure 3.8: Pulse height as a function of the applied voltage for α and β particles. The regions of the different operational modes are separated by vertical dashed lines. N_1 and N_2 are the numbers of primary electron-ion pairs for incident β and α particles, respectively. Detailed information on the operational modes can be found in the text. The figure is taken from Ref. [55].

Proportional mode ($G \approx 10^3 - 10^5$) In a high electric field, the electrons gain enough kinetic energy between two collisions to ionize further gas atoms inducing an electron avalanche. Over a wide range of electric fields, the output signal is proportional to the primary charge. This can be used to distinguish between different incident particles (particle identification). The proportional mode is of utmost importance for this thesis, since the CMS GEM chambers operate in this mode (see Sec. 3.4.3).

Limited proportional mode ($G \approx 10^5 - 10^8$) The proportionality between the output signal and the primary charge is perturbed by space charge effects. A cloud of ions is formed close to the anode due to their lower drift velocity. This counteracts against the electric field causing less amplification. In addition, this operational mode can lead to a higher discharge probability compared to the proportional mode.

Geiger mode ($G \gtrsim 10^8$) For even higher electric fields, the pulse height is saturating and independent of the primary charge. Detectors, operating in this mode, are called Geiger counters. They cannot distinguish particles based on their signal strength. The saturation is due to the high density inside the positive and negative charge distribution. The external electric field can be neutralized in between those charge distributions. This allows recom-

bination processes with the emission of photons. The photons can then produce another avalanche. In the end, the avalanche covers large parts of the anode. One drawback of the Geiger mode is the large dead time after each pulse (50-100 μs).

3.3.7 Signal generation

The signal generation inside a gaseous detector is one of the key elements determining its capabilities and performance. The produced charge inside the gas volume must be registered at the readout electrode in order to be further processed by the electrical readout. The signal generation on an arbitrary readout electrode usually relies on the principle of induction. Thus, the charges do not need to physically reach the electrode. The charges moving towards the readout electrode are inducing charges. The induced charges on the electrode can be registered as a current signal, called induced current. The Shockley-Ramo theorem [56, 57] offers a convenient way to calculate the induced current i_S on the electrode i of an arbitrary (multi-)electrode setup by

$$i_{S,i} = q\vec{E}_{w,i}\vec{v}, \tag{3.23}$$

where q is the charge of the particle, e.g. electron, moving towards the electrode. $E_{w,i}$ is the weighting field of the electrode i. The weighting field is obtained by setting the potential of all electrodes $U_{j\neq i} = 0$, while keeping the potential $U_i = 1$.[7] $E_{w,i}$ is independent of the electric field inside the detector and only depends on the geometry of the electrodes. $\vec{v}$ denotes the velocity of the moving charge, where the electric field needs to be calculated and plays an important role.

3.4 Evolution of gaseous detectors

In 1908, H. Geiger and E. Rutherford introduced a single-wire counter operating in the Geiger mode [58]. Since then, the success of gaseous detectors has continued to grow, mainly profiting from the cost-effective coverage of large volumes. The modern era of gaseous detectors begins in 1968, when G. Charpak introduced a multi-wire proportional chamber (MWPC) [59]. In parallel, the development and availability of cheap and compact electronics in the early 1970s made it possible to readout larger detectors with even higher granularity. The development of MWPCs enabled the precision tracking of ionizing particles. The latest evolution in gaseous detectors is the micro-pattern gaseous detector (MPGD). MPGDs overcome the limitations of MWPCs in rate capability, resolution, flexibility of geometry and aging.

3.4.1 Proportional counter

A basic type of a gaseous detector working in proportional mode is the proportional counter. Typically, simple symmetric geometries are used, where the anode is a thin wire and the cathode is placed around the wire in the shape of a cylinder. The incident particle ionizes the gas atoms and the primary (and secondary) electrons are moving towards the anode wire. The electric field rises with $1/r$, where r is the distance to the wire. Reaching the anode wire, the electrons have enough energy to create an avalanche. With a proportional counter and modern readout electronics with low noise, the production of single electron-ion pairs in the gas volume can be observed. With a typical gain of 10^4, a charge of around 1 fC is registered at the anode being enough to be distinguished from electronics noise [45].

[7] The potential value is an arbitrary number and, for simplicity reasons set to 1, because the weighting field is independent of U_i.

3.4.2 Multi-wire proportional chamber

The development of MWPCs determines a milestone in the history of gaseous detectors. The basic detection principle is similar to the one of a proportional counter. It is also operating in proportional mode. The new concept consists of a pattern structure of the anode wires allowing for a precise position measurement of the incident particle. A stack of several layers of such detectors permits precision tracking of ionizing particles. MWPCs consist typically of a plane of parallel wires with a distance of $\mathcal{O}(1\text{ mm})$. Above and below the wires, the cathode planes close the active volume of the MWPCs. The distance between the anode wires and the cathode plane is typically 3 to 4 times larger than the wire spacing. Fig. 3.9 gives an idea about the geometry and illustrates the working principle of an MWPC. The

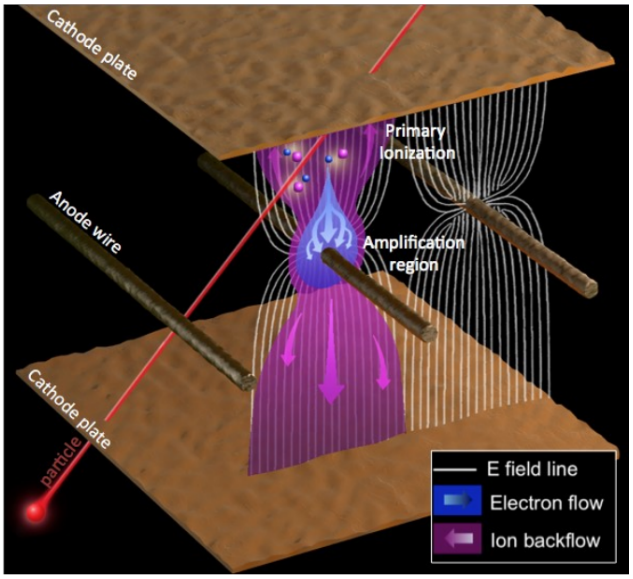

Figure 3.9: Working principle of an MWPC. The incident ionizing particle (red line) produces primary electron-ion pairs. The electric field lines are presented in white. The electron and ion flows are shown in blue and violet, respectively. The figure is taken from Ref. [13].

increasing demands of particle physics experiments, especially at the LHC, have revealed limitations in rate capability and granularity. The limitation in rate capability manifests itself in a decrease of the gas gain. The ions in the avalanche are slowly moving towards the cathode and generating a cloud of positive charges modifying the electric field around the anode. This causes a drop in gas amplification at particle fluxes above 10^4 Hz/mm^2 [53]. The granularity is limited due to the electrostatic repulsion of the anode wires, which results in a displacement of the wires. In general, it is difficult to reduce the wire spacing below $\mathcal{O}(1\text{ mm})$. The Cathode Strip Chambers of the CMS detector present an example of MWPCs operated in a high-energy physics experiment.

3.4.3 Micro-pattern gaseous detector

Micro-pattern gaseous detectors were developed with the main goal to overcome the limitations of MWPCs. The microstrip gas chamber (MSGC), as the first type of MPGDs, was introduced in 1988 by A. Oed [60] presenting an alternative to more expensive solid-state detectors for precision tracking in high rate environments. The main feature of the MSGC is a pattern of thin metal strips on a thin layer of an insulating substrate. The strips are alternatingly connected as cathodes and anodes. The small distance between anode and cathode reduces the travel time for ions in the detector drastically and, thus, prevents the build-up

of positive charge near the anode leading to a higher rate capability compared to MWPCs. Additionally, the small interstrip pitch gives a spatial resolution of the order of 100 μm.

This new technology also showed some weaknesses under sustained operation leading to imperfections on the electrodes. A high rate of destructive discharges can be the consequence [61]. Recent efforts led to the latest generation of MPGDs, e.g. micromegas[8] and GEM detectors. In the following, the two detector types are discussed with a focus on GEM detectors. In order to present alternatives to GEM detectors, the micromegas are discussed. Both types will be used in high-energy particle physics experiments: micromegas in ATLAS [62] and GEMs in CMS [10].

Micromegas Micromegas (MM) detectors were introduced in the mid-1990s [63]. Starting from the MWPCs, the fundamental idea is to replace the wire plane by a thin metallic micromesh. MM detectors consist typically of a drift electrode, a metallic mesh, and a readout board. The gas gap of a few millimeters between the drift electrode and the metallic mesh is called drift gap. The distance between the mesh and the readout electrode is around 100-150 μm. This gap is the amplification region with a large electric field of around 40 kV/cm. Variations of the distance of the amplification gap cause non-uniformities in the gas gain. The consequence is a degradation of the detector performance. To ensure a uniform amplification gap across the detector, insulating pillars can be inserted [62]. MM detectors will be used to reconstruct muons in the forward region of the ATLAS experiment. A schematic view of the ATLAS micromegas is shown in Fig. 3.10. Due to the small amplification gap

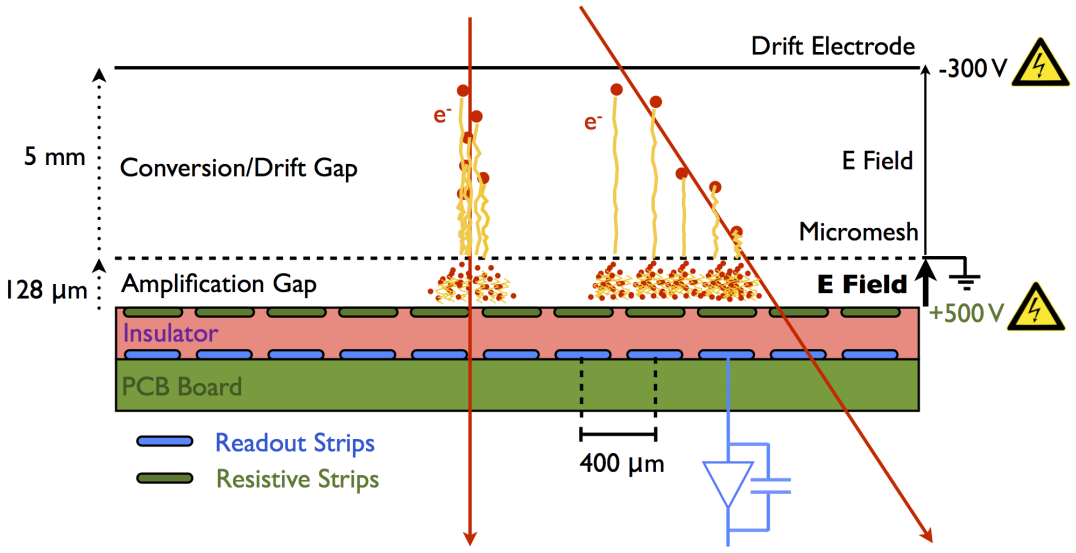

Figure 3.10: Working principle of micromegas for the ATLAS experiment at the LHC. The red arrows represent two examples of incident particles. The thick red points show the primary electrons drifting towards the micromesh. In the amplification region, an avalanche is sketched. The dimensions of the gaps are written on the left and the applied voltages on the right. The additional insulation layer (pink) protects the readout strips from discharges. The figure is taken from Ref. [64].

and fast collection of ions, the MM detectors have a higher rate capability than standard MWPCs [63]. A well-known challenge for MM detectors is the discharge rate. The rate can be decreased by using the drift gap as a pre-amplification region [65].

Gas Electron Multiplier The gas electron multiplier (GEM) detector was introduced in 1997 by F. Sauli [2]. GEM-based detectors are used in high-energy physics, as well as in

[8] An abbreviation for MICRO MEsh GAseous Structure.

several nuclear physics experiments, i.e. COMPASS [3], PHENIX [4], STAR [5], TOTEM [6], LHCb [7], and the CMS Phase-2 detector. Different types of the GEM technology have been developed over the years, e.g. thick GEMs [66] and μ-RWELL [67]. In the following, the standard GEM technology, as it is referred to in the literature, is described.

The heart of a GEM detector is the GEM foil, which consists of a thin (50 μm) layer of insulating polymer with a 5 μm layer of copper cladded on both sides. The foil is perforated with a hexagonal pattern of holes which is made by chemical etching. The hole pitch is typically 140 μm and the upper hole diameter is 70 μm[9]. The hole has a double semi-conical shape. In a simplified view, the shape is rotationally symmetric around the axis perpendicular to the foil plane. Thus, the hole shape is defined by three diameters, i.e. two outer diameters located on the top and bottom copper layer ($r_{\text{top}}, r_{\text{bottom}}$) and one inner diameter in the polymer (r_{middle})[10]. The hole dimensions depend on the etching procedure. There are two commonly used etching procedures: the single-mask and the double-mask technique [8]. Fig. 3.11 gives an overview of the main manufacturing steps performed during the two different production techniques. For large-size GEM foils, the single-mask procedure does not

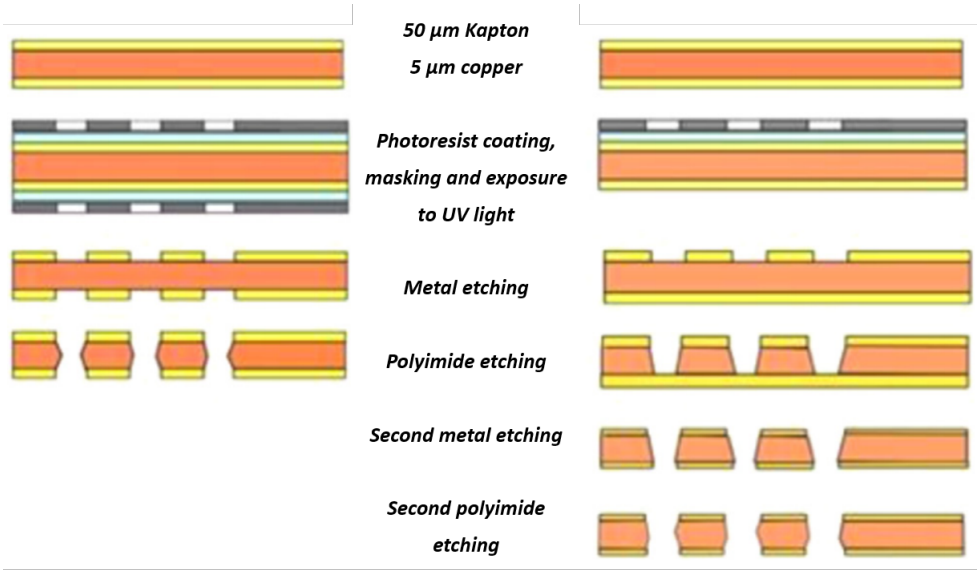

Figure 3.11: Illustration of the double-mask (left) and single-mask (right) manufacturing steps. The copper is depicted in orange, the polyimide in yellow color. The photoresistive mask is shown in gray color. The single-mask technique was developed to overcome alignment issues of upper and lower masks. The figure is taken from Ref. [8]. The text of the figure was re-written compared to the original figure due to bad readability.

need any alignment of top and bottom masks as in the double-mask procedure. On the other hand, with the double-mask technique one has a better control of the lower hole diameter and more symmetric holes can be etched. For the double-mask technique, the standard dimensions of the holes are $r_{\text{top}}/r_{\text{middle}}/r_{\text{bottom}}$ = 70/50/70 μm. The foils produced with the single-mask technique and having the same upper diameter of 70 μm, typically have a larger lower diameter. This leads to standard dimensions of 70/53/85 μm. Fig. 3.12 (left) contains a picture of a GEM foil taken with an optical microscope in a clean room in Aachen. Fig. 3.12 (right) shows a Scanning Electron Microscope picture of a GEM foil.

The detection principle is illustrated in Fig. 3.13. The GEM foil is surrounded by a gas

[9]The thickness of the layers, as well as the hole pitch and the hole diameters, are the standard GEM foil dimensions. Other thicknesses are also realized, e.g. in thick GEMs (THGEM).

[10]This holds, if the inner diameter is centered along the depth of the foil. For typical hole shapes investigated in this thesis, this is a good assumption.

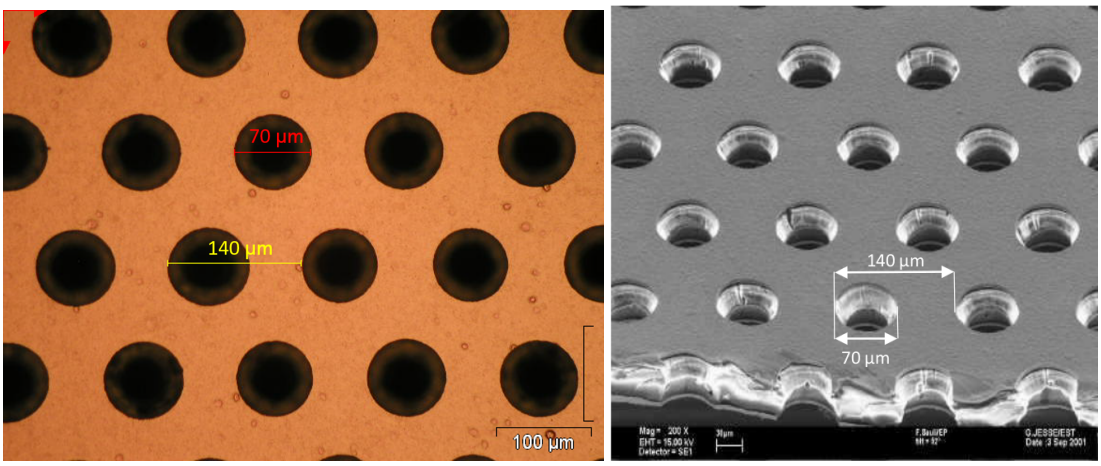

Figure 3.12: Left: Picture of a GEM foil produced by TECHTRA©. The hexagonal pattern of GEM holes with a pitch of 140 μm is depicted. The outer diameter of the holes is 70 μm. The picture was taken with an optical microscope in a clean room in Aachen. Right: Scanning Electron Microscope picture of a GEM foil. The polyimide foil with copper cladded on both sides can be seen. The arrows indicate the hexagonal pattern of holes with a pitch of 140 μm and an outer diameter of 70 μm. The figure is taken from Ref. [8].

volume. When an ionizing particle crosses the volume, primary electron-ion pairs are produced. Guided by an electric field, the electrons drift towards the GEM foil. A high electric field of around 60 kV/cm guides the electrons inside the holes and leads to the acceleration of electrons and, as a consequence, to gas amplification. Typically, an amplification factor of around 20 can safely be reached for one GEM foil.

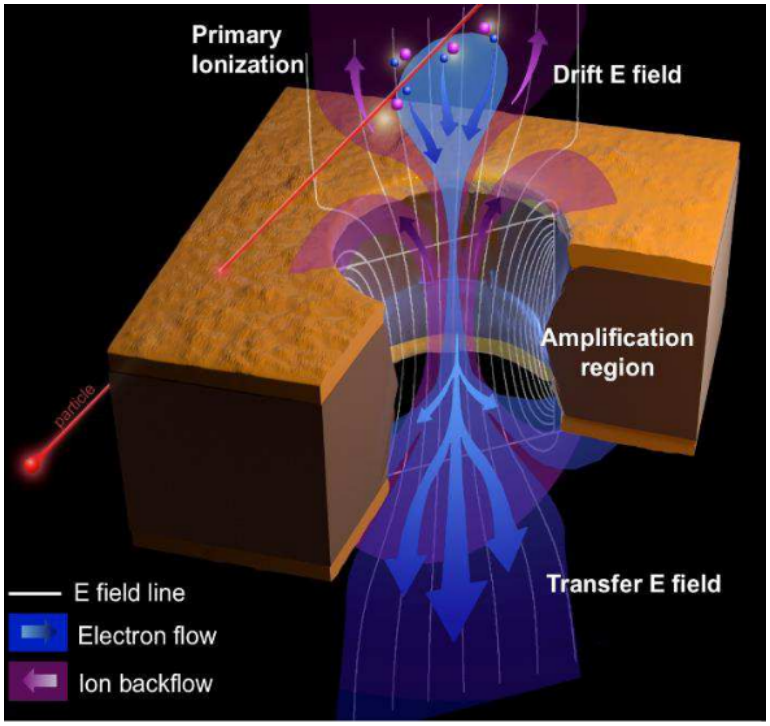

Figure 3.13: The working principle of a GEM foil. The red line indicates the path of an ionizing particle. The electric field lines are presented in white. The ion and electron flow are shown in purple and blue, respectively. The figure is taken from Ref. [10].

Triple-GEM technology The triple-GEM technology is equipped with a stack of three GEM foils. Consequently, three stages of amplification lead to a total amplification of $20^3 \approx 10^4$. In principle, one could also reach this amplification factor with a single or double-GEM detector. The drawback would be a higher discharge probability due to a higher electric field inside one foil. The triple-GEM detector is less affected by discharges (see Fig. 3.14). A

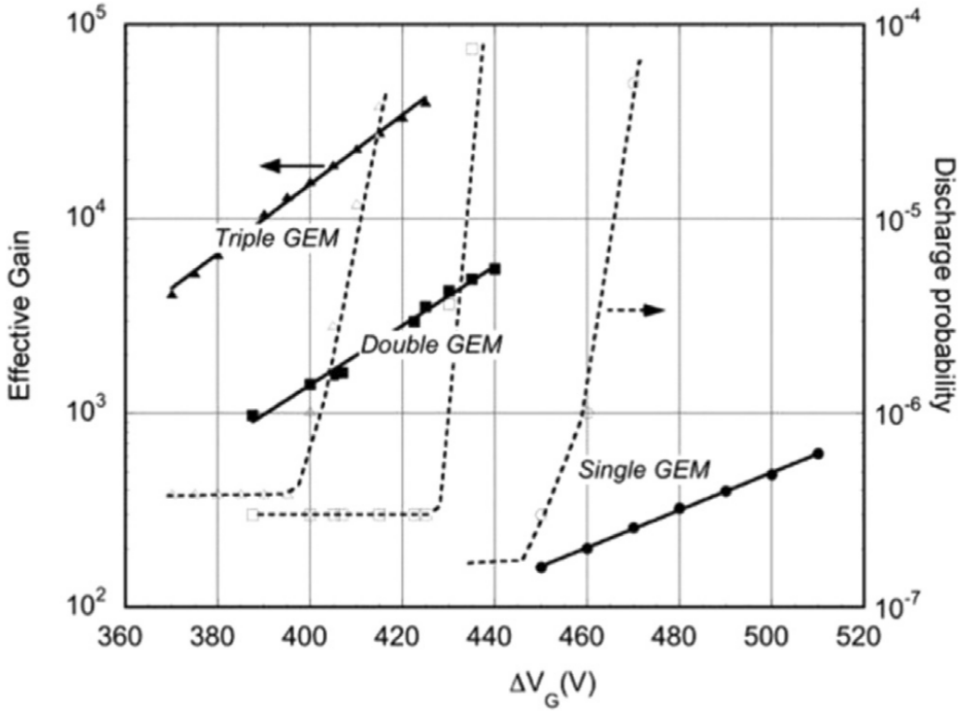

Figure 3.14: Effective gain (solid line) and discharge probability per incident α particle (dashed line) as a function of the GEM voltages ΔV_G. The curves are shown for the single-, double- and triple-GEM configurations. For the double-GEM and triple-GEM configurations, ΔV_G is the same for all GEM foils. The figure is taken from Ref. [8].

small hierarchy in the voltage differences applied to the three GEM foils (highest potential to the first GEM foil) can further help to reduce the discharge probability [68]. The discharge probability is a decisive factor for the longevity of the detector and its readout electronics.

Besides the stack of three GEM foils, a triple-GEM detector hosts the drift board and the readout board. These boards enclose the GEM stack and, together with the gas frames, close the gas volume of the chamber. In total, there are 7 electrodes (one electrode for the drift board and six electrodes for the three GEM foils), which need to be powered. The readout board is set to the electrical ground. The gap between the drift board and the upper GEM foil is called the drift gap. The gaps in between foils are called transfer gaps. The gap between the lower GEM foil and the readout board is called the induction gap. As an example, Fig. 3.15 presents the cross-section of the CMS triple-GEM chamber with gaps of 3/1/2/1 mm.

Due to the micro-pattern structure of the foils, a fast collection of the ions on the electrodes is achieved and, thus, GEM detectors are expected to sustain a high rate. Indeed, a rate capability of 100 MHz/cm^2 [8] has been measured for a GEM foil, exceeding those of MWPCs by several orders of magnitude. For triple-GEM detectors, recent R&D studies in the CMS GEM group show a decent behavior of gas gain up to 10 MHz/cm^2 [69].

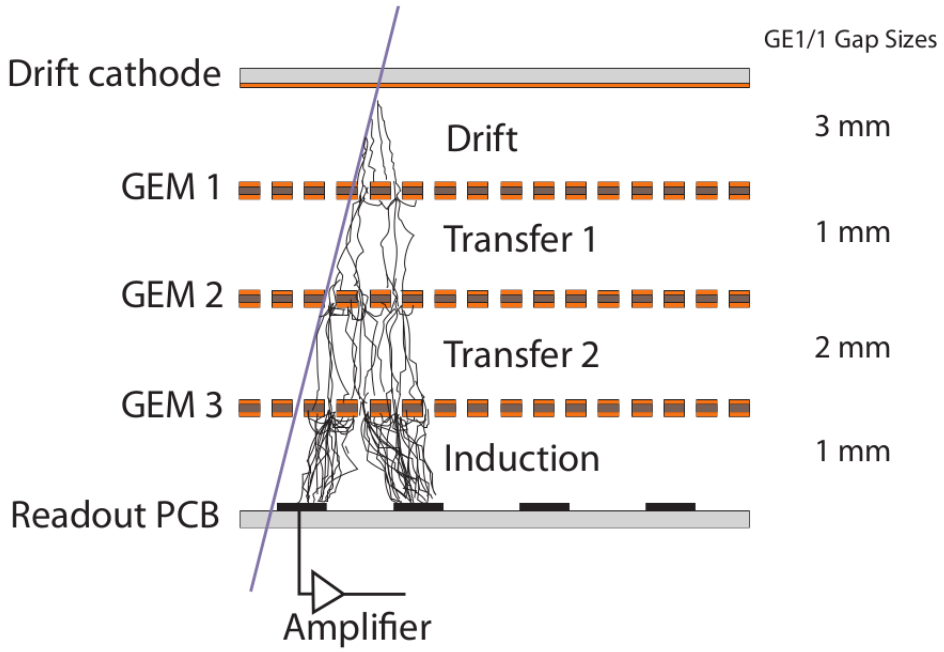

Figure 3.15: Sketch of the cross-section of a triple GEM chamber used for the CMS experiment consisting of a drift cathode, three GEM foils and a readout board [10]. A detailed description of the figure can be found in Sec. 5.2.2.

4 The CMS detector at the LHC and beyond

This section is devoted to the introduction of the LHC (Sec. 4.1) and the CMS detector (Sec. 4.2). Sec. 4.3 describes the LHC and CMS detector upgrades foreseen for the Phase-2 period.

4.1 The LHC

The Large Hadron Collider (LHC) is a circular particle accelerator with a circumference of 26.7 km. It is located underground near Geneva at the European Center For Nuclear Research (CERN). The LHC accelerates bunches of protons or lead ions in two opposite rings providing collisions to ATLAS [70], ALICE [71], CMS [72], and LHCb [73] at four interaction points. Before the particles enter the LHC, they go through the so-called injector chain of the LHC which is a series of pre-accelerators [74]. For the proton case, the particles are injected into the LHC with an energy of 450 GeV and are accelerated using RF cavities to the final energy of nominally 7 TeV. In 2010, the LHC was successfully commissioned for proton-proton collisions. The lifetime of the LHC consists, very coarsely spoken, of periods of data taking, called Runs, and periods of shutdown, called Long Shutdowns (LS)[1]. In the beginning of the high-energy operations, the LHC delivered collisions with a center-of-mass energy of $\sqrt{s} = 7$ TeV. In 2012, in the second part of the Run-1 period, the center-of-mass energy increased to 8 TeV. After some consolidation actions during Long Shutdown 1 (LS1), the LHC has operated at 13 TeV for the Run-2 period until the end of 2018 providing proton-proton collisions with the largest center-of-mass energy ever produced by mankind so far. A detailed description of the LHC can be found in Ref. [75]. The following discussion of the LHC and its evolution towards the HL-LHC is based on Ref. [76].

4.1.1 The LHC and accelerator basics

The main goal of the LHC is to provide a high rate of particle collisions to the experiments. The number of events per second of a given physics process $\mathcal{N}_{\text{proc}}$ produced by the LHC is given by

$$\mathcal{N}_{\text{proc}} = \mathcal{L} \cdot \sigma_{\text{proc}}, \tag{4.1}$$

where σ_{proc} is the cross section of the physics process under study and $\mathcal{L}$ is the instantaneous luminosity. To change the rate of produced events, the cross section or the luminosity must be changed.

LHC luminosity The (instantaneous) luminosity of the LHC can be written as [76]

$$\mathcal{L} = \gamma \frac{n_b N^2 f_{rev}}{4\pi\beta^* \epsilon_n} R, \qquad R = 1/\sqrt{1 + \frac{\theta_c \sigma_z}{2\sigma}} \tag{4.2}$$

where γ is the relativistic gamma factor, n_b the number of bunches per beam, N the number of particles per bunch, f_{rev} the revolution frequency, β^* the beta function at the interaction point (IP), ϵ_n the normalized transverse beam emittance, and R the geometric luminosity

[1] The term *Long Shutdown* allows to distinguish this period from the Year End Technical Stop (YETS), which is scheduled between years of data taking.

reduction factor due to the crossing angle at the IP omitting the Hourglass effect[2]. θ_c is the full crossing angle between colliding beams, while σ and σ_z denote the transverse and longitudinal RMS beam sizes. The LHC has performed extraordinary well in terms of luminosity delivered to the experiments. Exemplary, the evolution of the total integrated luminosity delivered to the CMS detector is shown in Fig. 4.1 for the Run-1 and Run-2 data taking periods. In total, Run-1 and Run-2 led to almost 200 fb^{-1}.

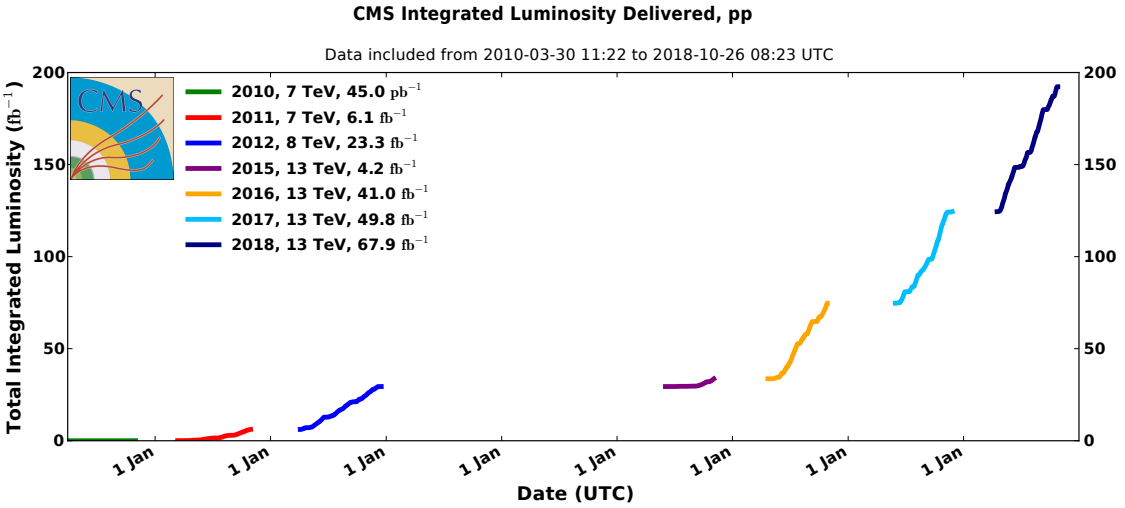

Figure 4.1: Total integrated luminosity delivered to the CMS detector from 2010 to 2018 [78]. The years, where no line is shown, are years of a shutdown of the LHC. At the beginning and end of every year of operation, there is a technical stop of the LHC. The years 2010-2012 belong to the Run-1 data taking period, while the years 2015-2018 belong to the Run-2 period.

LHC performance parameters In Tab. 4.1, the nominal LHC performance parameters are summarized, together with the parameters during Run-2 operations in 2018.

Parameter	Nominal (design report)	Run-2 (2018)
Number of bunches per beam n_b	2808	2556
Number of particles per bunch N (10^{11})	1.15	1.25
Bunch spacing (ns)	25	25
Revolution frequency f_{rev} (kHz)	11.2	11.24 [79]
β^* at IP (m)	0.55	0.30
Normalized transverse beam emittance ϵ_n (μm)	3.75	≈ 1.9
Crossing angle θ_c (μrad)	285	320-260
Beam energy in collision (TeV)	7	6.5
Total beam energy (MJ)	362	332
Peak Luminosity at IR1/IR5 (10^{34}cm^{-2}s^{-1})	1.18	2.1

Table 4.1: List of nominal values of the LHC performance parameters [80] and the corresponding values from 2018 [81] for proton-proton collisions. The interaction regions, IR1 and IR5, belong to the ATLAS and CMS experiments, respectively. The ϵ_n and N values are valid when the LHC operation is in the beginning of the stable beam mode. The time between two consecutive bunches is called bunch spacing.

[2] An explanation of what is meant by the Hourglass effect in this context is given in Ref. [77].

Cross sections of LHC physics The cross section of a process under study is fully determined by theoretical considerations. Consequently, the cross section itself is not relevant for accelerator physics. However, the cross section varies with the energy of the incoming particles, or - in the case of the LHC accelerator - with the center-of-mass energy which is, again, a parameter that is fixed by the setup and not by theory. Fig. 4.2 shows selected standard model cross sections including the total proton-proton (pp) cross section over a large window of center-of-mass energies.

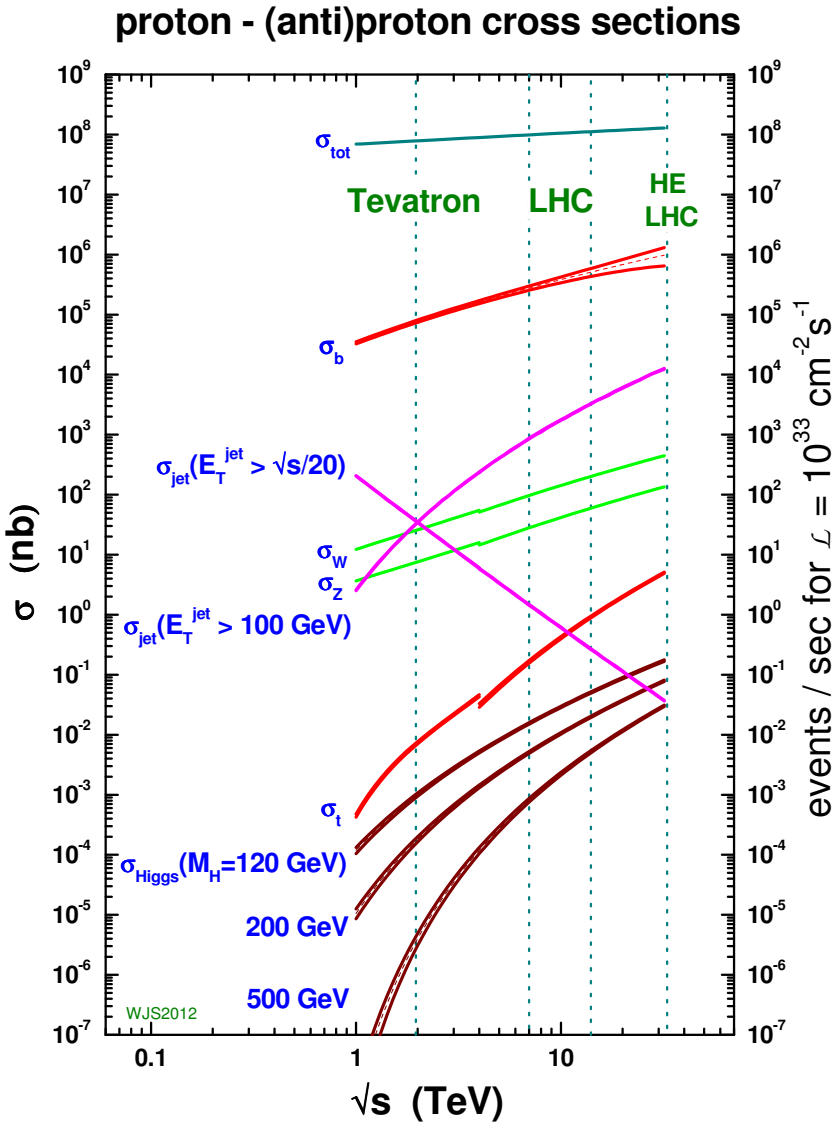

Figure 4.2: Standard model cross sections including total pp cross section at proton-(anti)proton colliders as a function of the hadronic center-of-mass energy [82]. The total pp cross section is based on a parametrization of the Particle Data Group. All other cross sections are calculated at either NLO or NNLO pQCD, using MSTW2008 parton distributions. The lack of continuity in some of the curves is due to the fact, that for $\sqrt{s} < 4$ TeV the cross sections are valid for proton-antiproton colliders and for $\sqrt{s} > 4$ TeV the cross sections are valid for proton-proton colliders.

LHC superconducting magnets The working principle of the LHC relies on superconducting multipole magnets. Inside the LHC tunnel, 1232 main dipole (15 m long) and 392 main quadrupole (3 m long) magnets are installed to steer the particle beam and collimate the beam bunches. Additionally, around 6000 superconducting corrector magnets are put underground. Around the interaction regions (IRs), dedicated quadrupoles and dipoles are inserted [83]. The cutting-edge technology of the superconducting magnets consists of cooling the NbTi superconductor material down to 2 K using superfluid helium allowing operation at magnetic fields above 8 T.

Due to cost-saving measures, the already existing tunnel of the Large Electron-Positron (LEP) collider has been used after its decommissioning in 2001 for the LHC project. This brings some constraints to the design of the LHC beam pipe, mainly because of the limited space inside the tunnel. With an internal diameter of 3.7 m, it is extremely challenging to install two completely separate proton rings. To overcome this challenge, the twin-bore magnet design has been adopted for the LHC which was introduced by John Blewett at the Brookhaven laboratory in 1971. A drawback of the twin-bore magnet solution is that the rings are magnetically coupled.

4.2 The CMS detector

In the beginning, a general description of the Compact Muon Solenoid (CMS) detector is provided. A more detailed discussion of the individual subdetectors of CMS is presented afterwards. The upgrades of the CMS detector for the Phase-2 data taking period are described in Sec. 4.3. This section is based on Ref. [72].

4.2.1 General information

The CMS detector at the LHC is installed about 100 meters underground close to Cessy, France. It is designed to provide the full coverage of the interaction region and high-precision measurement of the particles coming from the interactions of the colliding beams. The detector consists of a barrel region and two endcap regions. As the naming suggests, a core piece of the CMS detector is the superconducting solenoid, which provides a magnetic field to the CMS detector volume. Inside the solenoid, there is a homogeneous magnetic field of 3.8 T along the beam line direction. Due to the existence of the magnetic field, charged particles inside the detector volume are bent which allows measuring their momentum. The innermost (closest to the beam line) subdetectors of CMS are the pixel and outer tracker. Going outwards, the electromagnetic calorimeter (ECAL) and the hadronic calorimeter (HCAL) can be found. Outside of the superconducting solenoid, muon detectors are installed forming the muon system. To confine the magnetic field outside the solenoid, magnet return yoke made of iron is interleaved with the muon chambers. In total, the CMS detector measures 28 m in length, 15 m in width and 15 m in height and it weighs about 14×10^3 t, where the iron return yoke contributes to a large extent. Fig. 4.3 provides a perspective view of the CMS detector.

4.2.2 Coordinate system

To allow a description of positions and directions, a spatial coordinate system needs to be established for the CMS detector. The definition of the right-handed Cartesian coordinate system consists of setting the origin to the nominal interaction point (center of the CMS detector) and letting the x-axis point towards the center of the LHC. The y-axis points upwards and the z-axis points in the beam direction. For some calculations, it is more convenient to

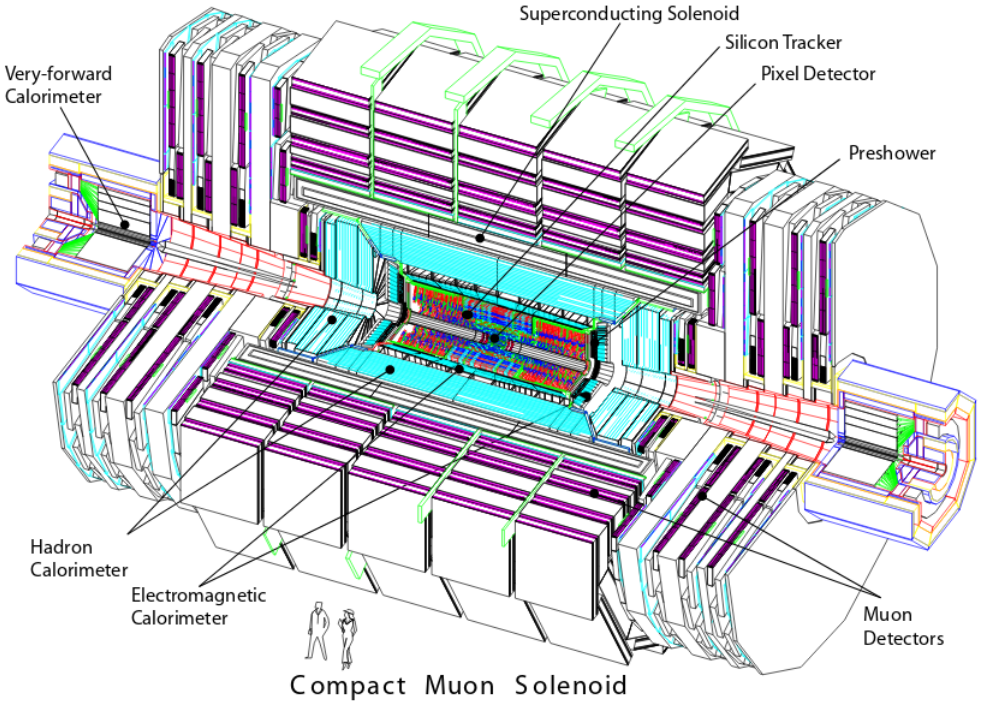

Figure 4.3: Perspective view of the CMS detector and its subdetectors [72].

use spherical coordinates instead of Cartesian coordinates. The azimuthal angle ϕ is measured in the $x-y$ plane starting from the x-axis. The polar angle θ is measured starting from the z-axis. One can transform the polar angle by writing

$$\eta = \ln\left(\tan\frac{\theta}{2}\right).$$

η is called pseudorapidity. Transforming the polar angle into the pseudorapidity makes sense because, for relativistic particles, differences in pseudorapidity are invariant under Lorentz transformations and, thus, better to handle in physics analyses. Another useful quantity is defined by

$$\Delta R = \sqrt{\Delta\eta^2 + \Delta\phi^2},$$

which is the distance of two different vectors (directions) in the $\eta - \phi$ plane. The x and y components of the momentum and energy of a particle make up the transverse momentum, p_T, and the transverse energy, E_T, of a particle. Consequently, the missing transverse momentum, p_T^{miss}, is the imbalance of momentum measured in the transverse plane.

4.2.3 Solenoid magnet

One of the main parts of the CMS detector is the superconducting solenoid magnet [84, 85]. The 4-layer winding superconducting solenoid is made of a stabilized reinforced NbTi conductor with a cold mass of 220 t. The dimensions of the solenoid are enormous: 6.3 m cold bore diameter, 12.5 m length. The radial thickness of the cold mass is 312 mm, resulting in a radiation thickness of the cold mass of 3.9 X_0[3]. The magnet is designed to provide a

[3]The radiation length X_0 gives, among other interpretations, the distance, that a high-energetic electron travels inside a material until it loses all but $1/e$ of its initial energy. X_0 is given in g/cm^2. Ref. [86] provides further details and value tables.

4 T magnetic field in the central region of CMS. During the Phase-1 period of the LHC, the magnet of CMS provides $|B| = 3.8$ T in the center of CMS. Once the aging behavior of the coil is better understood, one might re-evaluate the possibility to increase the magnetic field to the design value of 4 T [87]. A full prediction of the magnetic field strength and field lines inside the CMS cavern is shown in Fig. 4.4. At full current and with $|B| = 3.8$ T, an energy of 2.6 GJ is stored in the magnet. In order to return the flux, iron yoke is installed around the solenoid. Three layers of return yoke can be found in the barrel, as well as in each of the endcaps. The different layers of the iron yoke are depicted in Fig. 4.4. The total amount of iron yoke sums up to around 10 000 t.

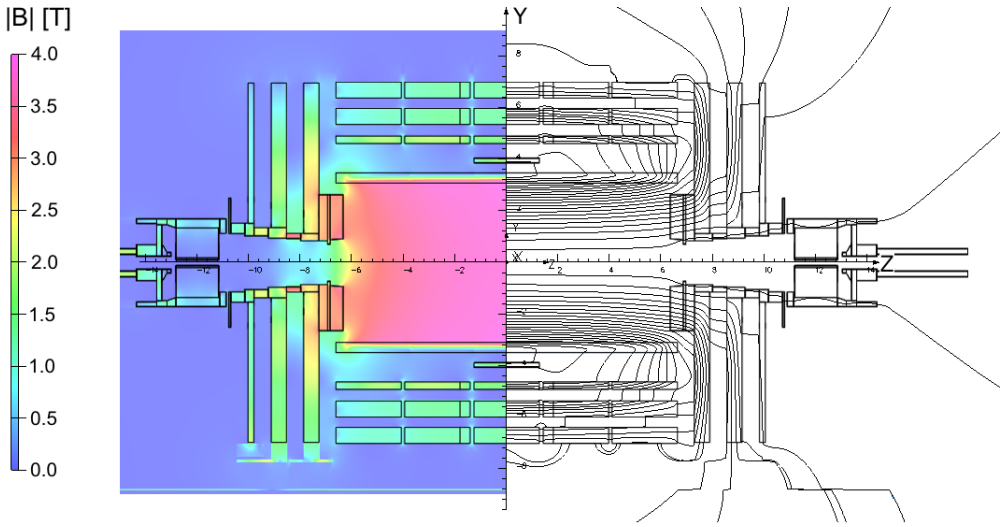

Figure 4.4: Magnet field value $|B|$ and field lines for the longitudinal cross-section of the CMS detector [87]. The prediction is based on the assumption of $|B| = 3.8$ T in the center of CMS. Every field line stands for a magnetic flux increase of 6 Tm^2.

4.2.4 Tracker

The subdetector closest to the beam line and, thus, closest to the proton-proton interactions is the tracker detector [88, 89]. The general purpose of the tracker is to efficiently and precisely measure the trajectory[4] of particles coming from the interaction region. One can deduce the momentum of a particle by measuring the bending of its trajectory in the magnetic field. Since the tracker provides precise tracking hits in r-ϕ and z, secondary vertex reconstruction can be performed in CMS. With its length of 5.8 m and its diameter of 2.5 m, it surrounds the interaction point. The endcaps of the tracker extend the pseudorapidity coverage to $|\eta| < 2.5$. The design of the tracker is motivated by various demands on the system. To ensure highly efficient and precise tracking, high granularity is needed. During LHC operation, around 1000 particles are expected to travel through the tracker for each bunch crossing, leading to a hit rate density of 1 MHz/mm^2 at a radius of 4 cm, which requires a fast response of the tracker[5]. Large particle fluxes are additionally increasing the risk of radiation damages and preventing longevity. To engage all of the above-mentioned challenges, the tracker design entirely relies on the silicon detector technology.

A schematic view of the tracker design of the CMS tracker is given in Fig. 4.5.

[4] In the following, the abbreviation track is also used for trajectory.
[5] The hit rate is decreasing to $\mathcal{O}$(kHz/mm^2) for larger radii of around 1 m.

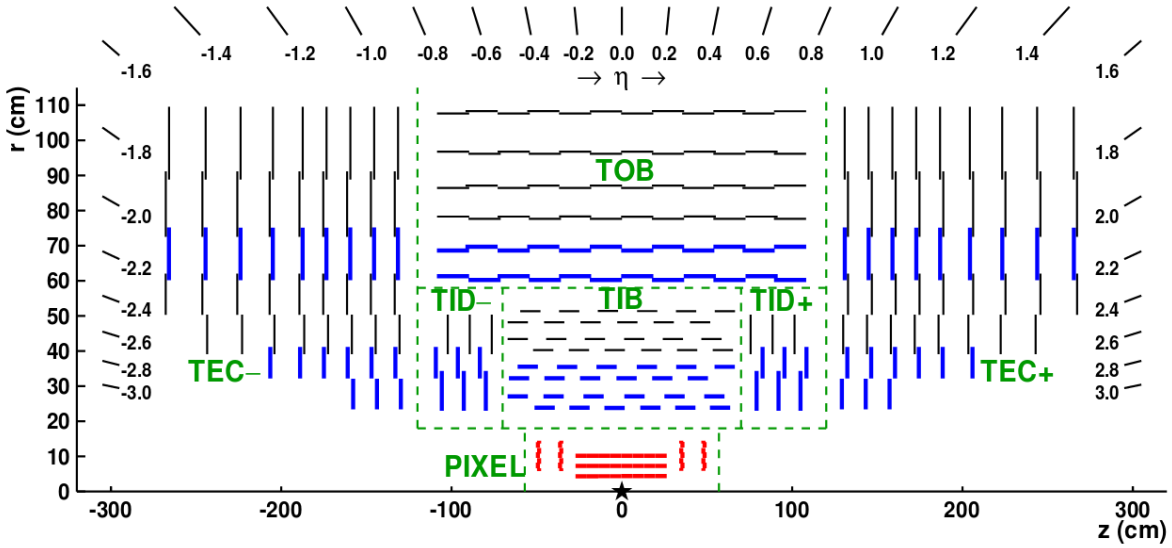

Figure 4.5: Schematic cross-section of the CMS tracker in the r-z plane, taken from Ref. [90]. The tracker design is symmetric with respect to rotations around the $z-$axis. The star at $r, z = 0$ indicates the approximate interaction point in the middle of the detector. In green, one can see the abbreviations for the different tracker subsystems and the green dashed lines help to separate which modules belong to which subsystem. Thin, black lines represent strip tracker modules providing two-dimensional hits, while thick, blue lines stand for the modules giving three-dimensional hits. The pixel layers are shown in thick, red color.

Pixel tracker The inner pixel detector includes three cylindrical barrel layers at $r = 4.4, 7.3$ and 10.2 cm and two pairs of endcap disks at $z = \pm 34.5$ and ± 46.5 cm. Overall, the 1440 modules include 66 million pixels and cover an area of 1 m^2. Each pixel of a module consists of a 285 μm thick silicon tile with dimensions of 100×150 μm^2 in $r\phi \times z$ coordinates. A charged particle traversing the silicon pixels creates electron-hole pairs. Together with the electric current applied to the modules, it gives rise to a signal that can be read out. Due to the powering of a large number of pixels, the detector heats up. The heating up is mitigated by mounting the pixels on cooling tubes. The pixel tracker provides three-dimensional (3D) position measurements. In the transverse plane, the hit position resolution is around 10 μm, and for the longitudinal direction around 20-40 μm due to the shape of the pixels.

Strip tracker The outer tracker consists of different submodules, namely the Tracker Inner Barrel (TIB) and Disks (TID), covering $20\,\mathrm{cm} < r < 55$ cm and $58\,\mathrm{cm} < |z| < 124$ cm. The TIB includes four cylindrical layers, while the TID consists of 4 disks. In the endcaps, there are the Tracker Outer Barrel (TOB) and Tracker Endcaps (TECs), covering $55\,\mathrm{cm} < r < 116$ cm and $124\,\mathrm{cm} < |z| < 282$ cm. The TOB comprises six cylindrical layers, while the TEC consists of 9 disks. The TIB, TID and inner four TEC rings have silicon strips of 320 μm thickness, while for the TOB and the outer three TEC rings silicon strips of 500 μm thickness are used. The strip pitch differs for all subsystems and is around 100 μm. The outer strip tracker counts in total $15\,148$ silicon modules or 9.3 million strips, covering a surface of about 198 m^2. 3D position measurement is not only possible in the pixel tracker, but also in some parts of the strip tracker, where a second strip detector module is mounted back-to-back to another module with a stereo angle of 100 mrad (shown as thick, blue lines in Fig. 4.5). Hits coming from these modules are called stereo while the others are called mono.

4.2.5 Calorimeter system

Electromagnetic calorimeter The main task of the electromagnetic calorimeter (ECAL) [91] is the detection of electrons, positrons, and photons. Even hadrons or MIPs can deposit a non-negligible and detectable amount of energy in the ECAL. The detection principle relies on the fact that these particles cause electromagnetic showers in the material of the calorimeter.

For CMS, high-resolution and high-granularity crystals are used as the calorimeter material. With its large Z (nucleus charge number) value, lead tungstate fulfills the requirements. This choice of material ensures a compact calorimeter thanks to its large density and small radiation length. On top, the light decay time is in the order of one LHC bunch crossing for 80% of the light yield, allowing a fast readout. In total, the ECAL consists of 61 200 lead tungstate ($PbWO_4$) crystals mounted in the barrel part, and 7 324 crystals in each of the two endcaps. In order to detect the photons of the electromagnetic shower, in the barrel, Avalanche Photodiodes (APDs) and, in the endcaps, vacuum phototriodes (VPTs) are used. The crystals emit blue-green scintillation light with a broad maximum at $420 - 430$ nm [92, 93]. The light output is relatively low: at 18°C about 4.5 photoelectrons per MeV are collected in both APDs and VPTs [94].

The energy resolution of the ECAL is measured to be

$$\frac{\sigma}{E} = \frac{2.8\%}{\sqrt{E/\text{GeV}}} \oplus \frac{12\%}{E/\text{GeV}} \oplus 0.3\%, \tag{4.3}$$

combining the stochastic, noise and constant term [95]. The errors are combined in quadrature.

Hadronic calorimeter The hadronic calorimeter (HCAL) [96] serves as a device for measuring the energy of hadrons and hadronic jets. With its large coverage, the HCAL contributes to a meaningful measurement of p_T^{miss}. To measure the position, energy, and arrival time of the particles, an active scintillation material is interleaved with an absorber material.

The HCAL is the outermost subdetector which is still located inside the solenoid coil. This restricts the radial size of the HCAL between the outer extent of the electromagnetic calorimeter (r = 1.77 m) and the inner extent of the solenoid (r = 2.95 m) and, consequently, it restricts the total material that can be placed there. The hadron barrel calorimeter (HB) covers a pseudorapidity range of $|\eta| < 1.3$. The HB is about 79 cm deep at $\eta = 0$ corresponding to 5.15 hadronic interaction lengths. Thus, the installation of the hadron outer calorimeter (HO) outside the solenoid as a *tail catcher* of deeply penetrating hadronic showers is needed. The hadron endcap calorimeter (HE) occupies $1.3 < |\eta| < 3.0$. The absorber material was chosen to be a specific type of brass, which consists of copper (70%) and zinc (30%) having an interaction length of 16.42 cm. It is complemented by plates of steel. The scintillation materials for the HB and HE subsystems are selected to fulfill the requirements of radiation hardness and long-term stability. In the very forward region and far outside (11.2 m from the interaction region), the hadron forward calorimeter (HF) allows extending the coverage up to around $|\eta| = 5$. The HF relies on a Cherenkov-based, radiation-hard technology.

In order to determine the energy resolution of charged pions, test beam studies have been performed with the complete calorimetric system resulting in

$$\left(\frac{\sigma}{E}\right)_{\text{pions}} = \frac{127\%}{\sqrt{E/GeV}} \oplus 6.5\%. \tag{4.4}$$

The total resolution is given by a stochastic term and a constant contribution [97].

4.2.6 Muon system

The name given to CMS is already suggesting that measuring muons belongs to the main goals of the detector. Interleaved with the iron yoke to return the magnetic field lines, the muon system is the outermost subdetector system in CMS. Since all other detectable SM particles coming from the interaction point should end up in either the electromagnetic or the hadronic calorimeter, only muons are left to detect[6]. The importance of the muon system for CMS is undoubtedly high with respect to the event trigger, muon reconstruction, and offline analysis.

The main goal of the CMS muon system is to efficiently and precisely reconstruct muons by itself (*standalone*), as well as together with the information coming from the tracker. The performance of the muon system must be excellent over the large range of possible muon momenta from $\mathcal{O}(\text{GeV})$ to $\mathcal{O}(\text{TeV})$.

The CMS muon system with its three subsystems, namely the Drift Tubes (DTs), the Cathode Strip Chambers (CSCs) and the Resistive Plate Chambers (RPCs), will be discussed in the following. Fig. 4.6 shows a quadrant of the CMS detector, highlighting the muon system. The following considerations are based on Ref. [98]. This section summarizes the details of the CMS muon system, while the general working principle of gaseous detectors is discussed in Sec. 3.

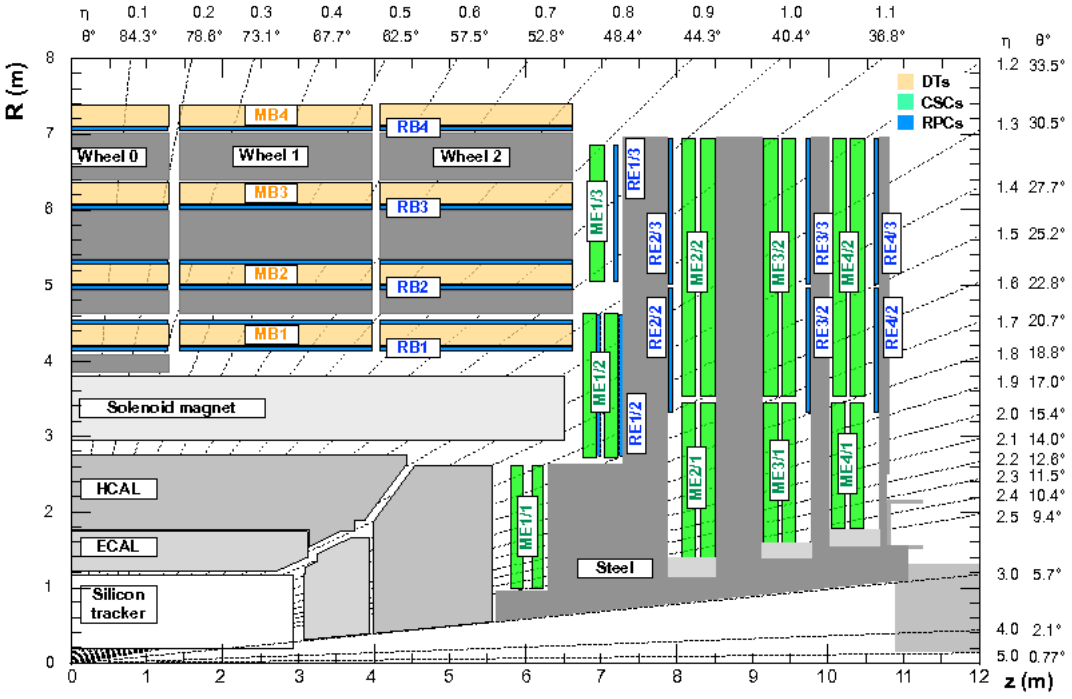

Figure 4.6: R-z cross-section of a quadrant of the CMS detector. The three different muon subsystems are highlighted. In the barrel region, the positions of the DTs (MB) and RPCs (RB) are depicted. The detectors in the barrel are organized in cylindrical wheels enclosing the magnet. Each wheel consists of 4 stations, where the first station is the innermost. In the endcaps, the positions of CSCs (ME) and RPCs (RE) are shown. The endcap muon system is divided into 4 stations, counting along the z-axis. The stations accommodate up to 3 rings. The figure is taken from Ref. [99].

[6]Neutrinos escape the detector without leaving any signal. They contribute to the missing transverse momentum in an event.

Drift Tubes Muon chambers based on the drift tube technology are located in the barrel region of the CMS detector up to $|\eta| = 1.3$. The drift tube technology can be used in this region of the CMS detector, because the expected detector occupancy is low compared to the forward region at higher η.

The chambers are arranged in 5 wheels. Each of the wheels contains 4 cylindrical stations. The wheels are identical in terms of chambers except for the wheels ± 1, where a cryogenic chimney is reducing the available space. Summing up the wheels, there are 60 chambers installed in each of the three innermost stations, and 70 chambers in the fourth station. A drift-tube chamber contains 3 (or 2 for the fourth muon station) Superlayers (SL). Each SL is made of 4 layers of staggered drift cells, the smallest unit of the DT chambers. In total, the DT system contains 172 000 sensitive wires. A sketch of the rectangular design of the drift cell is presented in Fig. 4.7.

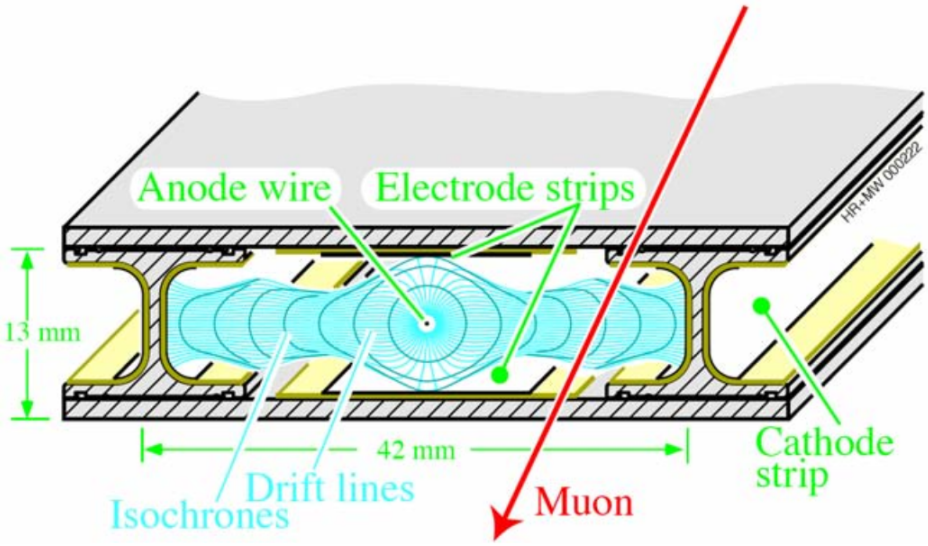

Figure 4.7: Sketch of the rectangular design of a drift cell. The anode wire is shown together with the electrode and cathode strips shaping the electric field inside the drift cell. The light blue lines indicate the electron drift lines. The dimensions of the drift cell are depicted in green. The figure is taken from Ref. [72].

High voltages are applied to the electrodes creating a strong electric field around the anode wire. The drift cell is filled with Ar/CO_2 (85%/15%). The chosen design of the drift cell is subject to various restrictions. The wire length is limited by the longitudinal space inside the iron yoke. The transverse dimension of the cell is motivated by the calculation of the electron drift time in Ar/CO_2 (85%/15%): 380 ns for 21 mm. This design ensures negligible occupancy while keeping the number of active channels low.

The orientation of the wires varies inside a DT chamber for the three SLs. The wires of the two outer SLs are oriented parallel to the beam axis providing a measurement in ϕ direction, which corresponds to the bending direction of the muons. The inner SL is equipped with wires oriented orthogonal to the beam line providing a measurement in z direction. In the fourth station, the inner SL is missing, resulting in only a ϕ measurement. For a single DT chamber, a global resolution in $r - \phi$ of 100 μm has been achieved. Not only the position measurement is essential, but also a precise time-tagging. An SL is capable of excellent time-tagging with a resolution of ≈ 3 ns [100]. This plays an important role in local and standalone reconstruction, as well as in identifying the correct bunch crossing for muons.

Cathode Strip Chambers The Cathode Strip Chambers (CSCs) belong to the class of multi-wire proportional chambers. Similar to the DT chambers, the working principle relies on gas ionization and electron multiplication. Fig. 4.8 (a) shows the cross-section of a chamber to illustrate the detection principle.

The CSC detectors are inserted in the CMS endcaps at pseudorapidities in the range of $0.9 < |\eta| < 2.4$. For the overlap region of the barrel and endcap ($0.9 < |\eta| < 1.2$), particles from the interaction region travel through both the DTs and the CSCs. For $0.9 < |\eta| < 1.6$, the CSCs are complemented by the RPCs which will be discussed in the following paragraph.

The total number of CSCs in CMS is 468. They can be found in the different disks of the endcaps. A single chamber has a trapezoidal shape and covers either $10°$ or $20°$ of the disk. The biggest CSC detector installed in CMS is 3.4 m long and 1.5 m wide. The CSC modules contain 6 planes of anode wires interleaved with 7 cathode panels with milled strips resulting in 6 gas gaps per chamber. The wires run azimuthally and the strips radially (with a constant $\Delta\phi$). The layout of a CSC is presented in Fig. 4.8 (b).

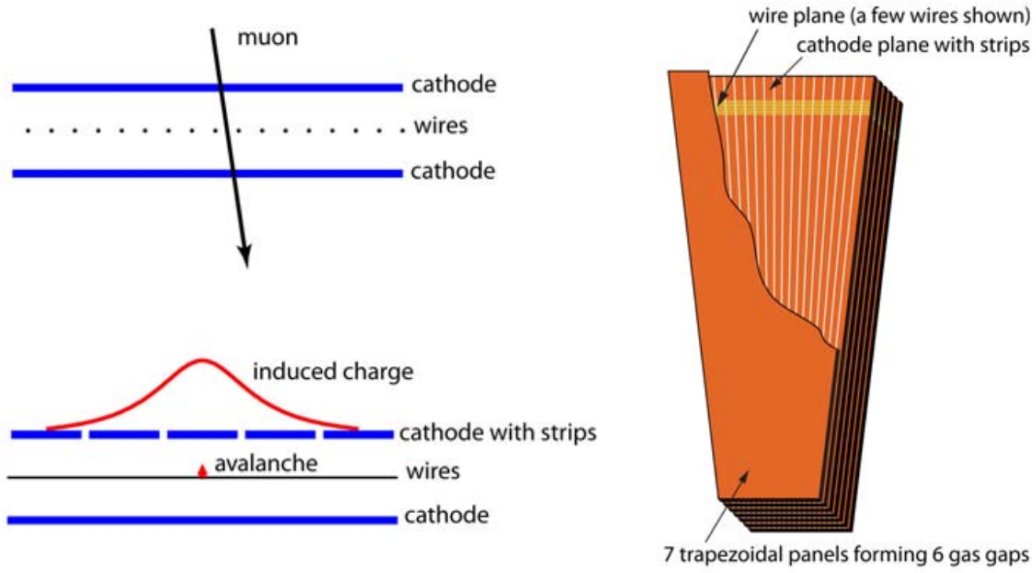

(a) (b)

Figure 4.8: (a) Working principle of the CSCs for a single gap. On top, a muon is passing through the gas volume of the chamber with the anode wires and cathodes. On the bottom, an avalanche together with the induced charge on the cathode strips is indicated. By interpolating these charges, a good position measurement of the avalanche along the wire direction can be obtained. (b) Sketch of the layout of a CSC. The 7 trapezoidal panels form 6 gas gaps. Exemplary, a few wires are shown running azimuthally. The cathode plane is depicted here with the strips running radially. The figures are taken from Ref. [72].

The detector design with a wire spacing of 3.2 mm and a strip pitch of $8.4(16)$ mm at the narrow (wide) end of the trapezoid ensures 2 mm resolution in $r - \phi$ direction at the trigger level and less than 150 μm at offline reconstruction. This precision can only be reached if one makes use of the original CSC idea, where the interpolation of the induced charge helps measuring the muon coordinate along the wire direction (ϕ direction in CMS coordinate system).

The CSCs need to sustain high rates (1 kHz/cm^2) being installed in the forward region of CMS. For the CSC system, a muon detection efficiency of 99% is required.

Resistive Plate Chambers The Resistive Plate Chambers (RPCs) are part of the CMS muon system in both the barrel region and the endcaps. In the barrel region, the RPCs complement the DT system in the 4 stations of the wheels. For the endcaps, the RPCs complement the CSC system except in the innermost rings of each station.

RPCs belong to the class of gaseous parallel-plate detectors. The chamber consists mainly of two parallel, highly-resistive plates, which are separated by a gas volume. In CMS, Bakelite is used with a bulk resistivity of $1-2\times10^{10}$ Ωcm. Graphite plates form an anode, which is set to ground, and a cathode at a negative high voltage. The RPCs are working in avalanche mode [101, 102]. The design of the RPC modules in CMS is a double-gap detector, where the readout strips are located between the gaps. They pick up the induced signal from both gaps. This allows operating the individual gas gap at a lower gain while increasing the total efficiency compared to the single-gap configuration. A schematic of the RPC module can be seen in Fig. 4.9.

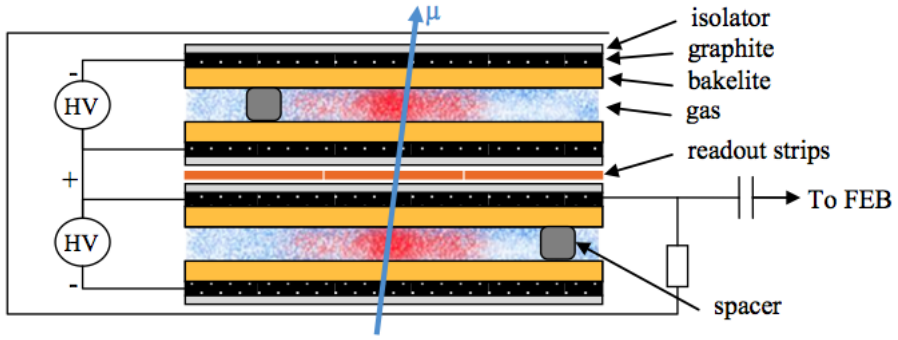

Figure 4.9: Schematic of the RPC module. The double-gap configuration is shown with the highly-resistive bakelite, as well as the plates of graphite, which make up the electrodes. The readout strips are located in between the two gaps. The induced signal is sent to the front-end board (FEB). To keep the gap size uniform across the detector, spacers are inserted. The figure is taken from Ref. [103].

The RPC system ensures efficient muon reconstruction and identification. On top of that, thanks to the excellent time resolution ($\approx$ 3 ns [98]), the RPC system is a good device to unambiguously tag the arrival time of an ionizing particle and associate it to the correct bunch crossing.

4.2.7 Trigger system

At a hadron collider, such as the LHC, a trigger system [104] is needed to reduce the rate of recorded data by selecting online interesting physics events. With the time difference of 25 ns between the BXs, an event rate of 40 MHz is obtained. Considering a typical event size of 1 Megabyte, the rate needs to be reduced to $\approx$ 1 kHz in order to transfer and store the data with currently available technology. This rate reduction is performed in two steps. The first step is called Level-1 (L1) trigger where not more than 100 kHz of event rate is forwarded to the High-Level triggers (HLTs). The HLTs reduce the event rate further to reach the required $\approx$ 1 kHz.

The L1 trigger relies on decisions given by the front-end electronics. The idea of the L1 system is to scan coarse, reduced data from the calorimeters and the muon system to find signatures of physical objects, that are defined by the needs of physics analyses, i.e. di-lepton and multi-lepton data for the Higgs analysis. The L1 trigger performs a fast summation of global p_T and p_T^{miss}. Thresholds of p_T and E_T are applied to these objects. While the L1 trigger system is deciding on whether the event is discarded or is passed to the HLT, high-

resolution data is stored in the buffers of the front-end electronics. Thus, the maximum time allowed for a L1 trigger decision is limited by the storage capacity of the buffers. In the case of the current CMS detector, it is 3.2 μs corresponding to 128 bunch crossings. Based on the L1 trigger decision, the front-end electronics of all subdetectors send out their data to the central data acquisition of CMS.

At the HLT level, the data is processed on dedicated computer farms. Initial filtering is done on a subset of the full event data with information from the calorimeters and muon system. An event rate reduction of one order of magnitude is achieved by this step. Eventually, the information of the tracker and the full granularity of the calorimeters, which is not available at L1, is used to decide if an event is permanently stored and fully reconstructed or discarded.

4.2.8 Event processing

The overall collection of software used for processing and reconstruction of CMS data and simulated events is called CMS software (CMSSW). An introduction is given in Ref. [105], including links to the CMSSW source code. All the software is built-up in a common modular framework. The information of an event is organized in the Event Data Model (EDM). This ensures a common starting point for all physics analyses. For data, the event contains the information coming from the HLT system, which is called RAW data. In the software, the event is filled either with RAW data from the detector or with the simulated event. Starting from this step, the RAW data follows the same processing path for both data and simulation. The RAW data is digitized and reconstructed, using the calibration and alignment information from the detector services. The reconstructed data (RECO) is stored in modular data objects. Since most analyses do not need the full event content (RAW+RECO), the data of an event is further reduced to the Analysis Object Data (AOD) format. This data format is the starting point of the analysis presented in Sec. 7.3[7].

4.2.9 Muon reconstruction

The standard muon reconstruction algorithms used in CMS are described in great detail in Ref. [106]. This section discusses the prompt[8] muon reconstruction algorithms. For the HL-LHC sensitivity study (Sec. 7), dedicated non-prompt (or displaced) reconstruction algorithms are used. The similarities and differences are discussed explicitly in Sec. 7.3.2. The basic concepts, as well as notation and definitions, are introduced in the following.

Muons, coming from the beam spot region, produce hits in the tracker system. With $p_T > 5$ GeV, muons typically reach the muon system, outside of the solenoid. The hits in the muon system are essential for muon triggering and identification. The reconstruction of muon trajectories begins with the separate reconstruction of the inner trajectory, using the tracker information, and the standalone trajectory, using the information of the muon system. The discussion is focused on the reconstruction with the muon system. Details about the track reconstruction in the tracker can be found in Ref. [90].

Standalone muon reconstruction The starting points of the standalone muon reconstruction are track segments in the muon chambers. Segments consist of matching hits in a muon chamber and play the role of seeds for the reconstruction. For each seed, a track finding algorithm, based on the Kalman-filter technique [107], is initialized to search for matching

[7] Further reduced data formats, i.e. miniAOD and nanoAOD, exist. However, the information on displaced muon reconstruction is not (yet) available in these reduced formats.

[8] Prompt denotes particles coming from the beam spot region of the detector.

hits in neighboring muon chambers. This algorithm is performed by going from the inner muon stations to the outer muon stations, updating the track parameters for each step. After that, the algorithm searches for tracks by going from the outer to the inner muon stations. The final track fit, which gives the standalone muon track, includes a beam spot constraint[9].

Global muon reconstruction For the global muon reconstruction, standalone tracks and tracker tracks are matched. The standalone track is propagated to the outer tracker layer and compared to the available tracker tracks. If matching pairs are found, another track fit is performed using the hits of both individual tracks.

4.3 The HL-LHC and CMS Phase-2 upgrades

In recent years, the LHC has played a fundamental role in the modern era of particle physics with the highlight of the Higgs boson discovery. To continue to play that role in particle physics for (at least) the next decade, the LHC and the experiments need to maintain or even extend their discovery potential.

4.3.1 Current limitations of the LHC

Before discussing the upgrades of the LHC towards Phase-2, it is important to recall the current limitations of the LHC in terms of operations for another one and a half decades with an even higher nominal luminosity. The following selection of limitations is inspired by Ref. [76].

- Inner triplet magnets: During operation, the components of the inner triplet quadrupoles and their corrector magnets are subject to radiation damage. After around 300 $\text{fb}^{-1}$of integrated luminosity (nominal target value for Phase-1) the components will have accumulated a dose of 30 MGy. This dose could already cause a failure of some corrector magnets and lead to a major breakdown. To avoid this, the inner triplet magnets must be replaced beforehand.

- Collimation: The planned increased beam intensities can be reached safely only if the impedance of the collimator materials is reduced. Too large electrical resistivity could trigger beam instabilities. The current system was not optimized for lowering the impedance but rather for robustness during the first years of the LHC. Furthermore, the system needs to be renewed to protect the new triplets at IR1 and IR5.

- Dispersion suppressor region (DSR): During Phase-1, a leakage of off-momentum particles into the neighboring main dipoles has been observed in the DSR, possibly contributing to LHC performance limitations. Dedicated and complex interventions are needed for the different IPs which consist, for example, of placing additional dipoles with higher bending strength compared to the existing ones. Due to space limitations at certain IPs, this is not a trivial task.

- Radiation to electronics: The electronics of the current magnet power converters are equipped with radiation-sensitive boards. There are two options to solve this problem: Either replace the existing boards with radiation-hard boards or move the electronics away from the beam. For the second option, the use of a novel technology, i.e. superconducting links (SCLs), is preferred to ensure powering in the low temperature

[9] To be exact, also the earlier steps in reconstruction impose a beam spot constraint (see discussion in Sec. 7.3.2)

environment of the HL-LHC magnets. Studies are currently trying to find the best solution for the HL-LHC.

4.3.2 The LHC towards Phase-2

The LHC will be upgraded allowing to operate the machine for another decade. Two main parameters of the accelerator are supposed to profit from the upgrade. The center-of-mass energy will be increased to 14 TeV and the instantaneous luminosity will be roughly quadrupled.

LHC roadmap By the end of the Run-2 period in 2018, the LHC delivered proton-proton collisions to the experiments with a center-of-mass energy of 13 TeV and an instantaneous luminosity of around 10^{34} cm^{-2}s^{-1}, summing up to more than 150 fb^{-1} of integrated luminosity. In 2019 and 2020, during the Long Shutdown 2 (LS2), mainly the upgrade of the LHC injector chain will take place allowing to exceed the current instantaneous luminosity by a factor of 2. The following data taking period (Run-3) is scheduled until the end of 2023[10]. A total integrated luminosity of 300 fb^{-1} is targeted. During LS3, major upgrades will be implemented roughly quadrupling the instantaneous luminosity with respect to Run-2. The data taking after these upgrades is called the Phase-2 or HL-LHC, aiming at 3000 fb^{-1}. In an ultimate scenario, an even higher integrated luminosity of 4000 fb^{-1} is expected[11]. The LHC roadmap from 2011 until Phase-2 is presented in Fig. 4.10.

Figure 4.10: LHC planning from the beginning of data taking in Run-1 (2011) until the start of Phase-2 (HL-LHC). The thick and thin red lines show the evolution of the center-of-mass energy and the instantaneous luminosity, respectively. In the light blue boxes on the bottom, one can find the expected integrated luminosity at the end of a Run period. The gray boxes indicate those periods where the LHC is shut down and major work for upgrades of the LHC and the experiments is performed. The figure is taken from Ref. [76].

HL-LHC performance parameters The performance parameters of the HL-LHC are summarized in Tab. 4.2. The table is repeating some of the content of Tab. 4.1 to allow a direct comparison with the parameters of the LHC.

[10] The end of Run-3 is subject to recent discussions. Run-3 will be expanded by one year.
[11] In this work, 3000 fb^{-1} is assumed for the HL-LHC period.

Parameter	Nominal (design report)	Run-2 (2018)	HL-LHC (standard)
Number of bunches per beam n_b	2808	2556	2748
Number of particles per bunch N (10^{11})	1.15	1.25	2.2
Bunch spacing (ns)	25	25	25
Revolution frequency f_{rev} (kHz)	11.2	11.24 [79]	11.25
β^* at IP (m)	0.55	0.30	0.2
Normalized transverse beam emittance ϵ_n (μm)	3.75	≈ 1.9	2.50
Crossing angle θ_c (μrad)	285	320-260	250
Beam energy in collision (TeV)	7	6.5	7
Total beam energy (MJ)	362	332	700
Peak Luminosity at IR1/IR5 (10^{34}cm^{-2}s^{-1})	1.18	2.1	5

Table 4.2: List of nominal values of the (HL-)LHC performance parameters taken from Ref. [76, 80] and the corresponding values from 2018 taken from Ref. [81] for proton collisions. The HL-LHC performance parameters of the standard projection are shown here. In Ref. [76], other projections are discussed.

Pileup at the HL-LHC The increased luminosity at the HL-LHC comes with a larger number of inelastic proton-proton collisions per bunch crossing. Fig. 4.11 shows the recorded luminosity of CMS as a function of the mean number of inelastic pp interactions per bunch crossing for the LHC in 2017. For the HL-LHC era, the mean value of pileup interactions

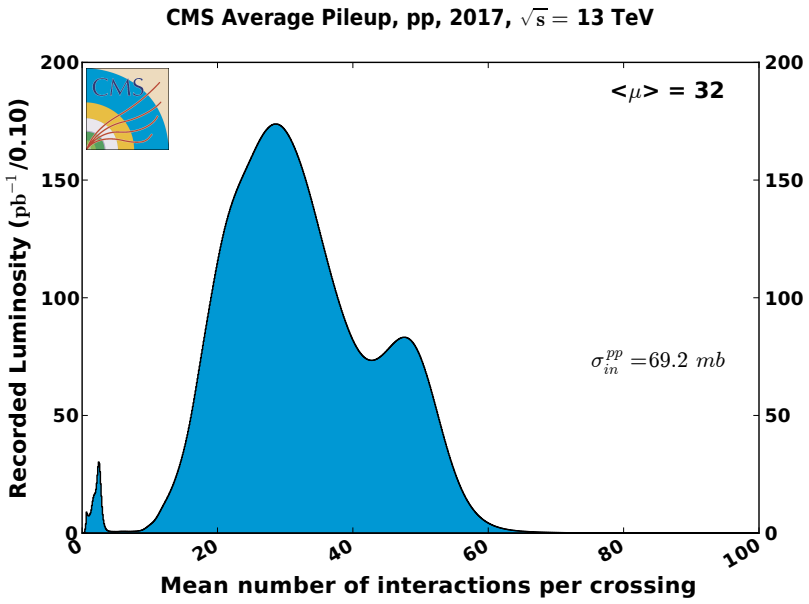

Figure 4.11: Recorded luminosity of CMS as a function of the mean number of inelastic pp interactions per bunch crossing for the 2017 proton-proton data taking at $\sqrt{s} = 13$ TeV. The mean number is $< \mu >= 32$. The value of the inelastic pp cross section at $\sqrt{s} = 13$ TeV is given in the figure. The figure is taken from Ref. [78].

is expected to be around 200, almost a factor 7 higher compared to 2017. The higher number of pileup interactions comes along with an increased rate of low-energy particles in the detectors. This introduces challenges for the detector performance due to increased trigger and background rates, especially in the forward region.

4.3.3 Overview of CMS Phase-2 upgrades

To cope with the harsher environment at the HL-LHC, the CMS detector has to be upgraded to maintain or even improve its performance. Main concerns for the CMS detector during Phase-2 consist of high pileup, higher background rates, and larger radiation doses leading to higher risks of detector or electronics damages. To illustrate the challenges, Fig. 4.12 (a) displays the expected absorbed dose inside the CMS cavern after the HL-LHC and Fig. 4.12 (b) shows an event with high pileup measured with CMS in 2016.

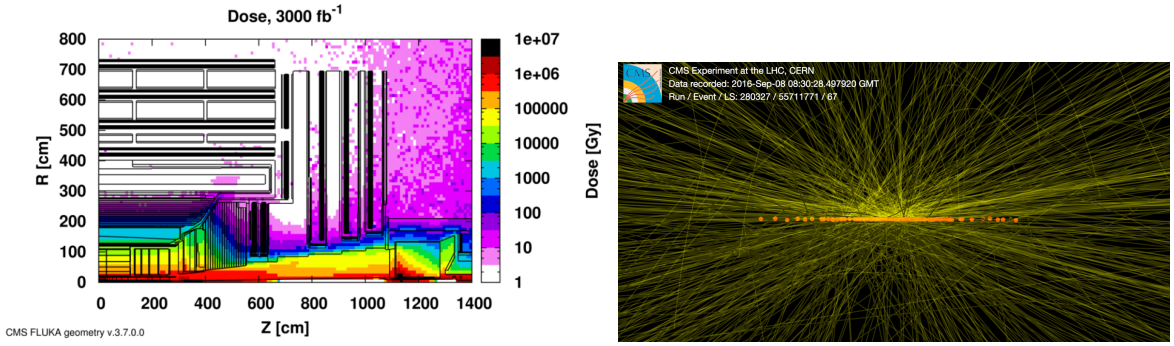

(a) (b)

Figure 4.12: (a) Absorbed dose inside the CMS cavern assuming an integrated luminosity of 3000 fb^{-1} (nominal HL-LHC value) obtained with simulations. The figure is taken from Ref. [108]. (b) A high-pileup event measured with the CMS detector in 2016 with 86 reconstructed vertices. The figure is taken from Ref. [109].

The Phase-2 upgrades of the CMS detector are divided in several steps. During the LS2, the EYETS, and the LS3, the existing subsystems will be upgraded and new subsystems will be installed for the first time. The following discussion is based on Refs. [108, 110].

Tracker After Phase-1 and before the start of Phase-2, the tracker subsystem must be completely replaced because of expected significant radiation damage. To maintain the excellent tracking capabilities at high pileup, the granularity of the complete Phase-2 tracker will be increased. For the pixel tracker, smaller pixels and thinner sensors will be installed increasing the impact parameter[12] resolution and ameliorating the separation power of two close-by trajectories. The outer tracker granularity will profit from shorter silicon sensor strips while leaving the strip pitch almost the same. A powerful consequence of the new outer tracker modules is the possibility of adding tracker information to the L1 trigger. In the forward regions, new pixel disks will extend the pseudorapidity coverage up to $|\eta| = 4$ matching the calorimetry coverage. The foreseen Phase-2 tracker design is sketched in Fig. 4.13. An extensive description of the Phase-2 tracker can be found in Ref. [111].

Calorimeter system The calorimeter system will already suffer from radiation before the end of Phase-1. Simulations show that the current CMS ECAL and HCAL cannot withstand the radiation exposure of the HL-LHC in the endcaps. Consequently, the endcap calorimeter system must be replaced. The new system, called High Granularity Calorimeter (HGCAL), ensures good transverse and longitudinal segmentation. The ultimate goal is to provide three-dimensional shower images. The concept of a sampling calorimeter is applied, where active and absorber materials are interleaved. In the electromagnetic case, silicon sensors act as an active material and tungsten and copper plates as an absorber. In the hadronic

[12] The impact parameter is defined in Sec. 7.3.

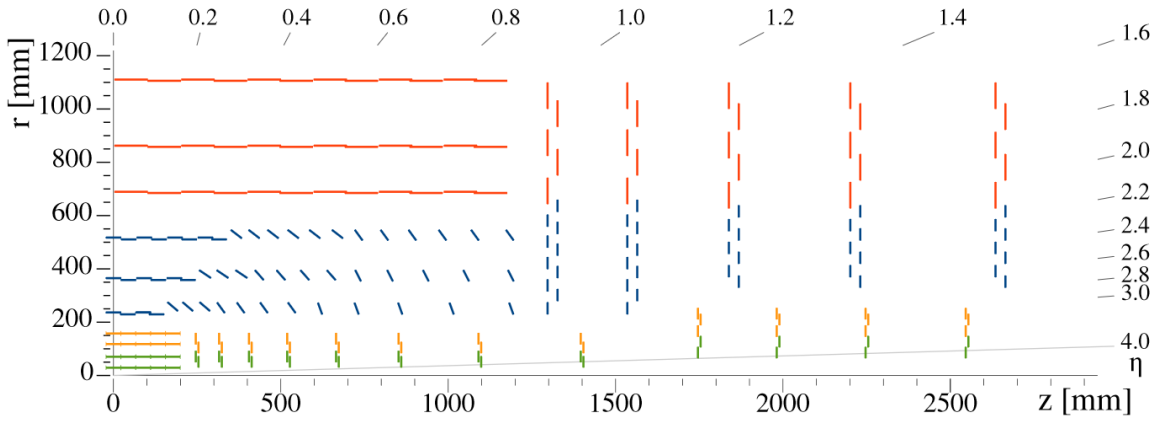

Figure 4.13: Sketch of the $r - z$ view of the Phase-2 CMS tracker system. The upgrade extends the coverage up to $|\eta| = 4$. The inner tracker consists of modules with two readout chips (green) and of modules with four readout chips (yellow). The outer tracker is made of modules with two strip sensors (2S), shown in blue, and modules with a strip and a pixel sensor (PS), shown in red. The figure is taken from Ref. [111].

case, brass and copper plates interleaved with silicon sensors are used in the inner part, and brass plates interleaved with plastic scintillating tiles are used in the outer part. A complete description of the Phase-2 calorimeter can be found in Refs. [112, 113].

Muon system The current CMS Phase-1 muon system has one region ($1.5 \leq |\eta| \leq 2.4$), covered only by the CSC detectors without another subsystem increasing redundancy. Meanwhile, it is very challenging to measure muon trajectories and muon momentum due to high background rates and decreasing magnetic field in this very same region. To ensure good L1 trigger acceptance in this region for the HL-LHC, additional muon chambers are foreseen complementing the existing CSC modules in the innermost ring of the first and second endcap station. There, the magnetic field is still large enough to perform a reasonable momentum measurement. The chosen detector type is the GEM technology. The third and fourth endcap stations will be equipped with improved RPCs (iRPCs) with lower granularity but excellent timing resolution. Additionally, the insertion of GEMs in the freed space of the new HGCAL is proposed, extending the muon system coverage up to $|\eta| \approx 3$.

Trigger and electronics One main difference between the Phase-1 and Phase-2 trigger system is the foreseen increase of the L1 trigger latency from 3.2 μs to 12.5 μs. This latency gives enough time to reconstruct the trajectories hardware-based in the tracker and match the information with the muon and calorimeter systems. For this upgrade, new front-end electronics are needed and for some subsystems, i.e. DT and CSC subsystems, the existing electronics must be replaced. With the new electronics, the L1 trigger rate can be increased to $\approx$ 500 kHz (for beam conditions with PU 140) while maintaining the thresholds of the Phase-1 period [114].

5 CMS GEM projects

This section starts with an overview of the upgrades of the CMS Phase-2 Forward Muon System related to the GEM technology (Sec. 5.1). In Sec. 5.2, the focus is on the first CMS GEM project, called GE1/1. The installation of GE1/1 is motivated (Sec. 5.2.1) and the GE1/1 detector layout is discussed (Sec. 5.2.2). Sec. 5.3 deals with the production of the GE1/1 chambers. In particular, the quality control steps performed in the Aachen GEM laboratory are discussed. Sec. 5.4 gives the current status of the GE1/1 project, as well as an outlook about future CMS GEM projects. The introductory part of this section is based on Refs. [10, 11].

5.1 Overview

The installation of new muon chambers using the modern GEM technology is an essential part of the CMS Forward Muon System Upgrade for the CMS Phase-2 detector. GEM detectors will be installed in the innermost ring of the first (GE1/1) and second (GE2/1) stations of the CMS endcaps. Another installation of GEM detectors, called ME0, is foreseen in the space freed-up by the upgrade of the calorimeter system. Fig. 5.1 provides an $r - z$ view of the CMS detector highlighting the endcap stations where the GEM detectors are inserted. In the following, the GE1/1 project is discussed in detail. The subsequent projects, namely GE2/1 and ME0, will profit a lot from the experience of GE1/1 regarding detector design and performance, as well as mechanics and readout electronics.

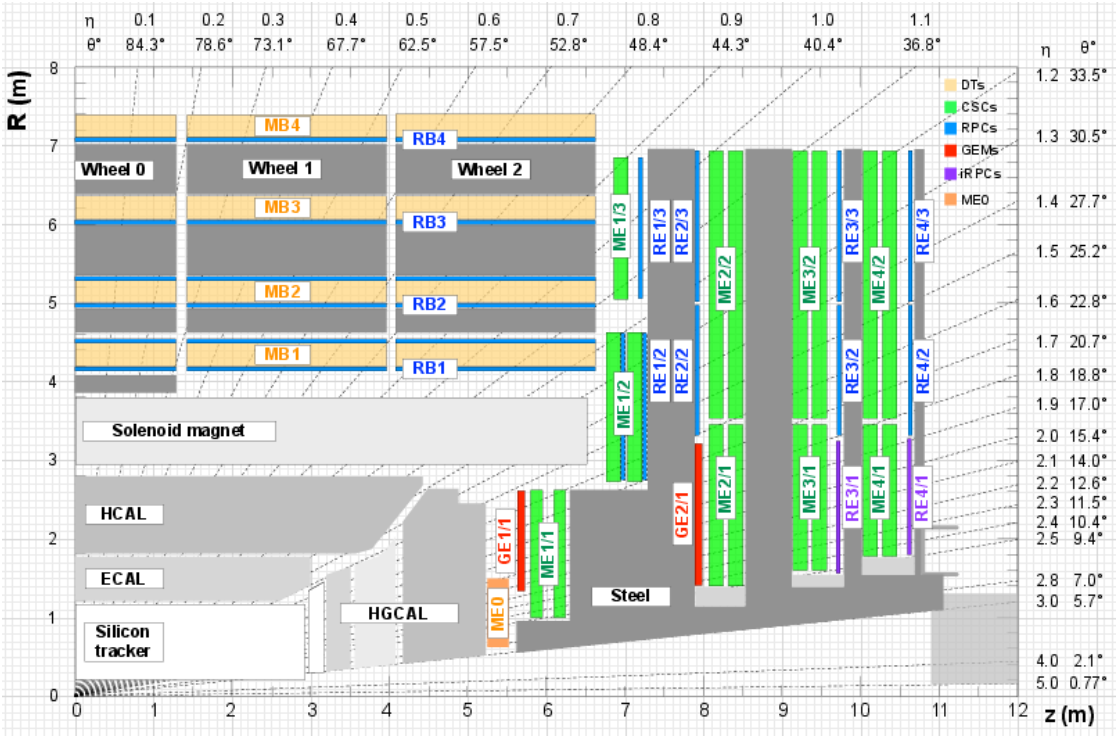

Figure 5.1: Sketch of the $r - z$ view of the CMS Phase-2 detector. The GEM stations (GE1/1, GE2/1, and ME0) are highlighted in red and orange. GE1/1 is the first major upgrade of the Phase-2 CMS muon system. In violet, those stations with iRPCs (RE3/1 and RE4/1) are shown. The other subsystems of the CMS muon system are labeled in the same way as for the Phase-1 detector (Fig. 4.6). The HGCAL is sketched in the forward region. The figure is taken from Ref. [11].

5.2 GE1/1 project

The GE1/1 project is the first major Phase-2 upgrade of the muon system. For the first time since the initial commissioning of CMS, a new subdetector system with a novel detector type is installed in CMS. For both CMS endcaps, the chambers are arranged in a disk covering $1.64 \leq |\eta| \leq 2.15$. One disk consists of 36 modules, called superchambers (SCs). A superchamber is formed by putting two single chambers on top of each other. A sketch of the GE1/1 disk and a sketch of a superchamber are shown in Fig. 5.2. The trapezoidal shape

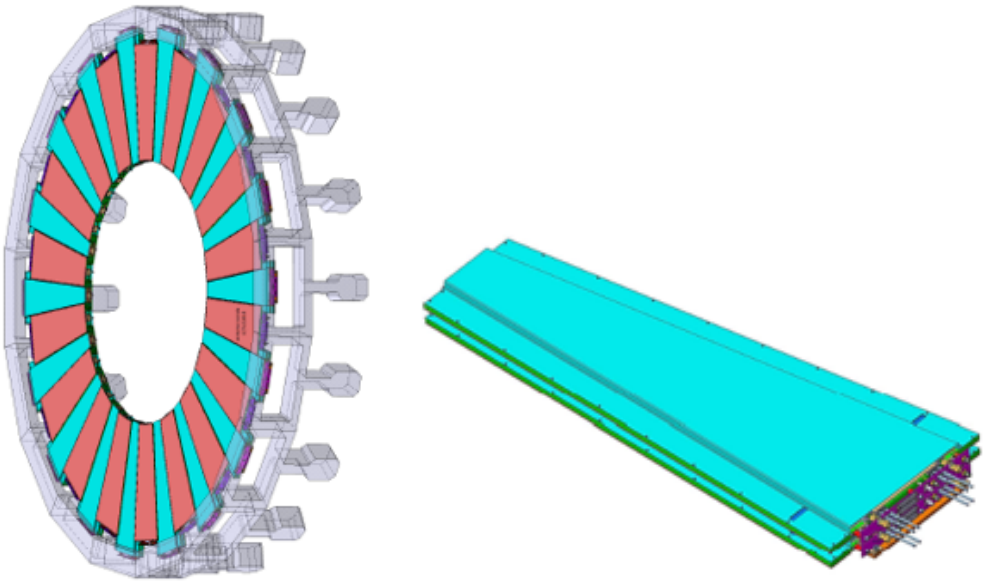

Figure 5.2: Sketch of one GE1/1 endcap disk including 36 superchambers (72 single chambers) and a sketch of one superchamber. The long chambers are shown in cyan while the short chambers are shown in a reddish color. The support structure of the GE1/1 disk limits the available space. To maximize the coverage with this constraint, long and short chambers are inserted. The figures are taken from Ref. [10].

of a superchamber with an opening angle of 10.15° provides some overlap between neighboring chambers and ensures full coverage. Due to mechanical constraints of the GE1/1 support structure, there are long and short chambers.

5.2.1 Motivation

The installation of GE1/1 is motivated by the challenges of the data taking at the HL-LHC. In the forward region of the CMS detector, background rates, radiation dose, and pileup will be significantly larger than during Phase-1. The GE1/1 GEM chambers will help to maintain or even improve trigger and reconstruction capabilities.

Trigger capabilities At the L1 trigger level, the measurement of the muon momentum strongly influences the trigger capabilities. The measurement is based on the bending of the muon trajectory inside the magnetic field. Since the magnetic field decreases significantly when going outside the solenoid, the bending power is dropping accordingly in this region of the detector. This leads to a poor momentum resolution. Thus, low-momentum muons are misidentified as high-momentum and pass the trigger thresholds. Without any upgrades of the forward muon system, the muon trigger rates would increase drastically at

the HL-LHC compared with current data taking. Together with the first CSC endcap station (ME1/1), the deployment of the GE1/1 station will help to reduce the rates (see Fig. 5.3).

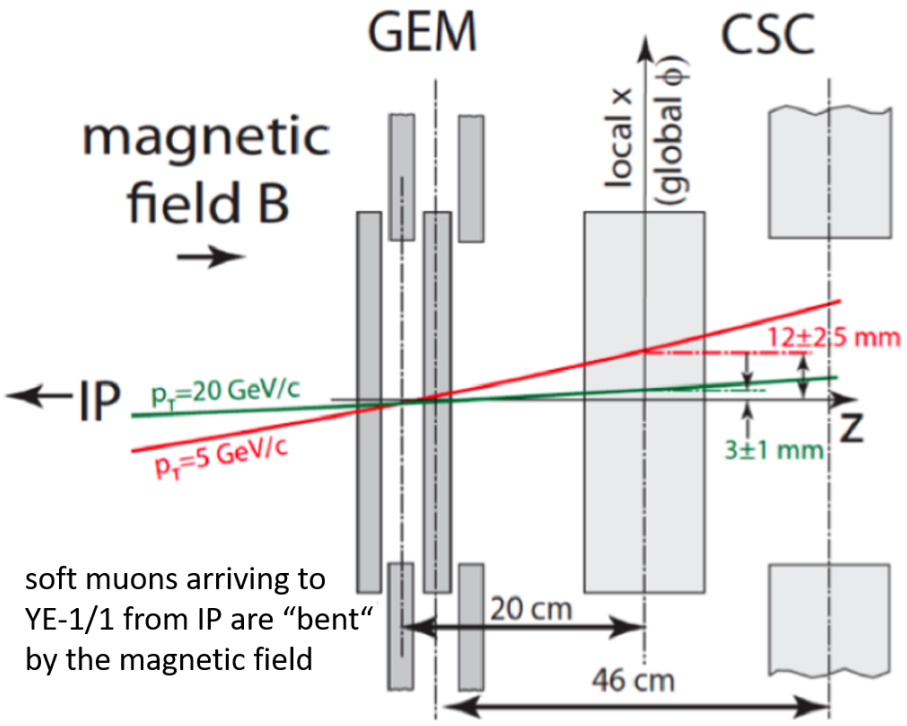

Figure 5.3: Sketch illustrating the principle of the muon momentum measurement combining GEM and CSC stations. Exemplary, two low-momentum muons coming from the interaction point (IP) to the magnet return yoke in the first endcap station (YE1/1) are shown in green ($p_T = 20$ GeV) and red ($p_T = 5$ GeV). Combining the position information of both stations allows to efficiently discriminate between those two muons. The figure is taken from Ref. [10].

Due to an excellent position resolution of both stations and an increase of the path length, that is traversed by muons within the first muon station, the muon momentum measurement is improved. This results in a decrease of the standalone muon trigger rate. The rate curve of the single muon trigger with and without the GE1/1 station is depicted in Fig. 5.4. The reduction of trigger rate allows reducing p_T trigger thresholds for Phase-2. This is essential to be sensitive to phenomena in the low-momentum region.

During Phase-2 with the new tracker and track trigger, a combined L1 trigger will be established providing even better measurements of muons coming from the interaction region. For muons emerging from the decay of long-lived particles or for other exotic particles produced in the detector, the new standalone muon trigger, relying only on the information given by the muon system, will provide high efficiency for these exotic signatures. The standalone trigger will serve as an add-on and backup of the combined L1 trigger.

Impact on physics searches Physics searches ranging from phenomena including new physics to Higgs measurements profit to a large extent from maintaining low-p_T trigger thresholds. Some of the striking examples illustrating the power of lowering thresholds are discussed in Ref. [10].

In the context of this thesis, another benefit of the GE1/1 station is worth mentioning. The combined usage of GEM and CSC detectors in the first and second muon station significantly improves the muon direction measurement, and thus, the momentum reconstruction

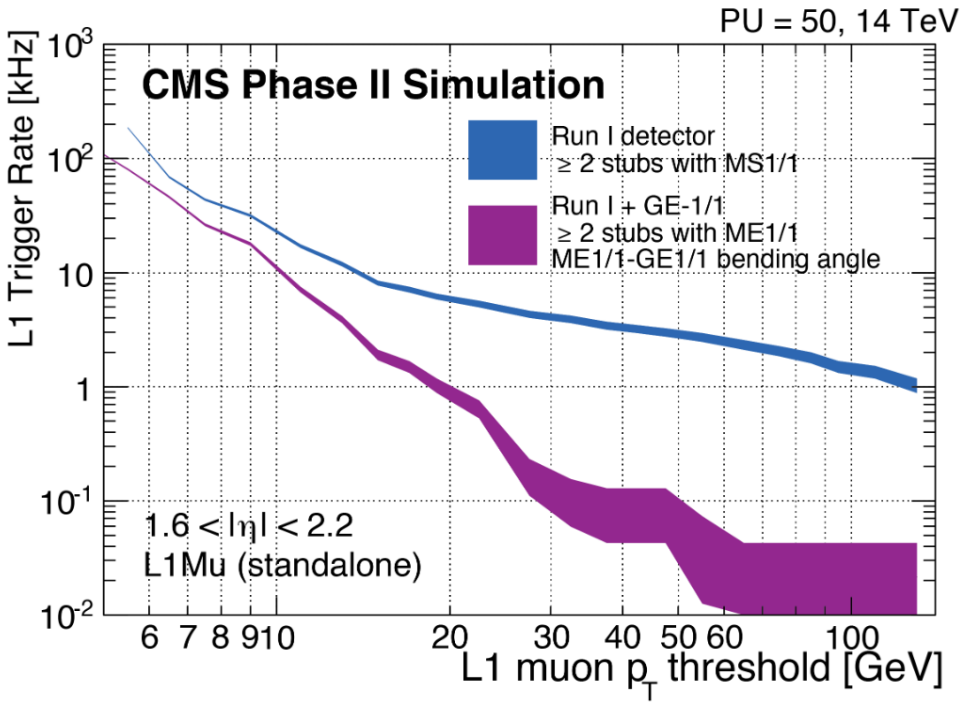

Figure 5.4: L1 muon trigger rates in the forward region as a function of the p_T thresholds with an average number of 50 pileup interactions per event. The L1 trigger rates with the Run-1 detector, i.e. only using the first CSC endcap station (ME1/1), and with the addition of the first GEM endcap station (GE1/1) are drawn in blue and purple, respectively. MS1/1 ($\equiv$ ME1/1) denotes the first muon endcap station of the Run-1 detector. Stubs are local measurements in the muon stations, that are used as trigger primitives. The range in η differs slightly from the pseudorapidity range covered by GE1/1. This is due to an old version of the detector geometry used in Ref. [10], which was written in 2015.

for displaced muons. Fig. 5.5 shows the direction resolution with and without the combination of GEM and CSC detectors for muons coming from the decay of a long-lived particle.

5.2.2 Detector design

In the beginning, this section deals with the requirements of the GEM chambers for the CMS GE1/1 use case. The parameters of the detector design are listed and some performance studies provided by the CMS GEM group are mentioned in the end.

Requirements To fully explore the potential for the trigger and physics performance, as indicated in Sec. 5.2.1, the GEM chambers have to meet some requirements.

- Maximum coverage: Obviously, the maximum coverage yields the maximum physics output.
- Rate capability of 10 kHz/cm^2: For the operation during HL-LHC, the maximum expected hit rate on the surface of the GE1/1 disk is $\approx$ 5 kHz/cm^2. With a safety factor of 2, one ends up imposing a rate capability of 10 kHz/cm^2.
- No aging up to 200 mC/cm^2 of integrated charge: The expected integrated charge for the operation during HL-LHC ($\approx$ 20 years) at the GE1/1 position closest to the beam line is around 100 mC/cm^2. Again, a safety factor of 2 is applied.

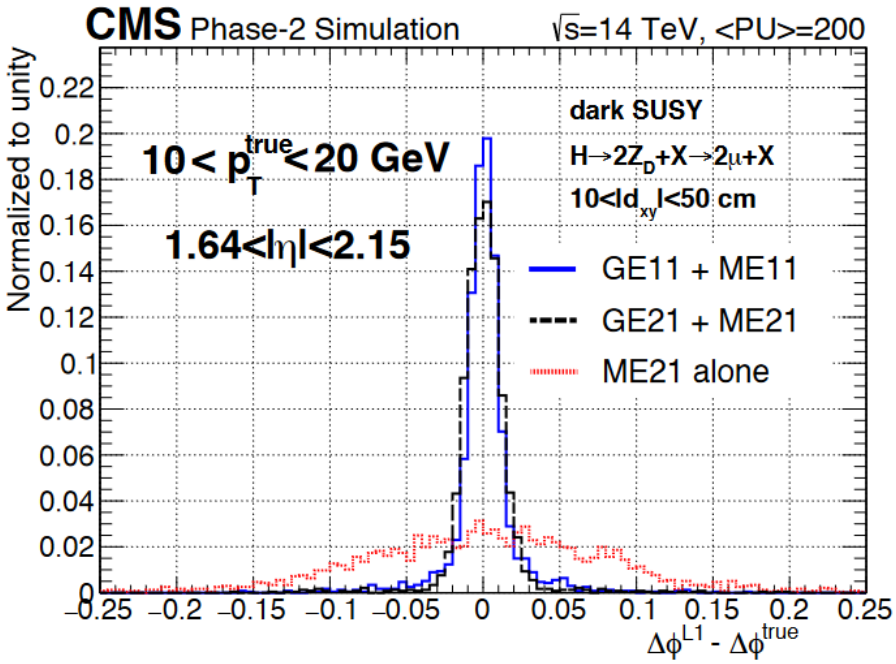

Figure 5.5: Resolution of the muon direction measurement $\Delta\phi^{\mathrm{L1}} - \Delta\phi^{\mathrm{true}}$. The study uses events with soft, displaced muons in the forward region. The solid blue line and the dashed black line show the resolution of the combined first and second muon stations, respectively. The dashed red line depicts the resolution using only the CSC detectors of the second muon station. The figure is taken from Ref. [11].

- Minimum detection efficiency of 97% for single chambers: Imposing a minimum single chamber efficiency of 97% for detecting MIPs, leads to a superchamber efficiency of 99.9% applying a logical OR of the two single chambers.
- Minimum angular resolution of 300 μrad: The angular resolution is defined here as the resolution on $\Delta\phi = \phi_{\mathrm{GE1/1}} - \phi_{\mathrm{ME1/1}}$, i.e. the difference between the GE1/1 and ME1/1 angular position measurement. An excellent angular resolution ensures good discrimination between low-p_T and high-p_T muons, which is essential for the trigger rate reduction.
- Minimum timing resolution of 10 ns for a single chamber: With the combined timing information from the two GE1/1 single chambers, 10 ns of timing resolution ensures good matching with the ME1/1 information while having a 25 ns bunch spacing.
- Maximum gas gain variations of 37% for a single chamber: Gain variations inside a single chamber may cause deterioration of efficiency, angular and timing resolution.

Recent performance studies, checking if prototypes of the GE1/1 detectors fulfill the requirements, are discussed later in this section. The requirements on the gas gain uniformity and the single chamber efficiency are examined by the GE1/1 quality control tests (Sec. 5.3.3).

Design parameters The GE1/1 detectors are based on the GEM technology, which is described from a general point of view in Sec. 3.4.3. Fig. 5.6 presents an exploded view of a single chamber for GE1/1. The CMS GEM chambers belong to the type of triple-layer GEM chambers, hosting a stack of three GEM foils. The stack is surrounded at the top and bottom by a drift and readout board, respectively. These components are mounted with a

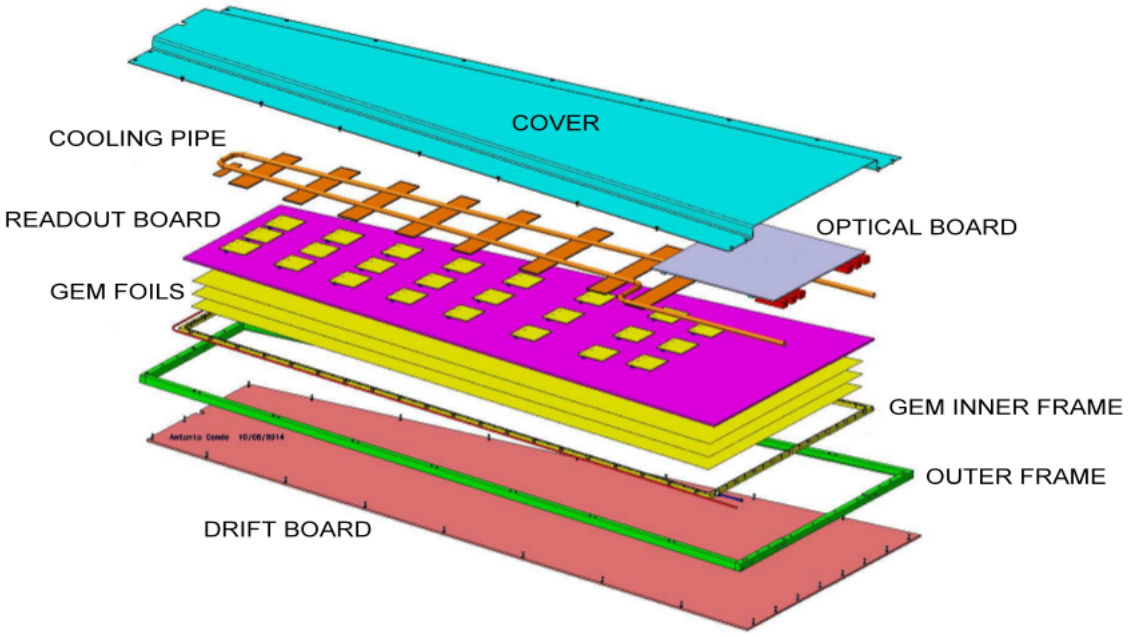

Figure 5.6: Exploded view of a GE1/1 chamber. The figure is taken from Ref. [10], which was published in 2015. Over the years, minor modifications of the chamber design have been implemented. For example, the optical board is not located at the long edge of the trapezoid, but in the middle of the chamber in the final design. The general concept, however, is shown correctly.

spacing of 3/1/2/1 mm between each other. A sketch of the cross-section of the CMS GEM configuration is depicted in Fig. 5.7. High voltages are applied to the drift boards, as well as to the top and bottom of the three GEM foils. The applied voltages gradually decrease

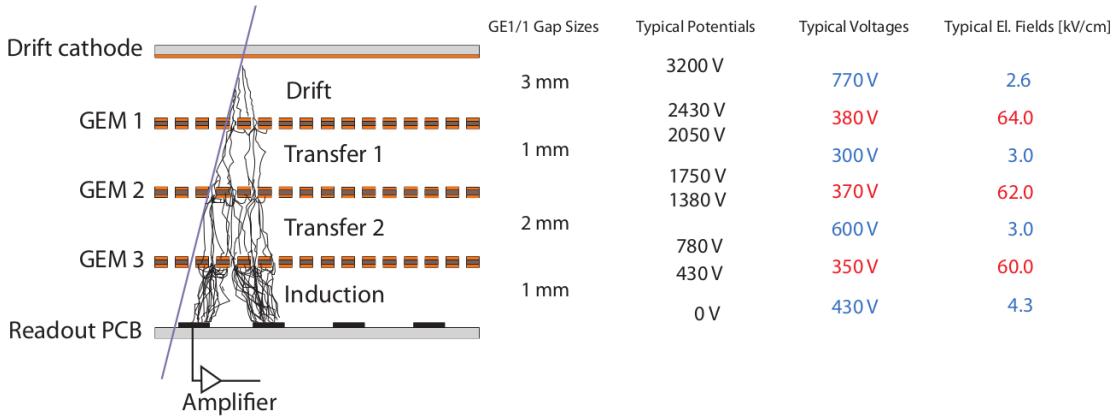

Figure 5.7: Sketch of the cross-section of a triple-GEM chamber consisting of a drift cathode, three GEM foils and a readout board. The drift, transfer 1/2 and induction gap are defined here. The table on the right provides typical voltages, potentials and electric fields of the gaps and inside the holes of the foils. The straight line indicates an ionizing particle traversing the detector and inducing an electron avalanche. The thin black lines give an idea of the drift lines of the avalanche electrons inside the GEM detector. The figure is taken from Ref. [10].

from drift to the third GEM foil. A standard gas mixture for GEM chambers is Ar/CO_2 (70/30), which is also chosen for the operation in CMS. Other gas mixtures were considered and studies with $Ar/CO_2/CF_4$ (45/15/40) have been performed. However, the significantly more eco-friendly solution without CF_4 is preferred. One striking feature of the CMS GEM detectors is their large size of 0.35 and 0.41 m^2 for short and long modules, respectively. Other experiments in high rate environments, such as LHCb [73] or COMPASS [3], make use of medium-size GEM chambers (30×30 cm^2). The enlarged active area makes the integration of GEM stations in CMS affordable. Throughout this thesis, the unprecedented large size of the CMS GEM detectors and its implications on components, reliability and detector performance is discussed. Tab. 5.1 gives an overview of the design parameters for the GE1/1 detectors.

Parameter	GE1/1
Chamber	
Shape of active area	trapezoidal; opening angle of 10.15°
Short chamber dimensions	L: 106.1 cm (center line), W: (23.1 - 42.0) cm, D: 0.7 cm
Long chamber dimensions	L: 120.9 cm (center line), W: (23.1 - 44.6) cm, D: 0.7 cm
Active readout area	0.345 m^2 (short ch.); 0.409 m^2 (long ch.)
Active chamber volume	2.6 l (short ch.); 3 l (long ch.)
Geometrical acceptance in η	1.61 - 2.15 (short ch.); 1.55 - 2.15 (long ch.)
Readout	
Structure	Truly radial readout strips
Number of η-segments in readout	8
Number of readout strips per η-segment	384
Number of readout strips per chamber	3072
Operation	
Gas mixture	Ar/CO_2 (70/30)
Nominal operational gas flow	1 chamber volume per hour
Number of gas inlets/outlets	1/1
Nominal operation gas gain	$1\text{-}2{\cdot}10^4$

Table 5.1: Design and operation parameters of the GE1/1 GEM chambers for the CMS experiment. The information of this table is taken from Ref. [10], except for the outdated geometrical acceptance, which is taken from Ref. [11].

Technical design of GEM foils The trapezoidal GEM foils produced for the GE1/1 project are identical to each other (except for details of the foil design for long and short chambers). Following the typical GEM design, they consist of a 50 μm thin polyimide foil with 5 μm of copper cladded on both sides. The (upper) hole diameter of 70 μm and the hole pitch of 140 μm also follow the common GEM standard. The foils for GE1/1 are produced with the single-mask technique. In this procedure, the etching of the hole pattern is done with one mask as opposed to two masks for the double-mask technique. The advantage for the production process, especially for large-size GEM foils, is that the alignment of the two masks becomes obsolete. The drawback is a more asymmetric hole compared to the double-mask technique, which results in a slightly larger hole diameter on the bottom of the foil. In Sec. 3.4.3, the etching procedures are described in detail and, in Sec. 6.2.3, the impact of hole geometries on the properties of GEM detectors is studied.

The side of the foil oriented towards the readout board is a continuous conducting surface, while the other side is segmented into HV sectors running across the width of the trapezoid. Fig. 5.8 shows schematically the HV segmentation of long and short GE1/1 foils.

The width of the sectors is adjusted when going from the larger base to the smaller base, so

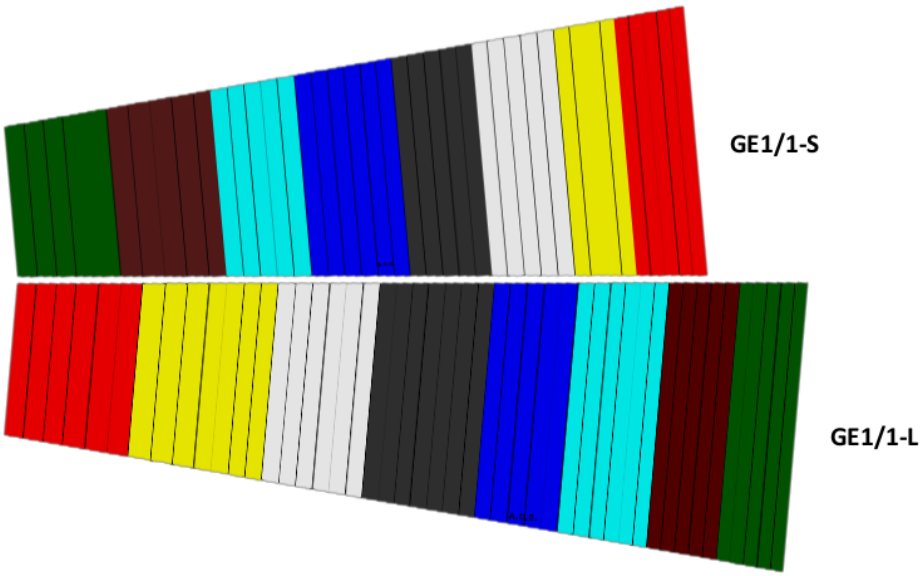

Figure 5.8: Schematic view of HV segmentation of GE1/1-S (short) and GE1/1-L (long) chambers. The corresponding readout sectors in η are color-coded. For long foils, there are 47 strips and, for short foils, there are 40 strips. The figure is taken from Ref. [10].

that each HV partition covers a similar total area. The segmentation limits the amount of charge that can flow during a discharge from top to bottom of the foil and, thus, limits the destructive power of discharges propagating towards the readout board/electronics. The strips are connected to a common HV supply point via individual traces with a 10 MΩ protective resistor mounted on top of the GEM foil. In the case of a shorted foil, thanks to the segmentation only a fraction of the surface is lost as a dead area. This holds, if the HV is given to the foils by an HV divider, as it is done during the quality control up to the gain uniformity tests. For the following quality control tests and the operation in CMS, a multichannel HV supply is used. In this case, the current is flowing through the shorted foil preventing to create the needed potential difference between top and bottom.

Mechanical structure of GE1/1 chambers The chamber assembly itself and, in case of problems, the re-opening of chambers, as well as the exchange of damaged foils, can be performed faster and easier without glue. The GE1/1 chambers will stay approximately two decades in the CMS detector. Thus, any outgassing of glue inside the detector volume may - even though unlikely - pollute the gas mixture and have an impact on the detector performance. To exclude this possibility, the mechanical design, which is shown in Fig. 5.9, completely avoids the usage of glue. When it comes to large-size GEM detectors, the technique of stretching the GEM foils is a delicate item. For GE1/1, stainless-steel screws are inserted in brass pullouts all around the trapezoid of the active area. The stack of GEM foils interleaved with spacers is held together with another stainless-steel screw. In the stack of spacers, a winding is foreseen for the pullout screws. By applying a predefined and fixed torque to those screws, the whole stack of GEM foils is stretched simultaneously. The stretching technique is a development of the CMS collaboration. The gas volume is closed by the gas frame plus o-ring.

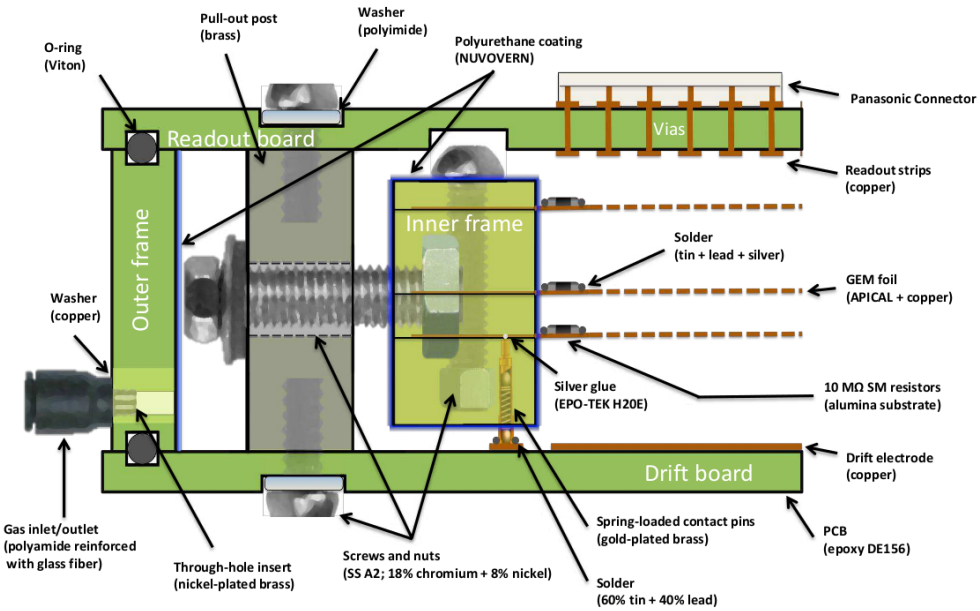

Figure 5.9: Sketch of the mechanical structure of the GE1/1 chambers. The main components are the drift and readout board on the bottom and top, respectively. The inner frame holds the stack of GEM foils. The outer frame, with the o-ring inserted, closes the gas volume. The figure is taken from Ref. [10].

HV distribution to the GEM foils and drift board The GEM foils are powered through HV pins mounted on the drift board inside the gas volume. The pins are equipped with a spring and get pushed to the corresponding electrode. The different electrodes (top and bottom of three GEM foils) are at different heights. Via traces on the drift board, the HV pins are connected to pads outside the gas volume. A schematic view showing the working principle of the HV pins is given in Fig. 5.10.

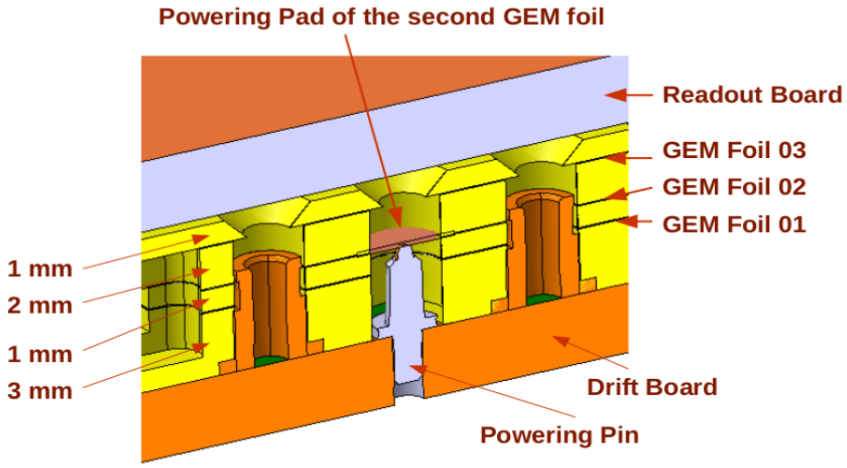

Figure 5.10: Schematic view of the HV distribution via pins. Exemplary, the powering of the second GEM foil is shown. The figure is taken from Ref. [115]

Readout board The readout board features 3072 truly radial readout strips. The layout of the readout strips is presented in Fig. 5.11 for a short GE1/1 chamber. Gold-plated copper

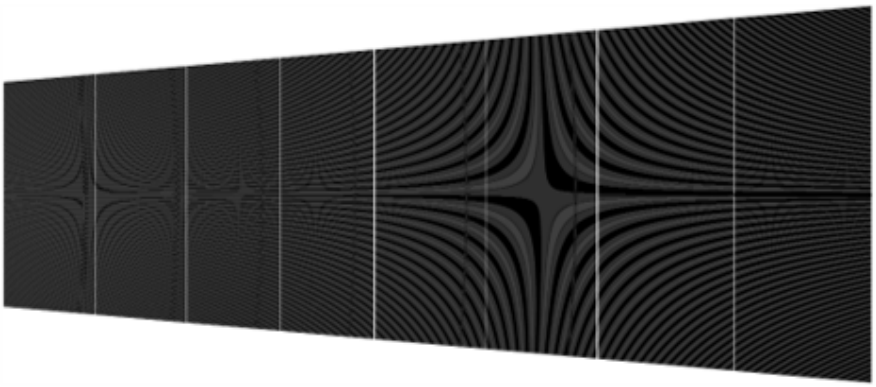

Figure 5.11: Layout of the readout strips for a short GE1/1 chamber. In total, there are 3072 radial readout strips grouped in 8 η-sectors.

is used as the strip material. The active area, that is spanned by the strips of one chamber, covers the angle of 10.15° allowing an overlap of 2-3 strips between chambers. The angular width of the strips measures 230 μrad and the strip pitch measures 463 μrad. The readout board is divided into 8 sectors along η. Each η-sector consists of 384 strips. For long chambers, the strip length varies from 11 cm to 19 cm for η-sector 1 and η-sector 8, respectively. The readout board has vias that connect the readout strips to the outer side of the readout board. On the outer side, traces are routed from the vias to 24 (8×3) 130-pin panasonic connectors. 128 pins are connected to the traces of the corresponding readout sector and 2 pins are connected to the common chamber ground. Each η-sector is divided into 3 parts. In the following, the 24 readout sectors are denoted as (η, ϕ)-sectors, where $\eta \in \{1, .., 8\}$ and $\phi \in \{1, .., 3\}$. Tab. 5.1 mentions some of the specifications of the readout board.

Readout electronics in CMS The readout electronics of the GEM detectors in CMS are divided in two parts, on-detector and off-detector electronics. Starting with the on-detector electronics, each readout sector is connected with a front-end ASIC (VFAT3). The VFAT3 has been developed for the readout and triggering of GEM detectors in CMS. It is based on its predecessor, called VFAT2 [116]. Basic features of the VFAT3 can be found in Ref. [11]. The VFAT3 is, on the other side of the ASIC, plugged into the GEM electronics board (GEB). The GEB is a flat printed circuit board (PCB) hosting the electrical links for powering, readout, and remote control of the VFATs. Another board, called Optohybrid (OH), is also plugged into the GEB. It is equipped with an FPGA and optical receivers and transmitters to allow the data transfer/control via optical fibers to/from the off-detector electronics. The trigger and tracking data is sent via the off-detector electronics to the CMS DAQ and trigger systems. Additionally, the trigger data is directly sent to the CSC boards to improve the L1 trigger capabilities (see Sec. 5.2.1).

Performance studies This paragraph is devoted to the discussion of a few studies performed during the R&D phase of the CMS GEM project. These studies demonstrate that the predefined requirements are met by GE1/1 prototype chambers.

For the detector efficiency measurement, a full-size GE1/1 prototype was tested in 20-120 GeV hadron beams at the Fermilab test beam facility (FTBF) flushing the chamber with the nominal Ar/CO_2 (70/30) gas mixture. The studies were performed either with an earlier version of the readout electronics or with a predecessor of the readout board used during

the quality control. The measured efficiency reaches a plateau of 97.1 $\pm$ 0.2 (stat)% for pions. An angular resolution of 136.8 $\pm$ 2.5 (stat) μrad was found for an emulated binary readout. This matches the expected resolution of strip pitch divided by $\sqrt{12} = 131.3$ μrad. The results are taken from Ref. [12].

The discharge probability was measured for the GE1/1 Technical Design Report (TDR) [10] with a ^{241}Am α-source. The measurement was performed at a higher gain (4-6 $\times$ 10^5) compared to the expected nominal gain for CMS operations ($\mathcal{O}(10^4)$) to obtain good statistics of discharges. Extrapolated to the nominal CMS working point, the discharge probability was found to be approximately 9×10^{-10} per α particle. The probability with incident MIPs is expected to be two orders of magnitude lower, since α-particles produce 10^2 times more primaries in the gas volume.

The rate capability has been studied intensively during the R&D phase, as well as in the latest phase of the CMS GEM project. The triple-GEM technology exceeds the required 10 kHz/cm^2 by several orders of magnitude [10].

Recent aging studies have shown that no aging effects are observed up to an accumulated integrated charge of 800 mC/cm^2 [9].

5.3 GE1/1 detector production

The goal of the GE1/1 detector production is to assemble, test, and qualify the amount of chambers needed for the GE1/1 endcap disks. In total, 144 GEM detectors (72 long and 72 short single chambers) are required for the installation during LS2 in 2019 and 2020.

5.3.1 Production community

Production sites in seven different countries around the world have been set up to assemble and test detectors. Besides sharing the knowledge among the members of the collaboration, this structure prevents large production stops. To ensure uniformity in production among the different laboratories, all candidate sites must undergo a predefined approval procedure. This includes intensive training of the staff, as well as a check of equivalent equipment, tools, readout system, and analysis framework. After successfully testing the setup with GEM prototypes, the candidate site is accepted to participate in the production of the GE1/1 chambers.

The central production site is a laboratory located at CERN, where all the components (drift boards, readout boards, GEM foils, gas frames, o-rings, screws, etc.) are received and inspected. All other sites are receiving components and/or detectors from the CERN site. In some sites, both the assemblies and the quality control (QC) tests take place (production sites). In other sites, only QC tests are performed (testing sites). One of the testing sites is located in Aachen. The chambers tested in Aachen are assembled at either Ghent or CERN and then shipped to Aachen. After full validation, the chambers are sent back to CERN. The structure of the GE1/1 production group is sketched in Fig. 5.12.

5.3.2 Overview of assembly and quality control tests

The GE1/1 GEM chambers have to undergo a precise protocol of quality control steps [117] before the installation in CMS. Fig. 5.13 provides an overview of the production workflow including assembly and QC tests. In the following, the production steps are discussed with a special focus on those steps performed in Aachen (QC3-5). Up to QC7, the test are performed with single chambers. After QC7, the single chambers are paired and, in QC8, the superchambers are tested.

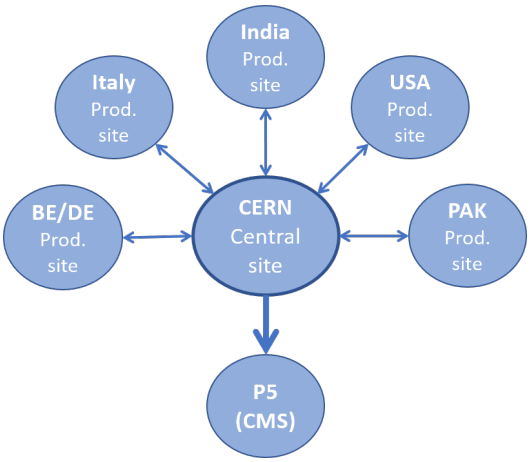

Figure 5.12: Illustration of the structure of the GE1/1 production community. The CERN site is the central site of the production group and acts, in addition, as a production site.

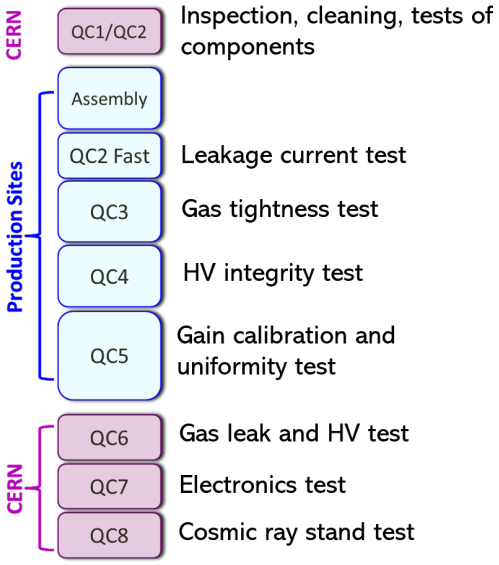

Figure 5.13: Overview of the production workflow. The reception and first tests of the detector components take place at CERN. Assembly and testing up to QC5 is done at the different production/testing sites. In Aachen, QC3 to QC5 are performed. After validation, all chambers are collected at CERN and QC6 to QC8 are carried out.

Powering of electrodes for QC tests There are two main approaches how to connect HV to the pads on the drift board and, thus, to the electrodes. One approach is to use a single HV channel connected to the drift board and to solder a divider distributing HV to the other electrodes according to its resistor values. The other approach consists of connecting each pad to an individual HV channel using a multichannel HV supply. For QC4 and QC5, the choice is to distribute HV to the electrodes via a ceramic divider what turned out to be a cost-effective solution during the R&D phase and to be easily adaptable by all production sites. A picture of the ceramic divider, as well as the resistance values[1], are given in Fig. 5.14. For all subsequent QC tests and in CMS, a multichannel HV supply is used. This is the reason, why two HV tests are listed in Fig. 5.13.

5.3.3 Assembly and first quality control tests

The assembly of the GEM chambers takes place in a clean room to minimize the probability that (dust) particles can enter the GEM holes which may cause electric shorts on the foils. Some of the assembly steps are shown in Fig. 5.15. After cleaning all the components, the assembly starts with forming the GEM foil stack. First, each foil is prepared to connect it to the HV pins. The three GEM foils are then put on top of each other, interleaved with the spacers. The alignment of the different components is guaranteed by dedicated alignment pins along the sides of the trapezoid. The alignment pins are removed when lifting the GEM stack. The protruding parts of the foils are cut off, so that the leftover trapezoidal stack can be put on the drift board. By applying a fixed torque to the pullout screws the complete stack of GEM foils is stretched. First, the torque is applied simultaneously along both the

[1]Whenever a divider is mentioned throughout the course of this thesis, these are the default values.

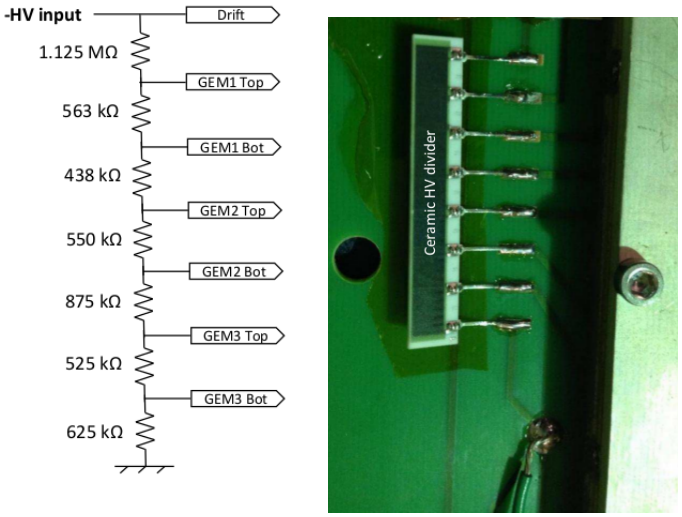

Figure 5.14: Left: Resistance values of the ceramic HV divider. GEM1 Top and GEM1 Bot denote top and bottom of the first GEM foil. The labels for the other electrodes follow this convention. Right: Ceramic divider mounted on the drift board. The figures are taken from Ref. [10].

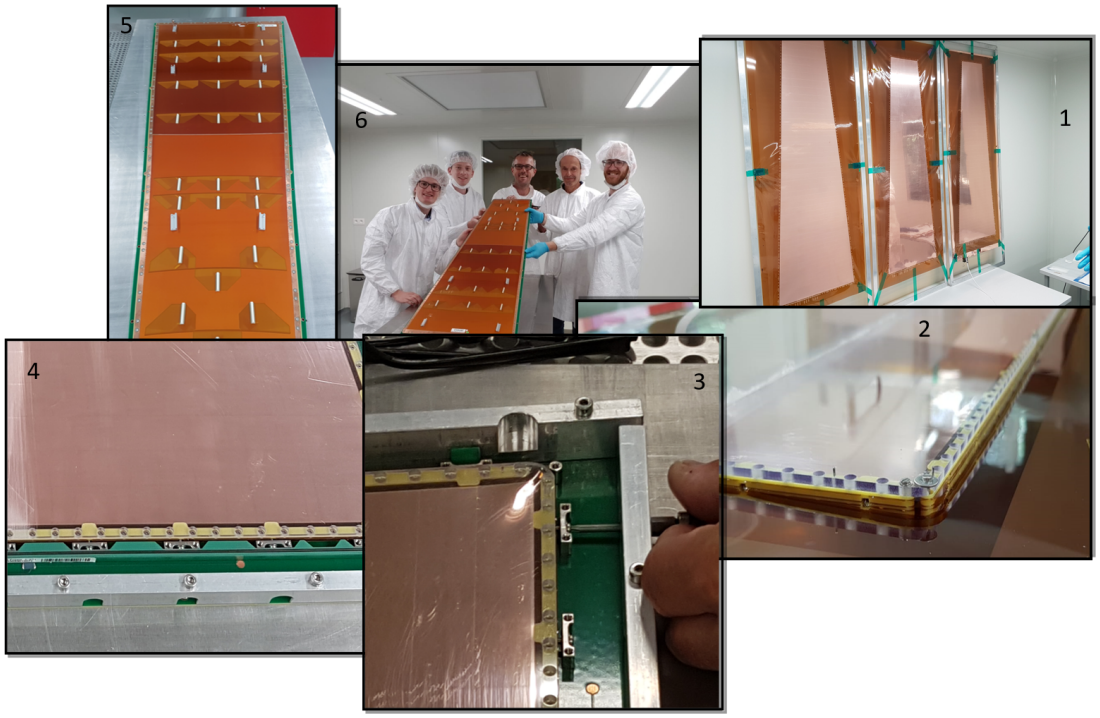

Figure 5.15: Collection of pictures taken at Ghent while assisting the Ghent production team during an assembly of a GE1/1 chamber. Clockwise, one can see highlights of the assembly procedure in chronological order: 1) Three GEM foils as they are received by the production site. The trapezoidal shape of the active foil area can be seen. The protruding part of the polyimide is removed during the assembly. 2) Corner of the trapezoid with the stack of GEM foils. In yellow, the spacers can be seen. 3) Stack of GEM foils put on top of the drift board. By applying a predefined torque to the pullout screws, the GEM foils are stretched. 4) Large base of the trapezoid. The spacers (yellow), brass pullouts, the external gas frame (green) and the o-ring (black) are shown. 5) Fully assembled GE1/1 chamber. The readout board with the 24 sectors can be seen. 6) Ghent and Aachen team after the assembly in the clean room.

edges and then along the long and short bases of the trapezoid. With the o-ring inside its groove, the gas frame is put in place. To close the chamber, the readout board, with the gas in- and outlet, is mounted on top and fixed by inserting screws in the windings of the pullouts. More details about the assembly steps can be found in Ref. [115].

Before leaving the clean room after the assembly, the impedance of the gaps and the GEM foils is tested with an insulation meter to verify that the foils are not electrically shorted and that different layers of the stack do not touch each other. If the chamber fails the test with the insulation meter, the foils can be cleaned or the torque applied to the pullout screws can be carefully and slightly increased. While increasing the voltage up to typically 500 V on the foils during the test, the number of sparks is registered. The measured impedance should exceed 10 GΩ for the GEM foils and 100 GΩ for the gaps. Once the maximum impedance is reached, no sparks should be observed within one minute of measurement time.

After the assembly, a unique name is given to each detector for further reference and tracking. The name consists of the prefix for the GE1/1 production, the generation of the detector, whether the detector is long (L) or short (S), the laboratory, where the detector was assembled, and a unique serial number, in chronological order of the assemblies. The final version of the detector is the 10th generation. Consequently, the first GEM detector assembled at Ghent for integration in the CMS GE1/1 station is called GE1/1-X-L-GHENT-0001. When showing the results of the measurements performed in Aachen, a shorter version is sometimes used in this section, e.g. GHENT-0001. Since only long chambers are tested in Aachen, this convention drops information that is the same for all tested chambers.

5.3.4 Gas tightness

Motivation The gas tightness is checked to ensure safe operation over a long period of time. Gas tightness minimizes the probability of polluting the gas volume with contaminants of any kind from the surroundings. Pollutants could severely impact the detector performance. Especially metallic dust entering the detector could harm the GEM foils.

Setup and procedure The chamber is connected via the gas in- and outlet to a gas panel and flushed with pure CO_2 for several hours. Upstream of the detector, pressure and temperature sensors are installed to measure the atmospheric pressure and temperature, and, most importantly, the overpressure inside the gas volume. The sensors are read out with an Arduino®. These sensors plus the chamber volume are surrounded by input and output valves. GE1/1 detectors can sustain an overpressure of up to 50 mbar, which is the reason why a safety valve is added. Fig. 5.16 shows a schematic overview of the setup.

While flushing the chamber with CO_2, the output valve is closed until the overpressure reaches 25 mbar. Then, the input valve is closed and the flow is set to zero. The valves are kept closed and the overpressure, as well as the atmospheric pressure and temperature, are registered every minute for one hour.

Results and interpretation Fig. 5.17 presents a typical result of a gas leakage test for the GE1/1 detector production. The overpressure as a function of time follows an exponential decay: $p(t) = p_0 \times exp(-\frac{t}{\tau})$, where p_0 denotes the initial pressure at $t = 0$ and τ is called the gas leak time constant. The parameter τ serves as an indicator of gas leakage. With a larger τ, the chamber is more gas tight. Fig. 5.18 shows the gas leak time constant of those GE1/1 chambers tested in Aachen (left) and of all GE1/1 chambers (right).

Passing the acceptance limit of $\tau = 3$ h ensures a maximum loss of gas flow rate around 0.02 l/h for the operation in CMS. Possible leaks could be due to a poor matching of the gas frame groove and o-ring diameter. Another leak source is the way of closing the chamber

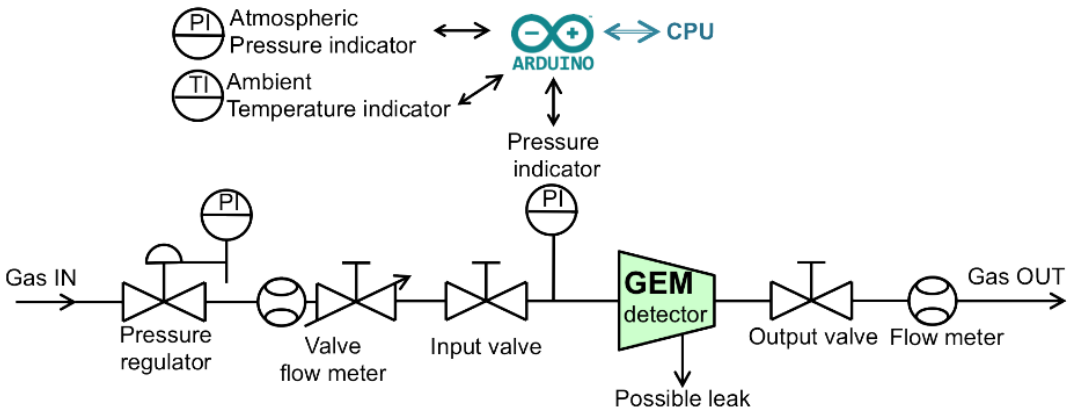

Figure 5.16: Schematic overview of the setup for the gas tightness test (QC3). The figure is taken from Ref. [117].

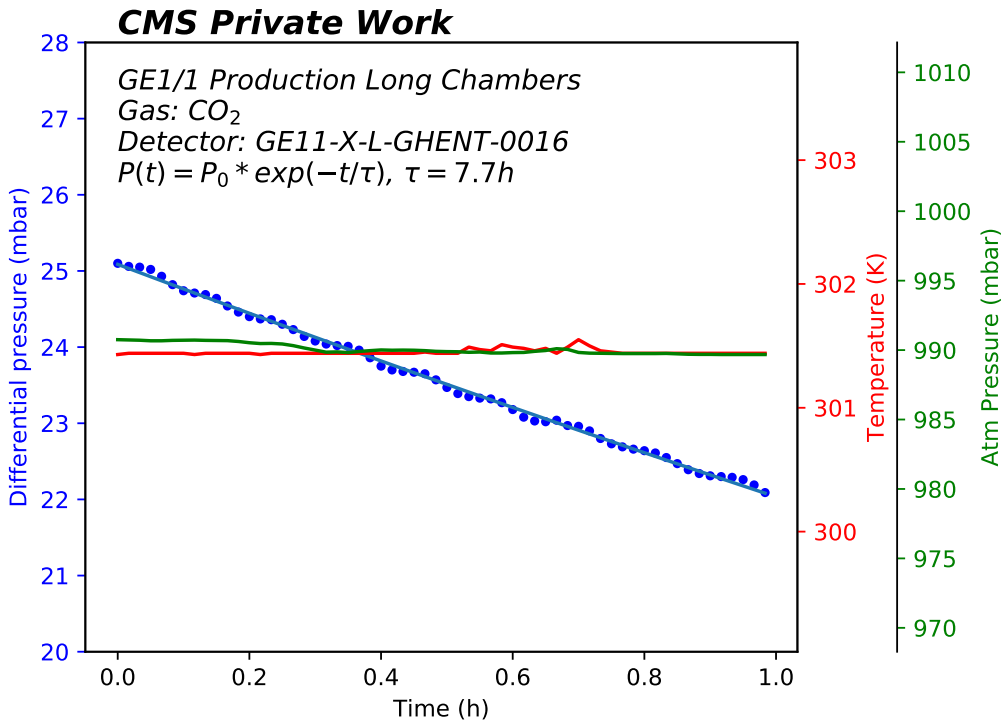

Figure 5.17: Typical result of a gas leakage test performed with a GE1/1 chamber from production. The green and red lines show the atmospheric pressure and temperature, respectively. The blue points represent the monitored overpressure and the light blue line depicts the parametrization of an exponential function.

by putting the drift and readout board on top and bottom. When fixing the boards by tightening the screws on top and bottom of the brass pullouts, the force is not applied on top of the o-ring but instead on the pullouts.

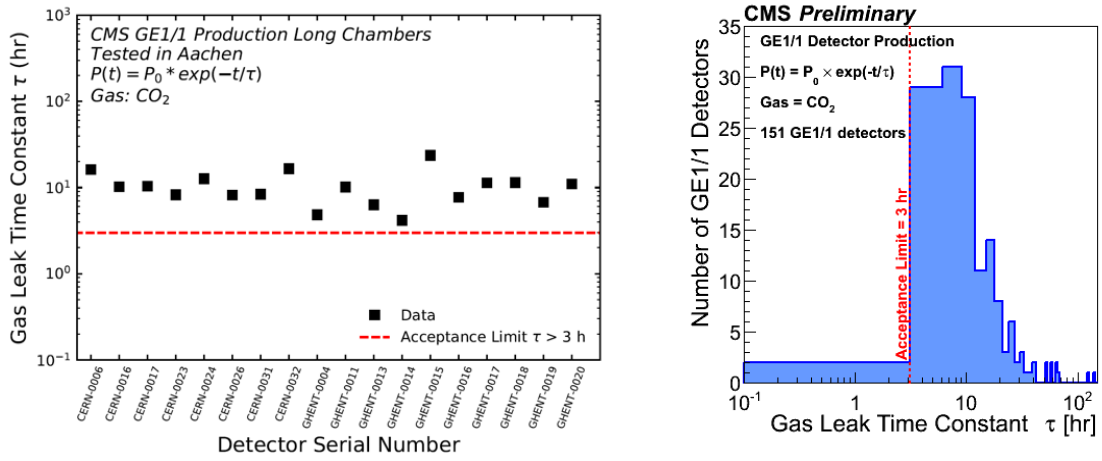

Figure 5.18: Left: Gas leak time constant of those GE1/1 detectors tested in Aachen. The gas leak time constant is shown as a function of the detector serial number. Right: Gas leak time constant of all GE1/1 detectors. The figure is taken from Ref. [118]. The dashed red line indicates in both figures the acceptance limit of $\tau = 3$ h. 149 GE1/1 chambers passed this test, while two failed.

5.3.5 HV integrity

Motivation During this measurement, the chamber is operated for the first time with HV connected. It is of utmost importance to check the integrity of the circuits and to identify possible malfunctions while slowly ramping up the HV. The intrinsic chamber noise is determined by recording the spurious signal rate. To ensure an excellent detector performance during operation, the rate of spurious signals should be well below the background hit rate in CMS at the GE1/1 position ($\mathcal{O}$(kHz/cm^2)).

Setup and procedure Before testing, the chamber is equipped with the ceramic HV divider (see Fig. 5.14) and a single HV channel is connected to the drift electrode. The chamber is flushed with pure CO_2 at 5 l/h, which ensures safe operation and the absence of amplification inside the GEM holes. The readout is done using a charge-sensitive preamplifier connected to the GEM3 bottom (G3b) electrode through a decoupling capacitance[2]. The output of the preamplifier goes to an amplifier/shaping unit and then to a discriminator with a preset threshold. At the end of the readout chain, a scaler registers the rate of spurious signals. The chain of data acquisition is presented in Fig. 5.19. The panasonic connectors on the readout board are equipped with 50 Ω terminations. The grounding is carried out using

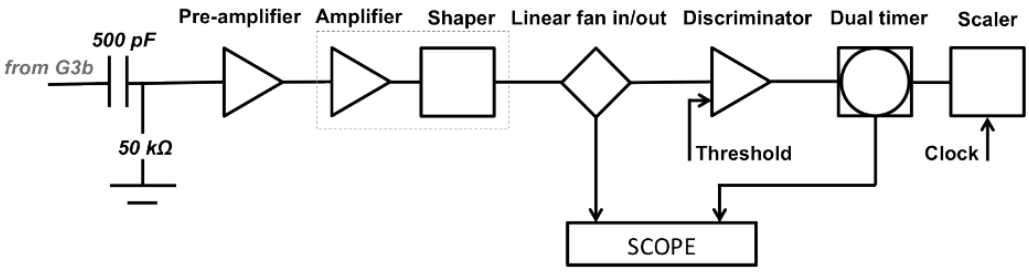

Figure 5.19: Data acquisition chain of the HV integrity test (QC4). The figure is taken from Ref. [117].

[2]The reader should note, that the bottom of GEM3 is under HV.

a trapezoidal PCB, matching the size of the GE1/1 chamber, with thin layers of copper on both sides. The ground of the chamber and of the terminations is connected to the plate. The grounding plate is also used during the gain measurements (QC5) as discussed in Sec. 5.3.6.

Stepwise, the HV is ramped up from 200 V to 4.9 kV. For each point, the current running through the divider, henceforth called divider current, and the rate of spurious signals is monitored. The expected divider current can be calculated by summing up all resistances in the circuit. This includes the resistances of the divider, in total 4.7 MΩ, and the low-pass HV filter, in total 300 kΩ. The filter is inserted after the HV supply to reduce noise coming from the supply unit. For the highest HV point of 4.9 kV, a divider current of 980 μA is expected.

Results and interpretation A typical outcome of the HV integrity test can be seen in Fig. 5.20. The applied HV and spurious signal rate as a function of the monitored divider current are depicted. The HV circuit shows an ohmic behavior for the whole range of applied voltages. The parametrization $U_{\text{applied}} = R_{\text{meas}} \times I_{\text{divider}}$ gives the measured total

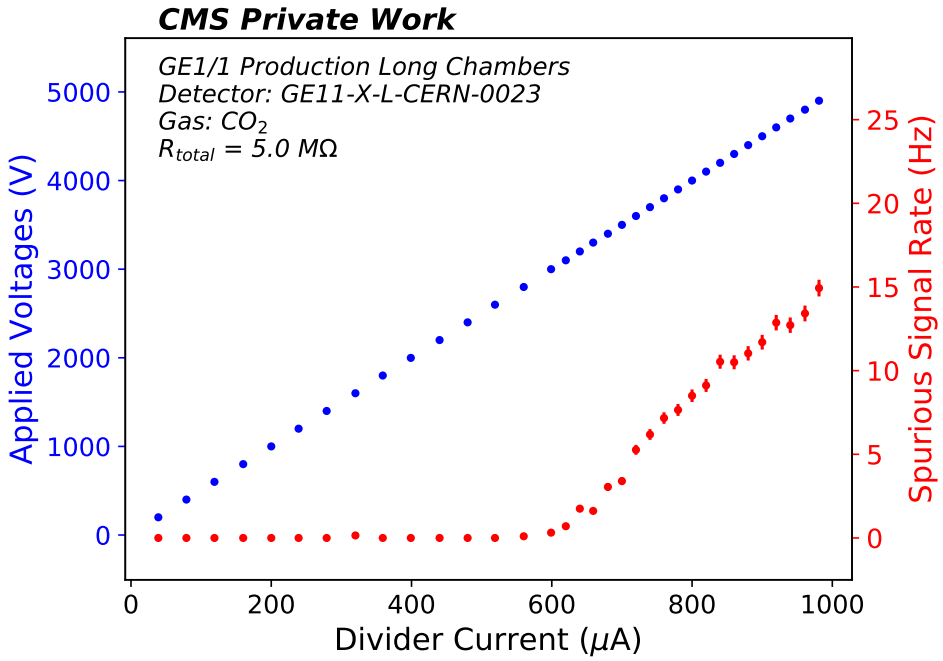

Figure 5.20: Typical result of an HV integrity test performed with a GE1/1 chamber from production. Blue points show the applied voltages for each step as a function of the divider current. The measured spurious signal rates are depicted as red points. The voltages are set, while the divider current is registered.

resistance of the circuit. The resistance deviation is defined as $(R_{\text{meas}} - R_{\text{tot}})/R_{\text{tot}}$. The resistance deviation and the spurious signal rate at 4.9 kV are used as the criteria for this QC test.

Summaries of the GE1/1 chambers tested in Aachen and of all GE1/1 chambers are given in Fig. 5.21 and 5.22, respectively. Since the measured resistances do not deviate much from the expected values, the integrity of the HV circuits is ensured. For all tested chambers, the spurious signal rate is well below the background hit rate in CMS at the GE1/1 position ($\mathcal{O}$(kHz/cm^2)). Spurious signals can be explained by corona discharges from the GEM active area along the internal frame to the anode strips [118].

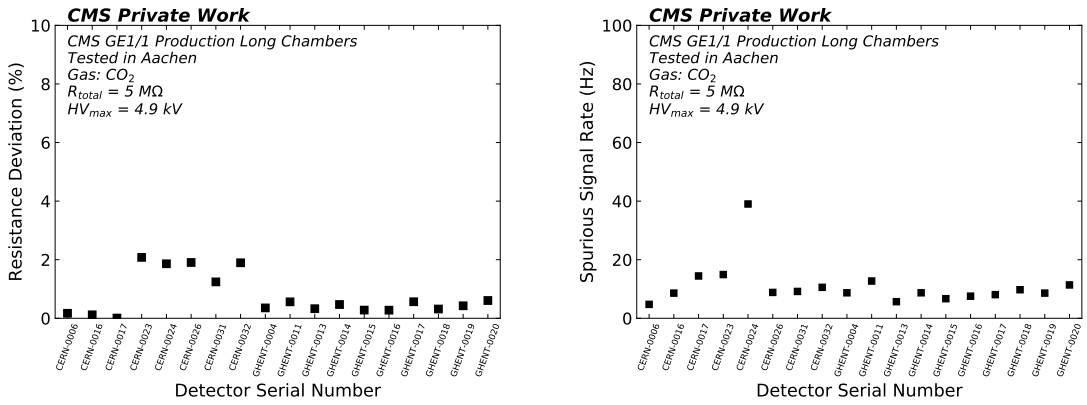

Figure 5.21: HV integrity results of the GE1/1 chambers tested in Aachen. Left: Resistance deviation from the nominal value as a function of the detector serial number. Right: Rate of spurious noise at the highest HV point of 4.9 kV as a function of the detector serial number.

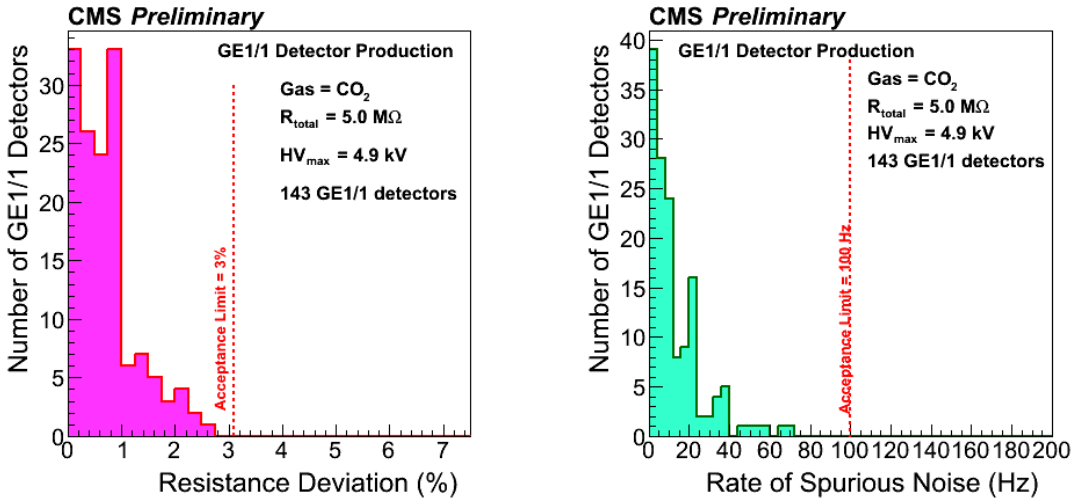

Figure 5.22: HV integrity results of the GE1/1 detector production. The resistance deviations from nominal values (left) and the rates of spurious noise (right) are presented. For both quantities, the acceptance limit is shown as a red dashed line. The total resistance of 5 MΩ is divided between the ceramic divider and the HV filter. The figures are taken from Ref. [118].

5.3.6 Gas gain measurements

Motivation For gaseous detectors in general, the gas gain is one of the most important parameters and should be thoroughly investigated and well-understood. For the GE1/1 chambers, one goal of the gas gain measurements is to determine the working point. An effective gas gain of 10^4 is desired. In CMS, the single chambers of one superchamber share the same HV supply. Thus, the working point is used as a criterion to match single chambers to a superchamber (Sec. 5.3.8). Striking features of the GE1/1 detectors are their large size and the innovative foil stretching technique. Thus, checking the uniformity of the gas gain over the entire active area is of utmost importance. The corresponding measurements are subsumed under the term QC5.

Setup The setup of the gas gain measurements can be seen in Fig. 5.23, sketched (top) and photographed (bottom). The gas gain measurements are performed by fully irradiating the chamber with photons from an X-ray gun (Amptek® Mini-X X-ray Tube). The X-ray gun accelerates electrons onto a silver target. As a consequence, photons of the characteristic K_α line with an energy around 23 keV are emitted. Typical rates are 1 MHz/mm^2 at a distance of 30 cm from the X-ray gun [119]. More information on the X-ray gun is provided in Sec. A.1. To operate safely in terms of radiation, the X-ray gun and the tested detector are put into a box. The box, hereafter referred to as the copper box, with the dimensions of 2 m $\times$ 1 m $\times$ 1 m consists of 4 mm thick walls made of copper. In addition to the shielding, it acts as a Faraday cage. The box dimensions are motivated by the fact that the maximum opening angle of the cone of emitted photons from the X-ray gun is 120°. With the copper enclosing the whole setup and the copper on the outside surface of the chamber, the photons of the X-ray gun unavoidably excite the copper atoms and induce fluorescence light. The detected photons do not come from the K_α line but rather from the copper fluorescence peak with an energy around 8 keV. The chamber is flushed with Ar/CO_2 (70/30), which is the nominal GEM gas mixture in CMS. The HV is distributed in the same way as for the HV integrity test, i.e. with the ceramic divider.

Readout electronics for gain measurements The readout is based on the Scalable Readout System (SRS) [120] developed by the RD51 collaboration [121]. The front-end electronics consist of Analog Pipeline Voltage (APV) hybrids [122], which have been originally developed for silicon tracking detectors in CMS [123]. Nowadays, the APVs enjoy a large number of applications, such as the readout of MPGDs. The readout electronics used for the gas gain measurements differ from the readout electronics for CMS (Sec. 5.2.2). The VFATs provide only digital output while the analog information of the signals is needed for this test.

Each APV hosts 128 channels matching the number of strips on the readout board for each sector. To fully equip one chamber, 24 APVs are needed. Each APV channel consists of a preamplifier coupled to a shaping amplifier. The output is sampled at a frequency of 40 MHz in a pipeline with a depth of 192 cells. Via high-definition multimedia interface (HDMI) cables, the analog output of the APVs is sent to 12-bit analog-to-digital converters (ADCs). The ADCs are hosted on dedicated adapter boards, called ADC cards. The ADC card plugs into a front-end concentrator (FEC) card. The FEC cards are responsible for the communication with the external devices, e.g. sending the data to the DAQ PC and configuring ADCs and APV hybrids. The SRS, as the backend-electronics system, houses the ADC and FEC cards. For the GE1/1 quality control, two ADC cards, with 8 HDMI inputs each, and two FEC cards are necessary to read out a complete chamber. The 24 APV hybrids are arranged in master-slave pairs connected by a flat cable. This is possible because the HDMI cables allow two serial analog streams.

When the FECs receive a trigger signal, the APVs start an acquisition window. With n time bins, the acquisition window can be set to $n\times$25 ns. A typical snapshot of the readout cycle of a single APV is presented in Fig. 5.24, where the number of time bins is set to 21. To maximize the acquisition time during the QC measurements, the number of time bins is set to 30.

In this data taking mode, the information of all APV channels is sent out for every event in every time bin. Even if there is a signal in one event detected by the GEM chamber, the large majority of strips contains only noise. This huge data flow can be avoided by the zero-suppression (ZS) mode. The firmware of the FEC card can be configured to suppress those strips with only noise, i.e. the data is not sent to the DAQ PC. To define the baseline and noise level of the channels, pedestals are taken. The ZS mode is used for the QC measurements with GE1/1 chambers.

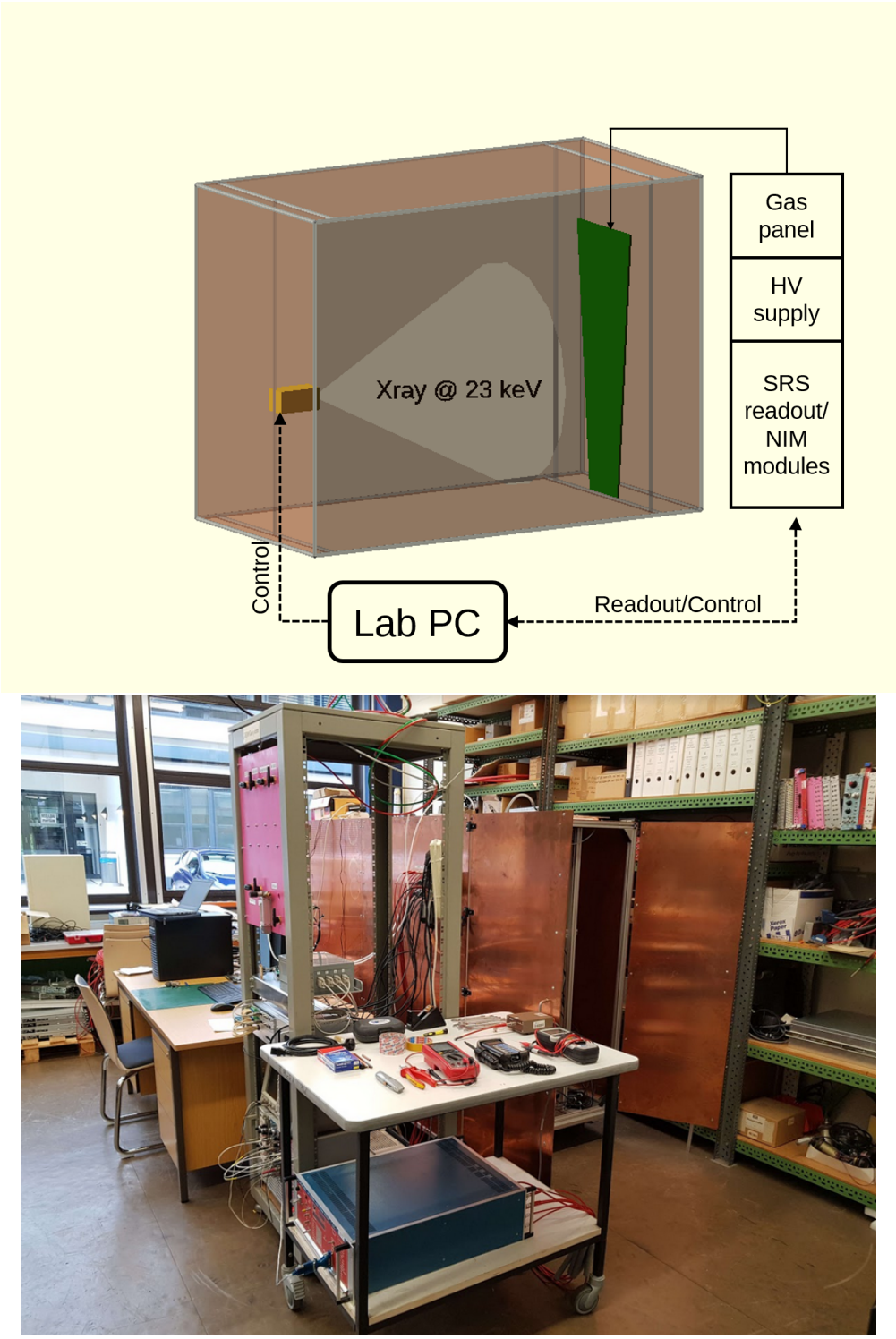

Figure 5.23: Top: Sketch providing a schematic view of the setup for the gas gain measurements with the opportunity to look inside the copper box. The PC is connected to the X-ray gun. In addition, the PC is used to control and read out the gas system and HV supply, as well as the readout system (SRS). Bottom: Picture showing the setup in the Aachen GEM laboratory with the copper box in the background, with doors open. The gas system and HV supply, as well as the SRS system, are stored in the rack in the middle of the picture. Behind the rack, the lab control PC is located. More pictures of the laboratory and hardware devices can be found in Sec. A.2.

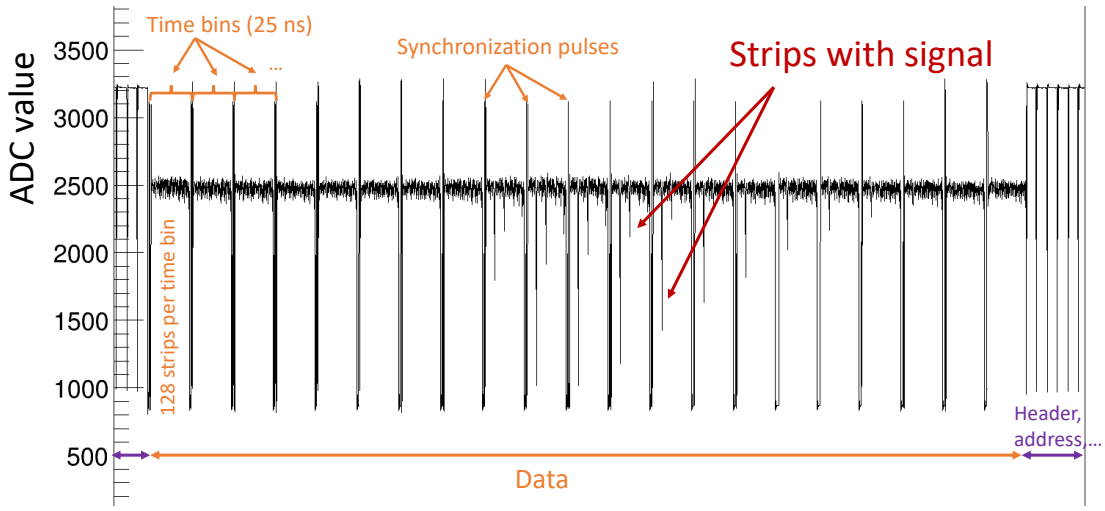

Figure 5.24: Typical example of the readout cycle of a single APV. The ADC values of the analog data are registered for 21 time bins. The time bins are separated by synchronization pulses. For each time bin, the data of all 128 channels is shown sequentially. The ordering of the strips does not correspond to the physical arrangement on the readout board. In the beginning and in the end, information, such as headers and addresses, is sent via digital signals.

Effective gain calibration - procedure Before the gain uniformity is studied, the effective average gas gain is measured in order to determine the working point of the chamber. For this test, APVs are plugged to all readout sectors[3] except to the sector in position (η,ϕ) = (4,2). Sector (4,2) is read out by a connector summing up the induced currents from all strips of this sector. The output is connected to a similar readout chain as in the HV integrity test: preamplifier, amplifier/shaping unit, discriminator, and scaler. This configuration is used for the rate measurement. To measure the induced current I_{RO}, the output is directly connected to and read out by a picoamperemeter (KEITHLEY 6487). The current is expected to be in the range of 0.1 nA$-$10 nA. Fig. 5.25 summarizes the data acquisition chain in a schematic overview.

The effective gain measurement is performed in a specific range of the divider current $I_{Divider}$. With the information from the HV integrity test, the values of the divider current can be translated into HV values. For each point in HV, the rate of signals, as well as the induced current, are measured and registered once with the X-ray source turned on, and once turned off. The induced current is registered with the picoamperemeter giving a measured value for the current at a rate of 10 Hz. For each HV point, 200 current values are read out and registered.

Effective gain calibration - results The effective gas gain is given by

$$G_{eff} = \frac{I_{RO}}{n_p \cdot q_e \cdot R_S}, \tag{5.1}$$

[3]The APVs are, in this test, solely used as terminations/grounding for the panasonic connectors on the readout board.

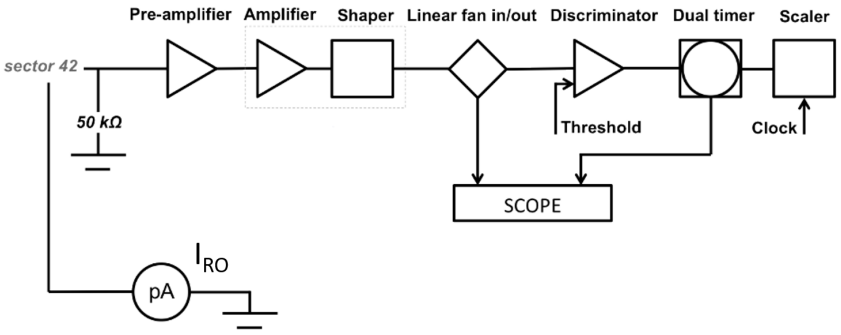

Figure 5.25: Data acquisition chain of the effective gain calibration measurement. The figure is taken from Ref. [117].

where I_{RO} denotes the current on the readout board, n_p the number of electrons from primary and secondary ionizations of the incident particle, q_e the elementary charge and R_S the signal rate. R_S and I_{RO} are measured as described above. For I_{RO}, the mean over the 200 measured values is used. To obtain the final value for both quantities, the values with the X-ray source turned off are subtracted. Exemplary, results for both quantities from the GE1/1-X-L-GHENT-0013 chamber are depicted in Fig. 5.26. The measured rate reaches a plateau once the amplification is large enough so that all signals from the copper fluorescence peak are passing the discriminator threshold. The induced current rises exponentially

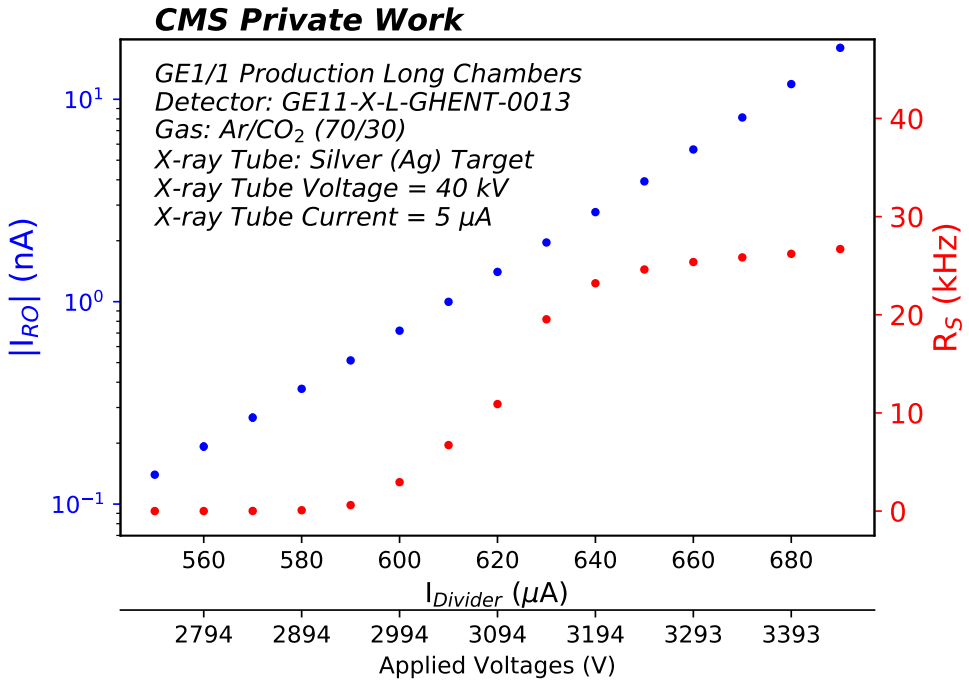

Figure 5.26: Results of the rate (red) and induced current (blue) measurement for the effective gas gain calibration of the chamber GE1/1-X-L-GHENT-0013. The results are shown as a function of the divider current, $I_{Divider}$, and as a function of the applied voltages. Fig. 5.20 is used to convert the divider currents into applied voltages. The axis of the induced current, I_{RO}, is displayed on a logarithmic scale, while the axis of the rate, R_S, is displayed on a linear scale.

with higher divider currents due to a higher amplification in the GEM holes.

For Ar/CO_2 (70/30), n_p can be estimated by

$$n_p = E_{inc} \times \left(\frac{0.7}{w_i(Ar)} + \frac{0.3}{w_i(CO_2)} \right), \tag{5.2}$$

where E_{inc} is the energy of the incident particle, $w_i(gas)$ the average energy required to produce one electron-ion pair in the gas. For the copper fluorescence spectrum induced by the X-ray gun, n_p is measured to be 346±2.9[4]. The error on the effective gas gain is determined by adding the errors of the quantities in Eq. 5.1 quadratically. For the signal rate R_S, the counting error of $\sqrt{N}$ is assumed, where N is the number of signals. For I_{RO}, a set of 200 values is measured. Thus, the standard deviation of the distribution is used as the error on I_{RO}. In this procedure, the dominating error comes from the readout current measurement, since the relative error on the rate scales with $1/\sqrt{N}$.

As an example, the effective gas gain curve of GE1/1-X-L-CERN-0006 is presented in Fig. 5.27. The effective gas gain is a function of the Townsend coefficient α, which depends on many factors, mainly on the electric field and environmental parameters, such as temperature and pressure. To be able to compare the measurements of all GE1/1 chambers, the gain has to be corrected for temperature and pressure according to

$$G \propto \exp(\alpha) \propto \exp(E \times T/T_0 \times p_0/p), \tag{5.3}$$

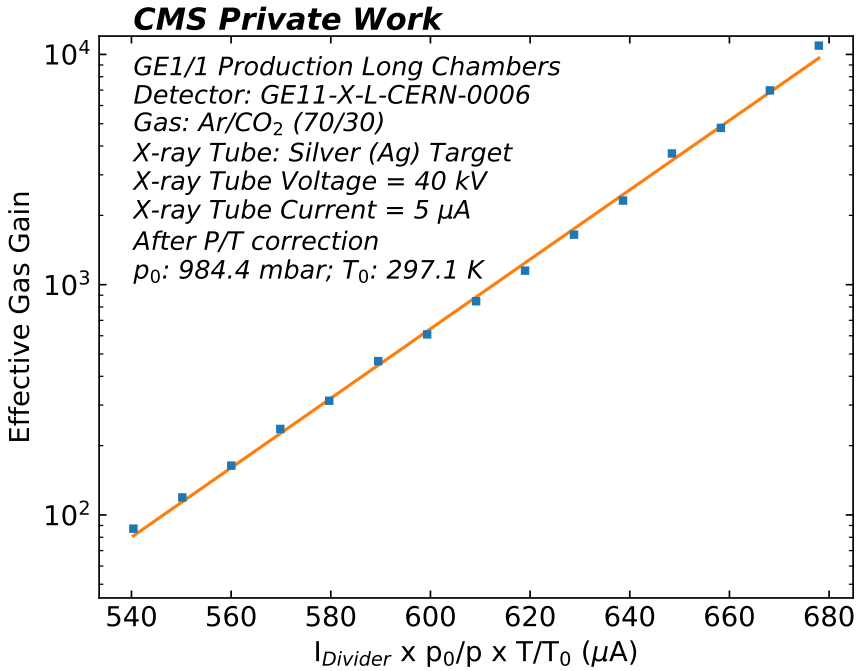

Figure 5.27: Effective gas gain as a function of the divider current taken with GE1/1-X-L-CERN-0006. The blue points represent the measurement while the orange line gives an exponential parametrization. The gas gain is normalized to the temperature and pressure of the CMS underground cavern (p/T correction). A collection of the results of the other GEM chambers tested in Aachen is given in Fig. A.11. The errors on the data points, typically around 2-4%, cannot be seen due to the logarithmic scale of the y-axis. However, it is important to be aware of this, not only for the GE1/1 QC measurement, but also for the measurements presented in Sec. 6.2.

[4]The measurement was performed during the early CMS GEM R&D phase by comparing gain measurements from different photon spectra. There is no public document available to be cited.

where T_0 and p_0 denote the reference temperature and pressure, respectively. These corrections are successfully applied in different studies [124, 125]. The effective gas gain is normalized to standard conditions in P5, i.e. p_0 = 964.4 mbar and T_0 = 297.1 K. A GE1/1 chamber passes this QC test, if the measured effective gain shows the expected exponential dependency on the divider current, if the measured gain is in the desired region of 10^4 around $I_{\mathrm{Divider}} = 700\ \mu$A and if the plateau of the signal rate is clearly visible.

Gain uniformity - procedure During the gain uniformity test, the divider current is set to the value, that corresponds to a gas gain of ≈ 600 in sector (4,2). This ensures that the signals are below the saturation limit of the APV hybrids. The external trigger is fed randomly to the FEC cards at a rate of roughly 500 kHz. Due to statistics reasons, 100 runs are taken for each QC5 test. A run contains typically 100 k events. Thus, the measurement time sums up to 6 hours. The X-ray gun is kept on during the whole test.

Gain uniformity - data acquisition and analysis The data acquisition is performed by using DATE (Data Acquisition and Test Environment) [126], providing a user-friendly GUI (Graphical User Interface) for the data transfer. The first part of the data analysis is based on the AMORE (Automatic MOnitoRing Environment) framework [127]. DATE and AMORE were originally developed for the Data Quality Monitoring (DQM) of the ALICE experiment and later adapted by the RD51 collaboration for the readout with the SRS.

The first part of the analysis, based on AMORE, consists mainly of the clustering. In ZS mode, the raw data contains the information of those strips with hits above the noise level. For each event, the hits of neighboring strips are organized in a cluster. The cluster object contains information about the cluster size, position, and total induced charge. On this level, cuts on the minimum and maximum cluster size or the cluster multiplicity (clusters per event in the detector) are possible to reject fake events, noise or cross-talk. As an output, the information of the hits and clusters are saved.

The second part of the analysis relies on the CMS GEM Analysis Framework [128]. Within this framework, the mapping of the channel number to the strip number is performed. The APVs are equipped with a multiplexer causing a difference between channel and strip number. Finally, the channel number can be mapped to the physical strip position on the readout board. At this stage, several cuts on cluster size and timing are applied. To select events that are fully included in the data, those clusters where the maximum cluster charge is in the first or last time bins are rejected, as well as clusters with a cluster size smaller than 2 strips. For further analysis and visualization, 4 strips are packed into a slice. This means 32 slices per readout sector. For each event, the maximum cluster charge per slice is stored in a histogram. For the whole detector, 24 $\times$ 32 = 768 cluster charge histograms are obtained for further usage. An example histogram is given in Fig. 5.28, showing the copper fluorescence peak on top of the Bremsstrahlung spectrum. The spectrum is parametrized by a sum of a Cauchy distribution (fluorescence peak) and a 5th order polynomial (Bremsstrahlung). After a quality check of the applied parametrization, the median of the Cauchy distribution, corresponding to the cluster charge value of the position of the fluorescence peak, is filled into a histogram for all slices. The cluster charge is a measure of the induced charge for an ionizing particle and, thus, a measure of the gas gain. Variations of the cluster charge over the area of the detector correspond to variations of the gas gain. The ratio of the standard deviation of this histogram over the mean of this histogram is used to check the gas gain uniformity of a GE1/1 detector. Fig. 5.29 shows the resulting histogram with its mean and standard deviation for GE1/1-X-L-GHENT-0016. For the tested chamber, gain variations of 21% are measured. Fig. 5.30 gives another representation of the fitted peak position as a function of the position of the slice on the readout board for all η-sectors. This

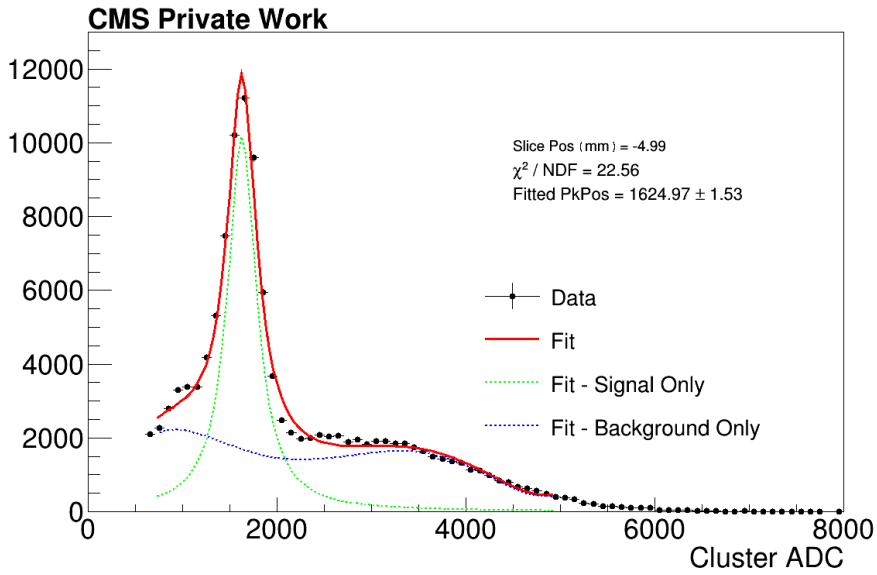

Figure 5.28: Example histogram for the measured cluster charge spectrum of a slice in sector (4,2) of the chamber GE1/1-X-L-GHENT-0016. The spectrum contains two main components, i.e. the copper fluorescence peak parametrized by a Cauchy distribution (green dashed line), and the Bremsstrahlung background parametrized by a 5th order polynomial (blue dashed line). The sum of both functions can be seen as a solid red line. The data points are shown in blue.

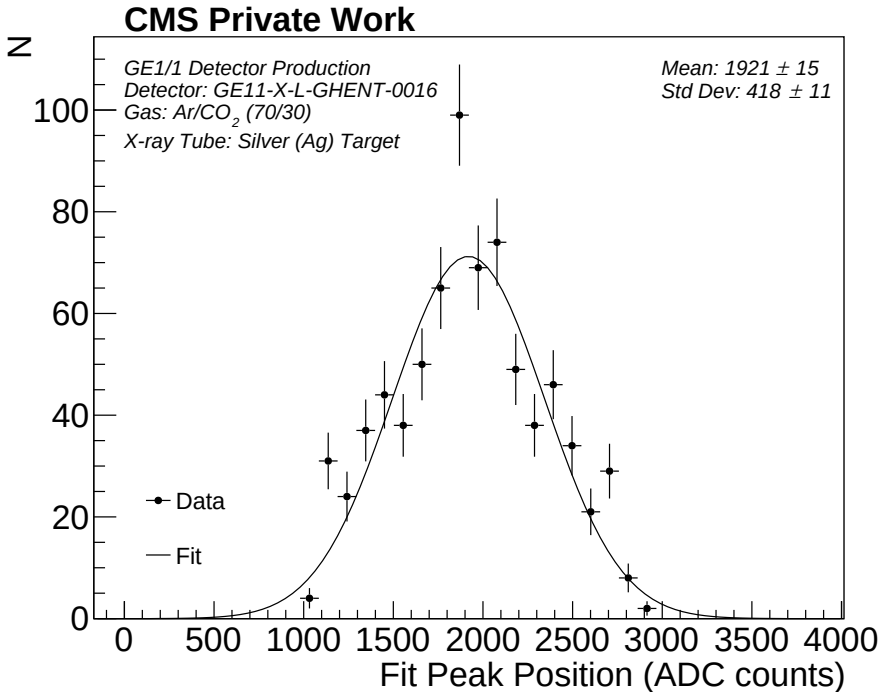

Figure 5.29: Histogram of the fitted peak position for the chamber GE1/1-X-L-GHENT-0016. The black points represent the distribution of ADC counts of the fitted fluorescence peak for all slices. For a better visualization, the distribution is parametrized by a Gaussian function. The criterion to pass the gain uniformity test is based on the ratio of the standard deviation over the mean of the histogram.

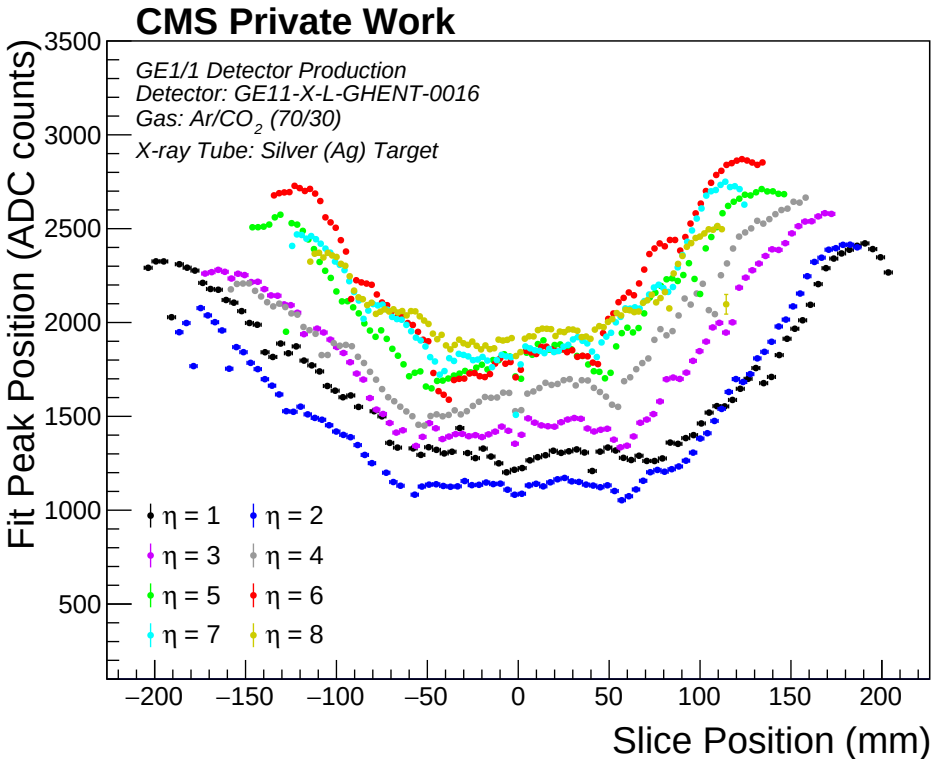

Figure 5.30: Fitted peak position as a function of the slice position on the readout board of the chamber GE1/1-X-L-GHENT-0016. The corresponding η-sector is shown color-coded. The peak position is proportional to the gas gain in the corresponding region of the chamber. The origin of the x-axis is the center of the width of the readout board. $\eta = 1$ corresponds to the long edge of the trapezoid.

representation provides a better understanding of how the gain varies over the area of the detector. In the ideal case, i.e. in the absence of gain variations, the fitted peak positions of the η-sectors would be horizontal lines that would be on top of each other. However, Fig. 5.30 reveals variations within the η-sectors, as well as comparing different η-sectors.

Gain uniformity - results and conclusion The results of the gas gain uniformity tests performed in Aachen are presented in Fig. 5.31. The acceptance limit for the gain variations is 50%. The chambers tested in Aachen pass this criterion. Studies of the detection efficiency and time resolution suggest that with a gain variation of 50% the performance of the GE1/1 detector is still within the specifications (see explanation in Sec. A.1). Investigating the gain variations further, one can observe two typical shapes of gain variations. Two examples of these typical shapes are displayed in Fig. 5.32, which shows the gain variations of GE1/1-X-L-CERN-0006 (top) and GE1/1-X-L-CERN-0032 (bottom). A uniform behavior is observed for GE1/1-X-L-CERN-0032, while GE1/1-X-L-CERN-0006 has systematically higher gain at the outer slice positions for all η-sectors.

In Ref. [125], different sources of non-uniformity are investigated and the expected orders of magnitude of non-uniformity for dominating effects are evaluated (see also Sec. 6). Variations of the drift and induction gap can cause non-uniformity of the gas gain. These gap variations could be due to a bending of the readout or drift PCB. This could be introduced by both a PCB already bent during production or a bending due to a non-uniformity of the heights of pullouts and external gas frame. Additionally, the GEM foil thickness and hole diameter are subject to variations. Adding the different contributions, the study pre-

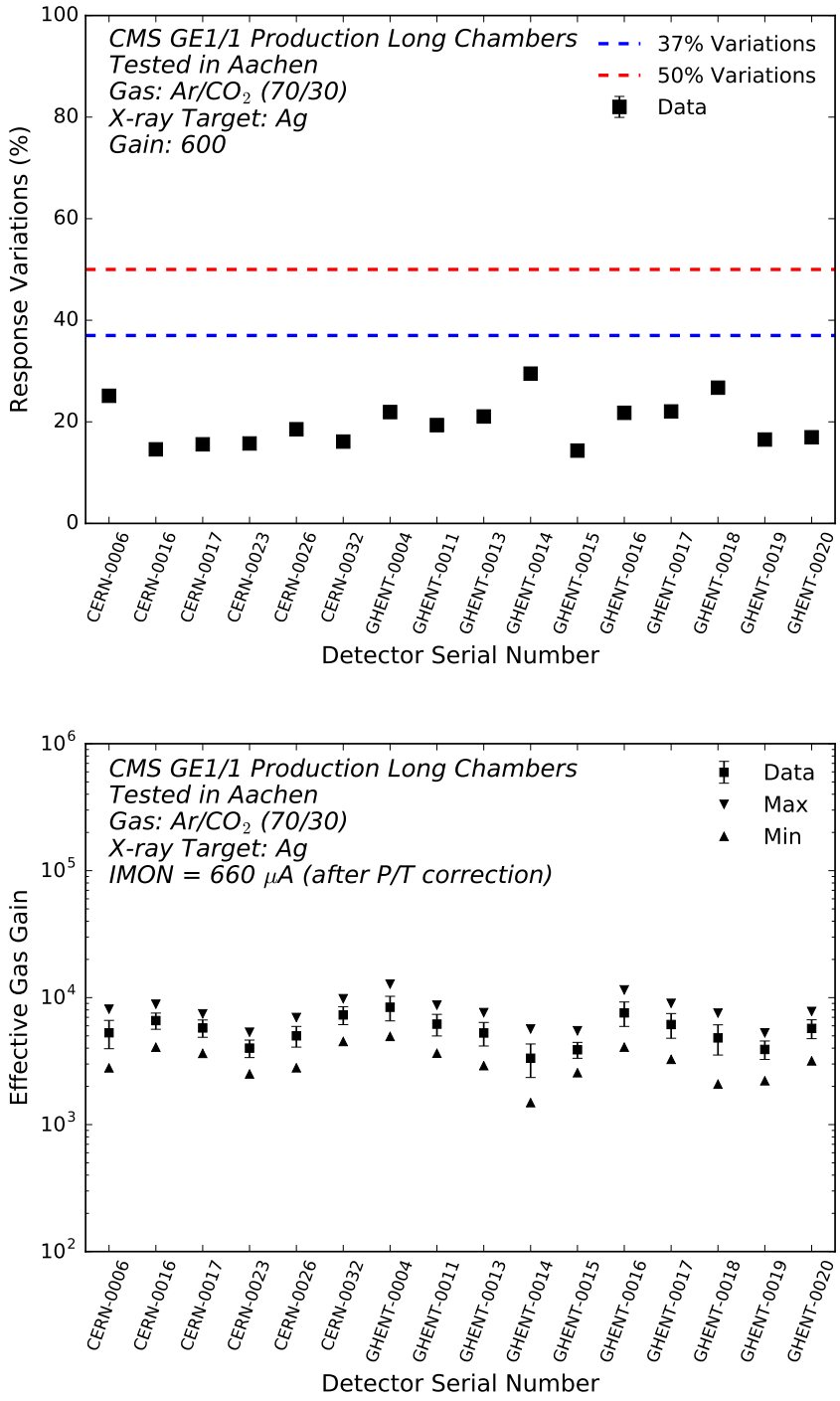

Figure 5.31: Results of the gain uniformity tests performed in Aachen. Top: Response variations as a function of the detector serial number. The data is shown in black. The QC criterion of 50% gain variations can be seen as a red dashed line. For illustration, a blue dashed line representing gain variations of 37% is also depicted. Bottom: Effective gas gain as a function of the detector serial number. The black points show the effective gas gain at the divider current of 660 μA. The size of the error bars is given by the standard deviation of the gain uniformity result (see Fig. 5.29). The minimum and maximum of the uniformity distribution are depicted as black triangles.

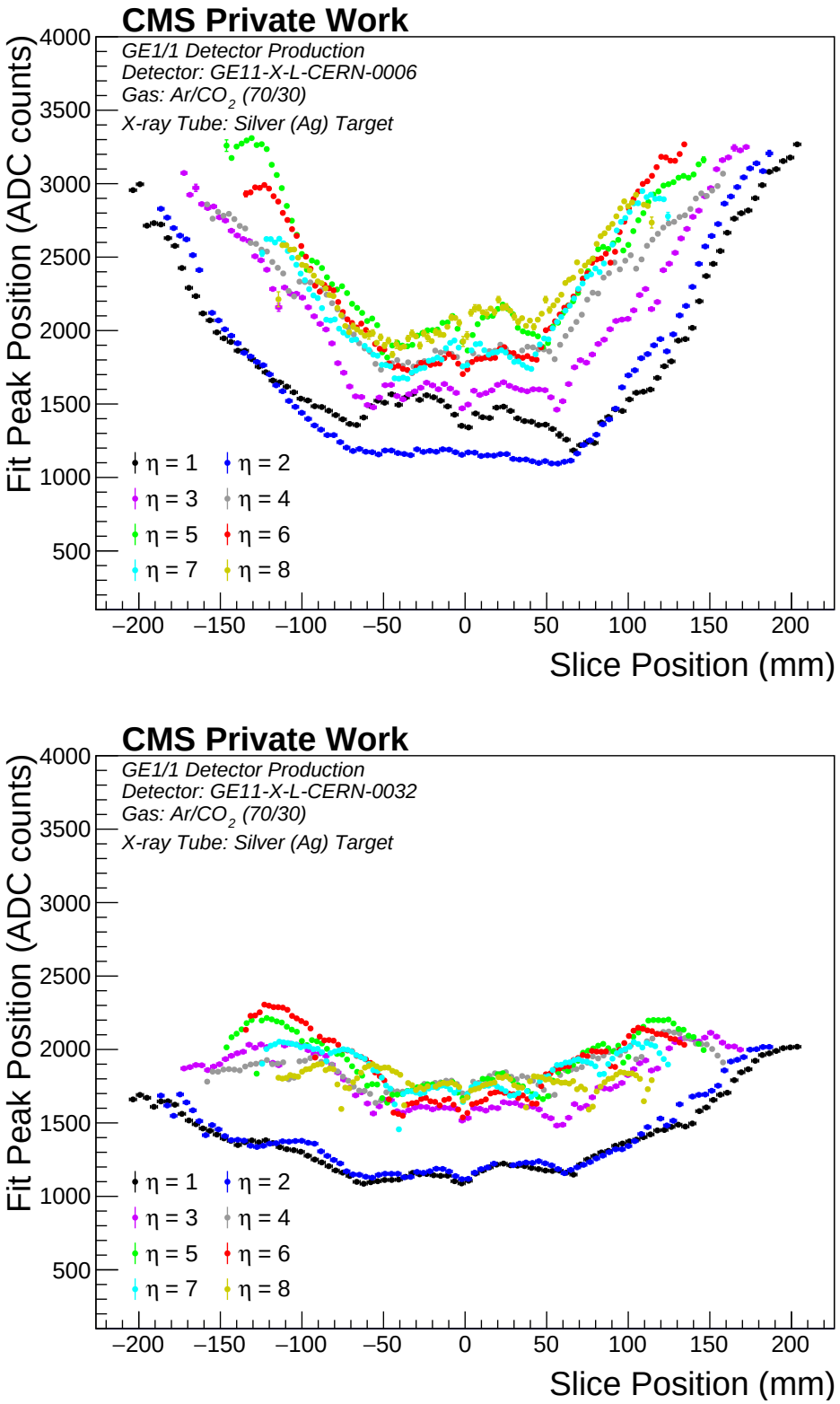

Figure 5.32: Gain variations of GE1/1-X-L-CERN-0006 (top) and GE1/1-X-L-CERN-0032 (bottom). A description of the figure can be found in the caption of Fig. 5.30. These two examples represent typical shapes of the gain variations for long GE1/1 chambers. The results from the other tested chambers are presented in Sec. A.9.

sented in Ref. [125] ends up with expected gain variations of 37%. For illustration purposes, this value is added to Fig. 5.31. All chambers tested in Aachen are below the value of 37%, which seems to be a rather conservative estimation.

The results of the complete GE1/1 production for the gain uniformity test can be found in Fig. 5.33. The variations for the tested GE1/1 chambers are well below the QC criterion of

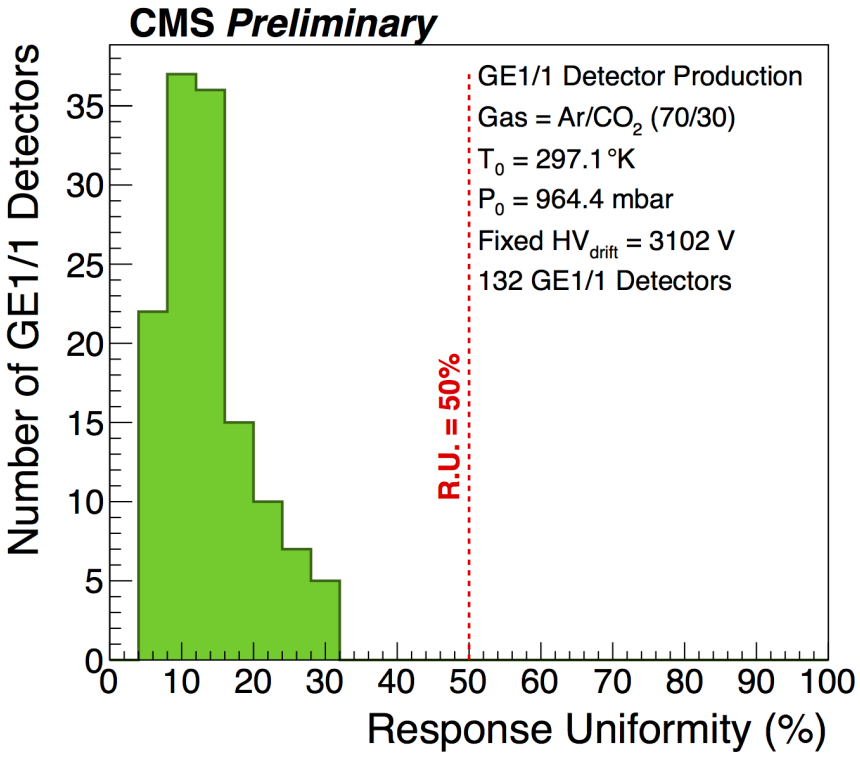

Figure 5.33: Results of the gain uniformity tests for the GE1/1 detector production. The number of tested GE1/1 detectors is shown as a function of the measured response uniformity. The vertical red line represents the acceptance limit of 50% gain variations. The figure is taken from Ref. [118].

50%. It is worth emphasizing, that this quantity reflects the property of a single chamber. To evaluate how compatible the chambers are, when it comes to the superchamber assembly, the effective gas gain value, which is measured in the gain calibration test, is relevant. The procedure of matching chambers to a superchamber is described in Sec. 5.3.8.

5.3.7 Statistics of GE1/1 production

By the end of 2018, the required amount of 144 single chambers, assembled and tested up to QC5, was reached[5]. This achievement is a milestone for the production community. In Aachen, the total number of tested chambers sums up to 21 long single chambers. In the early production phase, some chambers were sent back to the corresponding production sites with different issues. The observed issues were related to either gas tightness or shorted GEM foils. For the gas tightness, an exchange of the frame/o-ring combination can be performed. To repair a shorted GEM foil, a number of measures can be taken, e.g. cleaning the foils with a sticky roller or, in the case of non-metallic dust, charging up the foil in order to burn the dust particles. In the worst case, the foil has to be exchanged. After repair,

[5]To have some spare chambers, 161 single GE1/1 chambers were assembled and fully validated.

the chambers were tested successfully at CERN or at Ghent. The production speed of the Aachen site can be seen in Fig. 5.34. The absence of a learning curve in the production could be attributed to the detailed and rigorous qualification procedure of the production site inside the CMS GEM group (see Sec. 5.3.1).

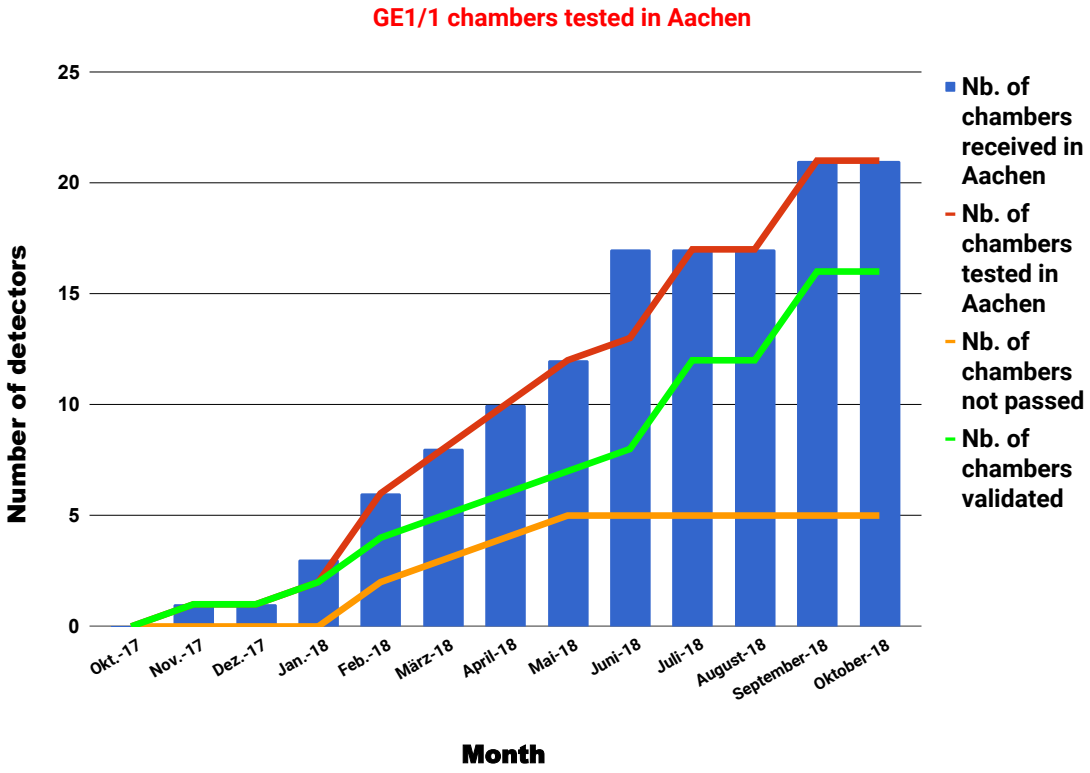

Figure 5.34: Number of tested chambers of the Aachen testing site during the GE1/1 detector production. The time axis ranges from the first reception of GE1/1 chambers at Aachen to the last test. The blue bar chart shows the number of chambers received in Aachen. The GE1/1 chambers tested are presented in red. The number of chambers successfully validated and not passing the QC criteria are depicted in green and orange, respectively.

5.3.8 Superchamber assembly

If the QC5 test is passed, the GE1/1 single chambers are sent to CERN. The picture in Fig. 5.35 depicts the carriers filled with the chambers received at CERN and being ready for superchamber assembly. After the reception, the chambers are connected to a multichannel power supply, which is used hereafter in the QC procedure and during operation in CMS. The QC6 test checks the HV stability of the chamber with the new multichannel power distribution. The QC6-8 tests are currently ongoing and, therefore, final results for the complete GE1/1 detector production are not (yet) available.

Matching single chambers Before the start of the superchamber assembly, the single chambers have to be matched according to their working point since the two single chambers in a superchamber share the same multichannel HV supply. The matching procedure is performed by looking at the effective gain measurement of sector (4,2) at a fixed HV point. Two neighboring chambers in that distribution are taken to form a superchamber. The HV

Figure 5.35: Picture of GE1/1 chamber storage in the GEM laboratory at CERN. The GE1/1 chambers are sent from the different production/testing sites to CERN after passing the QC5 gain uniformity test. In total, 161 validated GE1/1 single chambers are stored.

point can then be adjusted for each superchamber to get a uniform response across the set of GE1/1 chambers. The procedure reduces significantly the spread of the gas gain between chambers. Fig. 5.36 shows the gas gain of the different chambers before and after SC pairing for short and long chambers. The improvement after pairing is clearly visible.

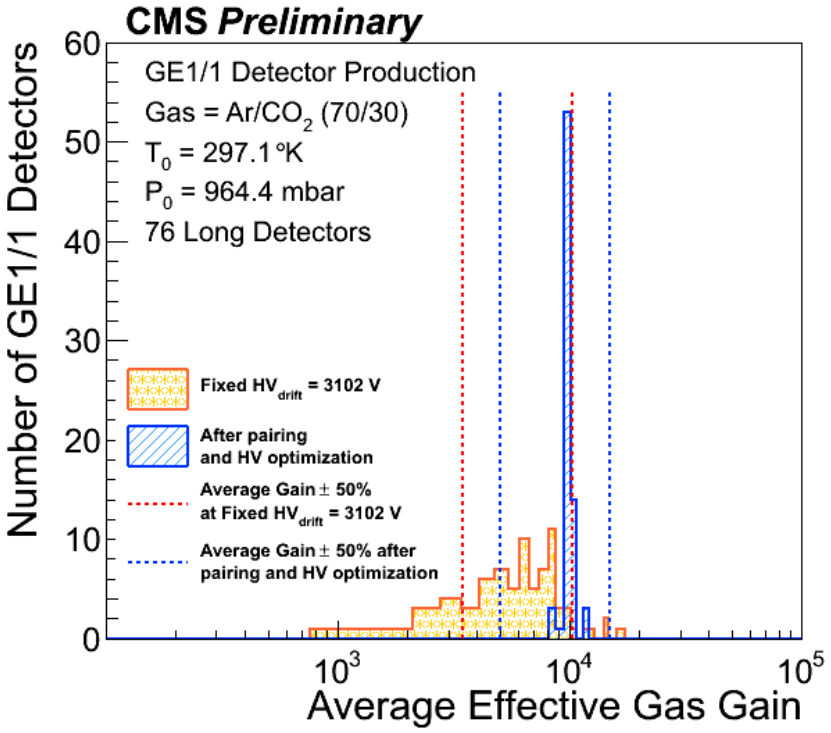

Figure 5.36: Histograms of the average effective gas gain for long detectors. The distribution is given at a fixed HV in light orange and after pairing in light blue. For short chambers, the distributions look very similar. The figure is taken from Ref. [118].

Services for a single chamber The first step of the superchamber assembly consists of equipping both single chambers with the front-end electronics, gas pipes, and fibers. All services run to the patch panel installed on the large side of the trapezoid. The front-end electronics are introduced in Sec. 5.2.2. The two parts of the GEB are mounted first. Then, the VFATs, FEASTs, and the Optohybrid (OH) are plugged and screwed on the GEB. The FEASTs are DC-DC converters for the LV distribution on the GEB designed by CERN [129]. The fibers for data transmission are connected with one end to the OH and with the other end to the patch panel. A photo collage showing the different components can be seen in Fig. 5.37. The cooling plate is put on top of the electronics, thermally connected via pads

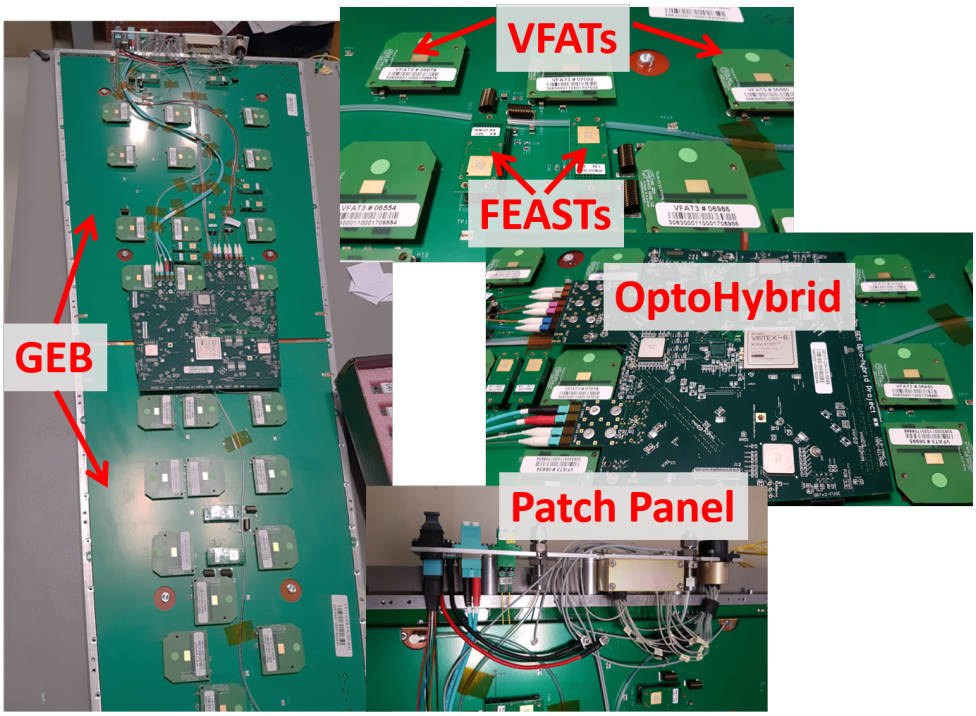

Figure 5.37: Photo collage of the front-end electronics and services mounted on a GE1/1 chamber. The GEB, VFATs, FEASTs, and OH can be seen. The patch panel is shown on the bottom right. The left picture presents a fully equipped chamber. The two parts of the GEB match the trapezoidal shape of the chamber. The pictures were taken in the GEM laboratory at CERN during a superchamber assembly.

and paste. Finally, an aluminum cover protects the front-end services. The electronics are tested during QC7 with respect to connectivity, settings of registers, and noise.

Mechanical pairing After both single chambers passed the QC7 electronics test, the two chambers are mechanically paired to a superchamber. In a dedicated working bench, the chambers are connected via two L-brackets on both ends of the large side of the trapezoid. On the short side, a rectangular bracket is used. In addition, on the short side, a pivot pin is inserted in order to simplify the insertion of the superchamber in the rail of the CMS endcap. The two chambers share gas and cooling. A photo collage illustrating the mechanical components of the pairing is presented in Fig. 5.38. Several mechanical parts, e.g. the aluminum cover, the L-brackets, the pivot pin and the patch panel, were designed and produced by the mechanical workshop of the Physics Institute IIIA at the RWTH Aachen University.

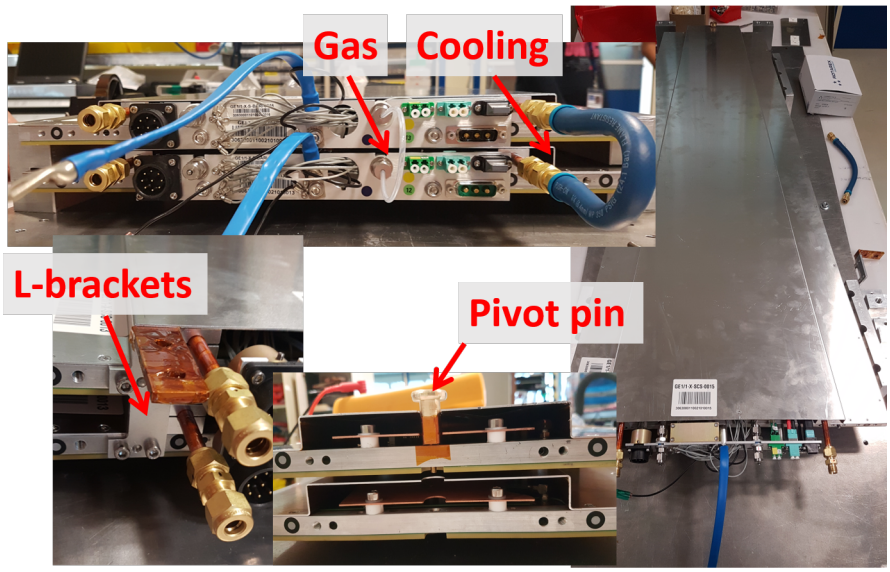

Figure 5.38: Photo collage of the mechanical pairing of two GE1/1 chambers to a superchamber. The L-brackets and pivot pin are shown. The gas and cooling pipes connecting the two chambers are depicted in the top left picture. The complete working bench with a superchamber inserted can be seen on the right. The pictures were taken in the GEM laboratory at CERN during a superchamber assembly.

5.3.9 Efficiency measurement with final electronics

Once the superchamber is assembled, it is inserted into a cosmic ray test stand (QC8). All services, i.e. gas, cooling, HV, LV, front-end and back-end electronics, are equivalent to CMS operations. First, the chambers are tested regarding electronics. In a second step, the detector performance is measured by determining the detection efficiency with cosmic muons. This is the final test before the superchamber is moved to P5. The acceptance limit for the single chamber efficiency is $\approx 97\%$.

5.4 Status and outlook

GE1/1 will be the first completely new installed subsystem since CMS commissioning in the year 2008. The detectors rely on the foil-based GEM technology, which was never before integrated in the CMS detector. These two facts illustrate that the completion of the assembly and validation of the needed 144 GE1/1 detectors determines a major milestone in the history of CMS and for the foreseen upgrades towards the CMS Phase-2 detector.

More than 144 single chambers - enough to fill the GE1/1 endcap - have been fully validated up to QC5. At the time of the finalization of this thesis, more than half of the 144 single chambers have been fully validated up to QC8, the final efficiency measurement with cosmic ray muons. During LS2 in 2019/2020, there are several time slots for the installation of the two GE1/1 endcaps. The first endcap with 36 GE1/1 superchambers was successfully installed in September and October 2019. The current efforts include the integration of the chambers into the CMS data acquisition and monitoring systems. The commissioning is expected to last until the end of 2020. In parallel, the installation of the second endcap is ongoing. The expertise and knowledge gained during the GE1/1 project is of great benefit for the upcoming GE2/1 and ME0 stations. These stations are foreseen to be installed until the mid-2020s.

6 Characterization of GEM detectors

In this section, novel, large-area GEM detectors are characterized. Such large GEM detectors have been mass-produced for the first time for the CMS GE1/1 project (see Sec. 5). During the quality control of the project, gas gain variations across the large detector area are observed. These variations can have a significant impact on the detector performance. To understand the origin of these variations, as well as deepening the knowledge on GEM detectors in general, further studies are performed. The measurements are carried out for different detector designs and environmental parameters. To further comprehend and interpret the results of the measurements, simulation studies are done.

Notations and conventions are defined in Sec. 6.1. Sec. 6.2 contains a collection of the gas gain measurements performed with GEM chambers in the Aachen GEM laboratory. In Sec. 6.3, GEM simulation studies are complementing the measurements. Sec. 6.4 sets side by side the results from measurements and simulations. The final outcome is compared with the existing literature in Sec. 6.5.

6.1 Notation and conventions

Throughout this section, the GE1/1 chamber design (Sec. 5.2) serves as a baseline/starting point of the studies. This includes e.g. foil spacing, gas mixtures, and HV distribution for the triple-GEM chamber studies. To simplify the labeling of the figures, the notation of the voltages needs to be defined. V_{Drift} denotes the voltage given to the drift board (drift voltage). Whenever this quantity is used, it implies that the other electrodes are powered with the respective voltages given by the CMS HV divider (see Fig. 5.14). This applies to both the measurements and the simulation studies. If the voltage distribution differs from the nominal CMS distribution, it will be stated explicitly. In that case, the values for the electric fields of the gaps and the voltage differences of the GEM foils are written in the corresponding figure.

6.2 Gas gain measurements

This section contains a collection of gas gain measurements performed in the Aachen GEM laboratory. For the performance of GEM detectors, the (effective) gas gain is of utmost importance. Several settings/parameters of the detector are changed and their influence on the effective gas gain is studied. The experimental setup is described in Sec. 5.3.6. The procedure is adapted from the effective gain calibration measurement of the GE1/1 QC test. The differences compared to the QC test are explicitly discussed in the following. The measurements are performed either with a GE1/1 prototype, a so-called GE1/1 Generation-V (GenV) chamber, or with a small test chamber with an active area of 10×10 cm^2. The small test chamber is hereafter referred to as 10×10 cm^2 chamber.

GenV chamber The design of the GenV chamber, as a GE1/1 prototype, is very similar to the final GE1/1 chamber design, which is described in Sec. 5.2.2. The main difference between the final GE1/1 and the GenV chamber is the arrangement of the routing from the readout strips to the readout connectors on the outer side of the readout board. However, this difference can be neglected when it comes to the gas gain measurements presented in the following. Thus, the results are comparable to and interpretable as results obtained with a CMS GE1/1 chamber. The GenV chamber was assembled at the CERN GEM laboratory

during the R&D phase of the GE1/1 project. The GEM foils inserted were produced at CERN with the single-mask etching technique. In contrast to the GE1/1 QC measurement, the GenV chamber is partly powered by a multichannel HV supply (CAEN SY127). 5 electrodes (Drift, GEM1 top/bottom, GEM2 top/bottom) are powered by individual HV channels. The remaining electrodes, i.e. GEM3 top/bottom, are connected via an HV divider to the readout board and powered by a single HV channel. This measure is necessary, because an electric short has developed in one of the HV sectors on the third GEM foil. Consequently, it is not possible to power the third GEM foil with the multichannel HV supply. The short on the third GEM foil has no influence on the gas gain measurement because the area of the shorted HV sector is not overlapping with the readout sector $(\eta, \phi) = (4, 2)$. Fig. 6.1 shows a picture of the GenV chamber inside the setup of the Aachen GEM laboratory.

Figure 6.1: Picture of the GenV chamber, which is used for the gas gain measurements in the Aachen GEM laboratory. The chamber is shown in the copper box of the test setup with services (multichannel HV and gas) connected. The chamber is equipped with the front-end boards. For the gas gain measurements presented in this section, the sector $(\eta, \phi) = (4, 2)$ is read out through a panasonic-to-lemo adapter (see Sec. 5.3.6). The sector and adapter are highlighted by the orange rectangle.

10×10 cm^2 chamber The 10×10 cm^2 test chamber was purchased from TECHTRA©. In addition, three sets of GEM foils for a triple-GEM detector (in total 9 foils) with different hole shapes were acquired. A detailed description of the sets of GEM foils can be found in Sec. 6.2.3. The chamber serves the purpose of being a flexible testing device. The following chamber setup is chosen as a default. The foil spacing is 3/1/2/1 mm and the electrodes are powered by a custom HV divider. The resistor values match those of the ceramic HV divider used for the GE1/1 QC (see Fig. 5.14). The readout board hosts a grid of strips in the x-y plane. The two layers of strips, one layer in the x-direction, the other one in the y-direction, are separated by a thin insulating layer. For each dimension, there are 256 strips, summing up to 2×2 readout sectors for the whole chamber. For the gas gain measurement, one sector is read out and the other sectors are terminated with an ohmic resistor. Fig. 6.2 contains a picture of the 10×10 cm^2 chamber.

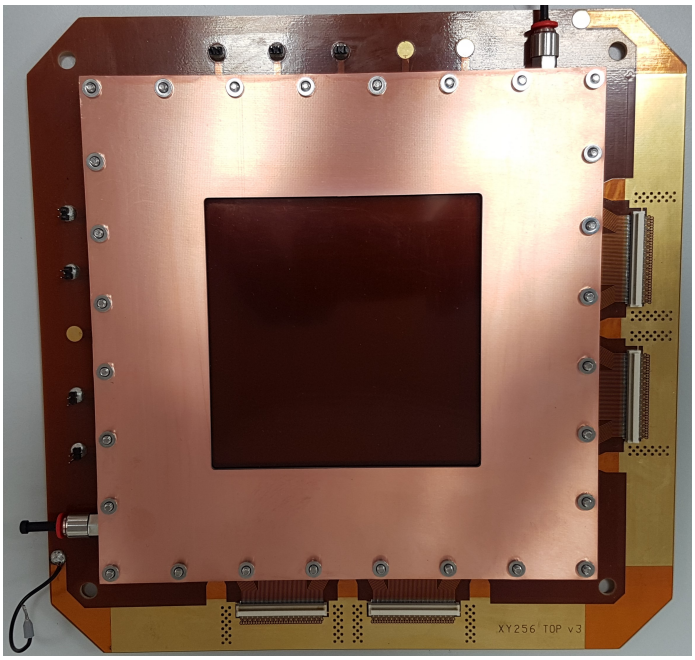

Figure 6.2: Picture of the bare 10×10 cm^2 chamber. The gas in- and outlet can be seen in the top right and the bottom left corner. The top of the chamber consists of a plastic foil and a quadratic copper plate with a quadratic cutout. The screws on the four sides close the gas volume. HV is given to the foils via the pins on the top and left side. On the right and bottom side, the panasonic connectors are depicted. The chamber is read out through these connectors.

The measurements are performed with these two GEM chambers. The GenV chamber is used for the variation of gas mixtures. The study on the electric field variations and the GEM hole shape is done with the 10×10 cm^2 chamber and the corresponding sets of GEM foils.

Investigations on pressure and temperature corrections Temperature and pressure corrections are applied for the gas gain measurements of the GE1/1 quality control procedure (see Eq. 5.3). To check, if these corrections are accurate, several measurements with the 10×10 cm^2 chamber are executed on consecutive days for one week. The measured pressure values vary between 990 mbar and 1000 mbar and the measured temperature values vary between 19.5 °C and 21.5 °C. The values are measured inside the copper box with an EXTECH RHT35 datalogger [130]. The specifications given by EXTECH claim a basic accuracy of ±3 mbar and ±0.5 °C for the pressure and temperature measurement, respectively.

The variations during one measurement, which takes typically one hour, are negligible. The mean of the temperature and pressure values over one measurement is used in the following. The double-mask foils are inserted and the chamber is flushed with Ar/CO_2 (70/30).

Eq. 5.3 is generalized to

$$G \propto \exp(\alpha) \propto \exp(E \times (T/T_0)^a \times (p_0/p)^b), \tag{6.1}$$

introducing the exponents a and b. An exponential dependence of the gas gain on the corrected electric field given by $E \times (T/T_0)^a \times (p_0/p)^b$ is expected. This assumption can be used to determine the parameters a and b. The values of a and b are varied around the standard QC values of 1. For each pair of values, the measured data is parametrized by an exponential function. The agreement between the data and the parametrization can be quantified by the coefficient of determination [131], which is defined by

$$R^2 := \frac{\sum_i (y_i - \hat{y}_i)^2}{\sum_i (y_i - \bar{y})^2}. \tag{6.2}$$

y_i denotes the i-th data point, $\bar{y}$ is the mean of the data points and $\hat{y}_i$ is the corresponding value of the parametrization. The summation is performed over all data points. The obtained values of $\log(R^2)$ in the two-dimensional plane of (a,b) can be seen in Fig. 6.3 . The

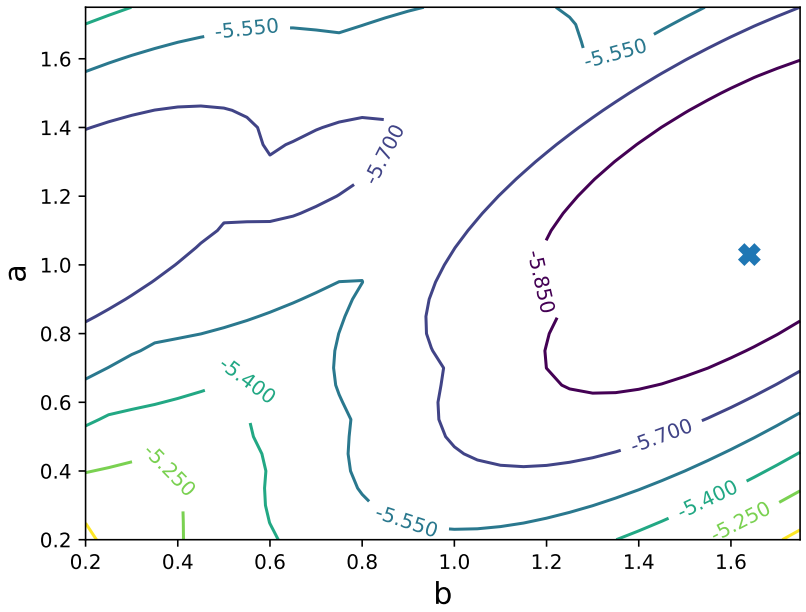

Figure 6.3: Coefficient of determination (R^2) for different values of a and b. The values of $\log(R^2)$ are color-coded in this two-dimensional representation. The position of the global minimum is shown as a blue cross.

minimum of the coefficient of determination corresponds to the best agreement. The global minimum in the investigated region is located at (a,b) = (1.0±0.1,1.6±0.2)[1].

To illustrate the effect of the different corrections for (a,b) = (1,1) and (a,b) = (1.0,1.6), Fig. 6.4 shows the results of the gas gain measurements with the 10×10 cm^2 chamber for both corrections. As constructed, a better agreement of the data points with the exponential

[1]The errors represent the variation of the global minimum, when scaling the gain values up and down according to the errors on the pressure and temperature.

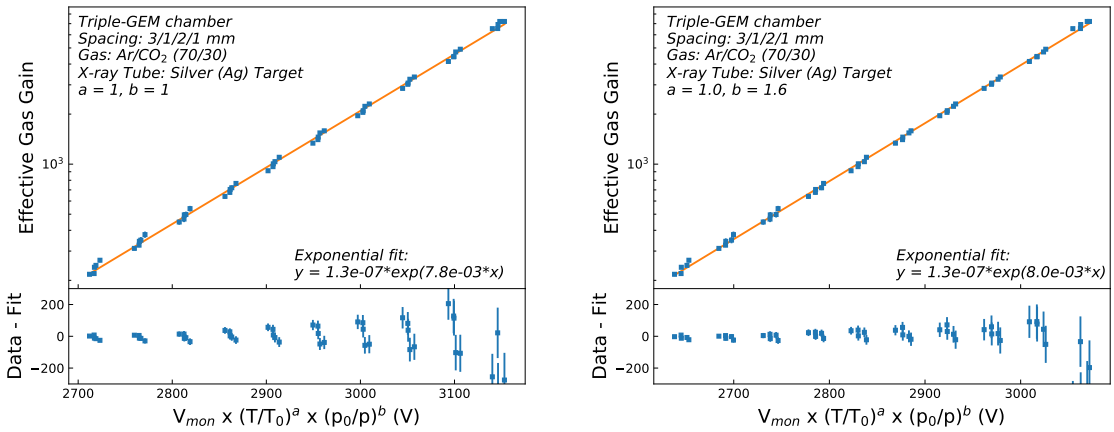

(a) (b)

Figure 6.4: Effective gas gain as a function of the monitored voltage for different pressure and temperature corrections. The residuals of the exponential parametrizations are plotted below. (a) The exponents in Eq. 6.1 are set to (a,b) = (1,1). (b) The exponents in Eq. 6.1 are set to (a,b) = (1.0,1.6), which corresponds to the global minimum of R^2 (see Fig. 6.3).

function is observed for (a,b) = (1.0,1.6) compared with (a,b) = (1,1). (a,b) = (1.0,1.6) is used in the following to correct for temperature and pressure variations.

6.2.1 Gas mixtures

The gas mixture inside the active volume strongly influences the gas gain of a gaseous detector. For the measurements with GEM chambers, the ratio of Ar/CO_2 is varied. Additionally, a contaminant is introduced to the nominal CMS gas mixture of Ar/CO_2 (70/30).

Ar/CO_2 variations The Ar/CO_2 gas mixture is varied around the nominal ratio of 70/30. The measurement is performed with the GenV detector. The results of the gas gain measurement are presented in Fig. 6.5 (a). As expected, with higher percentages of CO_2, the gas gain decreases. CO_2 acts as a quenching gas.

Adding N_2 If the GEM chamber is not completely gas tight, there is a chance that a small amount of contaminants can enter the gas volume from outside and change the gas mixture. Adding N_2 as a contaminant to the gas mixture mimics the effect of introducing air into a GE1/1 chamber. Fig. 6.5 (b) shows the effective gas gain for different N_2 fractions added to the nominal Ar/CO_2 gas mixture. There is an overall trend of a lower gas gain with increasing N_2 percentages. This is expected as N_2 is behaving as a quencher similar to CO_2. In general, the variations are rather small for contributions of up to 3%. Having in mind the gas tightness of the GE1/1 chambers (see Sec. 5.3.4), already a contamination of 1% is probably as high as one can have for the operation in CMS. The influence of other contaminants inside the gas mixture, e.g. O_2 and humidity, is studied with simulations [132].

6.2.2 Electric field variations

The properties of the electric fields drive the performance of a GEM chamber. Variations of the electric fields influence the drift behavior of the electrons, as well as the electron multiplication. The gas gain is mainly driven by the electric field inside the GEM foil, where

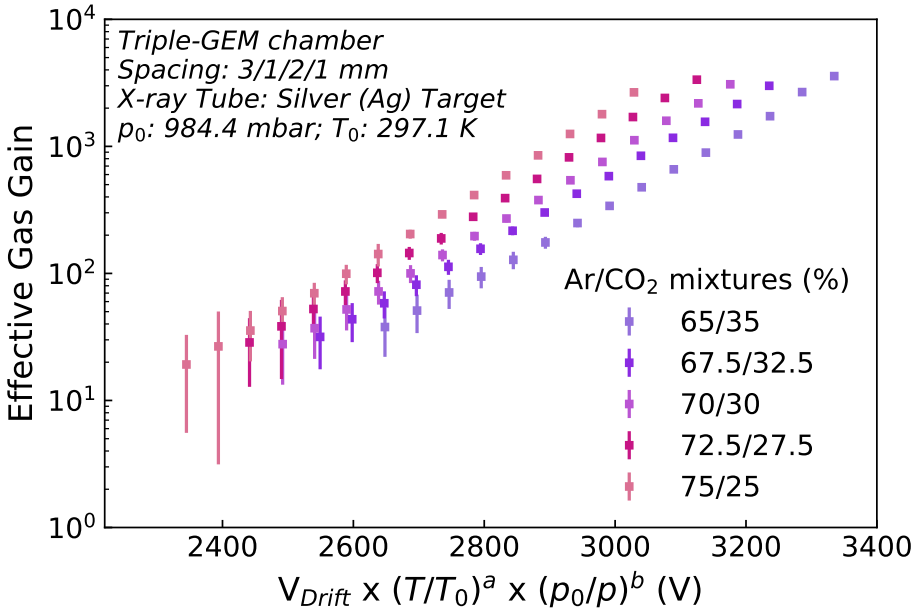

(a)

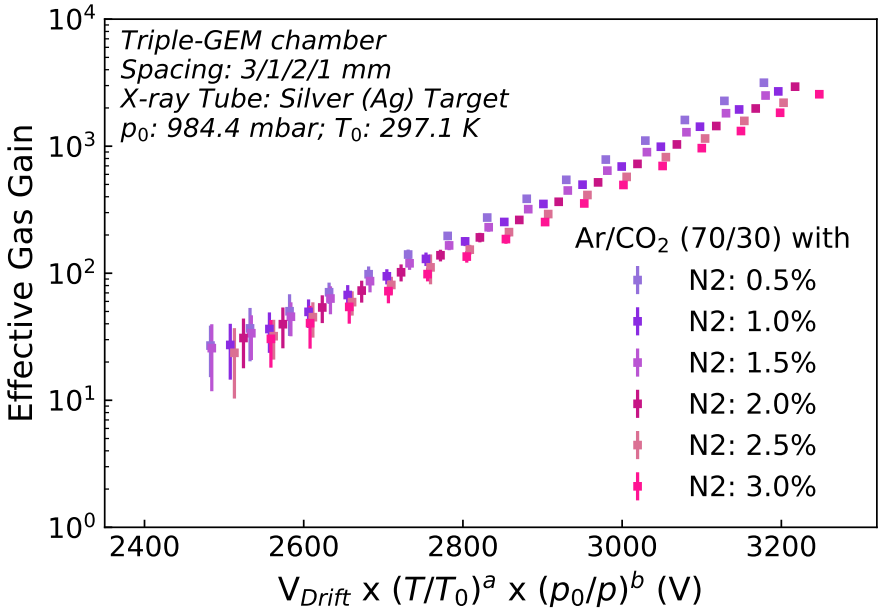

(b)

Figure 6.5: Effective gas gain as a function of the applied drift voltage. (a) The different mixtures of Ar/CO_2 are color-coded. (b) The different values of added N_2 fraction are color-coded. The voltage distribution to the electrodes follows the nominal CMS specification.

the amplification region is located. The electric fields in the drift, transfer and induction gap play an important role for the temporal and spatial resolution. They have a minor, however non-negligible, effect on the gas gain.

The studies investigate the observed gas gain variations of the large-size GE1/1 chambers (see Fig. 5.33). Possible sources can be variations of the drift or induction gap size. With the voltages kept constant, variations of the electric field strength inside the gaps are the consequence. A discussion of potential reasons for the gap size variations can be found in Sec. 5.3.6. A deeper and quantitative understanding of the effect of electric field variations is needed. For the measurements of the electric field variations, no pressure and temperature corrections are applied due to the negligible variations during the data acquisition.

Drift gap The voltage difference across the drift gap is varied, i.e. the voltage given to the drift board is changed while all other voltages are kept constant. The nominal CMS value of the drift field is around 2.6-3.0 kV/cm [10]. Fig. 6.6 presents the effective gas gain as a function of the electric field in the drift gap. For lower drift fields compared to the nominal

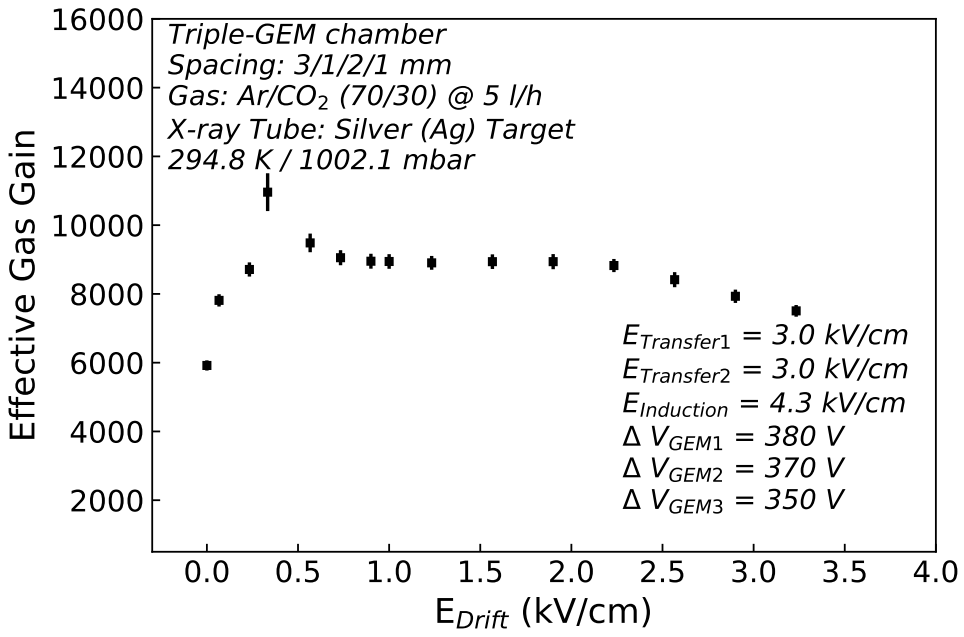

Figure 6.6: Effective gas gain as a function of the electric field in the drift gap. The drift voltage is varied while the other voltages are kept constant. The corresponding values of the voltages across the GEM foils and the transfer and induction fields are written in the figure. The nominal CMS value of the drift field is around 2.6-3.0 kV/cm.

CMS value, the gas gain stays approximately constant. Only below 0.5 kV/cm, the gas gain decreases. This behavior can be explained by the foil collection efficiency, which is defined in Sec. 6.3.5 and discussed together with the simulation studies. For a drift gap twice as large as the nominal 3 mm, the electric field is halved. The corresponding gas gain variations are $\leq 10\%$.

One should note, that this procedure neglects, on the one hand, the larger number of primary electrons produced, and on the other hand, the larger transverse spread of the elec-

tron cloud, in case of a larger drift gap. For the translation back to the original problem of a smaller/larger drift gap due to a bent drift PCB, these two topics play a role.

Thickness of GEM foil The thickness of the GEM foil, i.e. the thickness of the polyimide, can vary across the surface of large-size foils. A change in the depth of the GEM hole translates into a change of the electric field and, hence, the amplification. To understand the dependence of the gas gain on the change in the electric field, the voltage difference between the top and bottom of the GEM foil is varied. Fig. 6.7 gives the results of the measurement. The effective gain depends exponentially on the voltage difference across the GEM

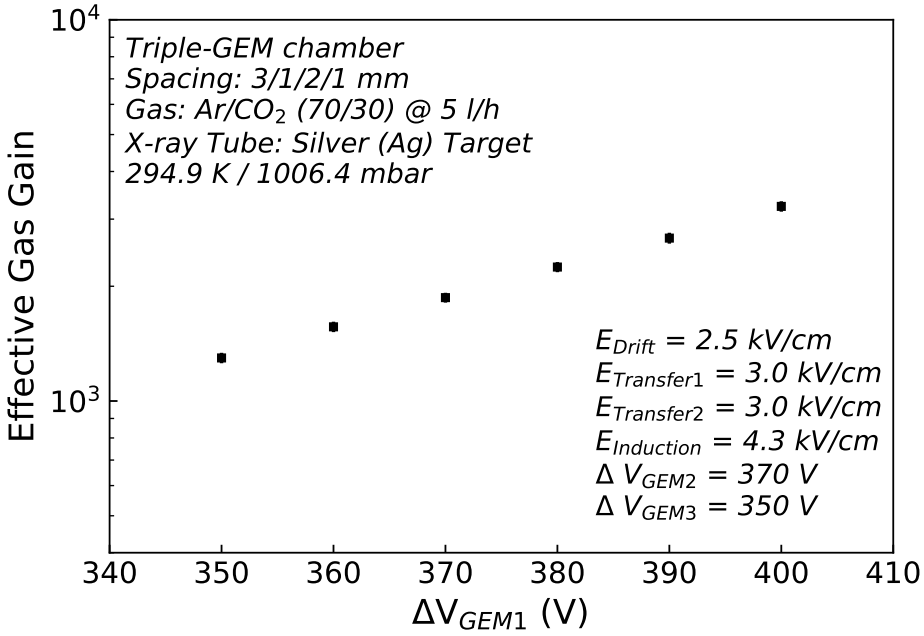

Figure 6.7: Effective gas gain as a function of the voltage difference across the GEM1 foil ΔV_{GEM1}. The other voltage differences across GEM2 and GEM3, as well as the drift, transfer and induction fields are kept constant. The corresponding values are shown in the bottom right corner.

foil, which is expected for the amplification region. To understand the impact on the effective gas gain, one needs to know that GEM foil producers claim 0.5% [125] precision on the polyimide thickness. This leads to $\leq 5\%$ gas gain variations.

Induction gap Unfortunately, the short on the third GEM foil of the GenV chamber makes it impossible to vary only the electric field of the induction gap. Instead of the GenV chamber, another 10×10 cm^2 chamber received from CERN for the QC qualification procedure is used[2].

Fig. 6.8 shows the effective gas gain as a function of the electric field in the induction gap. A stronger dependence of the gain on the induction field compared with the drift field is observed. This can be explained by the dependence of the induced current on the induction field (see Sec. 3.3.7). The nominal CMS value of the induction field is around 4.3 kV/cm [10].

[2]The 10×10 cm^2 chamber, purchased from TECHTRA, is equipped with an HV divider. In that configuration, the induction field cannot be individually varied.

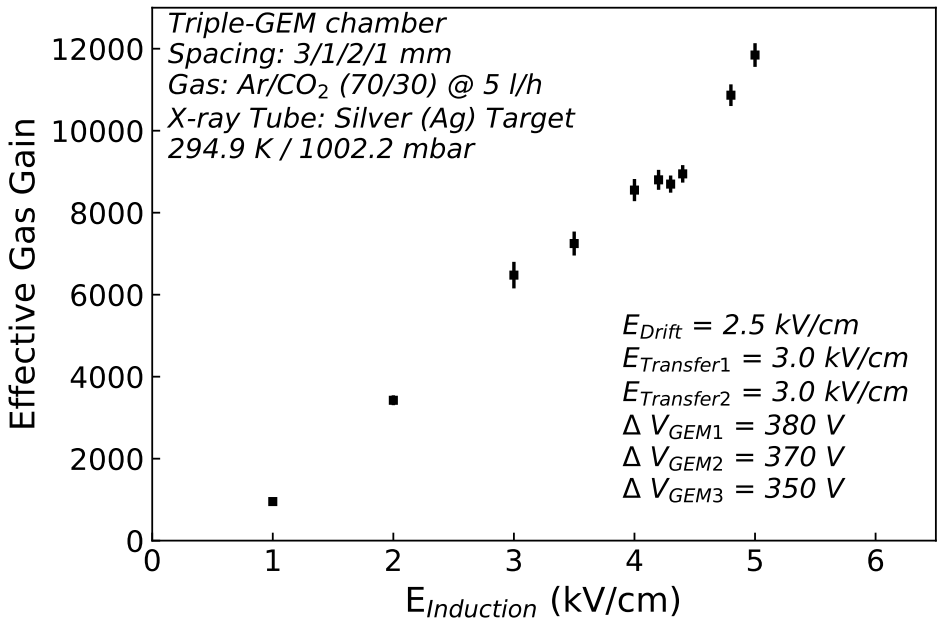

Figure 6.8: Effective gas gain as a function of the induction field. The drift and transfer fields, as well as the voltages across the three GEM foils are kept constant. The corresponding values are written explicitly in the figure. The nominal CMS value of the induction field corresponds to 4.3 kV/cm.

For a variation of 50% of the induction gap thickness, a variation of $\approx 30\%$ in gain follows. Compared to similar variations in the size of the drift gap, the gain variations coming from variations of the induction gap are dominating.

6.2.3 GEM hole shape

For the production of GEM foils, two etching procedures have been established over the years: the single-mask and the double-mask technique [8]. Both techniques have their advantages and drawbacks, which are discussed in Sec. 3.4.3. Especially for the CMS GEM project, it is important to better understand the dependence of the gas gain on the two etching techniques. The different techniques result in different typical shapes of the holes inside the GEM foil. For the double-mask technique, a symmetric double-conical shape is obtained with diameters of 70/50/70 μm. For the single-mask technique, a slightly asymmetric hole is obtained with typical diameters of 70/53/85 μm. Due to the hole asymmetry, the orientation of the GEM foil with respect to the readout and drift board matters. An illustration of the different orientations can be seen in Fig. 6.9. To test the impact of the hole shape on the effective gas gain, three sets of GEM foils are available for the 10×10 cm^2 chamber. The details of the three sets of GEM foils are given in Tab. 6.1. In addition to the single-mask and double-mask foils, a double-mask foil with an intended hole asymmetry was purchased to study possible systematic differences between single-mask and double-mask foils. With the double-mask technique, one has a better control of the dimensions of the inner diameter.

The outcome of the measurements for the different sets of GEM foils can be seen in Fig. 6.10. The double-mask scenario leads to the highest gas gain in a triple-GEM chamber compared with the single-mask OA and OB. Orientation A results in a higher gain than

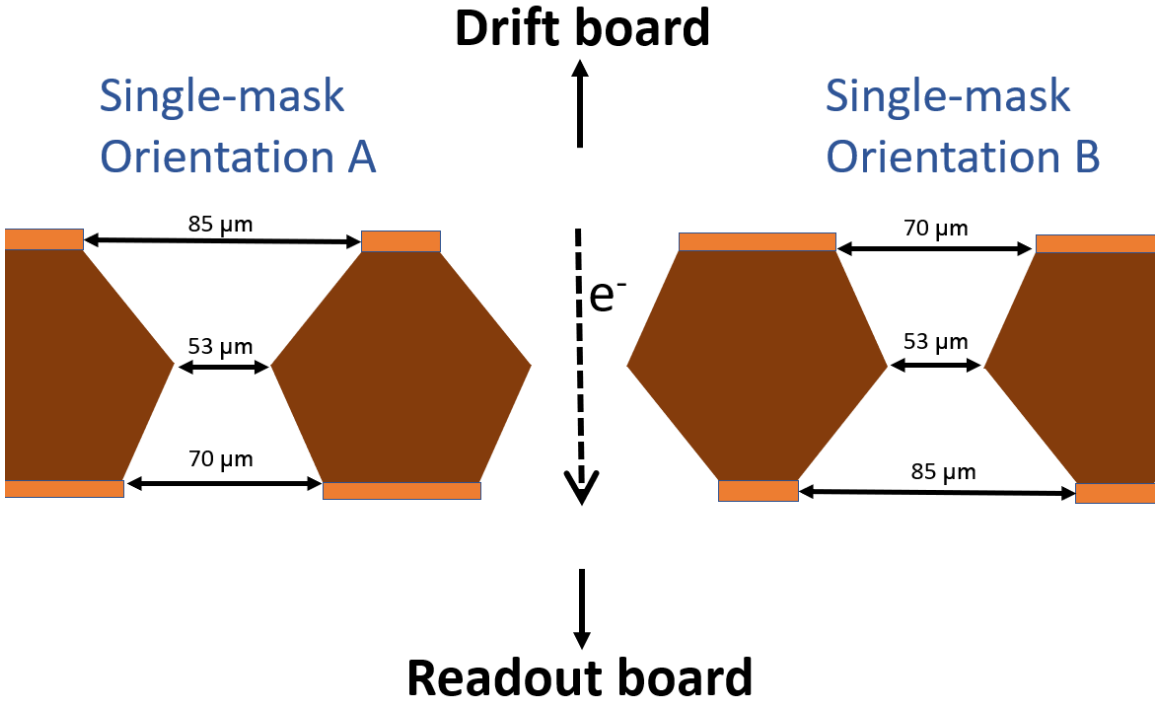

Figure 6.9: Illustration of the two possible orientations of the asymmetric holes produced by the single-mask etching procedure. Orientation A (OA) is defined by having the larger opening towards the drift board. For Orientation B (OB), the larger opening is pointing towards the readout board. In this sketch, the electrons (e^-) would move from top to bottom, indicated by the dashed arrow. Typical values for hole diameters are 70/53/85 μm. The notation of orientations is also used for the asymmetric double-mask foils.

Etching procedure/scenario	Typical hole geometry (± 3 μm)
Double-mask	70/50/70 μm
Single-mask OA	85/53/70 μm
Single-mask OB	70/53/85 μm
Double-mask (asym.) OA	85/50/70 μm
Double-mask (asym.) OB	70/50/85 μm

Table 6.1: Scenarios of the three sets of GEM foils for the 10×10 cm^2 chamber. The asymmetric double-mask scenario is denoting the case, where the foil has an intended hole shape asymmetry. This asymmetry results in a 15 μm larger hole diameter on the bottom side of the foil compared to the upper side. The specifications given by TECHTRA for the etched hole dimensions are ± 3 μm. This is a rather conservative assumption for the double-mask scenario, since the dimensions can be controlled better in this case. Orientation A (OA) and Orientation B (OB) denote the orientation of the larger hole opening towards the drift and readout board, respectively. For the double-mask foils, the holes are symmetric with respect to the double-conical shape. Thus, the concept of orientation is not needed.

Orientation B. As expected, the asymmetric double-mask and single-mask scenarios differ only slightly for both orientations. The small difference might be due to the larger diameter of the larger hole opening observed for double-mask foils. Measurements of the diameters with an optical microscope are discussed for both foil types in Sec. A.3.

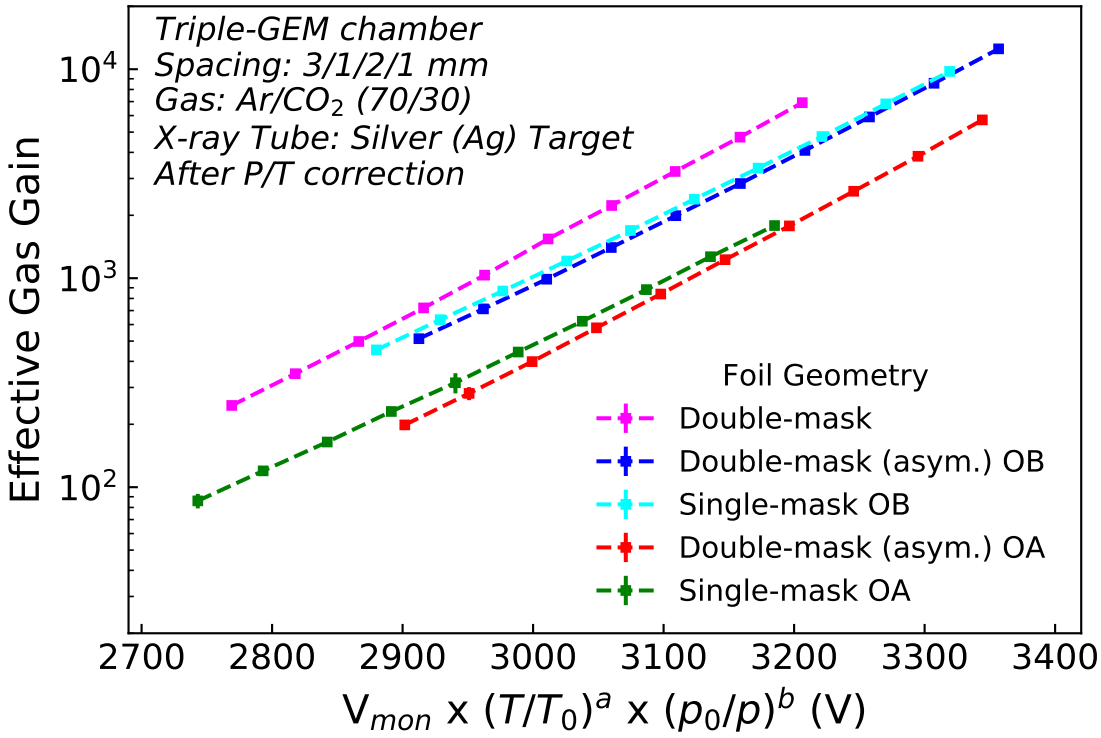

Figure 6.10: Effective gas gain as a function of the monitored drift voltage. The different hole geometries of the GEM foils are color-coded. Tab. 6.1 defines the abbreviations used in the legend of this figure. Pressure and temperature corrections are applied following the procedure described above.

6.3 GEM simulation studies

The simulation of processes inside gaseous detectors contributes, on the one hand, to a better understanding of measurements. On the other hand, the simulation offers a tool to estimate the impact of design changes on the detector performance. The following discussion is mainly focused on the gas gain of GEM detectors. The natural baseline for the studies is given by the detector design of the CMS GE1/1 GEM chambers (Sec. 5.2).

6.3.1 Simulation basics

The simulation of electron avalanches in GEM detectors is based on Garfield++ [133], which is a C++ reimplementation of the Fortran-based Garfield toolkit [54]. The geometry, material properties and voltages of the detector are given as an input to Ansys [134]. Ansys uses the finite element method (FEM) to calculate the electric field in the simulated volume. The information, contained in the list of nodes, is given as an input to Garfield++. For the avalanche simulation, Garfield++ is interfaced with MagBoltz [135] for the calculation of the electron transport and interfaced with HEED [136] for the primary ionizations from incident particles, e.g. muons and photons. The final results are obtained from Garfield++. The workflow of the simulation and the tools, that are used, are illustrated in Fig. 6.11.

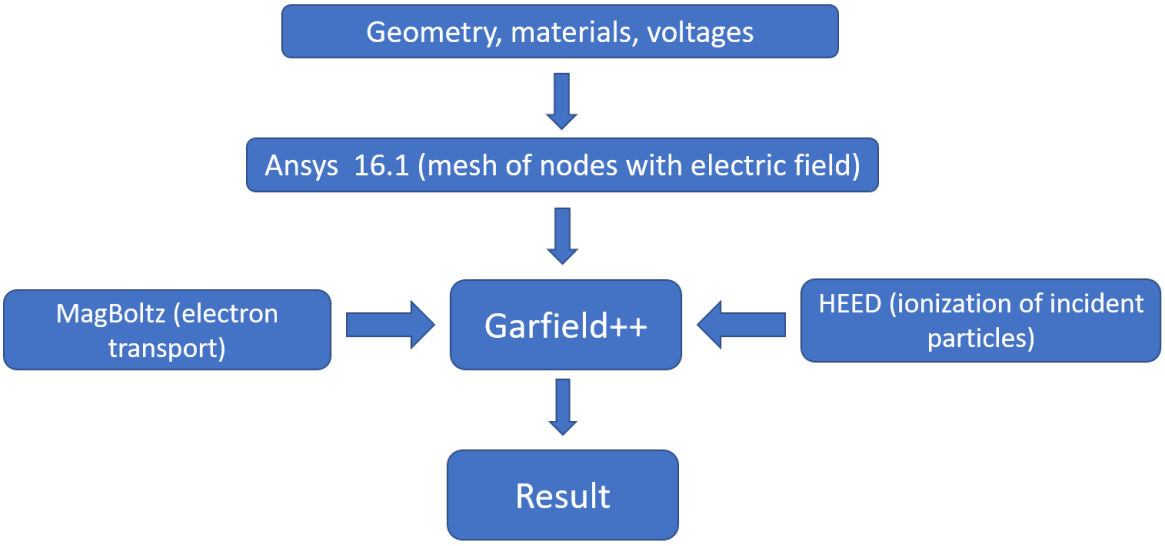

Figure 6.11: Simulation workflow based on Garfield++. The figure should be read from top to bottom as indicated by the vertical arrows. The horizontal arrows illustrate the interfaces of Garfield++ with HEED and MagBoltz.

Geometry and electric field In Ansys, the elementary unit cell of the GEM foil is defined by a cut-out of two quarter holes. This is shown in Fig. 6.12. It is enough to simulate this unit

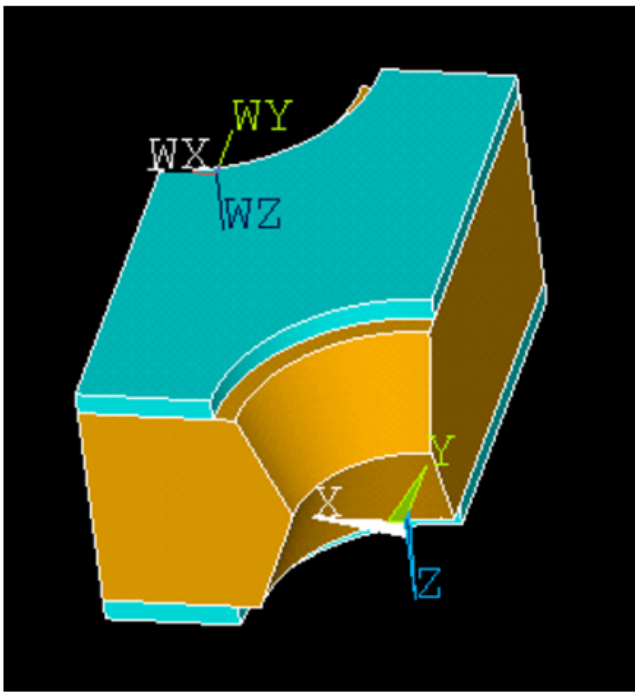

Figure 6.12: Elementary unit cell in Ansys consisting of two quarter holes. Based on the unit cell, the electric field is computed. The polyimide bulk material of the GEM foil is shown in orange. In light blue, one can see the copper layers on the top and the bottom of the foil. This picture is a screenshot of the Ansys graphical user interface [134].

cell due to the possibility to mirror periodically a given input of geometry and electric field in Garfield++. For a stack of foils, the unit cell is created with the desired spacing between the foils. The volume of simulation is extended to the drift and readout plane. The voltages

are applied to the different electrodes. To obtain correct results in terms of electric field, the conditions on the boundaries of the simulated volume have to be set. Ansys creates a mesh of nodes and calculates the electric field for every node inside the mesh. The lines of equipotential for a typical hole in a GEM foil together with the drift lines of massless particles are shown in Fig. 6.13. The Ansys scripts, used for the studies discussed in this thesis, are based on the slides of the RD51 simulation school 2011 [137].

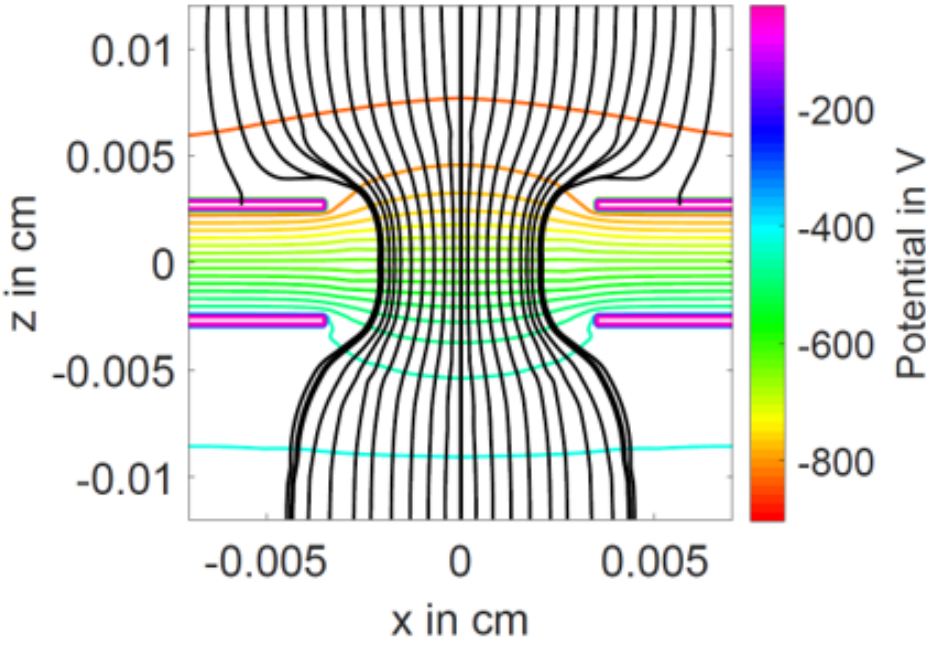

Figure 6.13: Simulation of a single GEM hole with Ansys. The lines of equipotential are represented by the colored lines. The black lines indicate the drift lines of massless, singly charged particles following the gradient of the potential. The drift lines start 1 mm above the foil.

Microscopic simulation of electron avalanche The avalanche simulation is performed with the Garfield++ toolkit. The output of the Ansys program is given as an input to Garfield++. By mirroring the geometry and electric field according to the symmetry of the GEM foil, an area of 1.4×1.4 mm^2 is created, which corresponds to $20 \times \frac{20}{\sqrt{3}}$ unit cells or roughly 100 holes. This area provides enough space for the complete avalanche inside a triple-GEM chamber. From measurements, one can translate the number of fired strips to a maximum avalanche size of 0.5×0.5 mm^2 [10]. Larger volumes of simulation would require more computing time. At this stage, the gas mixture and humidity, as well as environmental parameters, e.g. pressure and temperature, are set. The Penning transfer probability is set to 0.57 [138]. In principle, Garfield++ interfaced with MagBoltz can also handle the existence of a magnetic field. The magnetic field has an impact on the electron drift and, thus, on the temporal and spatial evolution of the avalanche. However, for the electron multiplication process, the magnetic field can be neglected. Consequently, the magnetic field is switched off for the gas gain studies presented here.

The simulation starts by placing an electron close to the drift board and assigning an initial energy and momentum, as well as a starting time. Interfaced with MagBoltz, Garfield++ simulates the electron motion towards the first GEM foil. The microscopic simulation step is determined by a time step, which is generated according to the nuclear interaction rate of electrons with the gas atoms inside the detector. For every time step, the kinematics of the

electron are re-calculated and updated for the next simulation step[3]. The simulation runs until this electron and all subsequently produced electrons end up on the surface of the material, i.e. the copper or the polyimide (Kapton®) of the foils or on the anode plane, which defines the end of the simulation volume. The output of the microscopic simulation consists of the energy, time, and momentum of all simulated electrons at their start and endpoint. The coordinates of all intermediate interactions are also stored. Fig. 6.14 shows an electron avalanche simulated with Garfield++ in a triple-GEM stack. In Garfield, not only the elec-

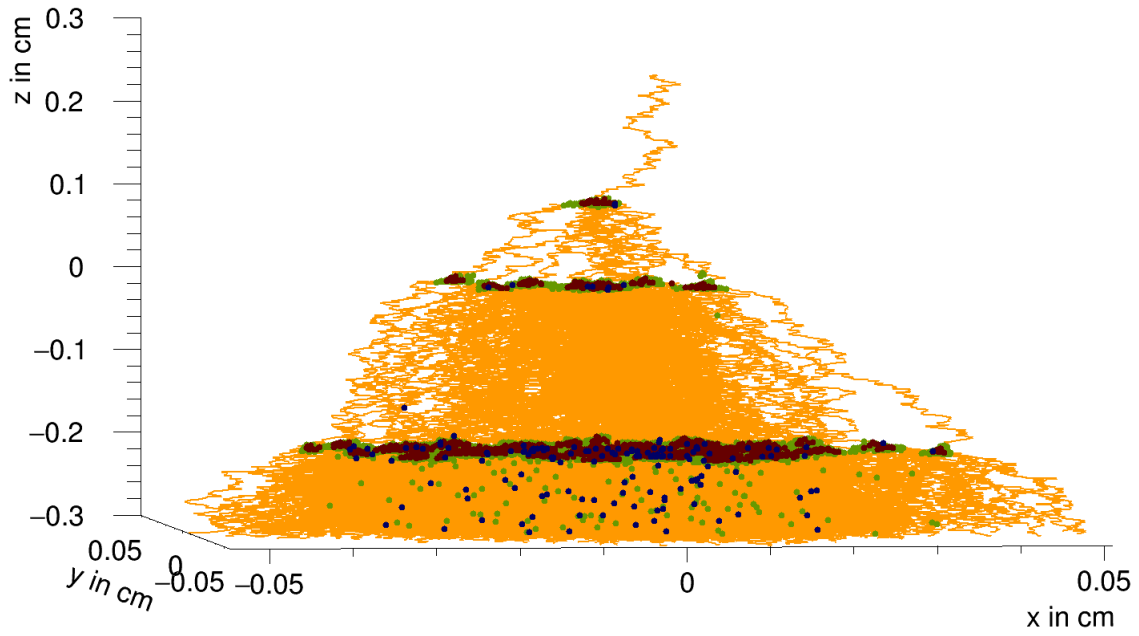

Figure 6.14: Electron avalanche of a single electron in a triple-GEM stack. The figure is obtained from the microscopic simulation in Garfield++. The electron drift lines are shown in orange. The positions of ionizations (brown), excitements (green), and electron captures (blue) are depicted. The location of the three GEM foils can be guessed by looking at the positions of the ionizations. The foil spacing is 3/1/2/1 mm. At $z = -0.3$ cm, this avalanche contains roughly 800 electrons. All simulated electrons, including those ending up on the foils, sum up to approximately 2×10^3. The figure is taken from Ref. [132].

trons are simulated, but also the ions of the avalanche. However, in this thesis, the results are solely based on the electron simulations. The interactions between ions and electrons are not simulated in Garfield++. An order-of-magnitude analysis reveals that the space charge due to the presence of the ions in one GEM hole, even inside the third GEM foil (third amplification stage), does not significantly disturb the electric field[4]. Consequently, the ions are not discussed further.

Simulation of ionizing particles The interaction of ionizing particles with a gas volume can be simulated by HEED. The type, energy, and direction of the incident particle are provided to the HEED interface in Garfield. For our purposes, muons and photons are used as ionizing particles. When the incident particle travels through the gas volume, primary ionizations take place in so-called clusters. Clusters may consist of one or more electrons because the initial electron can have enough energy to ionize further gas atoms in the vicinity

[3]Sec. A.4 provides more details and caveats of the microscopic simulation step.

[4]With roughly 20 ionizations per hole and a maximum of five electrons entering one hole of the third GEM foil, the number of ions inside such a hole is below $\mathcal{O}(100)$. This leads to electric fields that are three orders of magnitude below the external electric field.

of the primary interaction. With the information on the initial location, momentum, and energy of every primary (and secondary) electron, the microscopic simulation is performed as described above. Studies on the interface of HEED with Garfield can be found in Ref. [132].

Tab. 6.2 provides a comprehensive summary of the default simulation settings.

Simulation property	Default setting
Elementary unit cell	$2 \times \frac{1}{4}$ hole
Total size in Garfield++	$1.4 \times 1.4\ \text{mm}^2 \implies 20 \times \frac{20}{\sqrt{3}}$ unit cells (≈ 100 holes)
Foil material	50 μm Kapton® (FR4); 5 μm Cu on both sides
Foil properties	no rim; relative permittivity ϵ_r(FR4): 4.0 [133]
Hole shape	symmetric double-conical shape with diameters: 70/50/70 μm
Hole pitch	140 μm
Foil spacing	3/1/2/1 mm (triple-GEM); 2/1 mm (single-GEM)
Penning transfer	0.57 [138]
Readout	fully conductive surface

Table 6.2: Comprehensive summary of the default simulation settings. The elementary unit cell is illustrated in Fig. 6.12. The unit cell is periodically mirrored in Garfield++ to obtain the total size of the simulated volume. The settings given here are default values. For the different simulation studies, some of the values are varied. The variation is explicitly stated in the corresponding section.

6.3.2 HV distribution and simulation scenarios

Tab. 6.3 gives a summary of the simulation scenarios and the corresponding default HV configuration. The baseline for the triple-layer simulations is the nominal CMS HV distribution. If the HV distribution differs, it is explicitly stated in the text or in the corresponding figure. Sec. A.5 explicitly states the voltages given to the electrodes for all triple-layer studies.

	Single-layer	Triple-layer			
Foil spacing	2/1 mm	3/1/2/1 mm			
		Gap	Resistance (kΩ) of GE1/1 HV divider	Fraction of V_{Drift}	Example $V_{Drift} = 3200$ V
Electric field	$\Delta V_{Drift} = 664$ V $\Delta V_{GEM1} \in [374, 384, 394, 404, 414]$ V $\Delta V_{Induction} = 437$ V	Drift	1125	100	3200 V
		GEM 1	563	75.9	2429.8 V
		Transfer 1	438	64.1	2049.9 V
		GEM 2	550	54.7	1749.8 V
		Transfer 2	875	43.1	1379.8 V
		GEM 3	525	24.4	779.8 V
		Induction	625	13.4	430.1 V

Table 6.3: Overview of the simulation scenarios and the corresponding default HV configurations. The GE1/1 HV divider can be seen in Fig. 5.14.

To study the evolution of the electron avalanche, two different GEM detector scenarios are studied.

Single-layer This scenario describes a simulated GEM detector, which consists of a 2 mm drift gap and a 1 mm induction gap. In between, there is one GEM foil. This allows a fast simulation and helps to interpret the behavior of electron multiplication with a single GEM foil.

Triple-layer For the design of the triple-layer scenario, the simulated volume is motivated by the CMS GE1/1 design. The three GEM foils, as well as the spacing of the drift, transfer, and induction gap, follow this default design.

6.3.3 Definition of quantities

Fig. 6.15 illustrates the definitions of the quantities described in the following.

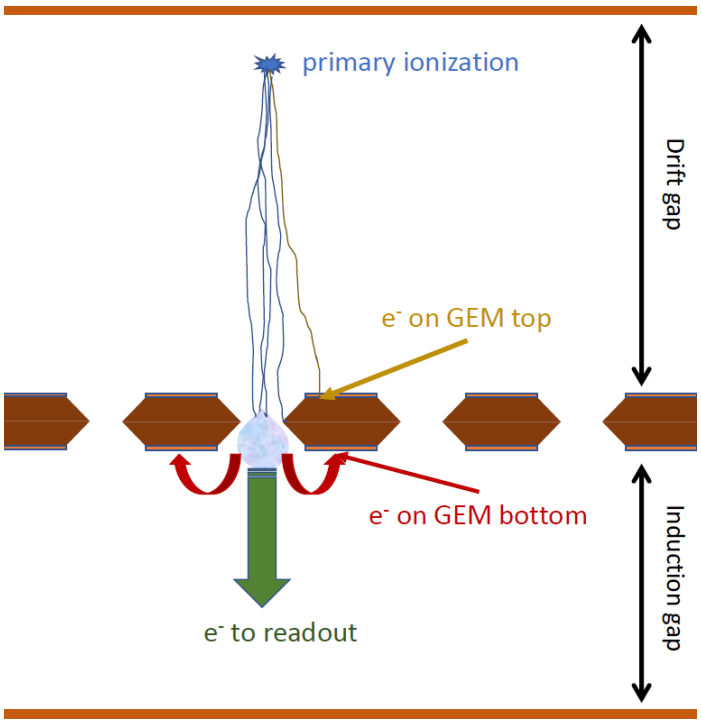

Figure 6.15: Illustration of the definitions of the investigated quantities in simulation. The region of the primary ionization is shown together with the drift lines of the primary electrons in blue. In ocher, a drift line of an electron ending up on the top of the GEM foil (copper layer) is depicted as an example. Those electrons ending up on the bottom of the foil are drawn in red color. In green, the electrons reaching the readout board are shown. Due to illustration purposes, the dimensions and proportions are not to scale.

Effective gas gain The effective gas gain is defined for the measurements in Eq. 3.21. For the simulations, this translates into

$$G_{eff} = \frac{\#(e^- \text{on readout})}{\#(\text{primary and secondary } e^-)}. \tag{6.3}$$

$\#(e^-\text{on readout})$ denotes the number of electrons with the endpoint on the readout plane. $\#(\text{primary and secondary } e^-)$ is the number of primary and secondary electrons in the drift gap. In this thesis, secondary electrons denote those electrons, which are produced around the primary ionization. Primary electrons with enough energy can create secondary electron-ion pairs close to the region of primary ionization (see discussion in Sec. 3.3.1). The secondary electrons do not denote the avalanche electrons. In principle, one could also study the total gas gain. However, the effective gas gain is a more suitable quantity when it comes to the comparison with data.

Collection efficiency When electrons drift towards a GEM foil, their drift lines are bent into the holes of the foils due to the strong electric field inside the holes. Nevertheless, depending on the magnitude and direction of the drift and amplification fields, some electrons are not guided into the holes. Instead, they are ending up on the copper foil and, thus, do not induce an electron avalanche. To quantify this effect, the collection efficiency is defined by

$$\epsilon_{coll} = 1 - \frac{\#(e^- \text{on GEM top})}{\#(\text{primary and secondary } e^-)}. \tag{6.4}$$

$\#(e^-\text{on GEM top})$ is the number of electrons having the endpoint of the drift line on the top copper layer of the GEM foil. The electrons coming from the drift gap can also end up on the surface of the polyimide inside the GEM hole. These electrons may or may not contribute to the electron multiplication. Either way, they are excluded in the definition of the collection efficiency. To unambiguously decide if those electrons have started an avalanche, the information of the ionizations of each electron must be available after the microscopic avalanche simulation. However, this information is rather tedious to obtain.

Extraction efficiency After the electron multiplication inside the GEM hole, a decisive parameter of the GEM foil/detector is the capability to extract as many electrons of the avalanche as possible to increase the signal strength. To quantify the behavior, the extraction efficiency is defined as

$$\epsilon_{extr} = \frac{\#(e^- \text{on readout})}{\#(e^-, \text{where } z_e \leq \text{GEM bottom})}. \tag{6.5}$$

$\#(e^-\text{on readout})$ is the number of electrons reaching the readout plane. $\#(e^-, \text{where } z_e \leq \text{GEM bottom})$ is the number of electrons with endpoints below or equal to the bottom of the GEM foil. The definition of the denominator also includes those electrons, which are captured by gas atoms in the induction gap between the bottom of the GEM foil and the readout plane. The following statement holds: the lower the extraction efficiency, the more electrons end up on the bottom of the GEM foil.

6.3.4 Gas mixtures

To study the influence of different gas mixtures on the gas gain in a triple-layer GEM scenario, the ratio of argon and carbon dioxide is varied around the nominal CMS value of Ar/CO_2 (70/30). The outcome of the simulation can be seen in Fig. 6.16. With a higher fraction of CO_2, acting as a quencher, the gas gain reduces. Not only the gas gain is affected by the gas mixture, but also other parameters, such as the drift velocity and the diffusion of the electron avalanche. This has an impact on the spatial and temporal resolution of the GEM detector [10].

6.3.5 Electric fields

The gas gain is studied by varying the electric field strength in the gaps, as well as varying the potential across the GEM foil. Fig. 6.17 shows the effective gas gain of a triple-layer GEM detector as a function of the drift field and as a function of the voltage difference across the first GEM foil. While these two quantities are varied, the other voltages are following the nominal CMS GE1/1 voltage distribution. The dependency of the gas gain on the voltage difference across the first GEM foil is rather trivial (see Sec. 6.2.2). The increase of the effective gas gain with lower drift fields can be explained by looking at the collection efficiency of the GEM foil in Fig. 6.18. The electrons are moving towards the GEM foil guided by

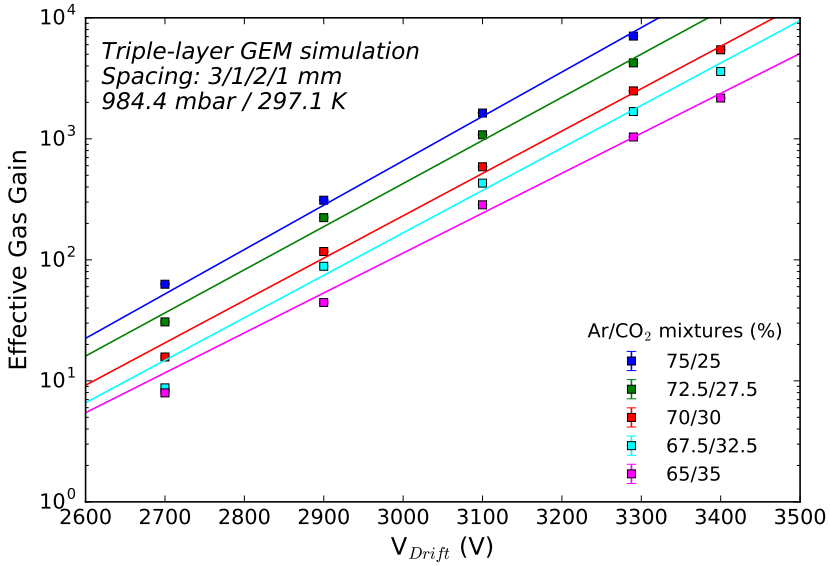

Figure 6.16: Effective gas gain, obtained with the triple-layer GEM scenario, as a function of the drift voltage. Color-coded one can see the different scenarios of Ar/CO_2 mixtures. The HV distribution is following the nominal CMS specifications. This simulation is performed with a GEM hole shape of 70/53/85 μm.

the drift field. With higher drift fields, the electrons are preferably drifting towards the top copper layer of the GEM foil. Thus, they do not enter the GEM hole and cannot induce an avalanche. This leads to a lower gas gain for higher drift fields.

6.3.6 Hole shape and pitch

Variations of the hole shape and hole pitch are studied in this section. The double-conical hole shape is determined by the outer diameters (top and bottom of foil) and one inner diameter (middle of foil). The height of the inner diameter is fixed in the middle of the GEM hole for all studies presented in this thesis. The centers of the openings are always aligned with respect to the vertical symmetry axis of the hole[5]. The hexagonal hole pattern is fully determined by its pitch. The default scenario for the simulation studies is a hole shape of 70/50/70 μm and a pitch of 140 μm. The parameters are varied around these values.

Hole pitch The typical hole pitch of the hexagonal pattern is 140 μm. Recent simulation studies using the single-layer GEM scenario suggest that a plateau of maximal effective gas gain is reached around this hole pitch [132]. This holds if the hole diameter is kept constant at 70 μm. For larger hole pitches than 140 μm, the collection efficiency drops. With a larger copper surface, more electrons end up right there and are not guided into the holes. For smaller hole pitches, a decrease in extraction efficiency is observed. This may be explained by the overlap of the electric fields of two neighboring holes. The overlap prevents the electrons from drifting towards the anode. This study presents a good example, why the single-layer simulation is a reliable way to determine the optimal parameters of GEM foils.

[5]Studies on the variation of the height, as well as other parameters, of the inner diameter can be found in Ref. [139].

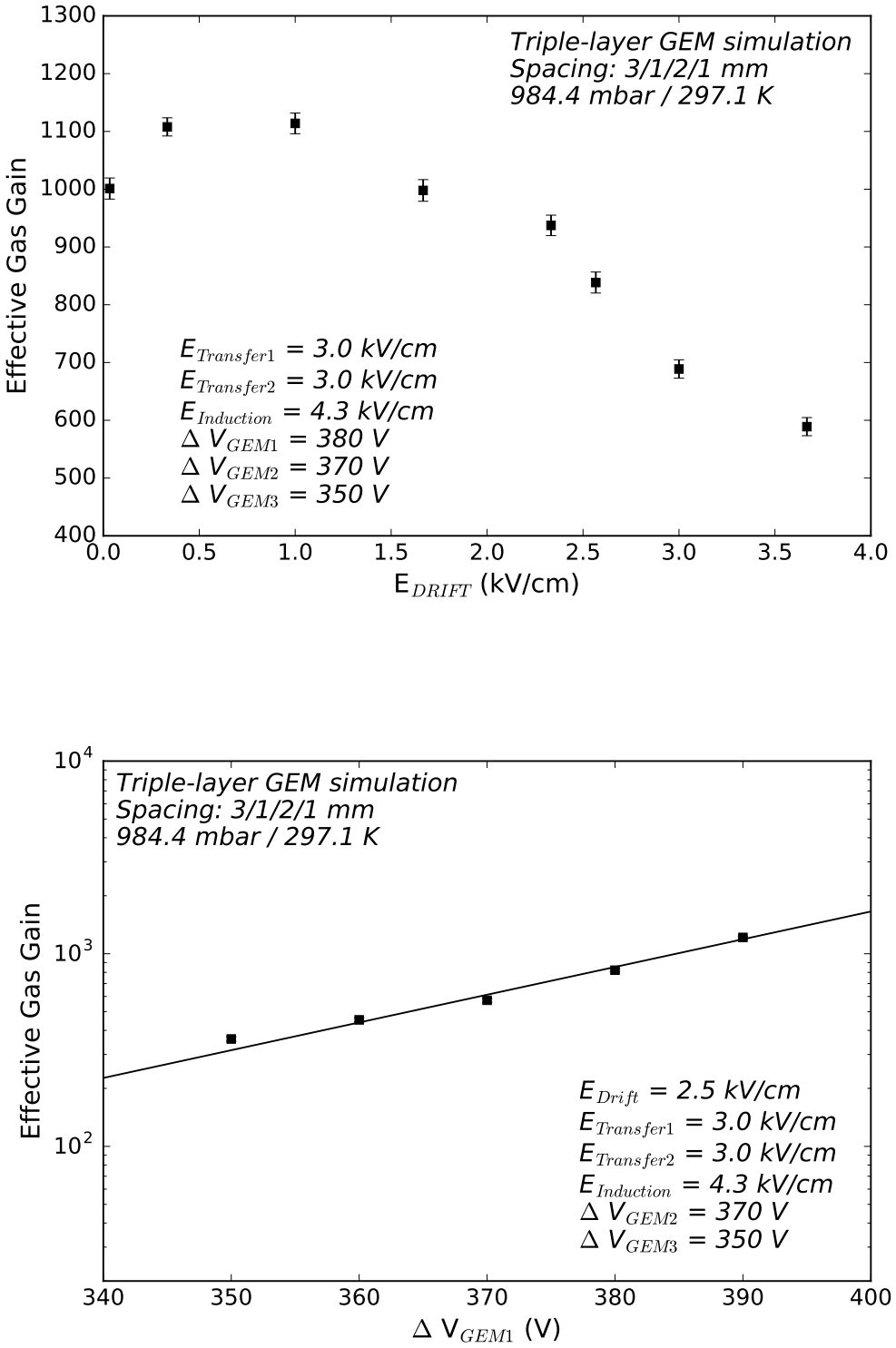

Figure 6.17: Effective gas gain, obtained with the triple-layer GEM scenario, as a function of the drift field (top) and as a function of the voltage difference across the first GEM foil (bottom). The values of the other fields and voltages are kept constant and are shown for both simulations.

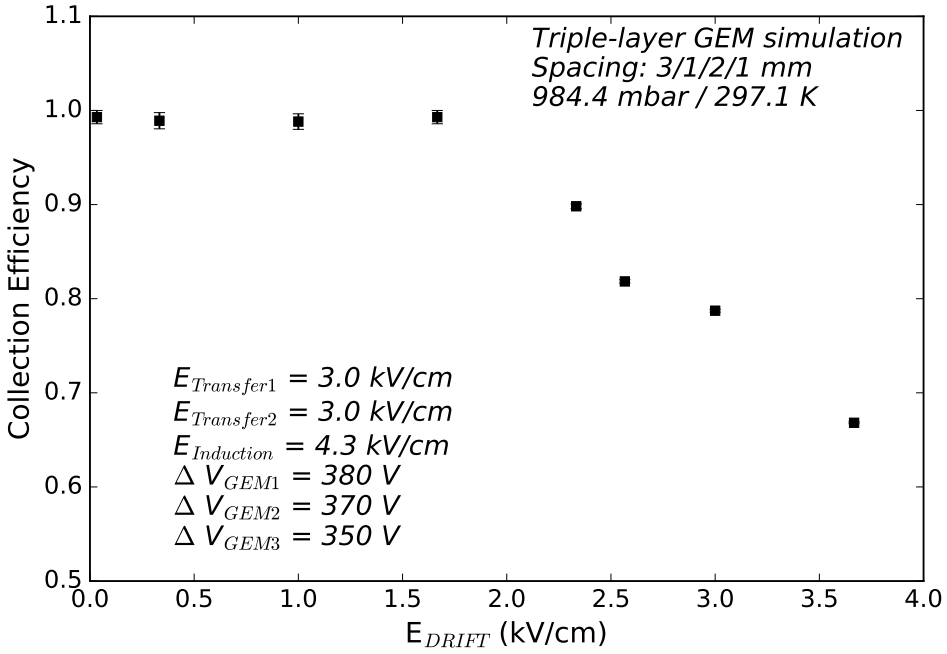

Figure 6.18: Collection efficiency of the first GEM foil for the triple-layer scenario as a function of the drift field. The electric field of the drift gap is varied while the other fields are kept constant.

Hole shape and asymmetry The hole shape is a parameter of the GEM foil, that strongly impacts its performance. The discussion in Sec. 6.2.3 motivates the investigation of the hole shape and provides an introduction to the topic. What concerns the simulation, single-layer studies [132] show that for a constant pitch of 140 μm the optimal value of the outer hole diameter is 70 μm assuming a symmetric hole. Effectively, the variation of the outer hole diameter is similar to the variation of the hole pitch, which means that the argument for a larger hole pitch holds also for a smaller hole diameter and vice versa. The extraction efficiency of a foil drops sharply for hole diameters larger than 85 μm on the bottom of the foil[6].

For the triple-layer scenario, simulations are performed following the typical hole shapes of the GEM foil etching procedures (single-mask and double-mask). As opposed to the simulation studies before, the GEM hole can have different outer diameters, resulting in an asymmetric shape. Tab. 6.4 gives an overview of the geometries used for the simulations together with the associated etching procedure. Fig. 6.19 presents the effective gas gain as a function of the drift voltage. For the examined range of voltages, the double-mask scenario has the highest effective gas gain, followed by the single-mask Orientation B. The lowest gas gain is obtained with single-mask Orientation A. However, single-mask Orientation A and B behave very similar.

[6]For the GE1/1 detector production, the single-masked foils with hole diameters larger than ≈ 90 μm are rejected.

Etching procedure	Simulated hole geometry	Abbreviation
Double-mask	70/50/70 μm	Double-mask
Single-mask	70/53/85 μm	Single-mask OB
Single-mask	85/53/70 μm	Single-mask OA

Table 6.4: Overview of the GEM hole geometries used for the simulation studies. The abbreviations in the right column help to match the simulated hole geometries to real foil types.

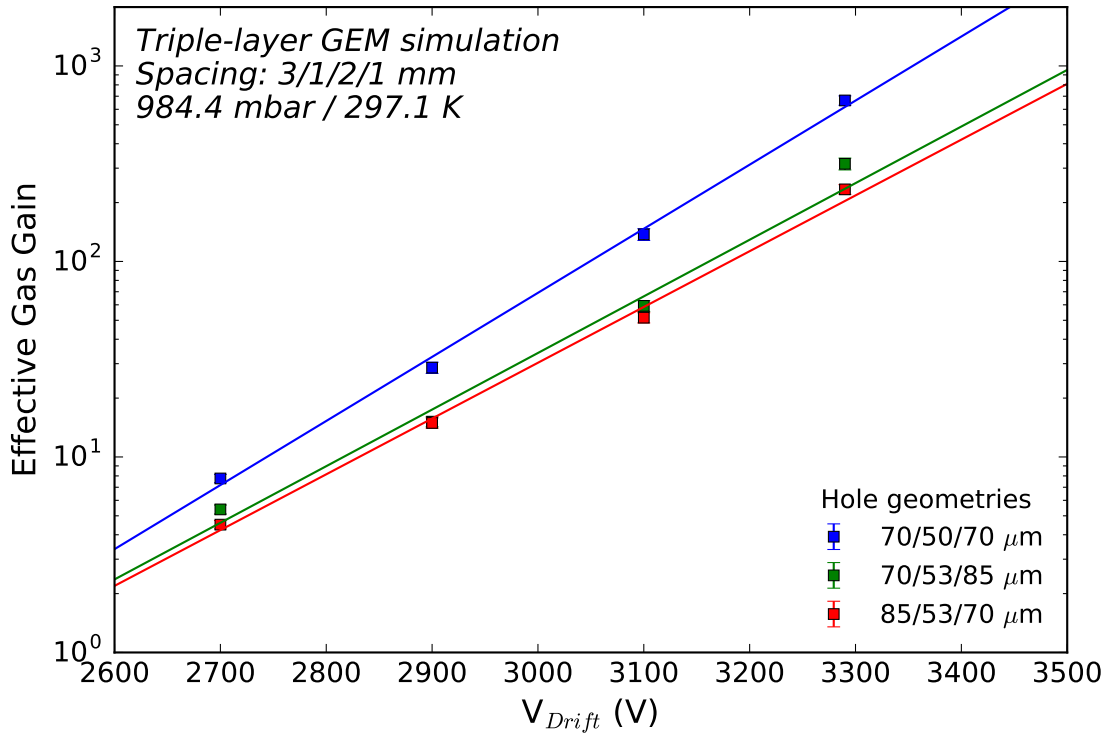

Figure 6.19: Effective gas gain as a function of the drift voltage. The three scenarios described in Tab. 6.4 are shown here.

6.3.7 Conclusive statements

The simulation of microscopic processes with Garfield++ has shown to be an excellent tool to analyze the electron avalanche inside the GEM detector. Adding quenching gases to the nominal gas mixtures leads to a lower gas gain. The electric fields were varied. It was found that the gas gain decreases for higher drift fields. This can be explained by an increasing number of electrons ending up on the top copper layer of the foil. The hole shape and pitch was intensively investigated. The simulations suggest that the nominal hole dimensions of 70/50/70 μm for a fixed hole pitch of 140 μm offer the largest effective gas gain.

6.4 Comparison of simulation and measurements

This section provides a comparison of the results from simulation and measurements. The general comparability of the two parts is discussed. The section ends with a conclusive statement.

6.4.1 Discrepancy between measurements and simulations

In general, the comparability between simulation and data for GEM detectors is a long-lasting challenge in the MPGD community. The main discrepancy manifests itself in a lower gas gain in simulations compared to data. This can be directly seen when merging the gas mixture studies in one plot (see Fig. 6.20). Numerous studies have been performed searching

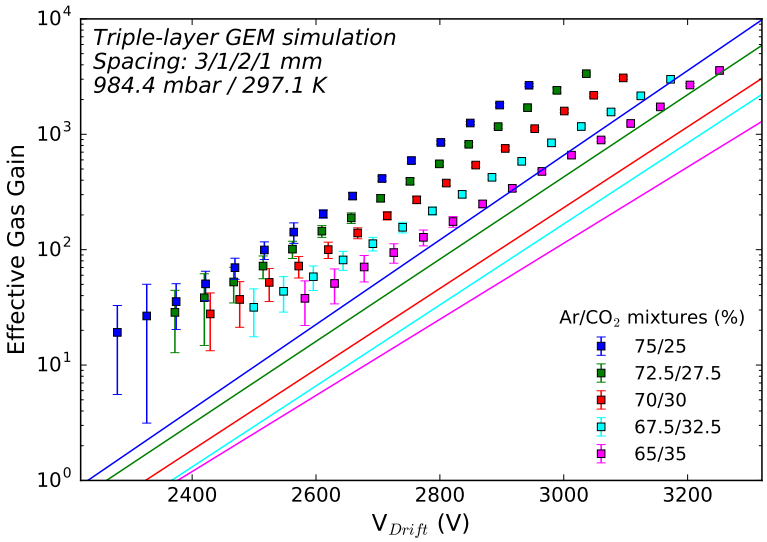

Figure 6.20: Effective gas gain as a function of the drift voltage. The simulation results are presented as solid colored lines. The data from the gas gain measurements are shown as points. The different Ar/CO_2 gas mixtures are color-coded.

for explanations of the discrepancy. The latest findings suggest that one contribution to the discrepancy may be due to the meshing procedure and electric field calculation of Ansys. Ref. [140] presents a comparison of the meshing procedure with GMesh [141] and Ansys and the impact on the resulting gas gain in simulations. To finally resolve the discrepancy between data and simulation, further studies are needed exceeding the scope of this thesis. Thus, the comparison of simulation and data is not performed on absolute numbers but on relative numbers. In other words, the general trends of the gas gain studies are compared.

Besides this general challenge to compare data and simulation, there is one other main difference between the simulation studies and the data. In simulations, the effective gas gain is calculated based on the number of electrons reaching the readout layer. During the measurement, the induced current on the readout board is measured. This introduces also a discrepancy between simulations and data. However, this cannot fully explain the differences shown in Fig. 6.20.

6.4.2 Conclusive statements

For the gas mixture studies, a similar behavior in simulation and data is observed when adding quenching gases (see Fig. 6.20). For the simulation, the CO_2 fraction was varied. For the measurements, on the one hand, the CO_2 fraction was varied and, on the other hand, N_2 was added.

For the electric field variations, the simulations help to understand better the outcome of the measurements. The measured effective gas gain stays more or less constant when decreasing the drift field from the nominal CMS value of 2.6 kV/cm down to 1 kV/cm. Simulations reveal that the foil collection efficiency is higher for lower drift fields. Overall, the effective gas gain curve from simulations increases slightly before it drops for very low drift fields. The increase appears also in data, however, less pronounced. For higher drift fields than 2.6 kV/cm, the gas gain decreases in both simulations and data.

The studies on the GEM hole shape show consistencies and discrepancies. The highest effective gas gain is associated to the double-mask configuration, both in simulation and data. In simulation, the single-mask Orientation A and B behave similar in terms of gain, while in data, Orientation B gives significantly higher gain than Orientation A.

For the interpretation of the results, one has to keep in mind that these studies are aimed at a better understanding of the gas gain of a triple-GEM chamber. When integrating the detector into a larger experiment, the performance has to be optimized in a multidimensional space. Parameters such as temporal/spatial resolution, discharge probability, and rate capability must be included in the considerations.

6.5 Comparison with literature and summary

Since the introduction of the GEM technology, roughly two decades ago, the MPGD community constantly improved the technology and, with the improvements, increased the understanding of the GEM detectors. In the following, the results of this thesis are discussed in a broader context.

For the induction and drift field variations, measurements were performed independently by the CMS GEM group. Fig. 6.21 presents the corresponding results. While the induction field variations yield a similar result compared to Fig. 6.8, the outcome of the drift field variations differs from Fig. 6.6 presented in this thesis. It is yet unclear, where the discrepancy comes from. Simulations suggest a similar behavior as observed in the measurements shown in this thesis. Former studies and measurements on single-GEM chambers found out that the foil transparency increases when lowering the drift field [8], which supports the outcome of this thesis.

Determining the difference in effective gas gain of single-masked and double-masked foils is a well-known topic, especially in the CMS GEM group. The single-mask technique offers the possibility to produce large-size GEM foils without aligning the masks. This is an important improvement in the development of GEM detectors. Former studies found out that the effective gas gain of the single-mask foils (Orientation B) is higher than the effective gas gain of the double-mask foils [13]. Fig. 6.22 presents the corresponding measurements. This is not in agreement with the results obtained in simulation and the results from the measurements presented in this thesis. Possible sources of the observed discrepancy are the spacing of 3(2)/2/2/2 mm compared with the 3/1/2/1 mm spacing in this work, the HV settings, and the applied pressure and temperature corrections. A similar ratio between single-mask Orientation A and B is observed in Ref. [142] compared to the measurements of this thesis.

Several conclusions can be drawn from the studies for the CMS GEM projects. Variations

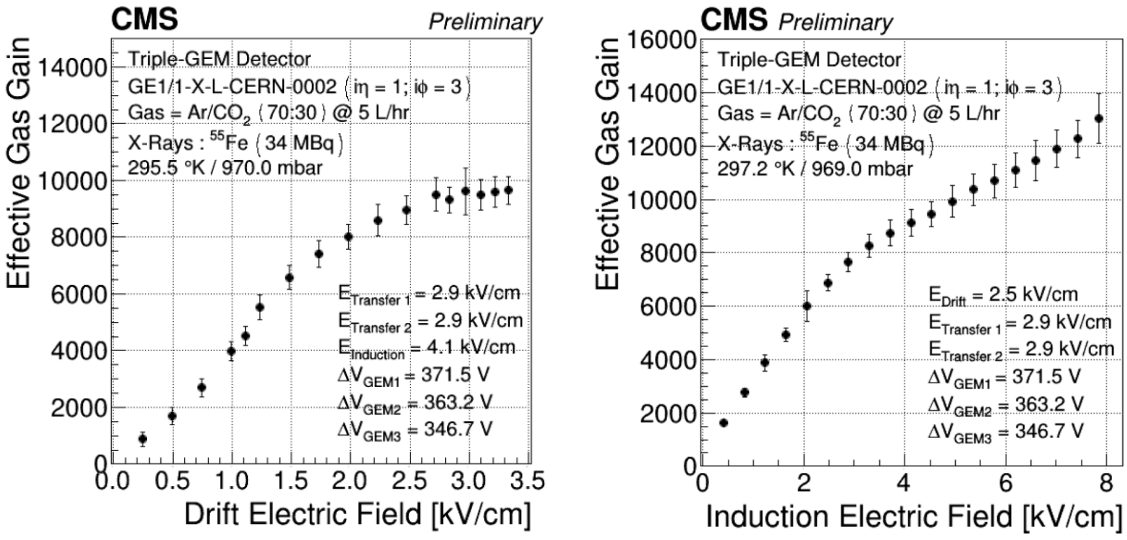

Figure 6.21: Effective gas gain as a function of the drift field (top) and induction field (bottom). The measurements were performed by the CMS GEM group in the CERN GEM laboratory. The figures are taken from Ref. [118].

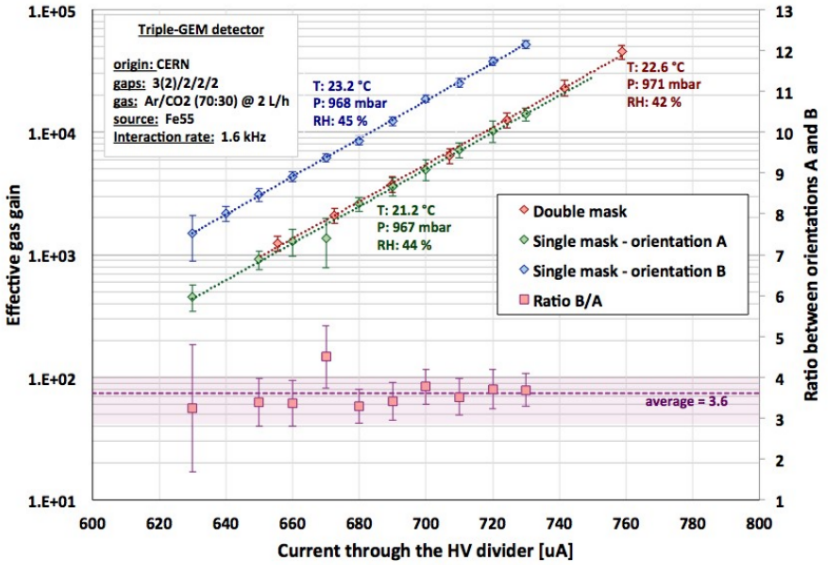

Figure 6.22: Effective gas gain as a function of the current flowing through the HV divider. The scenarios of different GEM foils are shown color-coded. In addition to the effective gas gain, the ratio between orientation A and B is depicted. The figure is taken from Ref. [13], where details about the measurements can be found.

of the drift and induction fields have a non-negligible effect on the effective gas gain. For the design of large-size CMS GEM chambers, the thicknesses of the drift and induction gaps need to be as uniform as possible across the detector area. This can be ensured by a uniform production of the drift and readout PCBs, as well as with additional standoffs in the active volume of the chamber. For the CMS GE2/1 project, the GEM foils may be produced by both the single-mask and double-mask technique for different modules of the chambers. Regarding the integration of the chambers into CMS, a uniform response across the modules is essential. This work illustrates the influence of the hole shape on the effective gas gain.

7 Sensitivity study on displaced muons at the HL-LHC

This section is devoted to discuss the sensitivity study on displaced muons with the CMS Phase-2 detector at the HL-LHC. After an introduction to the search strategy and important reconstruction variables (Sec. 7.1), two examples of BSM models are discussed (Sec. 7.2). The models predict long-lived particles decaying to muons inside the CMS detector. The processes foreseen by the models are interpreted as the signal in the analysis. The details of the analysis are described in Sec. 7.3. In Sec. 7.4, the statistical interpretation of the results is presented by determining the expected exclusion power and sensitivity.

7.1 Introduction and motivation

The upgrade of the LHC towards the HL-LHC (described in Sec. 4.3.2) offers a unique opportunity to search for exotic signatures due to the enormous expected amount of data. So far, searches for exotic long-lived particles have shown good agreement with the standard model expectation. Nevertheless, a large phase-space has not been explored yet. This study proposes a search for LLPs from BSM models at the HL-LHC and determines the expected sensitivity with the CMS Phase-2 detector (described in Sec. 4.3.3).

Two conceptually different approaches can be used to estimate the sensitivity of a given search at the HL-LHC. One approach is called a *projection* of a current analysis to the HL-LHC era. In a projection, parameters, such as signal and background efficiencies, systematic uncertainties and luminosities are rescaled to obtain the final results. The other approach consists of running a complete or parametrized simulation of the physics processes in the upgraded detector at the HL-LHC. This is called *upgrade analysis*. In this work, an *upgrade analysis* with a complete simulation of the CMS Phase-2 detector is presented.

7.1.1 Detector signature

In general, a wide spectrum of detector signatures can arise from long-lived particles, e.g. disappearing tracks, displaced vertices, out-of-time signatures, missing transverse energy or - as in our case - displaced (muon) tracks. There is a growing effort in particle physics experiments to search for long-lived particles from BSM models more thoroughly in a signature-driven way. This effort culminated in an LHC LLP white paper [22], where the current results are summarized and plans are outlined. The general idea of this sensitivity study is to search for a displaced signature in a model-independent way. A signature involving two displaced muons and missing transverse momentum is studied.

7.1.2 Identification variables

Before diving into the formalism of BSM models and the details of the analysis, it is worth summarizing the definitions of some reconstruction variables, which are important in searches for displaced signatures. The following content is based on Ref. [90].

- Primary vertices (PVs) are reconstructed by a sophisticated procedure using the information of the tracker. There are three main steps: the selection of the candidate tracks, clustering of the tracks that seem to originate from the same vertex and determining the vertex position using the associated tracks. According to a given weight at the end

of the procedure, the vertex can be associated with a pp collision. If no PV is found, the beam spot is used as a default.

- The beam spot denotes the profile of the luminous region, where the LHC bunches collide in CMS. The beam spot is determined as an average over all events in one luminosity section, corresponding to a time window of 23.3 seconds [143]. The center of the luminous region in x, y and z is determined, as well as the three-dimensional shape.

- The transverse impact parameter d_0[1] is defined as the distance of the closest approach of the extrapolated track to the primary interaction vertex in the transverse plane. Fig. 7.1 illustrates the definition of d_0. For prompt reconstruction, d_0 is typically constraint to 1 cm. In searches for prompt signatures, the transverse impact parameter is further constrained in the event selection. For displaced signatures, these constraints need to be relaxed or completely removed (see Sec. 7.3.2 and 7.3.5).

- The longitudinal impact parameter d_z is calculated in the $(\Delta\phi, z)$-plane. The z-axis corresponds to the beam line with $z = 0$ denoting the PV. The difference in the azimuthal angle is defined by $\Delta\phi = \phi - \phi_0$, where ϕ_0 corresponds to the azimuthal angle at the point of closest approach to the PV in the transverse plane (see definition of d_0). In the $(\Delta\phi, z)$-plane, the muon track can be parametrized by a straight line[2]. The interception of the extrapolated line with the z-axis is taken as the longitudinal impact parameter. In Fig. 7.2, d_z is illustrated.

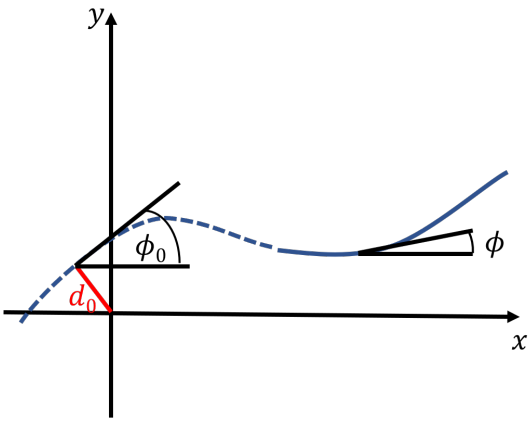

Figure 7.1: Sketch of the transverse impact parameter d_0. The red line illustrates d_0. The solid blue line shows the reconstructed track. The dashed blue line indicates the extrapolated track. Additionally, the azimuthal angle ϕ is indicated. ϕ_0 denotes the azimuthal angle at the position of closest approach of the extrapolated track to the PV in the transverse plane. ϕ and ϕ_0 are used in the definition of the longitudinal impact parameter.

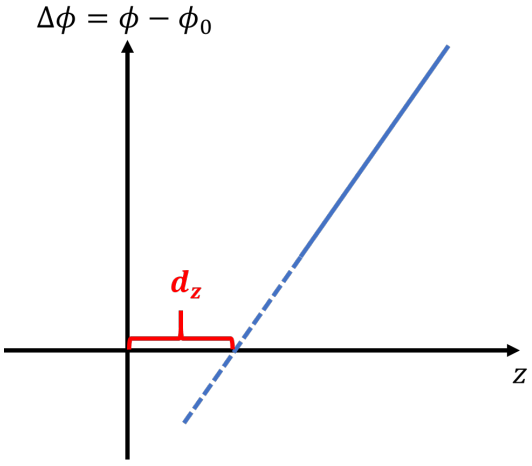

Figure 7.2: Sketch of the longitudinal impact parameter d_z in the $(\Delta\phi, z)$-plane. The solid and dashed blue lines represent the reconstructed and extrapolated track, respectively. The curly bracket in red color shows d_z. ϕ is the azimuthal angle, which varies along the track due to the bending inside the magnetic field. ϕ_0 is defined in the text and illustrated in Fig. 7.1.

[1]The transverse impact parameter is sometimes also denoted by d_{xy} in this thesis.
[2]Neglecting track reconstruction uncertainties and multiple scattering.

7.2 BSM models with long-lived signatures

On the quest for new physics beyond the standard model, long-lived signatures offer a great opportunity. For these signatures, a large phase-space in mass and lifetime is still uncovered by collider searches[3]. At the same time, the standard model offers a zoo of long-lived particles (see Fig. 2.4). Thus, new physics are likely to appear (also) in long-lived signatures. In the following, two BSM models predicting long-lived particles are introduced. These models are falling under the category of supersymmetric extensions of the standard model (SUSY). Dark SUSY predicts a light LLP, i.e. with a mass in the GeV range, called the dark photon. SUSY with a gauge-mediated symmetry breaking (GMSB) offers a heavier LLP candidate, i.e. with a mass in the TeV range, called the smuon. Before discussing peculiarities of these models, general aspects of SUSY are introduced.

7.2.1 General aspects of SUSY

Due to an additional symmetry in SUSY, each SM particle gets a superpartner, often called sparticle. The spin of the superpartner differs by half a unit compared to the SM partner, i.e. the fermions get a bosonic superpartner and the bosons get a fermionic superpartner. If SUSY was an exact symmetry of nature, SM particles and their superpartners would be degenerate in mass. Despite a huge effort on finding superpartners, none have been observed until now. Thus, if SUSY is realized in nature, it needs to be broken. The SUSY breaking can be realized in different ways with phenomenological consequences, e.g. for the mass hierarchy in the SUSY sector. A basic version of SUSY with a minimal additional particle content compared to the SM is called the minimal supersymmetric standard model (MSSM).

By imposing the conservation of R-parity, the decay of a sparticle into only SM particles is forbidden. The lightest supersymmetric particle (LSP) becomes stable and forms a potential candidate for dark matter. SUSY also offers a solution to the hierarchy problem by introducing cancellation terms in the loop corrections for the Higgs mass. These are only some examples, where SUSY helps to solve the limitations of the SM. An introduction to SUSY and a discussion of the benefits of SUSY can be found in Refs. [144, 145].

7.2.2 Dark photons in Dark SUSY

In Dark SUSY models, a dark sector[4] of fermions and gauge fields is added to the supersymmetric fields. An additional dark symmetry, $U_D(1)$, gives rise to a new particle, called dark photon (γ_D) [146, 147]. The dark photon acquires a mass with the symmetry breaking of $U_D(1)$. The communication of the dark sector with the SM gauge sector can be established through the kinetic mixing of the dark photon with the SM hypercharge $U_Y(1)$ by

$$\mathcal{L} \supset \frac{\epsilon}{2} F_{\mu\nu} F^{D,\mu\nu}, \tag{7.1}$$

where $\mathcal{L}$ is the complete Lagrangian of the model. $F^{D,\mu\nu}$ denotes the field strength tensor of the dark photon field and $F_{\mu\nu}$ is the field strength tensor of the hypercharge field[5]. The kinetic mixing is quantified by ϵ. The dark photon mixes with the SM photon and, thus, couples to the charged SM particles[6].

[3] The reason lies in the nature of the experiments. Trigger, reconstruction, simulation, and analysis efforts focus on prompt signatures.

[4] In the literature, this is also often called hidden sector.

[5] A definition of the field strength tensor can be found in the literature given in this section.

[6] The dark photon also mixes with the SM Z boson. However, the couplings to the SM fermions are suppressed by the large mass of the Z boson.

A model with a minimal particle content of the dark sector is described in Ref. [147]. The model is guided by the idea to incorporate SM Higgs decays to multilepton final states. Besides the massive dark photon and its superpartner, called dark gaugino, the dark sector contains two Higgs superfields in order to break the $U_D(1)$ symmetry. After $U_D(1)$ symmetry breaking, one obtains three dark neutralinos, as mixtures of the dark gaugino and the Higgsinos. Additionally, three dark scalars from the remaining degrees of freedom of the Higgs superfields are present. Writing Eq. 7.1 in a supersymmetric form yields, that, not only the dark photon and the SM photon kinetically mix, but also the dark gaugino and visible neutralinos. Thus, the LVSP[7] can decay into the dark sector and the dark matter candidate in Dark SUSY belongs to the dark sector. In the following, the lightest visible neutralino is denoted n_1 and the lightest dark neutralino is called n_D. n_1 is the LVSP and n_D is the LSP of this model.

Dark photon decay In the following, it is assumed that the dark photon only decays into SM charged fermions. The decay width calculations follow the procedure described in Ref. [148]. The dark photon couples to SM charged fermions in the same way as a photon, except that the couplings are scaled by ϵ. The decay width to leptons can be written as

$$\Gamma_{\gamma_D \to \bar{l}l} = \frac{1}{3}\alpha\epsilon^2 m_{\gamma_D}\sqrt{1-\frac{4m_l^2}{m_{\gamma_D}^2}}\left(1+\frac{2m_l^2}{m_{\gamma_D}^2}\right), \tag{7.2}$$

where m_l is the lepton mass and α is the electromagnetic fine-structure constant. The dark photon can also decay into SM hadrons. Inspired by $\Gamma_{\gamma_D \to \bar{\mu}\mu}$, the decay width into hadrons can be written as

$$\Gamma_{\gamma_D \to hadrons}(s = m_{\gamma_D}^2) = \frac{1}{3}\alpha\epsilon^2 m_{\gamma_D}\sqrt{1-\frac{4m_\mu^2}{m_{\gamma_D}^2}}\left(1+\frac{2m_\mu^2}{m_{\gamma_D}^2}\right) R(s = m_{\gamma_D}^2), \tag{7.3}$$

where $R(s) = \sigma_{e^+e^- \to hadrons}/\sigma_{e^+e^- \to \mu^+\mu^-}$ denotes the hadronic cross section ratio. $R(s)$ is depicted in Fig. 7.3. In Ref. [149], the hadronic cross section is given for $\sqrt{s} > 0.36$ GeV, which is sufficient for the dark photon mass range explored in this study.

Taking the different partial widths into account, the total lifetime τ_{γ_D} can be calculated by

$$\tau_{\gamma_D} = \frac{\hbar}{\Gamma_{tot}} = \begin{cases} \frac{\hbar}{\Gamma_{\gamma_D \to e^+e^-} + \Gamma_{\gamma_D \to \mu^+\mu^-} + \Gamma_{\gamma_D \to hadrons}(s=m_{\gamma_D}^2)} & , m_{\gamma_D} < 2m_\tau \\ \frac{\hbar}{\Gamma_{\gamma_D \to e^+e^-} + \Gamma_{\gamma_D \to \mu^+\mu^-} + \Gamma_{\gamma_D \to \tau^+\tau^-} + \Gamma_{\gamma_D \to hadrons}(s=m_{\gamma_D}^2)} & , m_{\gamma_D} \geq 2m_\tau, \end{cases} \tag{7.4}$$

where m_τ denotes the tau lepton mass. Tau leptons can decay leptonically, which would contribute to the branching fraction relevant for this search. However, this is neglected in the following. $\hbar$ is Planck's constant. If one defines $f(m_{\gamma_D})^{-1} = \frac{\Gamma_{tot}}{\epsilon^2}$, the lifetime can be rewritten as

$$\tau_{\gamma_D} = \frac{\hbar}{\epsilon^2} f(m_{\gamma_D}). \tag{7.5}$$

$c\tau_{\gamma_D}$ can then be determined via

$$c\tau_{\gamma_D} = c \cdot \frac{\hbar}{\epsilon^2} f(m_{\gamma_D}) = \frac{1.97 \cdot 10^{-13}}{\epsilon^2} \times \left(\frac{f(m_{\gamma_D})}{\text{GeV}^{-1}}\right) \text{ mm}. \tag{7.6}$$

The dark photon lifetime is proportional to $1/\epsilon^2$. For small ϵ, the dark photon is long-lived. Theoretical considerations suggest a small kinetic mixing of $\epsilon \approx 10^{-4} - 10^{-3}$ [146]. From the

[7] LVSP denotes the lightest visible supersymmetric particle.

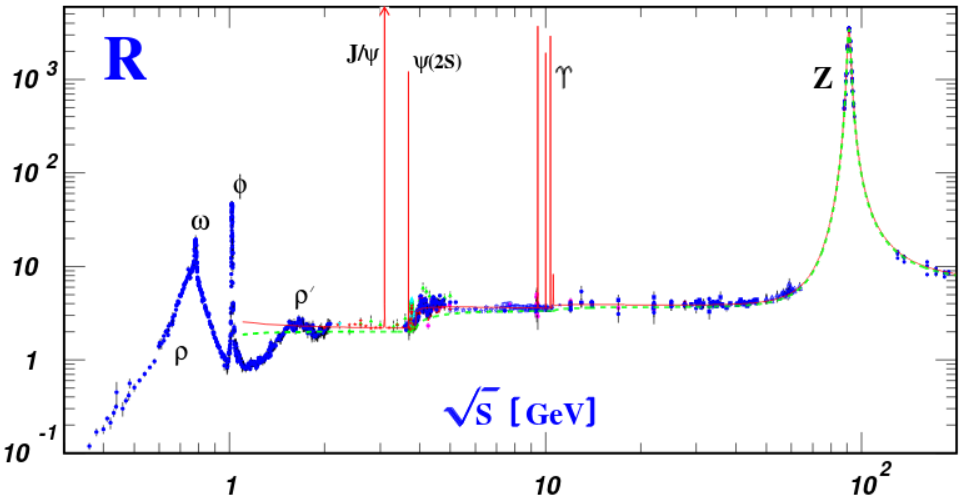

Figure 7.3: Hadronic cross section ratio as a function of the center-of mass energy $\sqrt{s}$. The blue points enter the partial width calculation for dark photons to hadrons including hadronic resonances, i.e. ρ, ω, and ϕ. Narrow hadronic resonances, e.g. Υ, J/ψ, and ψ(2S), are shown as red arrows. The figure is taken from Ref. [149].

experimental side, $\epsilon \lesssim 10^{-3}$ is in agreement with current bounds [148]. A priori, there is no reason for ϵ to be bound from below.

The branching ratio of dark photons decaying into muons is of utmost importance for this sensitivity study. Fig. 7.4 presents the branching ratio as a function of the dark photon mass. For dark photon masses close to masses of hadronic resonances, i.e. ρ, ω, ϕ, and ρ', the

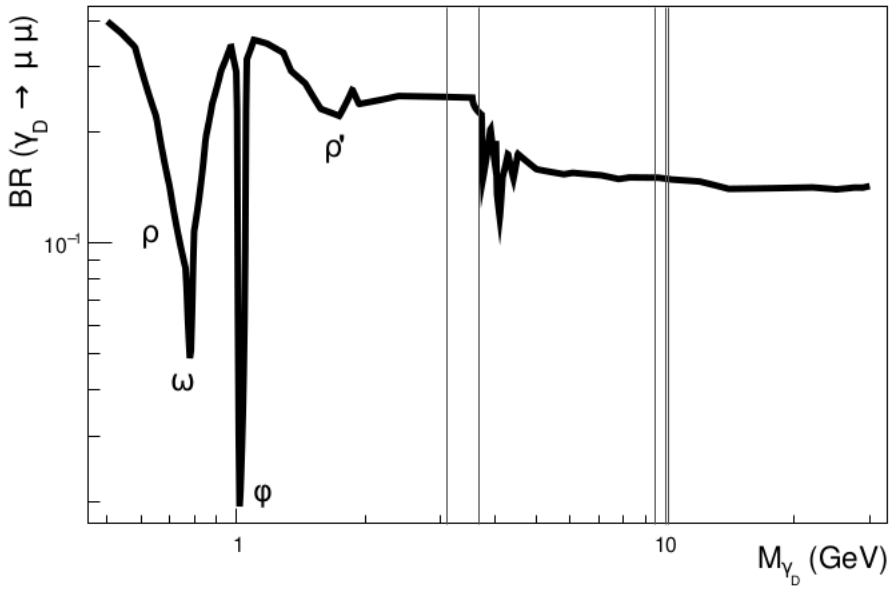

Figure 7.4: Branching ratio of the dark photon decaying into muons as a function of the dark photon mass. The shape is driven by the existence of hadronic resonances for low masses. For $M_{\gamma_D} > 10$ GeV, the branching ratio stays rather constant at around 15%. The vertical lines indicate the regions of narrow hadronic resonances, where the study claims no sensitivity. The plot was created by the author based on the data shown in Fig. 7.3.

branching ratio to muons is reduced. Narrow hadronic resonances (e.g. Υ, J/ψ, and ψ(2S)) are not considered. Hence, in the vicinity of these narrow hadronic resonances, the analysis does not claim any sensitivity. For $m_{\gamma_D} \gtrsim 5$ GeV, the branching ratio into muons remains more or less constant at around 15%.

Production of dark photons at the LHC Dark photons can be produced in cascade decays of the SM Higgs boson. The Higgs boson decays to a pair of lightest visible neutralinos (n_1). The visible neutralinos decay further into the lightest dark neutralino (n_D) and the dark photon, as shown in Fig. 7.5.

For the branching fraction $BR(H \to 2\gamma_D + X)$, where X denotes the particles produced in the decay of the SM Higgs boson apart from the dark photons, 20% is used as a default value. This value is in agreement with recent Run-2 studies [150]. It also takes into account the upper limit on invisible/non-conventional decays of the SM Higgs boson [151]. At the (HL-)LHC, the Higgs is produced dominantly via gluon-gluon fusion. The corresponding values and uncertainties of the Higgs production cross section are taken from Ref. [152] at $\sqrt{s} = 14$ TeV.

Final states with at least two displaced muons The analysis selection allows two or more displaced muons in the final state. Thus, cascade decays with two or four muons are considered. In the former case, one dark photon decays to a pair of muons while the other dark photon decays to other fermions (2-muon final state). In the latter case, both dark photons decay to muon pairs (4-muon final state). Both decay chains are illustrated in Fig. 7.5. In

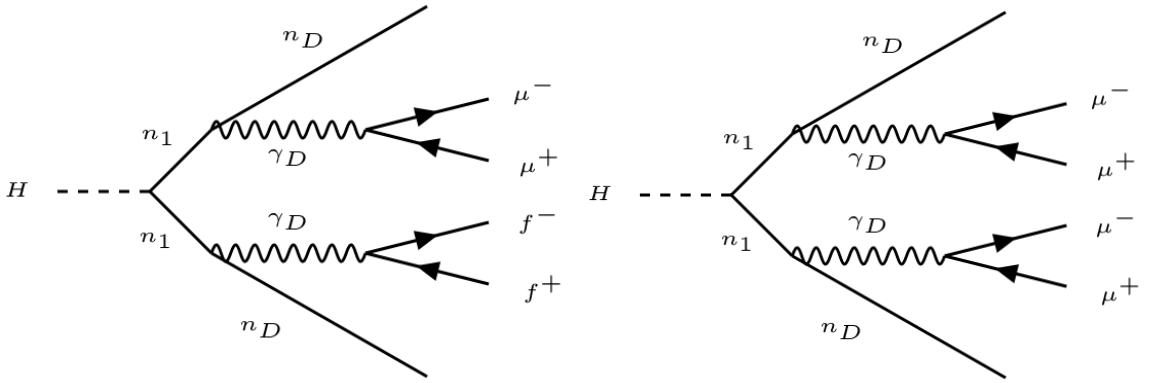

Figure 7.5: Illustration of the decay chains of a SM Higgs boson into a 2-muon final state (left) and a 4-muon final state (right). The SM Higgs boson decays to a pair of lightest visible neutralinos (n_1), which decay further into the dark sector, i.e. the dark neutralino (n_D) and the dark photon (γ_D). Both final states contribute to the signal event yield of the sensitivity study. The illustration is inspired by Ref. [150]. The figures are adapted to our needs.

addition to displaced muons, the final state contains missing transverse momentum originating from the dark neutralino in the $n_1 \to n_D + \gamma_D$ decay. In order to get an impression on the basic kinematic behavior of the muons in the final state, Fig. 7.6 shows (a) the transverse momentum and (b) the pseudorapidity of the four leading muons before reconstruction in the case of the 4-muon final state. Additional information on the kinematic behavior of the dark photons and displaced muons can be found in Sec. A.6.

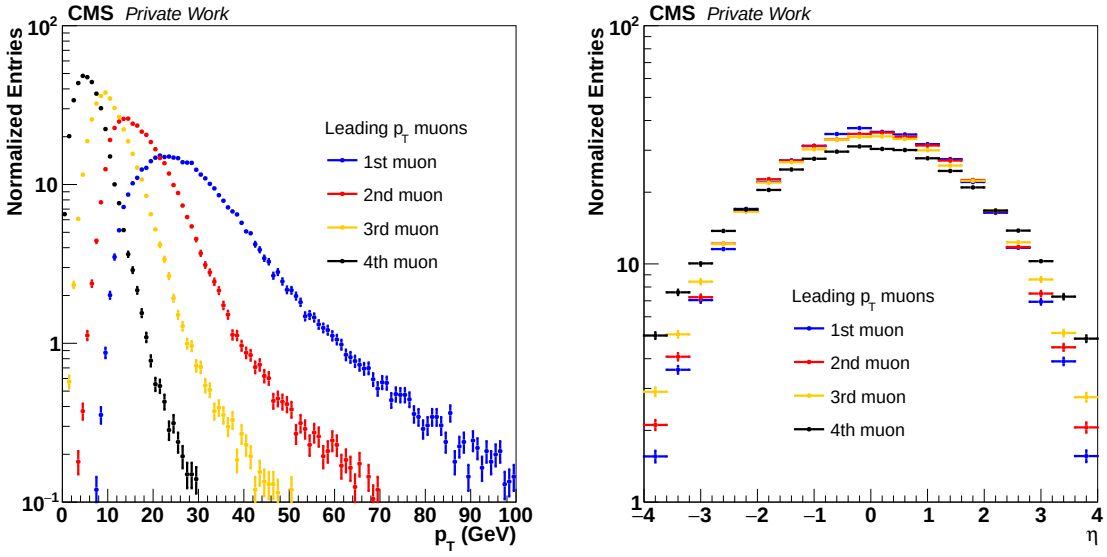

(a) (b)

Figure 7.6: Distribution of transverse momentum p_T (a) and η (b) of the four leading muons on generator level in the 4-muon final state. The dark photon has a mass of 20 GeV and a lifetime of 1000 mm.

Investigated parameter space For the simulated processes involving dark photons, neutralino masses $m_{n_1} = 50$ GeV[8] and $m_{n_D} = 1$ GeV are assumed. The search sensitivity is explored for dark photon masses and lifetimes in the following ranges: $1 \leq m_{\gamma_D}/\text{GeV} \leq 45$ and $10 \leq c\tau_{\gamma_D}/\text{mm} \leq 10^4$. A complete list of the dark photon mass and lifetime hypotheses can be found in Tab. 7.1.

m_{γ_D} (GeV)	$c\tau_{\gamma_D}$ (mm)	m_{n_D} (GeV)	m_{n_1} (GeV)
1	10,100,1000,5000,10000	1	50
5	10,100,1000,5000,10000	1	50
10	10,100,1000,5000,10000	1	50
20	10,100,1000,5000,10000	1	50
30	10,100,1000,5000,10000	1	50
40	10,100,1000,5000,10000	1	50
45	10,100,1000,5000,10000	1	50

Table 7.1: List of dark photon mass and lifetime hypotheses considered in this thesis. The mass of the dark neutralino n_D and the lightest visible neutralino n_1 are mentioned in the two most-right columns. These values are kept constant for all dark photon hypotheses.

7.2.3 Smuons in GMSB SUSY

A specific MSSM model is studied, where supersymmetry is broken in a gauge-mediated (GMSB) way, which means that the messengers of supersymmetry breaking are the gauge interactions [153]. One advantage of GMSB models is that strong flavor-changing neutral

[8] If the dark photon arises from the decay of the SM Higgs boson through the neutralino n_1, kinematics impose $2m_{n_1} \leq m_H$.

currents (FCNCs) are absent. This is important since current experimental results put strong limits on the strength of FCNCs in BSM models (see e.g. Ref. [154]).

In GMSB models, the gravitino ($\tilde{G}$) is typically the LSP, unlike in other versions of SUSY. This is due to the fact that the dynamical SUSY breakdown scale $\sqrt{F}$ can be as low as $\approx$ 10 TeV. The gravitino mass is related to $\sqrt{F}$ via

$$m_{\tilde{G}} = \frac{F}{\sqrt{3}M} = 2.37 \times 10^{-2} \left(\frac{\sqrt{F}}{10 \text{ TeV}} \right)^2 \text{ eV}, \tag{7.7}$$

where $M = (8\pi G_{Newton})^{-1/2} = 2.4 \times 10^{18}$ GeV. A special phenomenological role is assigned to the next-to lightest supersymmetric particle (NLSP). Assuming exact R-parity conservation, the NLSP can only decay into a gravitino, which is the LSP, and its standard model partner.

In general, MSSM models can be described by a small set of parameters. One of those parameters is $\tan\beta$, denoting the ratio of the vacuum expectation values of the two Higgs doublets. If $\tan\beta$ is not too large, the lightest sleptons are right-handed[9] and almost degenerate in mass [155]. In this SUSY scenario, each right-handed slepton can play the role of the NLSP. All other SUSY particles are a lot heavier and can, therefore, be neglected for this study. In the literature, this SUSY scenario is called slepton (co-)NLSP SUSY [156]. In the following, the NLSP is the right-handed smuon.

Long-lived smuon The smuon universally decays into a gravitino and SM muon by $\tilde{\mu} \to \mu + \tilde{G}$. The decay width can be written as

$$\Gamma(\tilde{\mu} \to \mu\tilde{G}) = \frac{1}{48\pi} \frac{m_{\tilde{\mu}}^5}{M^2 m_{\tilde{G}}^2} = 20 \left(\frac{m_{\tilde{\mu}}}{100 \text{ GeV}} \right)^5 \left(\frac{\sqrt{F}}{10 \text{ TeV}} \right)^{-4} \text{ eV}. \tag{7.8}$$

This leads directly to the lifetime $c\tau_{\tilde{\mu}}$ given by

$$c\tau = c \cdot \frac{\hbar}{\Gamma(\tilde{\mu} \to \mu\tilde{G})} = 9.87 \cdot 10^{-6} \left(\frac{m_{\tilde{\mu}}}{100 \text{ GeV}} \right)^{-5} \left(\frac{\sqrt{F}}{10 \text{ TeV}} \right)^4 \text{ mm}. \tag{7.9}$$

In GMSB SUSY, $\sqrt{F}$ is expected to be above $\mathcal{O}(10 \text{ TeV})$ to ensure sufficiently-large SUSY breaking in the MSSM sector [157]. If the gravitino is assumed to be the major component of the dark matter, a gravitino mass $m_{\tilde{G}} \gtrsim 10$ keV is ruled out by cosmological considerations. This would constrain $\sqrt{F}$ to values below 10^4 TeV. However, if one relaxes the assumption a bit and allows other candidates to contribute to the dark matter in the universe, e.g. the lightest visible particle in the GMSB messenger sector, $\sqrt{F}$ can be much larger [158]. Thus, the GMSB SUSY model can be probed in a broad range of masses and lifetimes of the smuon.

Production process at the LHC and detector signature At the LHC, smuons can be produced via a photon or a Z boson. Each of the produced smuons travels a certain distance through the detector until it decays into a muon and a gravitino. The gravitino, as the LSP of the theory, leaves the detector without any signal. The muons appear as a displaced track signature. The very weak interaction of the smuons with the detector material is neglected. Consequently, the detector signature consists of two displaced muon tracks and missing transverse energy. Fig. 7.7 illustrates the production process and the smuon decay.

[9] Handedness is meant with respect to the chirality of the electroweak theory.

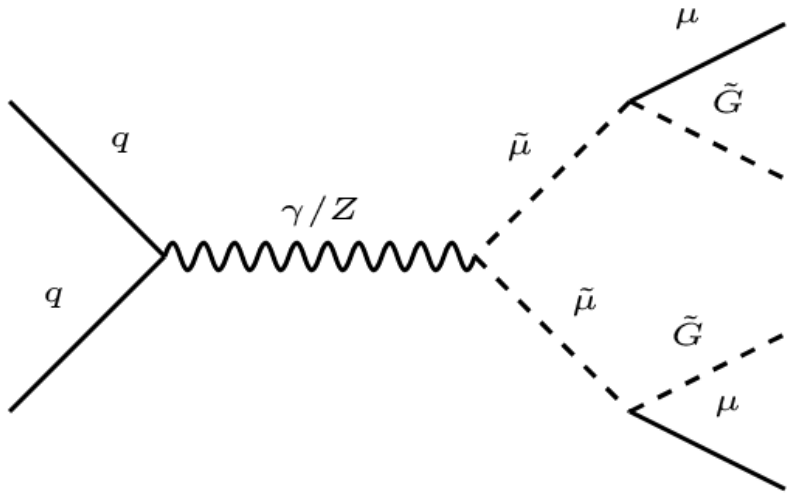

Figure 7.7: Illustration of the production process of a smuon pair at the (HL-)LHC via a photon or Z boson. The SUSY particles are shown as dashed lines. The smuon decays into a muon and a gravitino. Thus, the final state consists of two muons and two gravitinos.

Investigated parameter space The branching ratio of smuons decaying into muons is set to 100% by construction. A simplified mass hierarchy is assumed. Only the right-handed slepton sector is important for the detector signature. The right-handed stau and selectron masses are set to slightly higher masses than the corresponding smuon mass. For the simulation of the signal processes, smuon masses from 100 GeV to 1.5 TeV are considered. The lifetime varies from 1 mm to 1 m. Using Eq. 7.9, this translates into $\sqrt{F} \approx 10^2\ \mathrm{TeV} - 10^6\ \mathrm{TeV}$. This means that the gravitino mass is below 1 GeV for all simulated scenarios and far below the smuon mass hypotheses.

Tab. 7.2 summarizes the different smuon mass and lifetime hypotheses used in this study. For smuon masses of 100 GeV and 200 GeV, intermediate lifetime hypotheses are added. The

$M_{\tilde{\mu}}$ (GeV)	$c\tau_{\tilde{\mu}}$ (mm)	signal cross section (fb)
100	1,10,100,300,500,700,1000	221
200	1,10,100,300,500,700,1000	20.0
500	1,10,100,1000	0.445
1000	1,10,100,1000	0.0115
1500	1,10,100,1000	$4.63 \cdot 10^{-4}$

Table 7.2: List of smuon mass and lifetime hypotheses used in this study. The signal cross section of the smuon pair production via a photon or Z boson is shown at the HL-LHC with a center-of-mass energy of 14 TeV. The cross section values are obtained from the event generator MADGRAPH5 [159] at leading order. The uncertainty on the smuon production cross section is discussed in Sec. 7.3.7.

signal cross section of the smuon pair production at the HL-LHC is steeply falling with increasing smuon mass. This strongly limits the sensitivity towards higher masses. Fig. 7.8 presents the transverse impact parameter of the displaced muon tracks before reconstruction[10] for several lifetime hypotheses of smuons with $M_{\tilde{\mu}} = 500\ \mathrm{GeV}$. More kinematic dis-

[10]The transverse impact parameter on generator level is always defined with respect to the beam spot. Obviously, before reconstruction, there is no PV.

tributions are presented in Sec. A.6.

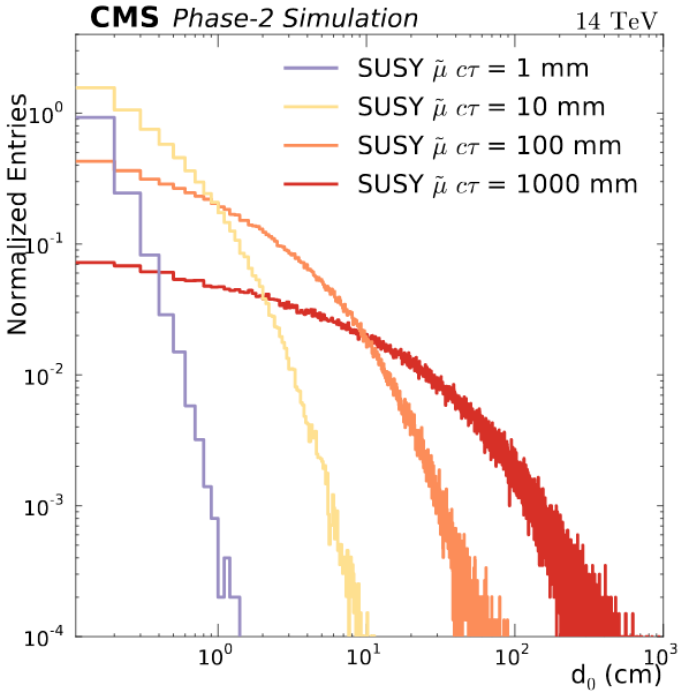

Figure 7.8: The transverse impact parameter, d_0, of the muons before reconstruction for several lifetime hypotheses, $c\tau$, of the smuon. The smuon mass is 500 GeV. Both axes are shown in a logarithmic scale.

7.3 Search for displaced muons

In the following, the search for displaced muons at the HL-LHC is described. The main topics are the triggering and reconstruction of displaced muons with the CMS Phase-2 detector. The simulation of the physics processes and the backgrounds are discussed. The event selection and the systematic uncertainties are described. The central theme of this analysis consists of the usage of special tools in the different parts, i.e. dedicated, non-prompt trigger and reconstruction, non-standard backgrounds, and event selection. This study serves as a motivation for future generations of physicists to look into displaced muon signatures at the HL-LHC.

7.3.1 Triggering on displaced muons

The general structure of the CMS Phase-1 trigger is described in Sec. 4.2.7. In Sec. 4.3.3, the main trigger upgrades, which are foreseen for Phase-2, are summarized. Level-1 trigger studies for displaced muons at the HL-LHC [114] are briefly discussed in the following[11]. The results of those studies are used as an input for this sensitivity study.

Level-1 muon trigger studies for Phase-2 A dedicated Level-1 (L1) trigger for displaced muons is implemented by using the direction information of combined hits from the DT stations in the barrel and from the CSC and GEM stations in the endcaps. The trigger algorithm

[11]HLT triggers for displaced muons are studied inside the CMS collaboration. However, public results are not yet available.

drops the beam spot constraint of the prompt muon trigger, but needs precise information of at least two muon stations to measure momentum. A veto of the tracks from the track trigger extrapolated to the second muon station is applied. This strategy allows to trigger efficiently on displaced muons with a transverse impact parameter of up to $d_{xy} \approx 100$ cm. Fig. 7.9 (a) shows the trigger efficiency of the displaced algorithm in the barrel region. The efficiency reaches a plateau at $p_T \geq 20$ GeV for the investigated ranges of muon displacement.

The trigger efficiency will benefit from the Phase-2 upgrades of the muon system in the forward region, which can be seen in Fig. 7.9 (b)[12]. The result illustrates the improvement in

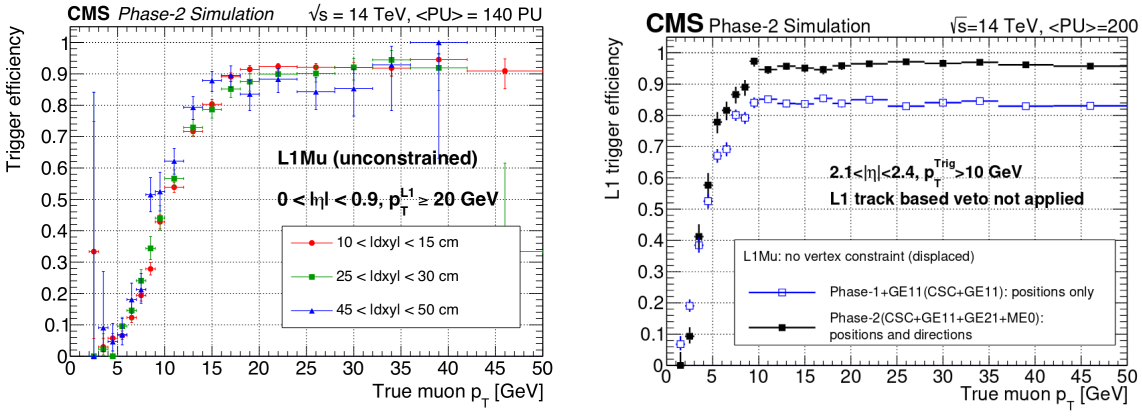

(a) (b)

Figure 7.9: (a) Level-1 trigger efficiency for the displaced muon trigger algorithm at the HL-LHC assuming transverse impact parameters between 10-15 cm (solid red circles), 25-30 cm (solid green squares), and 45-50 cm (solid blue triangles). (b) Level-1 trigger efficiency for the displaced muon trigger algorithm in the endcap region of the CMS detector. The blue points represent the efficiency using only CSC and GE1/1 position information, while the black points show the efficiency using GE1/1, GE2/1, and ME0 together with the CSC position and direction information. The figures are taken from Ref. [11].

trigger capabilities with the full Phase-2 forward muon system, i.e. combining information of GEM and CSC chambers in the first and second endcap station.

This sensitivity study requires at least two displaced muons in the final state. Thus, a displaced double-muon trigger could be used in principle. However, at the time of this study, such a dedicated trigger was not available or studied for the L1 trigger at the HL-LHC.

Another idea to improve trigger capabilities consists of using the information of the tracker at the HL-LHC. Unfortunately, the outer modules of the tracker cannot be used for displaced muon triggering because the foreseen Phase-2 track trigger requires an impact parameter below 1 cm.

7.3.2 Displaced muon reconstruction

An introduction to the standard muon reconstruction algorithms is given in Sec. 4.2.9. Here, those algorithms dedicated to the reconstruction of displaced muon tracks are discussed.

Displaced standalone muon reconstruction This analysis uses a dedicated reconstruction algorithm, which is designed for non-prompt muons leaving hits (only) in the muon system. Since it is solely relying on the information of the muon system, it is called displaced

[12] As opposed to the trigger efficiencies shown in Fig. 7.9 (a), the L1 track trigger veto is not applied here.

standalone (DSA) algorithm. The algorithm is seeded by groups of segments in the muon system. Segments are produced by matching hits in the subdetector system. The seeds used for the DSA algorithm are similar to those for cosmic muons, i.e. removing the constraint to the beam spot region, while not forcing the seed to point down as in cosmic reconstruction. Starting from the seeds, muon tracks are reconstructed with the Kalman-filter technique [107] similar to prompt muons. Compared with the standalone (SA) algorithm, the beam spot constraint is removed in the final fit.

Displaced muon reconstruction with tracker information Reconstructing displaced muon tracks with the tracker is generally possible[13]. This reconstruction procedure is seeded by the displaced standalone algorithm. By extrapolating the DSA track towards the tracker region, the algorithm looks for matching hits in the tracker layers going from the outer to the inner layers. The reconstructed tracks in the tracker can then be matched to the DSA track and, analogue to the prompt reconstruction, a displaced global muon can be reconstructed. The collection of displaced tracks contains the tracker information of the displaced global muons.

Reconstruction efficiencies of different algorithms The reconstruction efficiencies of the DSA, the displaced global, and standalone algorithms are compared, using a *muon gun*. The information on generator level consists of a displaced muon produced at a certain distance from the center of the detector. The muon gun produces displaced muons uniform in the transverse impact parameter d_{xy} for a given range. The information on generator level is processed by a full CMS Phase-2 detector simulation giving the reconstructed information. The displaced muons are generated with $p_T = 50$ GeV and within the geometrical acceptance of the redundant[14] muon system: $|\eta| \leq 2.4$.

The reconstruction efficiency is defined by

$$\epsilon_{reco} = \frac{\text{Nb. of reconstructed tracks with } \Delta R(\text{reco, gen}) \leq 0.1}{\text{Nb. of generated muons}}. \tag{7.10}$$

The numerator in Eq. 7.10 is increased by one, if there is a reconstructed track within a cone of $\Delta R \leq 0.1$ of the generated displaced muon. Fig. 7.10 depicts the reconstruction efficiency of the different algorithms as a function of the production radius of the generated muon. The efficiency of the displaced global muon algorithm falls off strongly for displaced muons produced outside the inner tracker layers. For a transverse production radius larger than 1 m, the muon is produced outside the tracker volume. Comparing the SA and DSA algorithms, a big difference for large production radii is observed. While the SA efficiency is falling, the DSA efficiency stays high up to a production radius of 4 m. For production radii larger than 4 m, the muon is not passing through the innermost muon chamber in the barrel, causing inefficiencies. Even for larger production radii, the DSA algorithm offers a 30% efficiency. The DSA efficiency drops to zero when the muon is produced outside the third muon station (6 m) and, thus, only traversing the outermost muon station. The DSA algorithm is not only more efficient for displaced muons; it also improves the transverse impact parameter and transverse momentum resolution for displaced muons [160].

Pointing and non-pointing displaced muons Different types of displaced muons can be identified. The LLP can decay into muons far away from the center of the detector and, nev-

[13]Clearly, only if the muons are created inside the tracker volume.

[14]Excluding the acceptance of the foreseen ME0 station, where the CMS Phase-2 muon system is not redundant.

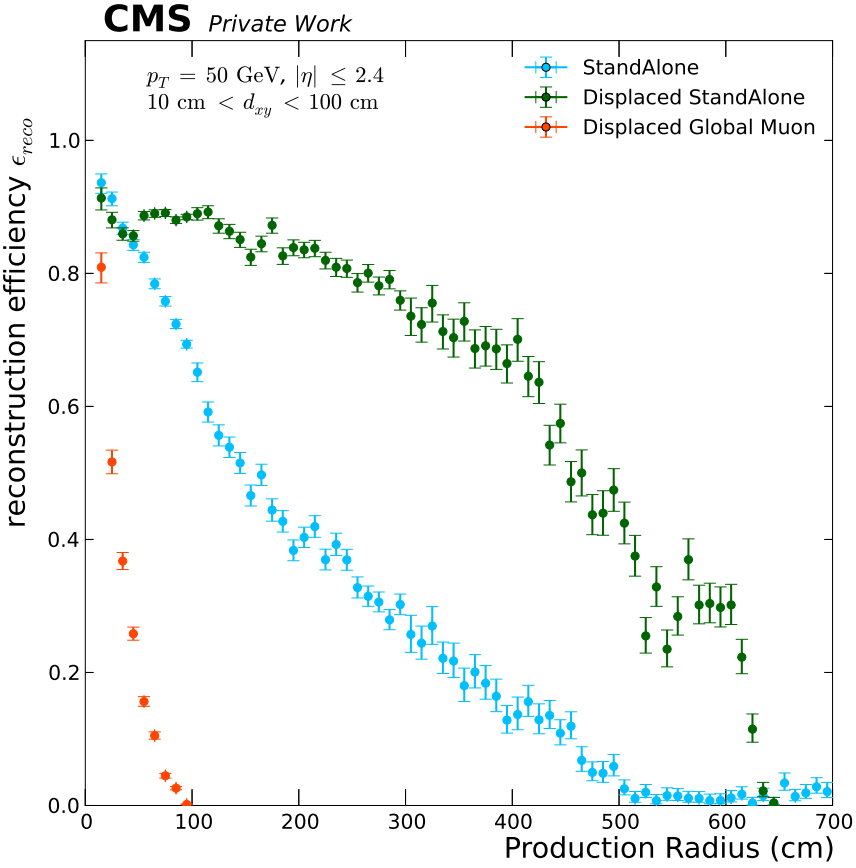

Figure 7.10: Reconstruction efficiency as a function of the production radius of the generated muon. The efficiencies are shown color-coded for the different algorithms. The transverse impact parameter d_{xy} of the generated muon varies uniformly between 10 cm and 1 m.

ertheless, with a boosted topology, the displaced muon can point back to the beam spot region (pointing muons). In this case, the SA algorithm should have compatible performance compared to the DSA algorithm. To check this assumption, the reconstruction efficiency of the algorithms is studied for different ranges in $|\eta|$. The outcome is presented in Fig. 7.11. With a higher pseudorapidity of the generated muon, the difference in reconstruction efficiencies of the DSA and SA algorithms for large production radii disappears. Having in mind that the muon is forced to have a large transverse impact parameter between 10 cm and 1 m, this phenomenon can be explained for large pseudorapidities by pointing muons. One should not conclude, that the DSA algorithm is completely useless in the forward region. The muon can have a low pseudorapidity while coming from the decay of a very forward LLP. This case contributes to Fig. 7.11(a), where the DSA algorithm performs a lot better than the SA algorithm.

Challenges with displaced track reconstruction The displaced global muon algorithm requires hits in at least 5 of the tracker layers. Thus, the track must go through one of the innermost tracker layers, which is not matching the typical signature of a signal in this study. When relaxing the requirement on the minimum number of tracker layers with hits, the algorithm is more sensitive to displaced signatures. This can be seen in Fig. 7.12, which presents a study on the displaced global muon algorithm. At the same time, the relaxation might introduce more fake candidates or increase the number of reconstructed tracks from backgrounds, e.g. cosmic ray muons. With further development, it might be possible to

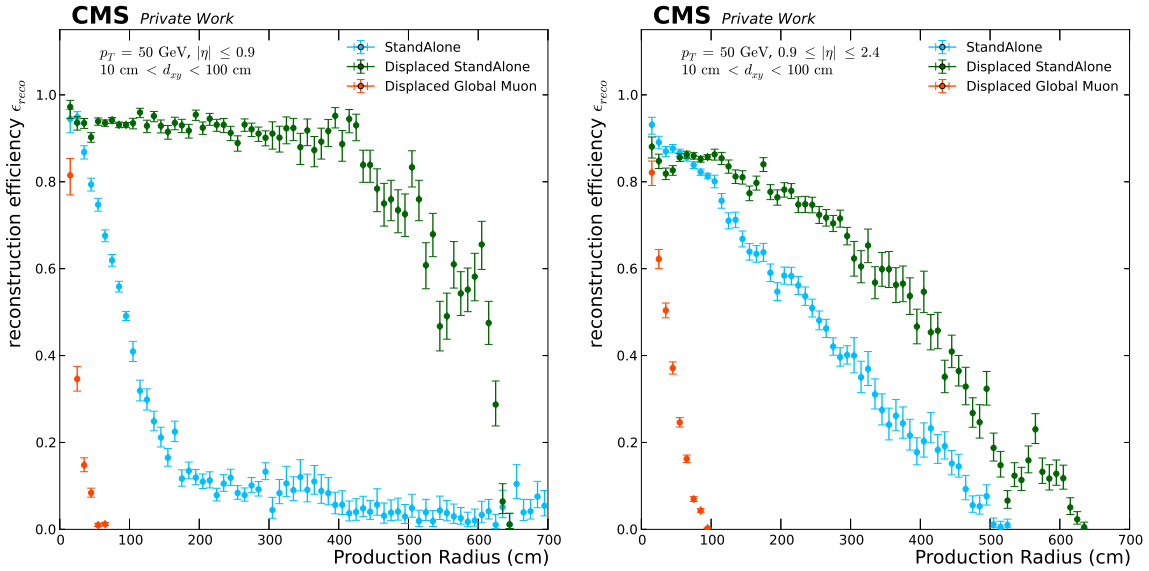

(a)

(b)

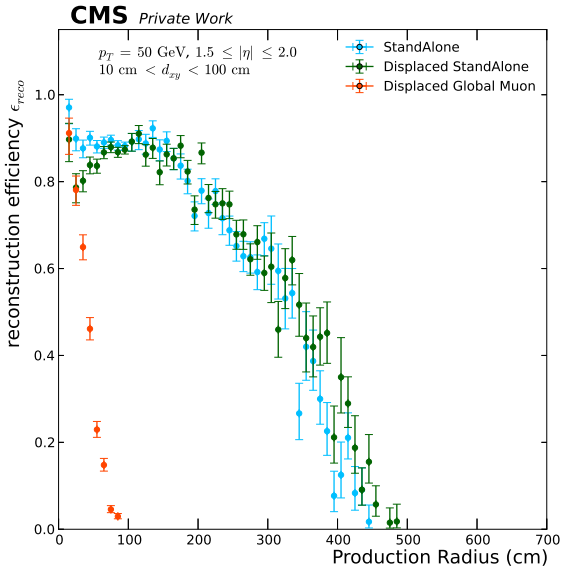

(c)

Figure 7.11: Reconstruction efficiency as a function of the production radius of the generated muon. Different ranges in pseudorapidity of the generated muon are shown: (a) $|\eta| \leq 0.9$, (b) $0.9 \leq |\eta| \leq 2.4$ and (c) $1.5 \leq |\eta| \leq 2.0$. More information can be found in the text and in the caption of Fig. 7.10.

efficiently reconstruct displaced tracks inside the tracker volume at the HL-LHC.

7.3.3 Backgrounds

The background processes of this sensitivity study are divided in two categories: the standard model processes and the non-standard backgrounds.

Standard model processes

- QCD multijet events are the dominant standard model background. In the decay of

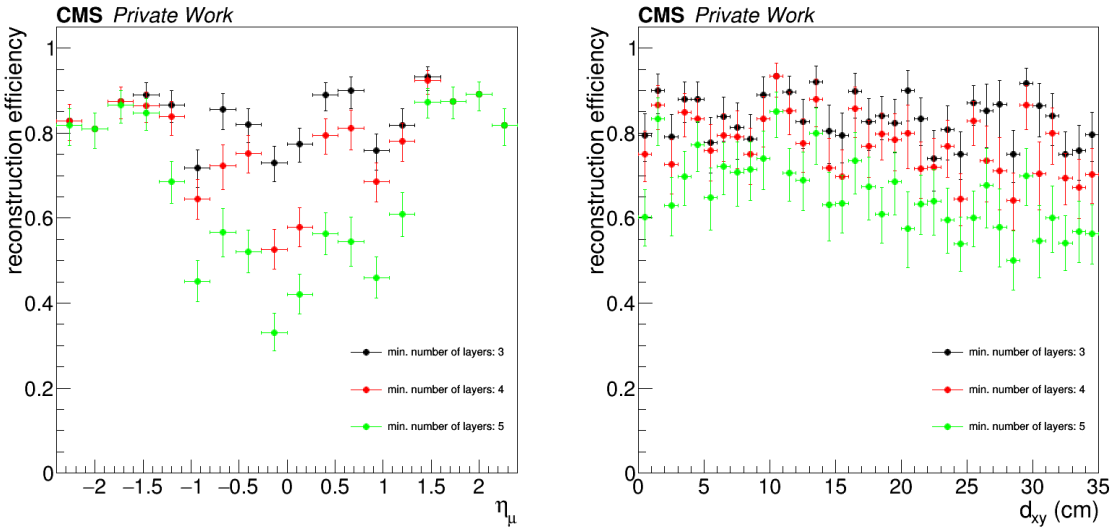

Figure 7.12: Reconstruction efficiency as a function of η (left) and d_0 (right) of the displaced global muon algorithm. The efficiency is shown for different cuts on the minimum number of tracker layers with hits. The nominal value in the displaced global muon reconstruction is 3. The study is performed with a displaced muon gun and a full simulation of the CMS Phase-2 detector. The displaced muons are produced uniformly in the transverse impact parameter from 0 cm to 35 cm. Information on the displaced muon gun is given in the text.

(heavy) quarks, displaced muons can be produced away from the primary interaction vertex. Neutrinos can be the source of missing transverse momentum.

- $t\bar{t}$ production can lead to displaced muons and neutrinos that contribute to missing transverse momentum.
- Drell-Yan (DY) processes denote the production of lepton pairs via a γ/Z resonance. Especially DY $\rightarrow \mu\mu$, can mimic the signal due to misidentifying prompt muons as displaced. The missing transverse momentum can be caused by instrumental effects.

Non-standard backgrounds

- Pileup interactions at the HL-LHC can lead to displaced muon signatures in the detector. Those muons typically have low momentum and are appearing in the forward region of the detector. The muons from pileup are rejected by the cut on p_T as explained in Sec. 7.3.5.
- Protons inside the bunches of the beam can interact with leftover molecules in the beam pipe (beam halo). This interaction near the CMS detector can produce muons which enter the underground CMS cavern and (more or less) horizontally traverse the detector. With their large displacement, these muons could be reconstructed as a displaced muon pair. The rate of beam halo muons scales with luminosity and, therefore, increases for the HL-LHC. However, these tracks have very low transverse momentum (see Fig. 14 (b) in Ref. [161]) and are rejected by the cut on p_T[15].

[15] A complementary or future treatment of beam halo muons at the HL-LHC could be the usage of a dedicated beam halo trigger based on the information of the electromagnetic and hadronic calorimeter and/or the forward muon chambers.

- Muons from cosmic rays traverse the CMS detector preferably from top to bottom and can be reconstructed as a pair of displaced muons. Sec. 7.3.5 introduces a cut on back-to-back kinematics of the muon pair. This cut suppresses the contribution of cosmic ray muons heavily. A suppression factor of 10^9 is calculated for a sample of cosmic ray muon events taken in 2017 with the active LHC clock while pp collisions were absent. As the rate of cosmic ray muons is independent of the collider conditions, this value is also valid for HL operation.

Fig. 7.13 presents an event display of a simulated $t\bar{t}$ event with high pileup. The event

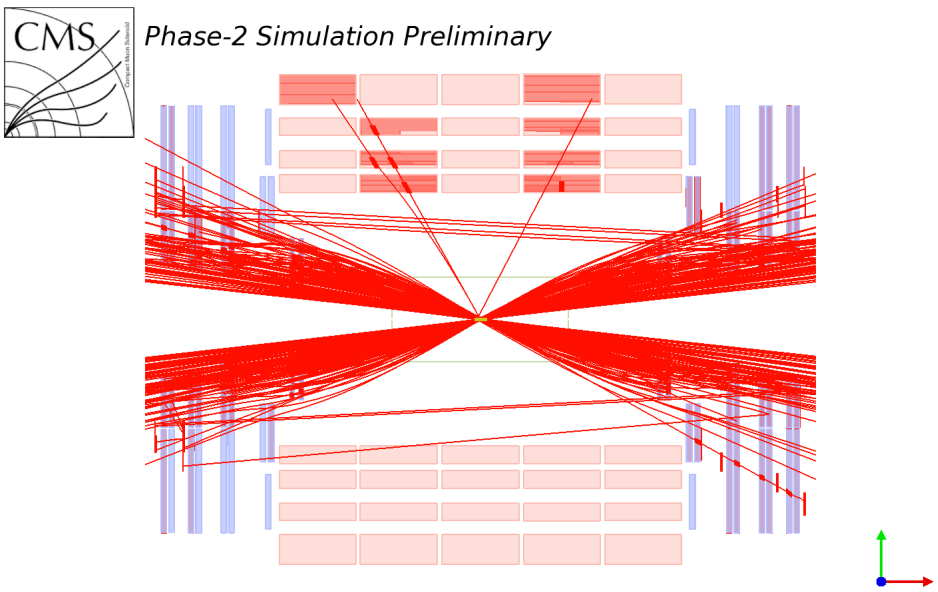

Figure 7.13: Event display of a simulated $t\bar{t}$ event with high pileup in the CMS Phase-2 detector. Reconstructed muons fulfilling $p_T > 1$ GeV are shown in this event display as solid red lines. The barrel and endcap muon chambers are highlighted in light red and light blue, respectively. The green rectangle indicates the region of the CMS tracker.

display contains all reconstructed muons with $p_T > 1$ GeV. Muons emerging from pileup are predominantly in the forward region of the detector. The horizontal lines, which do not come close to the center of the detector could be muons from beam halo.

7.3.4 Generators and event simulation

The event content for background and signal processes are based on Monte Carlo (MC) samples. The dark photon samples are generated with PYTHIA 8.212 [162, 163] and the smuon samples are produced with MADGRAPH5 [159], both at leading order. The QCD multijet background is also generated with PYTHIA 8.212 at leading order. The DY background is generated with MADGRAPH5_aMCNLO [164] and the $t\bar{t}$ background with POWHEG 2.0 [165–167], both with next-to-leading order cross sections. For the hadronization and parton showering step, PYTHIA 8.212 is used with the underlying event tune CUETP8M1 [168]. The generated events are processed through a full[16] simulation of the entire CMS Phase-2 detector based on GEANT4 [169]. The center of mass energy of $\sqrt{s} = 14$ GeV foreseen at the HL-LHC is used.

[16] As opposed to a faster simulation of a simplified detector or a parametrized simulation.

The average number of pileup interactions per bunch crossing is expected to be 200 for the HL-LHC. The simulations of physics samples include these inelastic pp interactions by overlaying additional simulated minimum bias events. The samples are labeled with PU200. Those samples without additional minimum bias events are called PU0. More details about the simulated background samples are given in the appendix (Tab. A.4).

7.3.5 Selection criteria

The offline event selection is guided by the idea of being as model-independent as possible.

Muon selection DSA muons are required to have $p_T \geq 15$ GeV and $|\eta| \leq 2.8$ to pass the selection criteria. The p_T cut value is motivated by the rejection of muons from pileup interaction. Fig. 7.14 (a) shows the transverse momentum of the reconstructed displaced muons for a specific mass and lifetime hypothesis of the dark photon. The figure compares the same physics sample, produced on the one hand with PU200 and on the other hand with PU0. The reconstructed displaced muons from pileup have $p_T < 15$ GeV. To select muon tracks with high quality, $\chi^2/ndof \leq 2$ is required. The track should have at least 17 associated muon hits for $|\eta| \leq 2.4$ and 6 associated hits in the region of the new ME0 station $2.4 \leq |\eta| \leq 2.8$. The DSA muon has to have a transverse impact parameter significance of $|d_0|/\sigma(d_0) \geq 5.0$. This cut helps to reject prompt muons. Fig. 7.14 (b) depicts the distribution of $|d_0|/\sigma(d_0)$ for the standard model backgrounds, as well as for two dark photon signal samples. Due to a large reduction of statistics in the simulated background samples, the cut

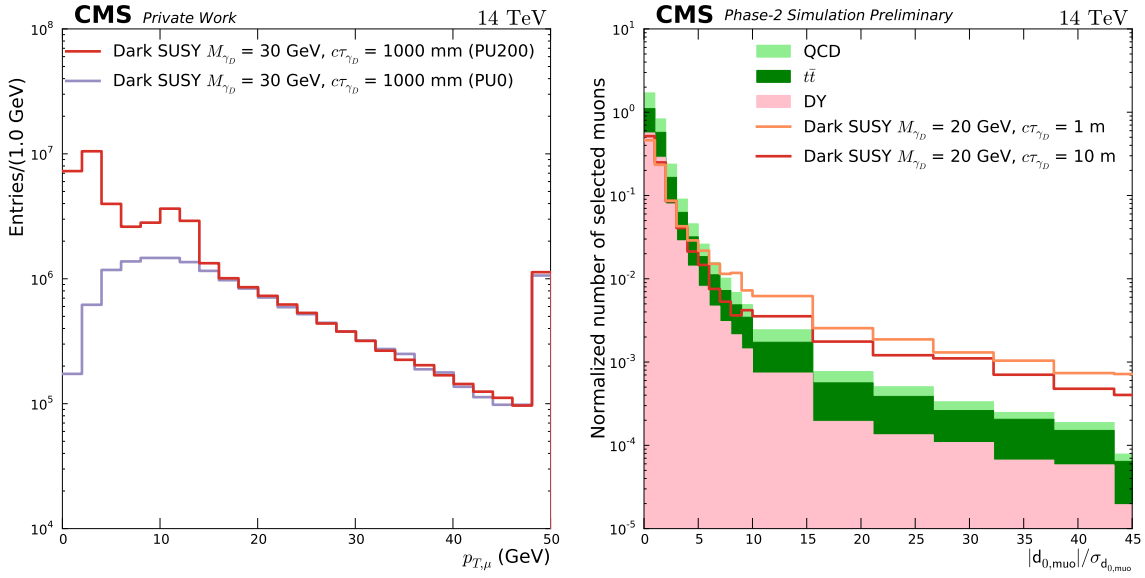

(a) (b)

Figure 7.14: (a) Transverse momentum of the reconstructed displaced muons ($p_{T,\mu}$) for a dark photon mass hypothesis of 30 GeV. The distribution is depicted for a sample with PU200 and for a sample with PU0 before the offline selection. The last bin is the overflow bin. (b) Normalized distribution of the transverse impact parameter significance $|d_0|/\sigma(d_0)$. The backgrounds are shown as a stacked histogram. The lines are indicating the distribution of the two dark photon samples. Those displaced standalone muons, which are passing the kinematic and track quality selection, are entering these histograms.

on $|d_0|/\sigma(d_0)$ is applied in a factorized way following the procedure presented in Ref. [170]. As a starting point, the distribution of the transverse impact parameter significance (Fig. 7.14

(b)) is considered. The fraction of muons passing the cut is calculated for the background and signal samples. The obtained value is used as a weight for each displaced muon in the final event selection. Exemplary, Tab. 7.3 contains some of the weights for signal and background samples.

Sample	GMSB SUSY				QCD	$t\bar{t}$	DY
	$M_{\tilde{\mu}}$=200 GeV		$M_{\tilde{\mu}}$=500 GeV				
	$c\tau = 100$ mm	$c\tau = 1000$ mm	$c\tau = 100$ mm	$c\tau = 1000$ mm			
Weight	7.72%	16.18%	9.03%	16.96%	1.59%	1.93%	1.62%

Table 7.3: Fraction of DSA tracks passing the impact parameter significance cut for a subset of the signal samples and the background samples. This fraction is used as a weighting factor for each displaced muon after full event selection. Tab. A.3 provides the weights for all simulated samples.

Event selection At least two DSA muons fulfilling the muon selection criteria are required in a selected event. If there are more than two DSA muons, the muons with the highest p_T are selected. For the highest-p_T muon in an event, $p_T \geq 20$ GeV is imposed to account for the single displaced muon trigger threshold (see Fig. 7.9). The two muons must have opposite charge ($q_{\mu,1} \cdot q_{\mu,2} = -1$) and must be separated by $\Delta R > 0.05$ in order to reject duplicated tracks. For the suppression of cosmic muon background, the three-dimensional angle between the two selected DSA muons should be less than $\pi - 0.05$ (not back-to back). From the studied BSM models, missing transverse momentum is expected to be part of the detector signature. Thus, $p_t^{\text{miss}} \geq 50$ GeV is imposed.

7.3.6 Search regions

In order to discriminate further the background from the signal, the impact parameters d_0 and d_z are used. The discriminating variable R_{Muon} is defined by

$$R_{\text{Muon}} = \sqrt{d_0^2 + d_z^2}. \tag{7.11}$$

The impact parameters d_0 and d_z are defined and illustrated in Sec. 7.1.2.

The search regions are defined using the event yield after full selection as a function of the distances $R_{\text{Muon-1}}$ and $R_{\text{Muon-2}}$. By definition, $R_{\text{Muon-1}}$ and $R_{\text{Muon-2}}$ are non-negative numbers, which limits the possible values to one quadrant of the two-dimensional space. The event yield can be calculated taking into account only those events where $R_{\text{Muon-1,Muon-2}} \geq R_{\text{low}}$. Increasing the lower limit R_{low} starting from 0 cm, rejects the SM backgrounds step-by-step. For large R_{low}, the signal is cut away. The value of R_{low} is determined by optimizing the sensitivity in terms of exclusion limits (see definition in Sec. 7.4). In Sec. A.7, the exclusion limit as a function of R_{low} is shown exemplary for one dark photon mass and lifetime hypothesis. The obtained search regions with the corresponding event yield for signal samples and background samples for an integrated luminosity of 3000 fb^{-1} are summarized in Tab. 7.4. The final value of R_{low} is dependent on the background, as well as on the corresponding signal process. The procedure, however, can be used independent of the BSM model.

7.3.7 Systematic uncertainties

For a sensitivity study at the HL-LHC, the evaluation of systematic uncertainties is a complicated topic. Many systematic uncertainties in current physics analyses are determined

Search Region	Event Yield								
		Signal					Background		
		m_{γ_D}[GeV]							
	$c\tau$[mm]	1	5	10	20	30	$t\bar{t}$	Drell-Yan	QCD
R_{low} =80 cm	10000	0.00 ± 0.00	0.18 ± 0.15	0.22 ± 0.20	8.9 ± 2.2	29.8 ± 4.8	0.95 ± 0.19	2.06 ± 0.47	3.76 ± 0.78
R_{low} =80 cm	5000	0.04 ± 0.03	0.83 ± 0.37	0.79 ± 0.56	35.3 ± 6.3	75.6 ± 10.4	0.95 ± 0.19	2.06 ± 0.47	3.76 ± 0.78
R_{low} =80 cm	1000	0.06 ± 0.03	2.53 ± 0.89	12.8 ± 3.7	87.0 ± 13.3	132 ± 16	0.95 ± 0.19	2.06 ± 0.47	3.76 ± 0.78
R_{low} =10 cm	100	0.96 ± 0.14	5.6 ± 0.7	11.7 ± 1.7	16.7 ± 2.4	12.9 ± 1.7	31.7 ± 1.2	215 ± 5	174 ± 5
R_{low} =1 cm	10	4.02 ± 0.25	13.6 ± 0.8	10.5 ± 0.5	13.7 ± 0.8	9.3 ± 0.6	1020 ± 6	13320 ± 30	1150 ± 10

Table 7.4: Search regions with the signal and background event yields and statistical uncertainties after the full event selection for an integrated luminosity of 3000 fb^{-1}. For each search region, the corresponding R_{low} is given in the first column. The corresponding signal efficiencies of the dark photon mass hypotheses can be found in Sec. A.7. Only a subset of the available dark photon mass points is listed here.

using real data. This study tries to identify the dominant systematic uncertainties and estimates their magnitude based on current studies and projections for Phase-2. There are two scenarios defined, following the definitions in Ref. [171].

The first scenario called *current systematics* assumes the uncertainties of the Run-2 data taking in 2016. For the cross sections, a default uncertainty of 5% is used. A 10% systematic uncertainty is assumed for the Higgs production cross section via gluon-gluon fusion [152]. For the smuon pair production, a 6% uncertainty is taken into account following the recommendations of the LHC SUSY Cross Section Working Group for 13 TeV (see e.g. Ref. [172–174]). For the $t\bar{t}$ cross section, 15% is applied. This is comparable to the systematic uncertainty applied for Run-2 searches [175, 176]. The other uncertainties are taken from Ref. [177].

The second scenario is called *expected systematics* or *S2+* scenario. Ref. [171] provides recipes how to treat different classes of uncertainties in order to estimate their magnitude at the HL-LHC. Floor values are assumed for the muon identification uncertainty (1%) and luminosity (1%). To determine the systematic uncertainty on the trigger efficiency, Fig. 7.9 is taken into account. The efficiency varies with respect to the transverse displacement. The uncertainty is set to 10% for the Phase-2 scenario. The cross section uncertainties are scaled down by a factor 2 compared to the *current systematics*.

Tab. 7.5 provides a summary of the systematic uncertainties and their values for the two scenarios.

Source	Current systematics	Expected systematics
Luminosity	6%	1%
Trigger efficiency	7.5%	10%
Identification	2%	1%
Cross section (QCD, Drell-Yan)	5%	2.5%
Cross section ($t\bar{t}$)	15%	7%
Smuon prod. cross section	6%	3%
Higgs prod. cross section	10%	5%

Table 7.5: Summary of systematic uncertainties. Two different scenarios (current/expected systematics) are used for the sensitivity study. The values are taken from different references, which can be found in the text. The 6% uncertainty for the luminosity in the *current systematics* scenario is taken from early Run-2 searches [177].

7.4 Statistical interpretation

Based on the event yield after full selection (Tab. 7.4) and the systematic uncertainties (Tab. 7.5), the results of this study are interpreted. The discovery sensitivity is determined and exclusion limits are set on the BSM models, introduced in Sec. 7.2.

7.4.1 Basics

Before discussing the results of the statistical interpretation, the basic concepts of discovery sensitivity and exclusion limit are defined. The introduction is based on Ref. [178]. The Higgs Combine tool [179], which is based on RooStats [180], is used to perform the statistical interpretation.

Exclusion limit In the context of this study, the purpose of limit setting is to exclude a region of the parameter space of BSM models by using the consistency between standard model background and the measured data[17]. This study uses the Bayesian approach, which is derived from Bayes' theorem. In Bayesian statistics, the probability, that A happens, can be reinterpreted as the degree of belief, that A is true. Thus, one can write

$$P(\text{theory}|\text{data}) \propto P(\text{data}|\text{theory}) \cdot P(\text{theory}). \tag{7.12}$$

$P(\text{theory})$ denotes the prior probability that the theory is true. $P(\text{data}|\text{theory})$ is called likelihood (L). The likelihood describes the probability to measure the data assuming the theory. $P(\text{theory}|\text{data})$ is called posterior probability and denotes the probability that the theory is correct looking at a given data set. The posterior probability allows setting exclusion limits on physical parameters, e.g. the production cross section of the signal process.

In the following, the terms *theory* and *data* are filled with physical quantities. The *theory* under investigation is represented by the signal event yield s. The *data* is expressed in terms of the number of observed events N_{obs}. Eq. (7.12) can be written as

$$P(s|N_{obs}) = \frac{L(N_{obs}|s) \cdot \pi(s)}{\int L(N_{obs}|s') \cdot \pi(s') \mathrm{d}s'}. \tag{7.13}$$

The denominator is used to normalize the probability density function. $\pi(s)$, denoting the prior probability of the theory, is defined and explained in the following. The prior probability can be written as

$$\pi(s) = \begin{cases} 0 & , s < 0 \\ 1 & , s \geq 0 \end{cases}. \tag{7.14}$$

This version is called a flat prior. The choice of a flat prior is rather arbitrary. In Bayesian statistics, there is no fundamental rule to assign a prior probability to a theory. Here, the choice is motivated by the following considerations. A priori, the number of signal events is expected to be $s \geq 0$ and every non-negative number of signal events should have the same probability due to a lack of further knowledge. The functional form of the likelihood distribution $L(N_{obs}|s)$ in Eq. 7.13 follows a Poisson distribution

$$L(N_{obs}|s) = \frac{(s+b)^{N_{obs}}}{N_{obs}!} \exp(-(s+b)), \tag{7.15}$$

[17] In our case, data is not available. In the end of this paragraph, the step from observed (with data) to expected (only simulated samples) limit setting is described.

where b denotes the expected number of background events. An integration over the probability in Eq. (7.13) is performed setting the integral value to 0.95. This results in

$$0.95 = \int_{-\infty}^{s_{up}} P(s|N_{obs}), \tag{7.16}$$

which determines s_{up}, the upper limit at 95% confidence level (CL). This value can be translated into an upper limit of a production cross section in the context of a signal model.

In the following, the treatment of (systematic) uncertainties in the limit setting is discussed. The statistical uncertainty is handled by the Poisson probability. The concept of nuisance parameters is used to model the systematic uncertainties listed in Tab. 7.5. The discussion is based on Ref. [181]. All systematic uncertainties are treated as multiplicative uncertainties. This means that the uncertainties are included by multiplying an additional prior probability for each nuisance parameter to the likelihood distribution in Eq. (7.15). The choice for the prior is a log-normal distribution

$$\pi_{\mu_\alpha,\sigma_\alpha}(x) = \frac{1}{x\sigma_\alpha\sqrt{2\pi}} \exp\left[-\frac{(\ln x - \mu_\alpha)^2}{2\sigma_\alpha}\right], \tag{7.17}$$

where μ_α denotes the mean value of the nuisance parameter α, and σ_α stands for the corresponding uncertainty. Exemplary, for the systematic uncertainty on the luminosity, one would obtain

$$\mu_{\alpha_L} \pm \sigma_{\alpha_L} = (3000 \pm 30)\ \mathrm{fb}^{-1} \tag{7.18}$$

in the *expected systematics* scenario[18]. The choice of a log-normal distribution is motivated by the fact, that the multiplicative nuisance parameters represent physical quantities with non-negative values. The logarithmic term in the exponent respects this physical constraint. Another property of the log-normal distribution, that justifies the choice, is, that a product of log-normal distributions is still a log-normal distribution. Additionally, the signal and background yields are scaled by the mean value of the nuisance parameter μ_α. Including the systematic uncertainties, the likelihood distribution in Eq. (7.15) is replaced by

$$L(N_{obs}|s,\alpha) = \frac{(s(\mu_\alpha) + b(\mu_\alpha))^{N_{obs}}}{N_{obs}!} \exp(-(s(\mu_\alpha) + b(\mu_\alpha))) \cdot \pi_{\mu_\alpha,\sigma_\alpha}. \tag{7.19}$$

Consequently, also the posterior probability in Eq. 7.13 depends on α. This dependence on the nuisance parameters is eliminated by integration

$$P(s|N_{obs}) = \int P(s,\alpha|N_{obs})\mathrm{d}\alpha. \tag{7.20}$$

In general, the integral in Eq. 7.20 is analytically not solvable due to its high number of dimensions (= number of systematic uncertainties). Therefore, a numerical approach is applied using the Markov Chain Monte Carlo (MCMC) method [182].

For the expected limit setting, which is calculated for this HL-LHC sensitivity study, the number of observed events N_{obs} is replaced by a random number following the background estimate from MC samples. The limit setting is performed several times so that a median expected limit can be determined and the corresponding one (68%) and two (95%) sigma bands can be calculated.

[18] In this example, μ_α is equal to the luminosity value used to calculate the signal and background yield. In general and for other nuisance parameters, these values can differ.

Discovery sensitivity To determine the discovery potential of a given signal assumption, the profile likelihood ratio is used. The starting point is the likelihood function L. The expected profile likelihood ratio is

$$\lambda(\mu) = \frac{L(\text{exp.}|\mu = 0, \alpha_0)}{L(\text{exp.}|\mu = \hat{\mu}, \hat{\alpha})}. \tag{7.21}$$

The nominator evaluates the likelihood function for the background-only hypothesis ($\mu = 0$). α_0 denotes the nuisance parameters under the background-only hypothesis. The denominator describes the same likelihood function evaluated for the signal hypothesis ($\mu = \hat{\mu}$) and the corresponding nuisance parameters ($\hat{\alpha}$)[19]. It is now convenient to define

$$q_\mu = -2 \cdot \ln \lambda(\mu). \tag{7.22}$$

If $\lambda(\mu)$ has a Gaussian form, q_μ can be expressed by a sum of non-negative components. If the expected event yield is in good agreement with the signal strength, the likelihood ratio is $\lambda(\mu) \approx 1$, which means that q_μ is close to zero. From simulation, the expected likelihood ratio, q_{exp}, is determined based on the expected signal and background estimation. The level of agreement between expectation and hypothesized μ can be expressed by the p-value

$$p = \int_{q_{exp}}^{\infty} f(q_\mu|\mu)\mathrm{d}q_\mu. \tag{7.23}$$

The unknown component is the sampling distribution $f(q_\mu|\mu)$. Wilks' theorem states, that the probability density function (PDF) of the test statistic q_μ approaches a χ^2-PDF for a large number of degrees of freedom in the tested theory [183]. In a final step, the significance Z is defined by

$$p = \int_Z^{\infty} \frac{1}{\sqrt{2\pi}} e^{-x^2/2}\mathrm{d}x = 1 - \Phi(Z), \tag{7.24}$$

where Φ is the cumulative distribution of the standard Gaussian. To claim a discovery, the background-only hypothesis ($\mu = 0$) needs to be rejected. This corresponds to a significance of $Z \geq 5$ or a p-value below $2.87 \cdot 10^{-7}$. An evidence is found if $3 \leq Z \leq 5$.

7.4.2 Results

In the following, the results of the sensitivity study are presented. To identify the dependence on the various parameters, e.g. luminosity, trigger, and reconstruction technique, three scenarios are defined.

- *Phase-2* scenario:
  - Integrated luminosity: $3000\ \text{fb}^{-1}$
  - Pileup scenario: PU 200
  - Higher-efficiency trigger benchmark scenario (90%)
  - Reconstruction: Dedicated displaced standalone (DSA) algorithm
  - Systematic uncertainties: *expected systematics* scenario (see definition in Tab. 7.5)
- *Phase-2 standalone* scenario:

[19] The treatment of the nuisance parameters is performed analogue to the limit setting, which is described above.

- The same assumptions are made as in the *Phase-2* scenario, except for the usage of the reconstruction algorithm: The SA reconstruction efficiency is assumed to be ≈1/3 of the dedicated DSA reconstruction efficiency (see discussion in Sec. 7.3.2).

- *Phase-1* scenario:
  - Integrated luminosity: $300\ \mathrm{fb}^{-1}$
  - Pileup scenario: PU 200
  - Lower-efficiency trigger benchmark scenario: A potential decrease in trigger performance might occur over the course of Run-3 due to aging and increasing PU. Thus, an overall 60% trigger efficiency is assumed in this scenario.
  - Reconstruction: Dedicated displaced standalone (DSA) algorithm
  - Systematic uncertainties: *current systematics* scenario (see definition in Tab. 7.5)

For all scenarios, exclusion limits and discovery sensitivities are calculated assuming either the dark photon (Sec. 7.2.2) or the smuon (Sec. 7.2.3) interpretation.

Dark photon interpretation The results of the limit setting for the dark photon interpretation are depicted in Fig. 7.15. Fig. 7.15 (a) presents the outcome for a dark photon with

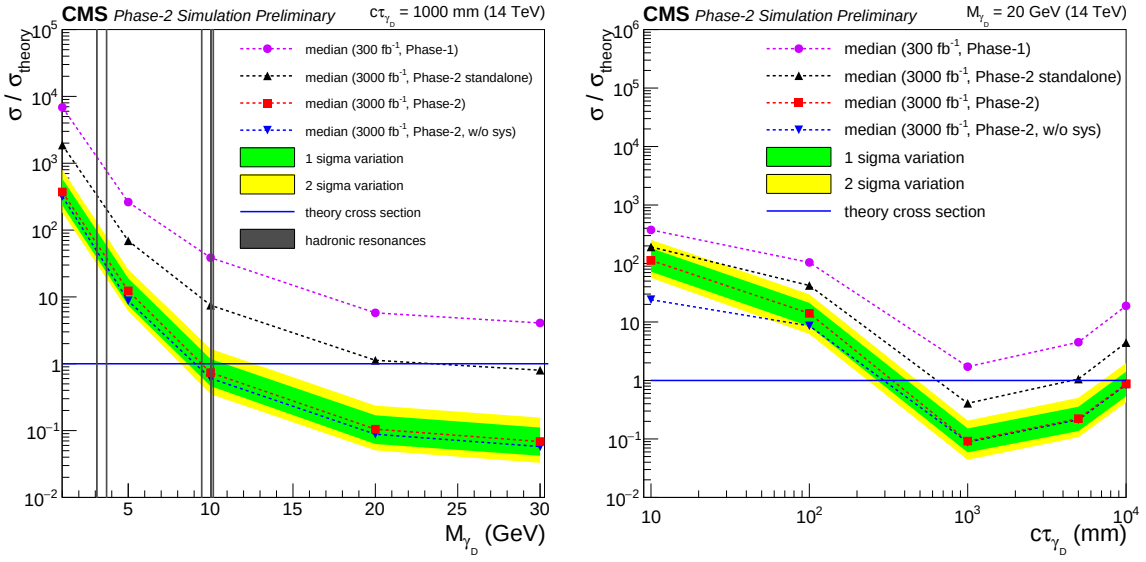

(a) (b)

Figure 7.15: 95% CL upper limits on production cross section σ/σ_{theory} for several dark photon mass hypotheses and a fixed lifetime of $c\tau = 1000\ \mathrm{mm}$ (a) and a fixed mass of $M_{\gamma_D} = 20\ \mathrm{GeV}$ as a function of the dark photon lifetime (b). The limits are shown as points in different marker styles for the different scenarios. Along with the scenarios defined in the text, another Phase-2 scenario, which neglects the systematic uncertainties, is displayed. For some points, the *Phase-2* scenario is on top of this scenario and, thus, not visible. For visualization purposes, the points are interconnected with a dashed line. 1σ and 2σ variations of the expected upper limit are represented by green and yellow bands, respectively. The regions of hadronic resonances are depicted in gray.

$c\tau = 1$ m as a function of the dark photon mass, while Fig. 7.15 (b) shows the result for a fixed mass of 20 GeV as a function of the lifetime. The Phase-2 DSA scenario offers the best sensitivity. For $c\tau = 1$ m, dark photon masses above $\approx 9\ \mathrm{GeV}$ can be excluded. In the Phase-2 SA scenario, masses above $\approx 20\ \mathrm{GeV}$ can be excluded. This illustrates the importance of the use of the dedicated displaced muon reconstruction algorithm. Neglecting

the systematic uncertainties does not affect the exclusion limit significantly in the Phase-2 DSA scenario. In the Phase-1 scenario, the study is not sensitive over the range of mass and lifetime hypotheses.

The exclusion range in terms of lifetime can be determined for all generated mass points. The same procedure can be done for the discovery potential, i.e. the range where the significance Z exceeds 5. Converting the $c\tau$'s to values of the kinetic mixing parameter ϵ (see Eq. 7.6), offers the possibility to show the search sensitivity in the $\epsilon - m_{\gamma_D}$ plane (Fig. 7.16). For $10^{-8} < \epsilon < 10^{-7}$ and $10 \leq m_{\gamma_D}/\mathrm{GeV} \leq 45$, the study predicts sensitivity. The exclu-

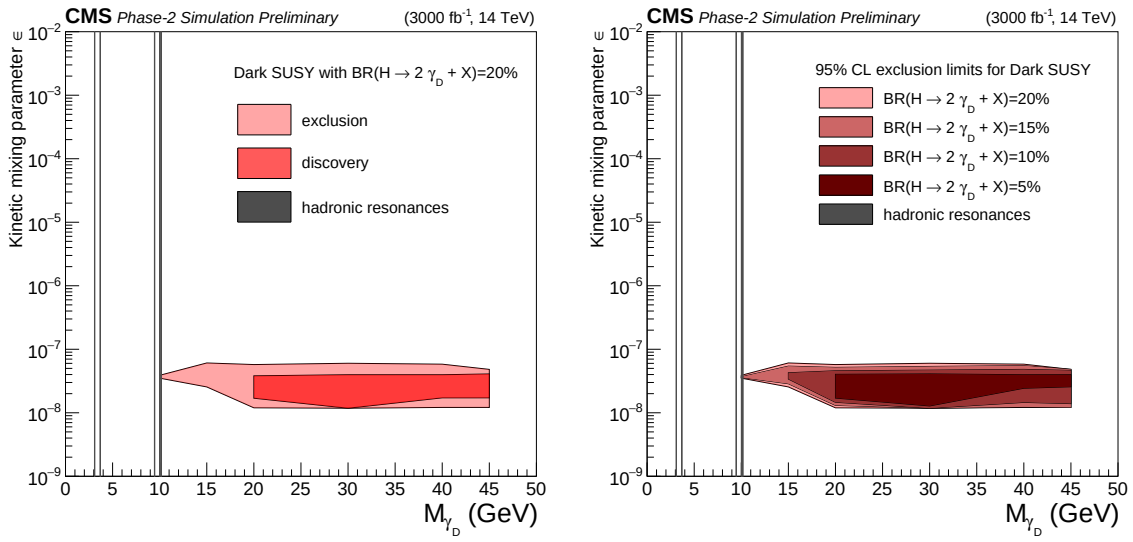

(a) (b)

Figure 7.16: Sensitivity of the displaced muon search for the dark photon interpretation in the $\epsilon - m_{\gamma_D}$ plane. (a) The light red area gives the parameter space, which is excluded at 95% CL. The dark red area defines the region, where the significance Z exceeds 5, corresponding to an expected discovery. In this figure, $BR(H \to 2\gamma_D + X) = 20\%$ is assumed. (b) Illustration of the excluded parameter space at 95% CL for different values of $BR(H \to 2\gamma_D + X)$ (shades of red). For both figures, the regions of hadronic resonances are shown in gray. These regions are excluded from the sensitivity study.

sion and discovery potential depend on $BR(H \to 2\gamma_D + X)$. The study is sensitive for 5% $\leq BR(H \to 2\gamma_D + X) \leq$ 20%.

In the following, the limiting factors in terms of sensitivity are discussed. For $\epsilon \geq 10^{-7}$, the standard model background is dominating. For $\epsilon \leq 10^{-8}$, a significant fraction of the dark photons are decaying outside the active volume of the detector, or the displacement of the muons is too large to be reconstructed efficiently. In the dark photon mass, the sensitivity is limited to $m_{\gamma_D} \leq 45$ GeV by simple kinematic considerations ($m_{n_1} = 50$ GeV and $m_H = 125$ GeV). For $m_{\gamma_D} < 10$ GeV, it becomes more likely that the muons from the dark photon decays do not pass the assumed displaced single-muon trigger threshold of 20 GeV. Consequently, for the left and upper border of the shaded areas in Fig. 7.16, there is room for improvement for a hypothetical Phase-2 search, while the right and lower border are more or less given by hard limits (model specifications and detector volume).

In case of the discovery of a dark photon at the HL-LHC, one might want to determine the hypothetical dark photon mass. The dark photon mass can be estimated by the invariant mass of the di-muon system

$$M_{inv} = \sqrt{(p_{\mu_1} + p_{\mu_2})^2}, \tag{7.25}$$

where p_{μ_1} and p_{μ_2} are the four-momenta of the selected displaced muon pair. The invariant mass is shown in Fig. 7.17 for dark photon mass hypotheses of 20 GeV and 30 GeV, as well as for the backgrounds. The distribution illustrates that one might be able to distin-

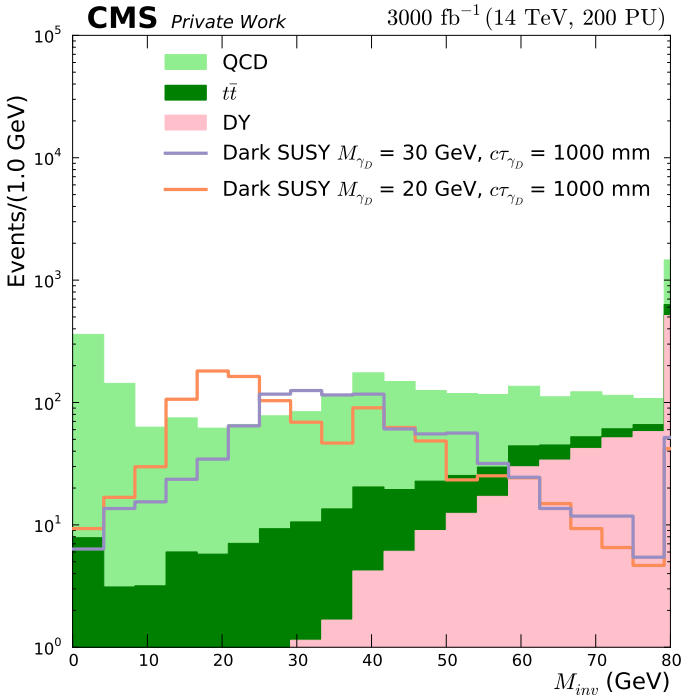

Figure 7.17: Invariant mass distribution for signal (colored lines) and background samples (staggered histograms) after the event selection. The invariant mass is calculated based on the momenta of the selected displaced muon pair. The momentum measurement is performed with the information of the muon system. The last bin is the overflow bin.

guish between a dark photon mass of 20 GeV and 30 GeV. One has to keep in mind, that the reconstruction of the displaced muons is solely based on the information of the muon system. The constraint to the primary interaction region cannot be used to improve the momentum measurement, as it is done for the prompt standalone muon reconstruction. The search strategy is not optimized for the reconstruction of the dark photon mass in order to follow the signature-driven approach.

Heavy smuon interpretation The outcome of the limit setting procedure for the smuon interpretation is depicted in Fig. 7.18. Fig. 7.18 (a) shows the results as a function of the smuon mass for a fixed lifetime of 1 m. The limits as a function of the smuon lifetime for a fixed mass of 200 GeV can be seen in Fig. 7.18 (b). For the Phase-2 DSA scenario, $M_{\tilde{\mu}} \lesssim 200$ GeV can be excluded. For the Phase-2 SA scenario, the study excludes $M_{\tilde{\mu}} \lesssim 150$ GeV. The Phase-1 scenario is not sensitive in the investigated range of mass hypotheses. For $M_{\tilde{\mu}} = 200$ GeV, smuons with a lifetime $c\tau \gtrsim 300$ mm can be excluded.

The discovery potential of smuons in the GMSB SUSY model is presented in Fig. 7.19. Fig. 7.19 (a) shows the p-value for a fixed smuon mass of 200 GeV as a function of the lifetime, while Fig. 7.19 (b) depicts the p-value for the investigated parameter space of lifetime and mass hypotheses. Similar as in the dark photon interpretation, the use of the dedicated displaced reconstruction algorithm increases significantly the sensitivity for a discovery. The Phase-1 scenario yields no sensitivity in the GMSB SUSY model. For $M_{\tilde{\mu}} \approx 100$ GeV and $100 < c\tau_{\tilde{\mu}}/\text{mm} < 1000$, the study finds sensitivity to the discovery of long-lived smuons at the HL-LHC.

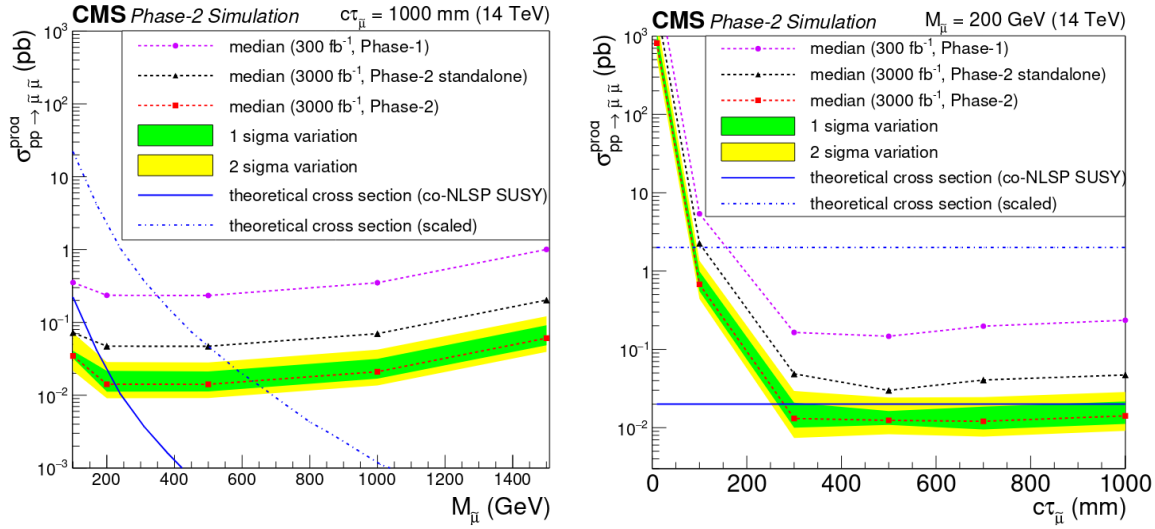

(a) (b)

Figure 7.18: 95% CL upper limits on the smuon production cross section $\sigma(q\bar{q} \to \tilde{\mu}\tilde{\mu})$ for $c\tau = 1$ m and different mass hypotheses (a) and for $M_{\tilde{\mu}} = 200$ GeV and various lifetime hypotheses (b). The style of the figure is similar to Fig. 7.15. Two cross section lines are shown in both figures. The solid blue line represents the cross section of the GMSB SUSY model, while the dashed blue line shows the same cross section scaled by a factor of 100. This reflects the sensitivity potential of this study for BSM models with larger production cross sections than the GMSB SUSY model and also predicting heavy LLPs decaying to muons.

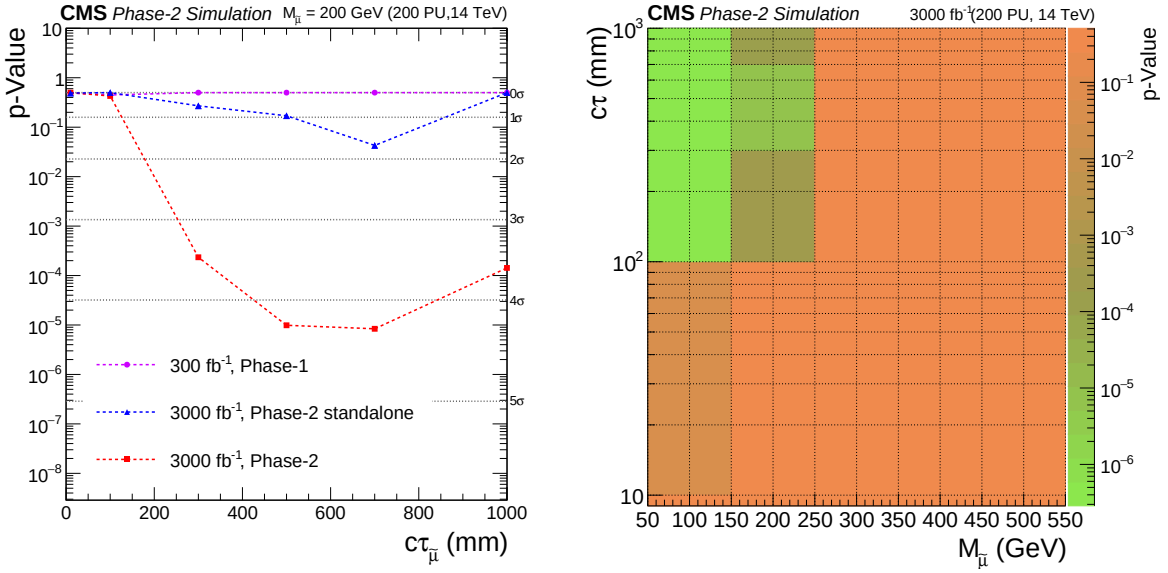

(a) (b)

Figure 7.19: (a) p-value as a function of the smuon lifetime for a fixed smuon mass hypothesis of $M_{\tilde{\mu}} = 200$ GeV. The different scenarios are color coded. Dashed gray lines can be seen, which show integer values of the significance Z. A significance of 3σ or 5σ corresponds to an evidence or discovery, respectively. (b) Discovery sensitivity in the parameter space of mass and lifetime hypotheses for the Phase-2 scenario assuming an integrated luminosity of 3000 fb^{-1}. The binning is chosen according to the available generated smuon samples (see Tab. 7.2).

A limiting factor, in terms of sensitivity, is the steeply falling cross section for larger smuon masses (see Tab. 7.2). Since the final state consists of high-p_T muons, the trigger threshold at 20 GeV or discriminating low-p_T muons in the event selection do not affect the sensitivity as much as in the dark photon interpretation.

7.4.3 Comparison with recent studies

The results obtained in this HL-LHC sensitivity study are compared to existing results of dark photon searches. The comparison is performed in the $\epsilon - m_{\gamma_D}$ plane. Fig. 7.20 (a) provides an overview of the existing results. As in Fig. 7.16, the closed areas represent the excluded parameter space of the different searches. Along with the searches at the LHC from CMS [14] and ATLAS [15] at $\sqrt{s} = 8(13)$ TeV, constraints from heavy-ion colliders (PHENIX [16]), cosmological observations [17], and low-energy electron-positron colliders (KLOE [18], BaBar [19]) are shown.

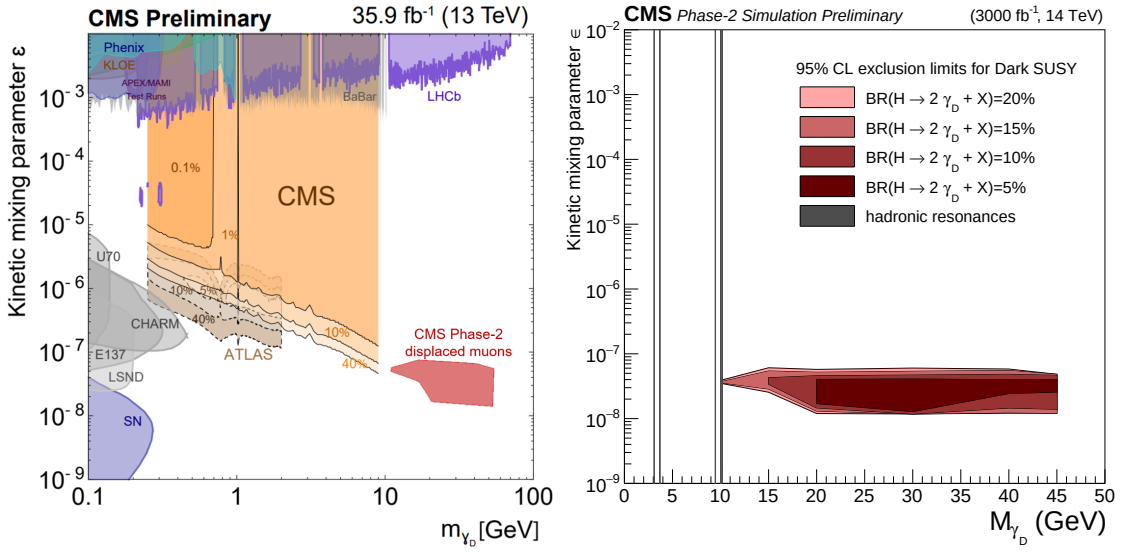

(a) (b)

Figure 7.20: Excluded parameter space in the $\epsilon - m_{\gamma_D}$ plane for dark photon searches. (a) Overview of existing results from various experiments. The references can be found in the text. For the CMS and ATLAS results, different values of $BR(H \to 2\gamma_D + X)$ are assumed. The figure is taken from Ref. [150] and adapted in such a way, that the parameter space, where this study is sensitive (CMS Phase-2 displaced muons), is added. (b) Results of this sensitivity study for Phase-2. $BR(H \to 2\gamma_D + X)$ is varied from 5% to 20%. This range is justified in Sec. 7.2.2. The resulting exclusion limits are shown in different shades of red. The vertical gray lines illustrate the regions of hadronic resonances, where this study does not claim any sensitivity.

One striking feature is the different shape of excluded parameter space between the recent CMS result and this CMS Phase-2 sensitivity study. At the same time, the shape of the excluded region from the ATLAS result is more similar. The main reason is the use of the dedicated displaced muon reconstruction algorithm instead of the standard reconstruction algorithms. By relaxing the constraint, that the muons come from the primary interaction region, the sensitivity to lower values of the kinetic mixing parameter ϵ and, hence, longer lifetimes of the dark photon is enhanced. Combining the two search strategies (prompt and displaced signatures) would lead to the best coverage of the parameter space.

7.5 Summary

The current searches for long-lived particles are in agreement with the standard model expectation. Despite huge efforts, a non-negligible amount of the possible phase-space for long-lived particles has not been explored yet. Long-lived particles can manifest themselves in various exotic signatures in particle detectors, such as the CMS detector at the LHC. At hadron colliders, LLP searches require dedicated triggering, reconstruction, and analysis techniques.

This study determined the sensitivity of a search for long-lived particles with a signature of two or more displaced muons at the HL-LHC. The results were interpreted for two BSM models. Expected exclusion limits, as well as discovery sensitivities, were determined. For the class of Dark SUSY models predicting long-lived dark photons, this study claims sensitivity to a phase-space not covered by recent studies. For the HL-LHC era, sensitivity to the discovery of dark photons with $10^{-8} < \epsilon < 10^{-7}$ and $10 \leq m_{\gamma_D}/\mathrm{GeV} \leq 45$ was shown. Higher values in ϵ and lower values in m_{γ_D} can be (co-)covered by searches looking for prompt signatures. The HL-LHC offers the opportunity for a discovery of long-lived smuons from GMSB SUSY models for mass hypotheses around $\mathcal{O}(100)$ GeV and lifetime hypotheses around $\mathcal{O}(100)$ mm.

The study is sensitive to both types of long-lived particles. The lighter dark photons manifest themselves in a more forward and boosted topology of the muons. The heavier smuons are produced via a photon or a Z boson, which leads to muons appearing preferably in the central region of the detector.

Different scenarios were defined in order to highlight the dependence of the search sensitivity on the integrated luminosity, as well as on trigger and reconstruction techniques. A key component of the study is the usage of the dedicated displaced reconstruction algorithm for muon tracks. The trigger and reconstruction performance of the CMS Phase-2 muon system is of utmost importance to exploit the full sensitivity potential.

8 Conclusion

The Large Hadron Collider together with its general multi-purpose detectors, such as the CMS experiment, drives the advance of insights in the field of high-energy physics. Despite record collision energies and integrated luminosities, as well as excellent detector performances, no significant signs of new physics beyond the standard model have been found at the LHC until 2020. To increase the sensitivity, the LHC will be upgraded. After its upgrade, the Phase-2 of the LHC will shape the future of high-energy particle physics for the next decade, or possibly beyond.

This work focused on the transition of the CMS experiment towards the HL-LHC concerning detector technologies and strategies for new physics searches. In the field of detector technologies, the existing detector will be complemented by a modern and novel gaseous detector technology: the gas electron multiplier (GEM). In the field of search strategies, displaced muons as exotic detector signatures were studied. The findings of this work in these fields are summarized below.

For the first time, large-area ($\mathcal{O}(1\ \mathrm{m}^2)$) GEM detectors have been mass-produced for the integration in the CMS experiment (GE1/1). The CMS GEM group was able to assemble, test, and qualify the needed 144 GEM detectors for the installation in 2019-2020. This marks a major milestone in the history of the CMS experiment, and for the detector upgrades towards Phase-2. This huge amount of work cannot be done by a few physicists, which is why the detector production was distributed among the institutes of the CMS GEM group. The quality control tests ensured - among others - gas tightness, HV integrity, and low detector noise. An important figure of merit for the performance of these GEM detectors is the response uniformity across the large detector area. The response uniformity was measured by illuminating the detector surface with X-rays and reading out the $\approx\ 3000$ channels of one detector in parallel. The results showed an acceptable, however, non-negligible level of gain variations. The reasons for the variations are assumed to come - at leading order - from the bending of the readout and drift board. To quantify these effects, additional studies, combining results from measurements and simulations, were described in this thesis. By varying the drift and induction field, mimicking the larger drift/induction gap, the influence on the gas gain in a GEM detector was determined. The results revealed that the dominating effect is the variation of the induction field. Furthermore, the influence of other design and environmental parameters was discussed. Large GEM detectors need large-size GEM foils. For the production of the foils for the GE1/1 chambers, the single-mask etching technique was used, as opposed to the double-mask technique. A higher effective gas gain was seen for the double-mask foils compared with single-mask foils both in measurements and simulations.

The sensitivity study, presented in this thesis, revealed great potential to search for the exotic signature of displaced muons using the CMS Phase-2 detector at the HL-LHC. The search strategy was constructed in a signature-driven and model-independent way. To illustrate the potential, two different BSM models predicting long-lived particles decaying to displaced muons were considered: heavy smuons from GMSB SUSY models and light dark photons from Dark SUSY. For the smuon interpretation, the study predicts sensitivity to discover a smuon with a mass hypothesis around 100 GeV and a lifetime hypothesis around 100 mm. For the Dark SUSY interpretation, the discovery of a hypothetical dark photon with $10^{-8} < \epsilon < 10^{-7}$ and $10 \leq m_{\gamma_D}/\mathrm{GeV} \leq 45$ is possible. ϵ denotes the kinetic mixing parameter, which quantifies the kinetic mixing between the standard model photon and the dark photon. The dark photon results were compared to recent searches at the LHC, as well as to the outcome of low-energy experiments. The comparison revealed a higher sensitiv-

ity to larger lifetimes, in particular, compared with previous CMS searches. Being sensitive to heavier and lighter long-lived particles, the search showed its model-independent predictive power. A strong impact of dedicated trigger and reconstruction techniques on the search sensitivity was observed.

Despite many challenges, the CMS GEM group was able to successfully mass-produce large-size GEM detectors for the application in high-energy physics for the first time in history. The GEM detectors have proven to be an excellent option for a new subsystem of the CMS Phase-2 detector. With the large amount of data at the HL-LHC, searches for rare, exotic signatures, such as displaced muons, are promising. Dedicated tools in physics searches for displaced muons will increase the sensitivity significantly. One can look forward to a bright future at CMS, the HL-LHC, and particle physics in general.

A Appendix

A.1 Details on GE1/1 quality control tests

X-ray gun from Amptek The X-ray gun used for the GE1/1 quality control tests was purchased from Amptek. The working principle of the X-ray gun relies on a tube, where a high voltage is applied between the cathode and anode. The cathode consists of a tungsten filament. The high voltage is accelerating the electrons towards the anode, which is a silver target. The interaction of the accelerated electrons with the anode material leads to the output spectrum of the X-ray gun, which is used to irradiate the GEM chambers during the GE1/1 QC procedure. Fig. A.1 shows the different output spectra for different voltage settings. The spectrum mainly consists of the characteristic K_α and K_β lines of silver at around

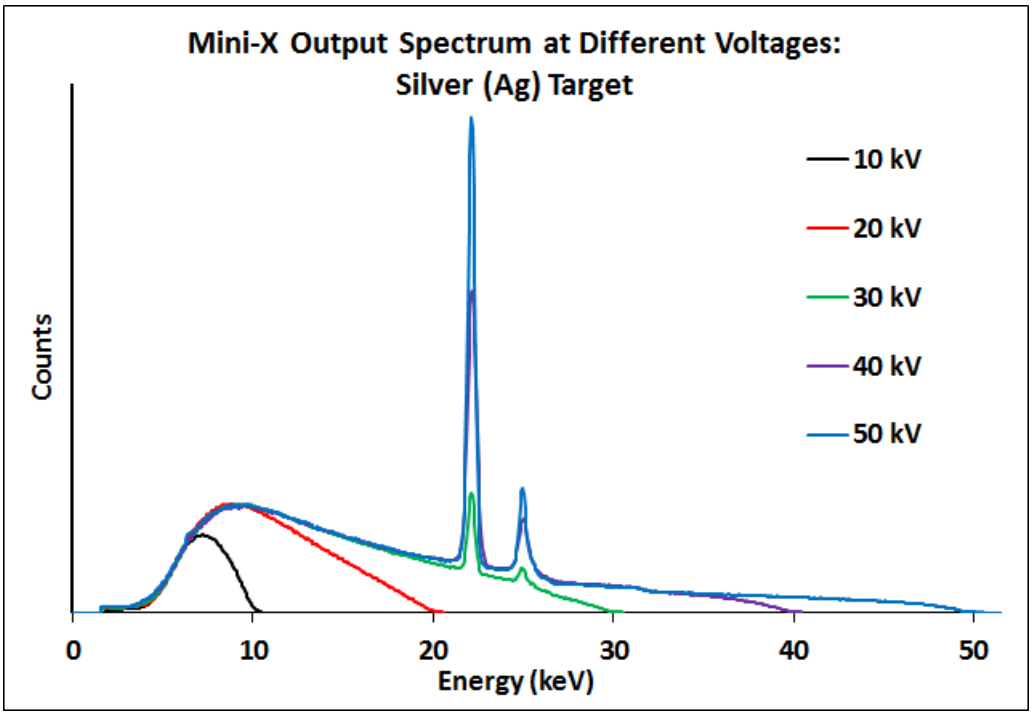

Figure A.1: Output spectra for various voltage settings of the X-ray gun. 40 kV is used for the GE1/1 QC procedure and the other gas gain measurements performed in Aachen. This figure is taken from Ref. [119].

23 keV. The underlying continuous spectrum comes from Bremsstrahlung effects. There are two main settings of the X-ray gun: the applied tube voltage and the tube current. The tube current is directly related to the emitted rate of photons. The current is limited by the power limit of the tube for a given tube voltage. Typical values of tube voltage and current for the gas gain measurements presented in Sec. 6.2 are 40 kV and 5 μA. 40 kV and 90 μA are used for the gain uniformity measurement of the QC procedure.

Gain uniformity and impact on performance To understand the impact of the gas gain non-uniformities across the detector surface for a GE1/1 chamber, the performance as a function of the gain is studied by varying the HV supplied to the electrodes of the detector. Fig. A.2 presents studies on the muon detection efficiency (left) and the time resolution (right) with a GE1/1 prototype detector. Fig. A.2 shows, that the performance in efficiency

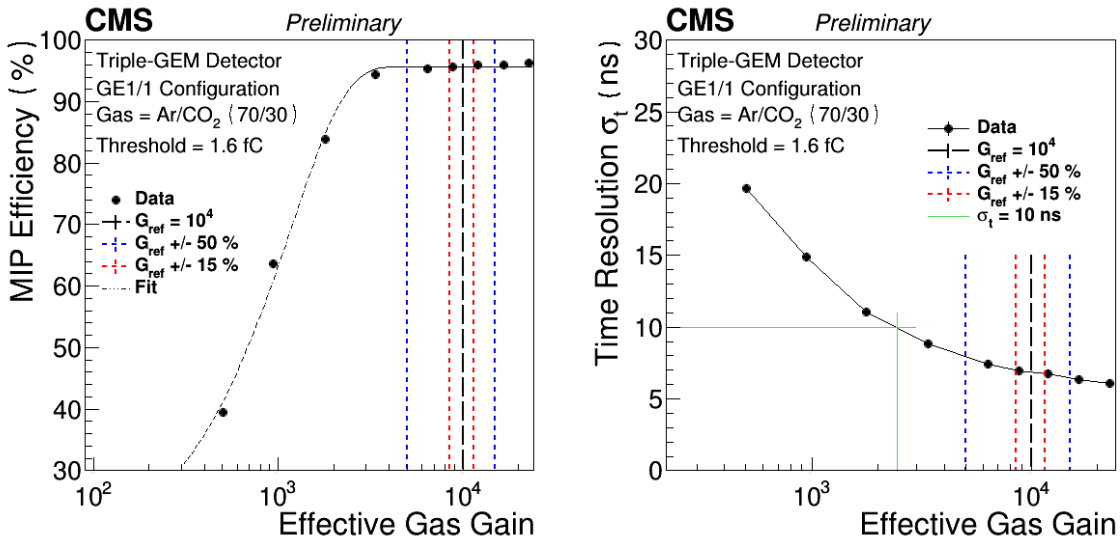

Figure A.2: MIP detection efficiency (left) and time resolution (right) of a triple-GEM detector prototype with the GE1/1 configuration. The data is depicted in black. The vertical dashed lines illustrate different gas gains of the detector. The GE1/1 GEM chambers are typically operated at a gas gain of around 10^4. To mark this working point, a black line is drawn. For the $\pm$15% and $\pm$50% variations of the effective gas gain, blue and red lines are shown. For the time resolution, the required value of 10 ns for CMS operation is illustrated by the green lines. The figures are taken from Ref. [184].

and time resolution is not deteriorated by gas gain variations of $\pm$50% across the surface of the GEM detector. This motivates the criterion for the QC5 gain uniformity test (Sec. 5.3.6). One has to keep in mind that the criterion relies on the standard deviation of the gain distribution across the detector surface. Thus, certain areas of the detector surface have even larger variations than 50% compared to the mean. This may have a significant impact, in particular, on the detection efficiency. QC8 is devoted to reveal possible efficiency drops.

A.2 Inventory of Aachen GEM laboratory

The Aachen QC setup is used for the GE1/1 quality control tests (Sec. 5.3.3) and for the gas gain measurements described in Sec. 6.2. This section provides additional information and pictures of the setup in Aachen. Fig. A.3 (a) shows the complete rack inside the laboratory. The gas distribution system can be seen in the upper part of the rack. Fig. A.3 (b) presents a detailed view of the lower part of the rack. The SRS system, the picoamperemeter (KEITHLEY 6487) and the NIM (Nuclear Instrumentation Standard) crate are depicted. The NIM crate is filled, among other things, with the HV power supply (ISEG NHQ 205M). The setup has been constructed for and has been approved within the GE1/1 quality control. The approval procedure includes testing the setup with a small GEM prototype, as well as with a large-size GE1/1 prototype. After the testing of the GE1/1 chambers, the setup has been updated. The gas system, consisting mainly of separate gas lines equipped with flowmeters, has been replaced by a more sophisticated system. This upgrade allows to set the ratio of a desired gas mixture manually instead of buying a premixed bottle. In addition, the single-channel HV modules are complemented by the possibility to power the 7 triple-GEM electrodes individually (CAEN SY 127). To control the new devices and to automatize the measurements, dedicated software packages have been written. Without these upgrades, a large fraction of the measurements described in Sec. 6.2 would have not been possible.

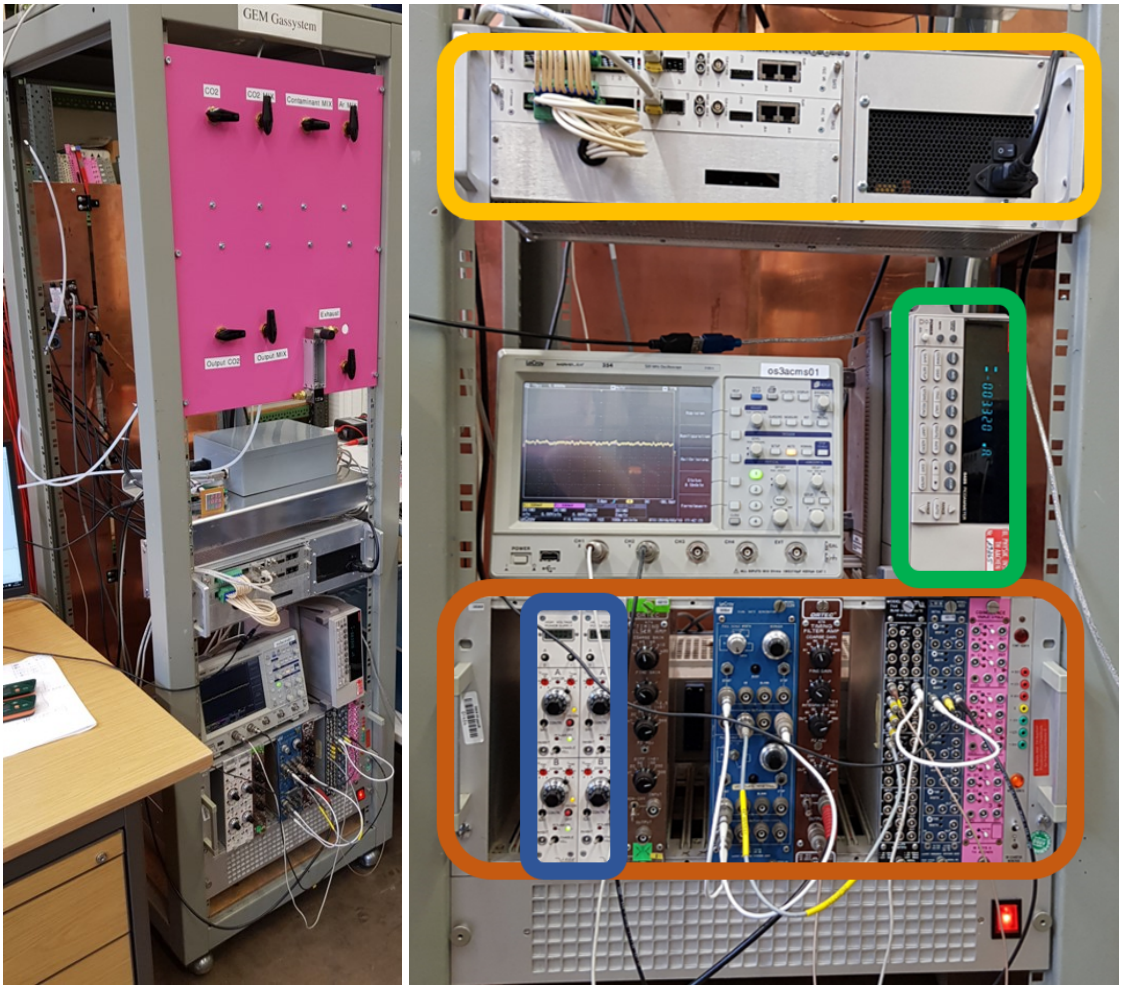

Figure A.3: (a) Picture of the rack inside the Aachen GEM laboratory. The rack houses e.g. the system for gas distribution, various sensors, and the SRS system. (b) The lower part of the rack accommodates the SRS system (yellow), the picoamperemeter (green), the single-channel HV supplies (blue) and the NIM crate (brown). The NIM crate contains the readout electronics for QC4 and QC5.

A.3 Measurements of GEM hole openings

The size of the hole openings of the GEM foils plays an important role when investigating the effective gas gain of a GEM detector. Therefore, measurements of the hole openings are performed with an optical microscope for the asymmetric double-mask and the single-mask foils purchased from TECHTRA. The optical microscope is located in a clean room. The 10×10 cm^2 GEM foils are put under the microscope and pictures are taken with a digital camera. The pictures of the camera are analyzed with a dedicated software tool, where the user can measure distances on the picture. Exemplary, Fig. A.4 presents captured pictures of the top and bottom of an asymmetric double-mask foil. The difference between small and large hole openings is clearly visible.

The outcome of the measurements of the large hole openings for different GEM foils is presented in Tab. A.1. The smaller openings are also measured. They are not listed in Tab. A.1 because a better uniformity is observed between the smaller openings of single-mask and double-mask foils. The variations of the larger openings could be a reason for the small difference in gas gain between the single-mask and the asymmetric double-mask foils

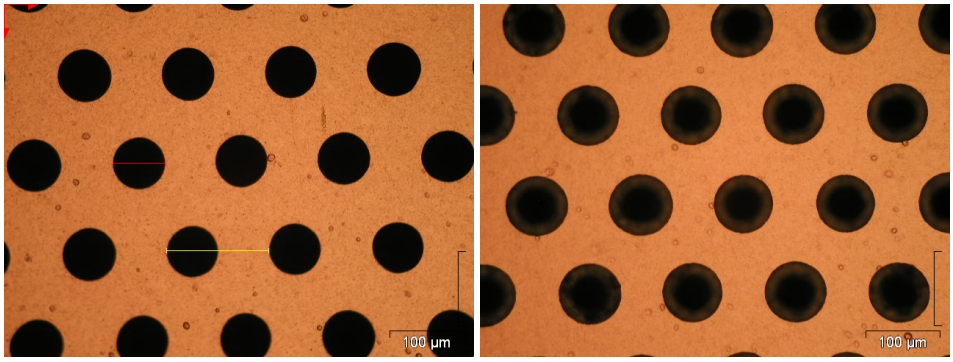

Figure A.4: Pictures of a GEM foil produced by TECHTRA. The pictures were taken with an optical microscope. Left: Top side of an asymmetric double-mask GEM foil with a nominal hole diameter of 70 μm. Right: Bottom side of an asymmetric double-mask GEM foil with a nominal hole diameter of 85 μm.

Foil number	Larger hole diameters	
	Single-mask	Double-mask (asym.)
1	83 μm	85 μm
2	83 μm	85 μm
3	80 μm	86 μm

Table A.1: Measurements of the large hole diameters for asymmetric double-mask and single-mask GEM foils produced by TECHTRA. The measurements are based on pictures taken with an optical microscope. Three foils of each type are available. The larger hole diameter measures nominally 85 μm.

(see Fig. 6.10).

A.4 Microscopic simulation step in Garfield++

The Garfield++ simulation of electron avalanches in gaseous detectors is based on the microscopic simulation step. Fig. A.5 illustrates what is happening for a time step Δt inside the active simulation volume. The time step Δt is randomly generated according the nuclear interaction rate of the electron with the gas atoms. The initial coordinates and momentum of the electron at the starting point are denoted x_0 and p_0. Based on the electric field at the starting point, the coordinates and momentum at the endpoint $t_1 = t_0 + \Delta t$ are determined. These are called x_1 and p_1. This approach neglects the variation of the electric field along the path traveled during one time step. With a typical mean time step of around 10 ps, one can estimate the typical distance step to be 5 nm, assuming a drift velocity of 5 cm/μs. The relative variations of the electric field on this distance scale inside a GEM hole are below 10^{-3}.

A.5 HV distributions in Garfield++ simulations

The HV distribution used for the triple-layer GEM simulations follows the nominal CMS configuration (Sec. 6.3.2). Tab. A.2 states explicitly the voltages given to the 7 electrodes present in the triple-layer GEM configuration. In Fig. 6.16 and Fig. 6.19, the x-axes are la-

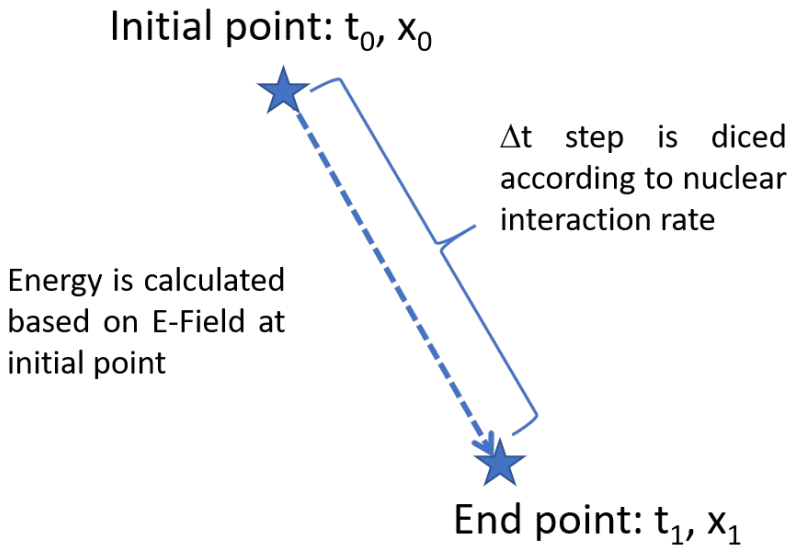

Figure A.5: Illustration of the microscopic simulation step in Garfield++. The start and end point are drawn as blue stars. The time step is illustrated by the blue arrow with a dashed line.

Gap	Resistance (kΩ) of GE1/1 HV divider	Fraction of V_{Drift}	$V_{Drift} = 2700$ V	$V_{Drift} = 2900$ V	$V_{Drift} = 3100$ V	$V_{Drift} = 3300$ V	$V_{Drift} = 3400$ V
Drift	1125	100	2700 V	2900 V	3100 V	3300 V	3400 V
GEM 1	563	75.9	2050.1 V	2202.0 V	2353.8 V	2505.7 V	2581.6 V
Transfer 1	438	64.1	1729.6 V	1857.7 V	1985.9 V	2113.9 V	2178.0 V
GEM 2	550	54.7	1476.4 V	1585.7 V	1695.1 V	1804.4 V	1859.1 V
Transfer 2	875	43.1	1164.2 V	1250.5 V	1336.7 V	1422.9 V	1466.1 V
GEM 3	525	24.4	658.0 V	706.7 V	755.5 V	804.2 V	828.6 V
Induction	625	13.4	362.9 V	389.8 V	416.6 V	443.5 V	456.9 V

Table A.2: Overview of the voltages used in the simulations of the triple-layer scenario. The voltages follow the HV distribution given by the ceramic divider used for the GE1/1 quality control, which is shown in Fig. 5.14.

beled V_{Drift}. This quantity is a placeholder for the values given in the corresponding column of Tab. A.2.

A.6 Kinematic distributions of simulated signal processes

GMSB SUSY kinematics For the GMSB SUSY processes, basic kinematic distributions before reconstruction (generator level) are illustrated in Fig. A.6. The distributions show the expected tendency of higher-p_T muons and higher missing transverse momentum for larger smuon masses. For a smuon mass of 1.5 TeV, high-p_T muons in the TeV range are likely to appear. The gravitino coming from the decay of the smuon is responsible for the p_T^{miss}. With larger smuon masses, the decay products (with fixed mass) obtain more kinetic energy. $\Delta R(\mu_1, \mu_2)$ is distributed around π, which is a back-to-back kinematic due to the large mass of the smuons. Due to the cosmic muon rejection cut, parts of the signal is suppressed.

Dark SUSY kinematics Additional information is given on the kinematic behavior of the dark photons and the resulting displaced muons. Fig. A.7 presents the distributions of ΔR between the two long-lived dark photons emerging from the cascade decay of the SM Higgs

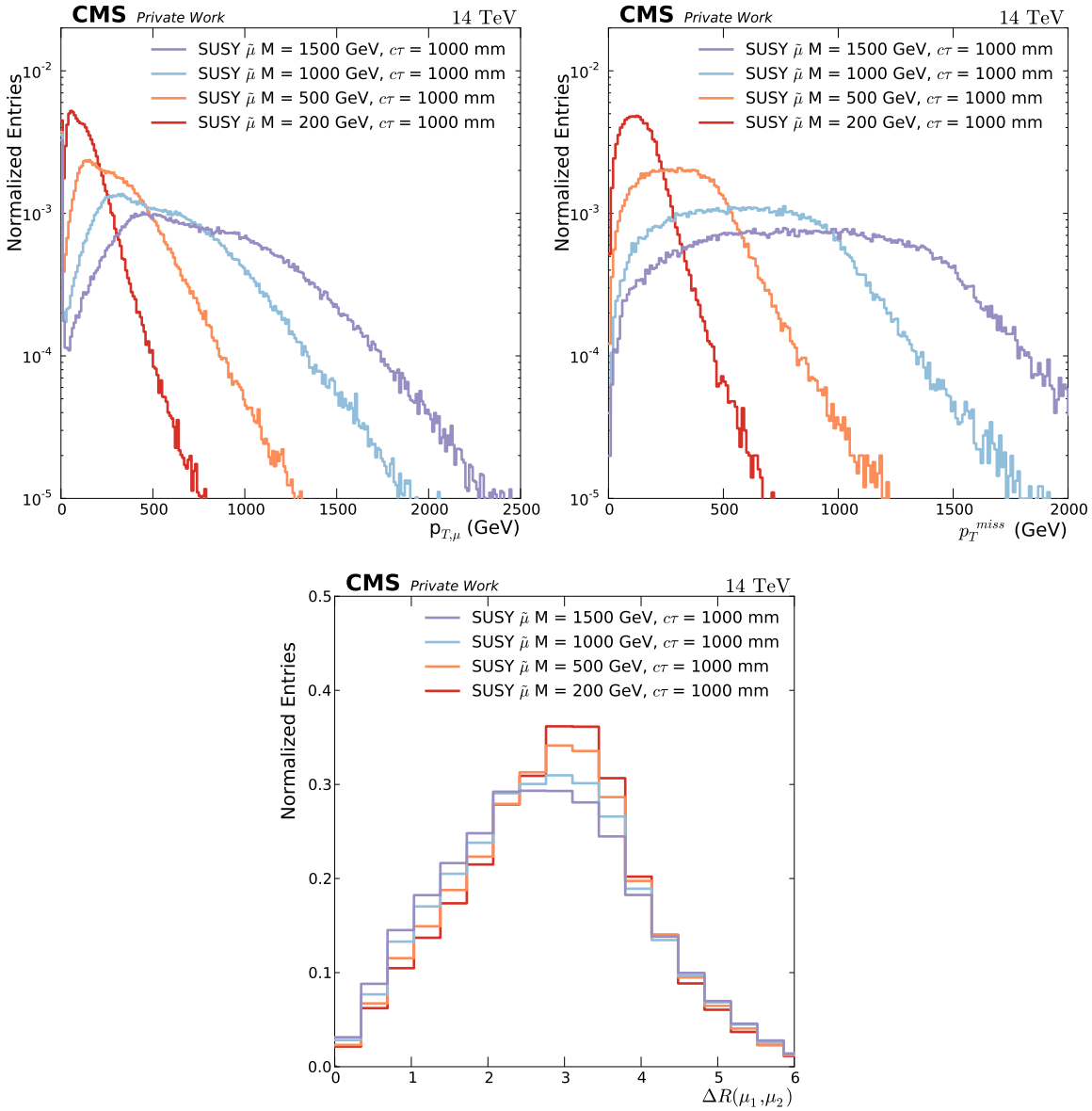

Figure A.6: Distributions of the transverse muon momentum $p_{T,\mu}$ (top left), the missing transverse momentum p_T^{miss} (top right), and $\Delta R(\mu_1, \mu_2) = \sqrt{(\Delta\phi)^2 + (\Delta\eta)^2}$ (bottom) before reconstruction. The distributions are presented for different smuon mass hypotheses between 200 GeV and 1.5 TeV.

boson (left) and the ΔR between the displaced muons coming from the decay of one of the long-lived dark photons (right). With a decreasing mass of the dark photon, the displaced muons are preferably close-by due to the boosted topology of the decay.

A.7 Determination of search regions and signal efficiencies

The search regions, defined in Sec. 7.3.6, have the purpose to further reduce the background contribution after the common event selection. The lower limit of a search region, called R_{low}, is obtained by scanning the exclusion limit. Exemplary, the scanning of the 95% CL upper limits on production cross section for a dark photon hypothesis can be seen in Fig. A.8.

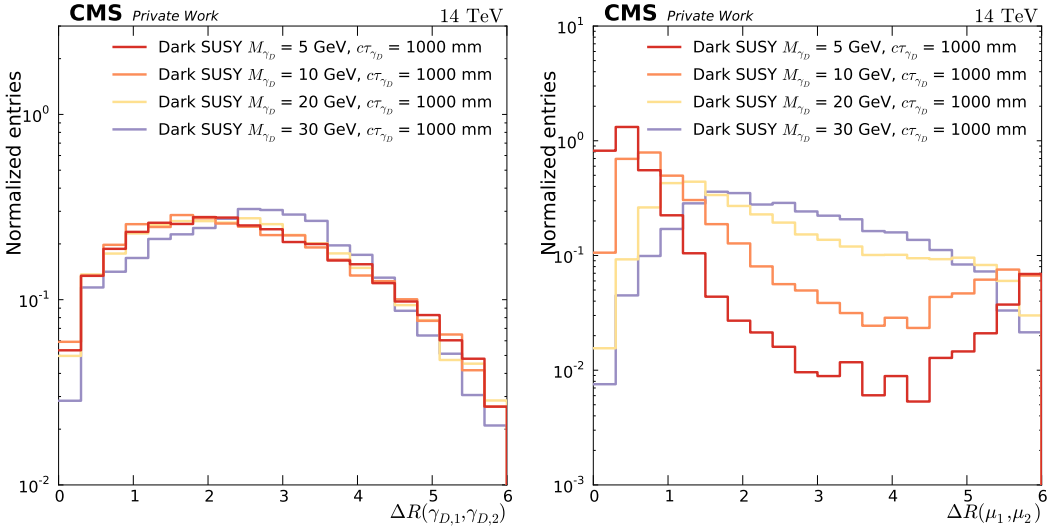

Figure A.7: Left: Distributions of ΔR between the two produced long-lived dark photons on generator level. Right: Distributions of ΔR between the displaced muons coming from the decay of one of the long-lived dark photons on generator level. The distributions are shown for various mass and lifetime hypotheses of the dark photon.

The obtained R_{low} is the one with the best exclusion limit. This procedure is performed for

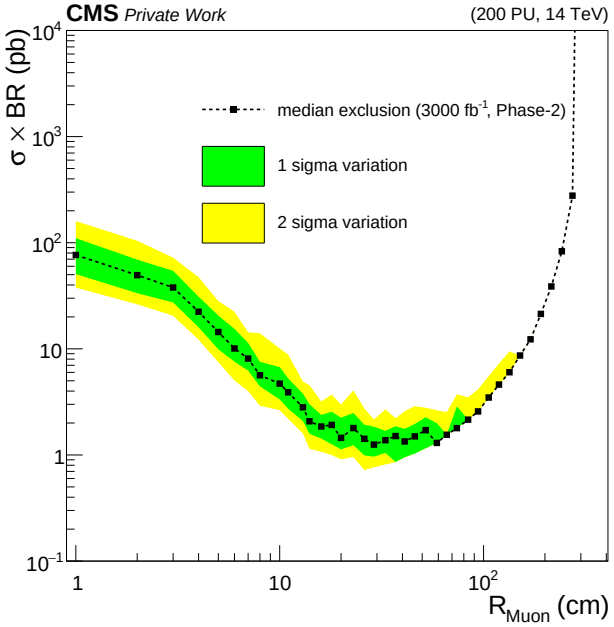

Figure A.8: Scanning of 95% CL upper limits on production cross section for a dark photon with $m_{\gamma_D} = 20$ GeV and $c\tau_{\gamma_D} = 1000$ mm.

the various mass and lifetime hypotheses.

The signal efficiencies of the dark photon hypotheses in the 2-muon and 4-muon final states are shown in Fig. A.9 and Fig. A.10, respectively. With an increasing dark photon mass, the signal efficiency rises due to the displaced muon trigger threshold at 20 GeV and the offline selection cut at 15 GeV for the second selected displaced muon in the final state. For all investigated dark photon mass hypotheses, the efficiency rises between $c\tau_{\gamma_D} = 100$ cm and $c\tau_{\gamma_D} = 1$ m. The cut on the significance of the transverse impact parame-

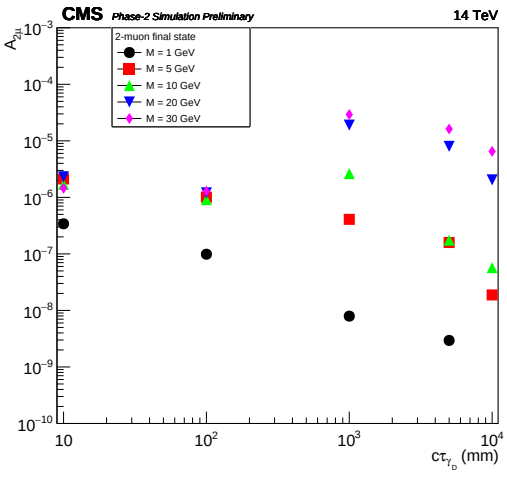

Figure A.9: Signal efficiency of the dark photon hypotheses in the 2-muon final state. The efficiencies are depicted as a function of the dark photon lifetime. The different mass hypotheses are color-coded.

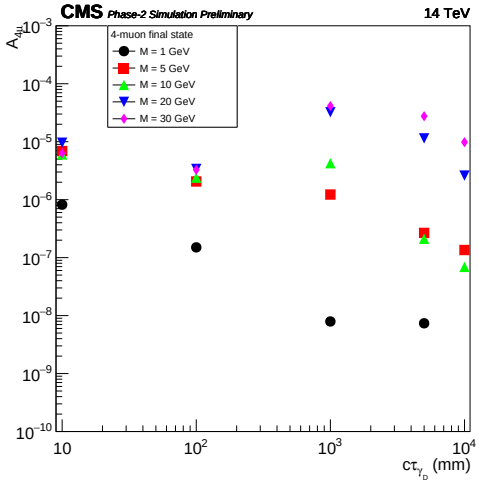

Figure A.10: Signal efficiency of the dark photon hypotheses in the 4-muon final state. The efficiencies are depicted as a function of the dark photon lifetime. The different mass hypotheses are color-coded.

ter inside the muon object selection plays the dominant role. For higher lifetimes, it becomes more difficult to reconstruct those muons producing hits only in the outer layers of the CMS muon system. Thus, a lower signal efficiency is obtained.

A.8 List of event samples for sensitivity study

The sensitivity study presented in Sec. 7 relies on physics samples obtained with the full simulation of the CMS Phase-2 detector. Tab. A.3 lists all samples that are used in the analysis together with the corresponding efficiency of the transverse impact parameter significance cut. Detailed information on the background samples is given in Tab. A.4.

Sample	Efficiency in %
DarkSUSY_mH_125_mGammaD_1_cT_10000_TuneCUETP8M1_14TeV_pythia8	2.37034035656
DarkSUSY_mH_125_mGammaD_1_cT_1000_TuneCUETP8M1_14TeV_pythia8	2.57039445433
DarkSUSY_mH_125_mGammaD_1_cT_100_TuneCUETP8M1_14TeV_pythia8	2.62629787977
DarkSUSY_mH_125_mGammaD_1_cT_10_TuneCUETP8M1_14TeV_pythia8	1.97117327466
DarkSUSY_mH_125_mGammaD_1_cT_5000_TuneCUETP8M1_14TeV_pythia8	2.0264681555
DarkSUSY_mH_125_mGammaD_5_cT_10000_TuneCUETP8M1_14TeV_pythia8	3.10331152092
DarkSUSY_mH_125_mGammaD_5_cT_1000_TuneCUETP8M1_14TeV_pythia8	4.92619598079
DarkSUSY_mH_125_mGammaD_5_cT_100_TuneCUETP8M1_14TeV_pythia8	2.80473762132
DarkSUSY_mH_125_mGammaD_5_cT_10_TuneCUETP8M1_14TeV_pythia8	2.07468879668
DarkSUSY_mH_125_mGammaD_5_cT_5000_TuneCUETP8M1_14TeV_pythia8	3.73565040908
DarkSUSY_mH_125_mGammaD_10_cT_10000_TuneCUETP8M1_14TeV_pythia8	5.19965024774
DarkSUSY_mH_125_mGammaD_10_cT_1000_TuneCUETP8M1_14TeV_pythia8	8.78682367669
DarkSUSY_mH_125_mGammaD_10_cT_100_TuneCUETP8M1_14TeV_pythia8	2.86992938085
DarkSUSY_mH_125_mGammaD_10_cT_10_TuneCUETP8M1_14TeV_pythia8	1.83388272436
DarkSUSY_mH_125_mGammaD_10_cT_5000_TuneCUETP8M1_14TeV_pythia8	6.4874657266
DarkSUSY_mH_125_mGammaD_20_cT_10000_TuneCUETP8M1_14TeV_pythia8	7.93765529704
DarkSUSY_mH_125_mGammaD_20_cT_1000_TuneCUETP8M1_14TeV_pythia8	11.7508650519
DarkSUSY_mH_125_mGammaD_20_cT_100_TuneCUETP8M1_14TeV_pythia8	3.38848594742
DarkSUSY_mH_125_mGammaD_20_cT_10_TuneCUETP8M1_14TeV_pythia8	1.92575026576
DarkSUSY_mH_125_mGammaD_20_cT_5000_TuneCUETP8M1_14TeV_pythia8	10.0644090568
DarkSUSY_mH_125_mGammaD_30_cT_10000_TuneCUETP8M1_14TeV_pythia8	8.35322195704
DarkSUSY_mH_125_mGammaD_30_cT_1000_TuneCUETP8M1_14TeV_pythia8	12.4079915878
DarkSUSY_mH_125_mGammaD_30_cT_100_TuneCUETP8M1_14TeV_pythia8	3.1146815536
DarkSUSY_mH_125_mGammaD_30_cT_10_TuneCUETP8M1_14TeV_pythia8	1.6582617782
DarkSUSY_mH_125_mGammaD_30_cT_5000_TuneCUETP8M1_14TeV_pythia8	11.1501983101
DarkSUSY_mH_125_mGammaD_40_cT_10000_TuneCUETP8M1_14TeV_pythia8	8.35322195704
DarkSUSY_mH_125_mGammaD_40_cT_1000_TuneCUETP8M1_14TeV_pythia8	12.4079915878
DarkSUSY_mH_125_mGammaD_40_cT_100_TuneCUETP8M1_14TeV_pythia8	3.1146815536
DarkSUSY_mH_125_mGammaD_40_cT_10_TuneCUETP8M1_14TeV_pythia8	1.6582617782
DarkSUSY_mH_125_mGammaD_40_cT_5000_TuneCUETP8M1_14TeV_pythia8	11.1501983101
DarkSUSY_mH_125_mGammaD_45_cT_10000_TuneCUETP8M1_14TeV_pythia8	8.35322195704
DarkSUSY_mH_125_mGammaD_45_cT_1000_TuneCUETP8M1_14TeV_pythia8	12.4079915878
DarkSUSY_mH_125_mGammaD_45_cT_100_TuneCUETP8M1_14TeV_pythia8	3.1146815536
DarkSUSY_mH_125_mGammaD_45_cT_10_TuneCUETP8M1_14TeV_pythia8	1.6582617782
DarkSUSY_mH_125_mGammaD_45_cT_5000_TuneCUETP8M1_14TeV_pythia8	11.1501983101
DisplacedSUSY_SmuonToMuNeutralino_M-100_CTau-1000_TuneCUETP8M1_14TeV-pythia8	15.1778413204
DisplacedSUSY_SmuonToMuNeutralino_M-100_CTau-100_TuneCUETP8M1_14TeV-pythia8	6.27822062835
DisplacedSUSY_SmuonToMuNeutralino_M-100_CTau-10_TuneCUETP8M1_14TeV-pythia8	1.59808869873
DisplacedSUSY_SmuonToMuNeutralino_M-100_CTau-300_TuneCUETP8M1_14TeV-pythia8	12.5071106223
DisplacedSUSY_SmuonToMuNeutralino_M-100_CTau-500_TuneCUETP8M1_14TeV-pythia8	14.6091459065
DisplacedSUSY_SmuonToMuNeutralino_M-100_CTau-700_TuneCUETP8M1_14TeV-pythia8	14.6091459065
DisplacedSUSY_SmuonToMuNeutralino_M-200_CTau-1000_TuneCUETP8M1_14TeV-pythia8	16.181591345
DisplacedSUSY_SmuonToMuNeutralino_M-200_CTau-100_TuneCUETP8M1_14TeV-pythia8	7.71923779756
DisplacedSUSY_SmuonToMuNeutralino_M-200_CTau-10_TuneCUETP8M1_14TeV-pythia8	1.6794710435
DisplacedSUSY_SmuonToMuNeutralino_M-200_CTau-300_TuneCUETP8M1_14TeV-pythia8	14.3389993073
DisplacedSUSY_SmuonToMuNeutralino_M-200_CTau-500_TuneCUETP8M1_14TeV-pythia8	15.9825966968
DisplacedSUSY_SmuonToMuNeutralino_M-200_CTau-700_TuneCUETP8M1_14TeV-pythia8	16.363043225
DisplacedSUSY_SmuonToMuNeutralino_M-500_CTau-1000_TuneCUETP8M1_14TeV-pythia8	16.9594287569
DisplacedSUSY_SmuonToMuNeutralino_M-500_CTau-100_TuneCUETP8M1_14TeV-pythia8	9.03606470432
DisplacedSUSY_SmuonToMuNeutralino_M-500_CTau-10_TuneCUETP8M1_14TeV-pythia8	1.89008911406
DisplacedSUSY_SmuonToMuNeutralino_M-1000_CTau-1000_TuneCUETP8M1_14TeV-pythia8	17.1288206842
DisplacedSUSY_SmuonToMuNeutralino_M-1000_CTau-100_TuneCUETP8M1_14TeV-pythia8	9.06128736041
DisplacedSUSY_SmuonToMuNeutralino_M-1000_CTau-10_TuneCUETP8M1_14TeV-pythia8	2.11554334399
DisplacedSUSY_SmuonToMuNeutralino_M-1500_CTau-1000_TuneCUETP8M1_14TeV-pythia8	17.327239811
DisplacedSUSY_SmuonToMuNeutralino_M-1500_CTau-100_TuneCUETP8M1_14TeV-pythia8	9.07199922058
DisplacedSUSY_SmuonToMuNeutralino_M-1500_CTau-10_TuneCUETP8M1_14TeV-pythia8	2.39546265666
DYJetsToLL_M-50_TuneCUETP8M1_14TeV-madgraphMLM-pythia8	1.62049956627
QCD_Pt-20toInf_MuEnrichedPt15_TuneCUETP8M1_14TeV_pythia8	1.59268291856
TTTo2L2Nu_TuneCUETP8M1_14TeV-powheg-pythia8	1.93729712805

Table A.3: All simulated samples used in the HL-LHC sensitivity study. The corresponding efficiency of the transverse impact parameter significance cut is shown in the right column.

Generator	Process	Kinematic Cuts	σ_{used} (pb)	N_{sim}
Drell-Yan				
MADGRAPH5_aMCNLO	DYJetsToLL	$M_{ll}/\text{GeV} > 50$	869.0	$\approx 3.74 \cdot 10^6$
$t\bar{t}$				
POWHEG 2.0	$t\bar{t} \to 2l2\nu$	-	864.4	$\approx 2.5 \cdot 10^6$
QCD				
PYTHIA 8.212	QCD μ enriched	$20 < \hat{p}_T/$ GeV, $p_T^\mu > 15$ GeV	302672	$\approx 2.89 \cdot 10^6$

Table A.4: Information about the simulated background samples. The generator, the simulated processes, the kinematic cuts, the cross sections at the HL-LHC (σ_{used}), and the number of simulated events (N_{sim}) are given in the different columns from left to right. The cross section values are taken from the generator information.

A.9 Collection of quality control plots

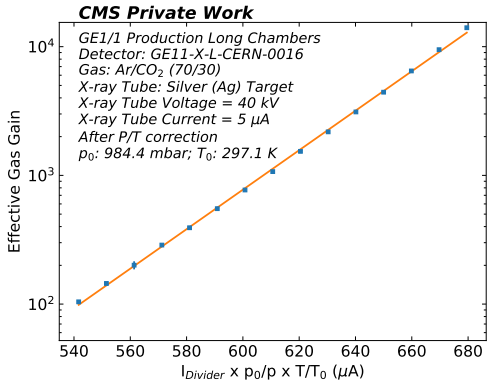

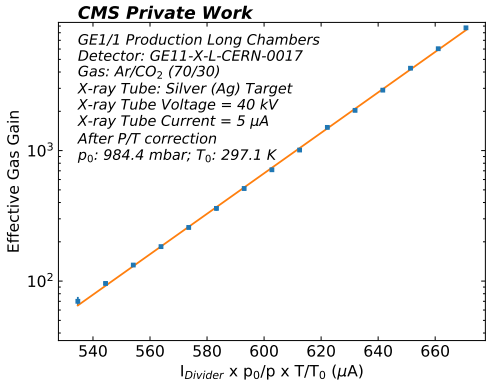

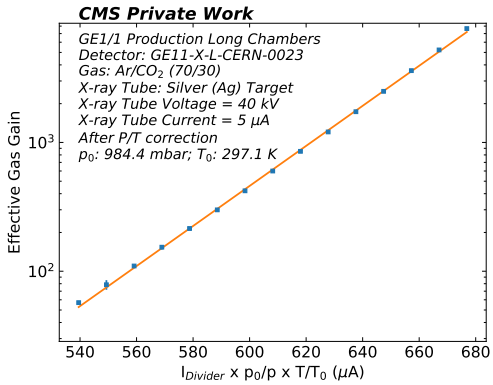

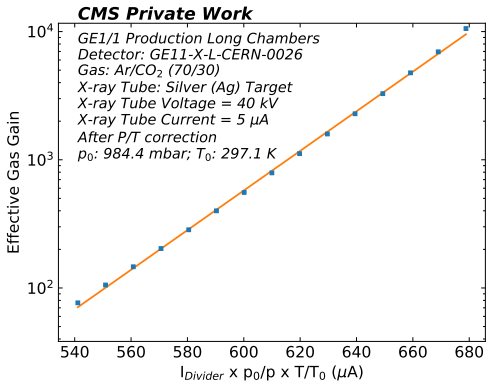

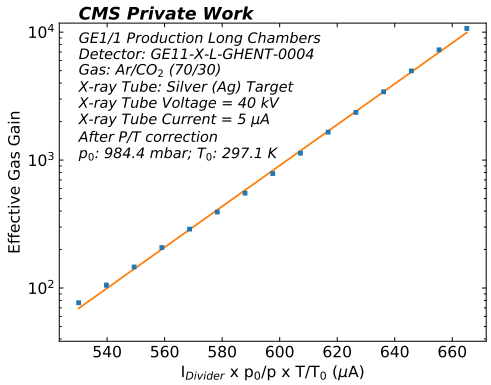

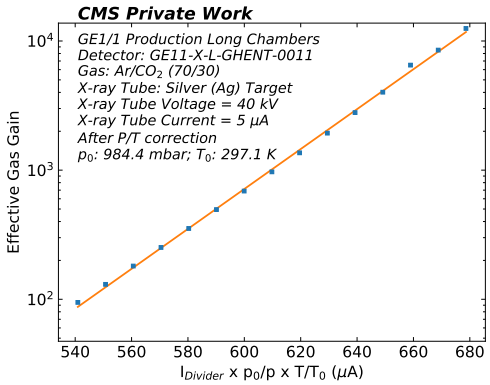

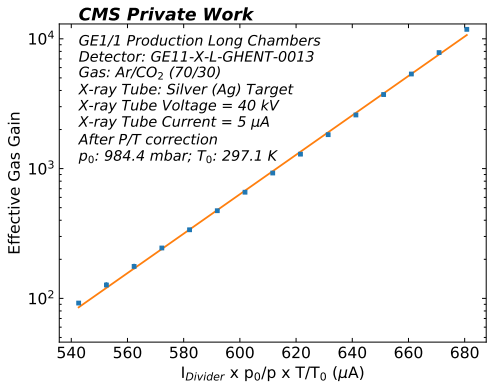

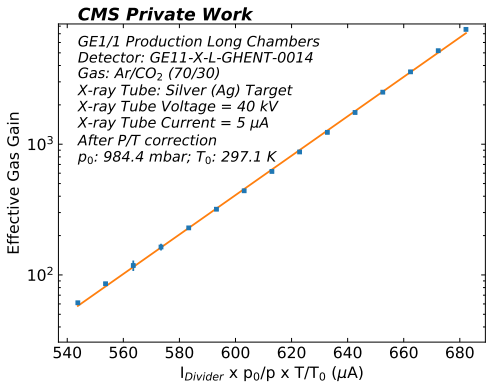

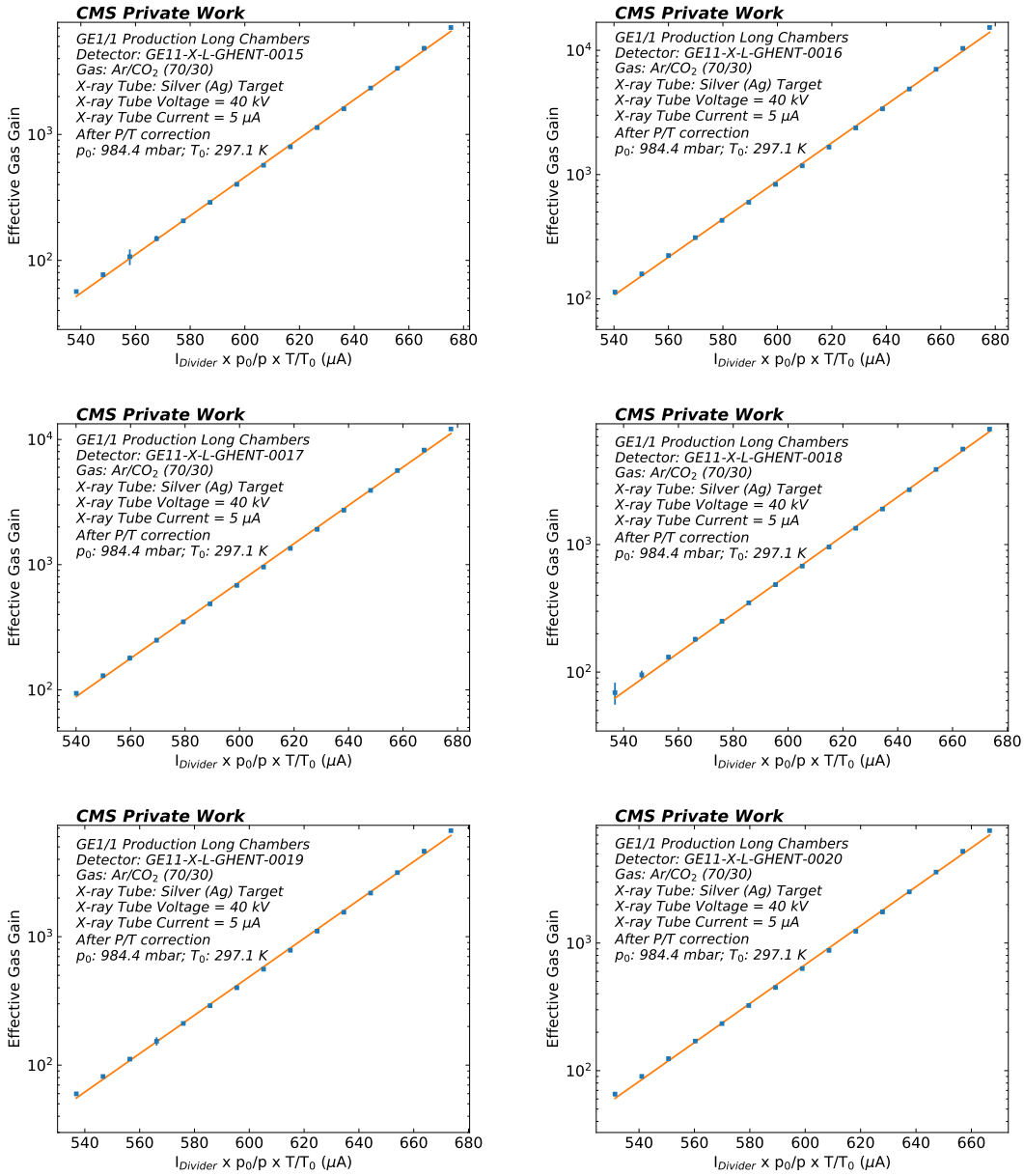

Figure A.11: Collection of the results from the effective gas gain measurements performed for the GE1/1 quality control procedure (see discussion in Sec. 5.3.6).

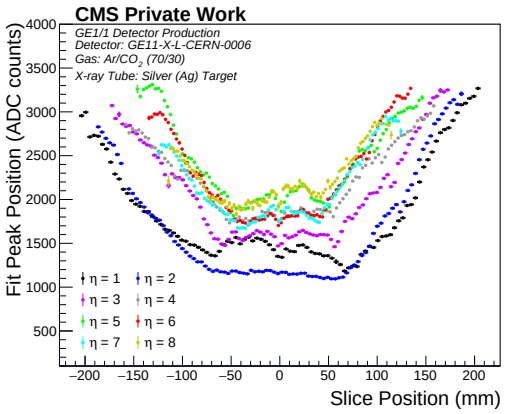
CMS Private Work
GE1/1 Detector Production
Detector: GE11-X-L-CERN-0006
Gas: Ar/CO2 (70/30)
X-ray Tube: Silver (Ag) Target
Fit Peak Position (ADC counts)
Slice Position (mm)
η = 1 η = 2
η = 3 η = 4
η = 5 η = 6
η = 7 η = 8

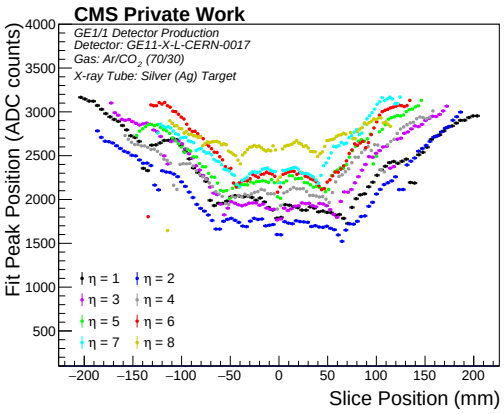
CMS Private Work
GE1/1 Detector Production
Detector: GE11-X-L-CERN-0017
Gas: Ar/CO2 (70/30)
X-ray Tube: Silver (Ag) Target
Fit Peak Position (ADC counts)
Slice Position (mm)
η = 1 η = 2
η = 3 η = 4
η = 5 η = 6
η = 7 η = 8

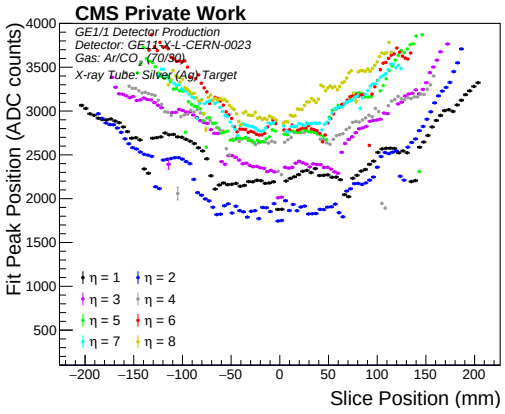
CMS Private Work
GE1/1 Detector Production
Detector: GE11-X-L-CERN-0023
Gas: Ar/CO2 (70/30)
X-ray Tube: Silver (Ag) Target
Fit Peak Position (ADC counts)
Slice Position (mm)
η = 1 η = 2
η = 3 η = 4
η = 5 η = 6
η = 7 η = 8

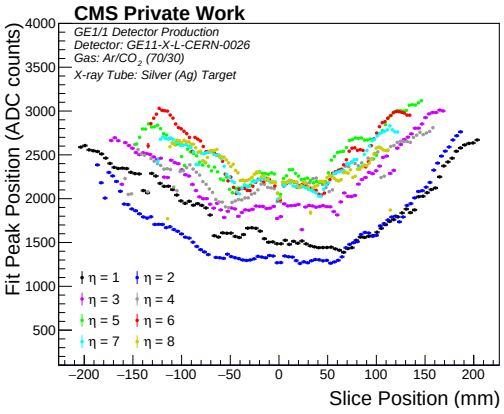
CMS Private Work
GE1/1 Detector Production
Detector: GE11-X-L-CERN-0026
Gas: Ar/CO2 (70/30)
X-ray Tube: Silver (Ag) Target
Fit Peak Position (ADC counts)
Slice Position (mm)
η = 1 η = 2
η = 3 η = 4
η = 5 η = 6
η = 7 η = 8

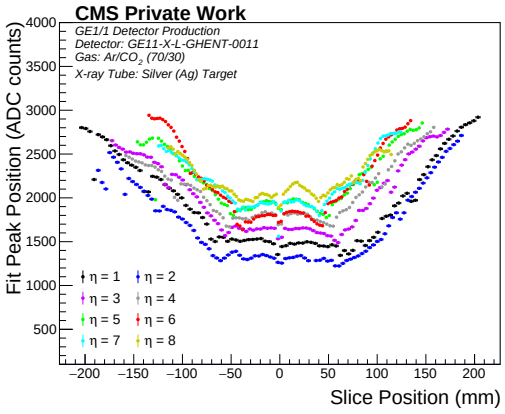
CMS Private Work
GE1/1 Detector Production
Detector: GE11-X-L-GHENT-0011
Gas: Ar/CO2 (70/30)
X-ray Tube: Silver (Ag) Target
Fit Peak Position (ADC counts)
Slice Position (mm)
η = 1 η = 2
η = 3 η = 4
η = 5 η = 6
η = 7 η = 8

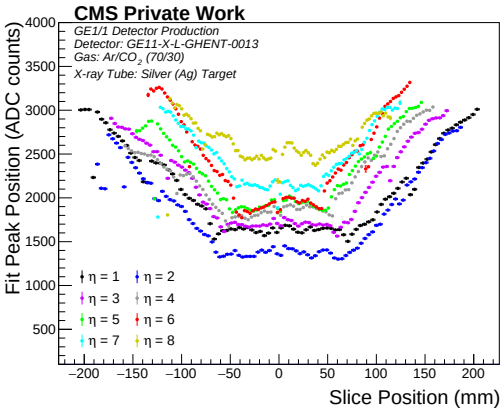
CMS Private Work
GE1/1 Detector Production
Detector: GE11-X-L-GHENT-0013
Gas: Ar/CO2 (70/30)
X-ray Tube: Silver (Ag) Target
Fit Peak Position (ADC counts)
Slice Position (mm)
η = 1 η = 2
η = 3 η = 4
η = 5 η = 6
η = 7 η = 8

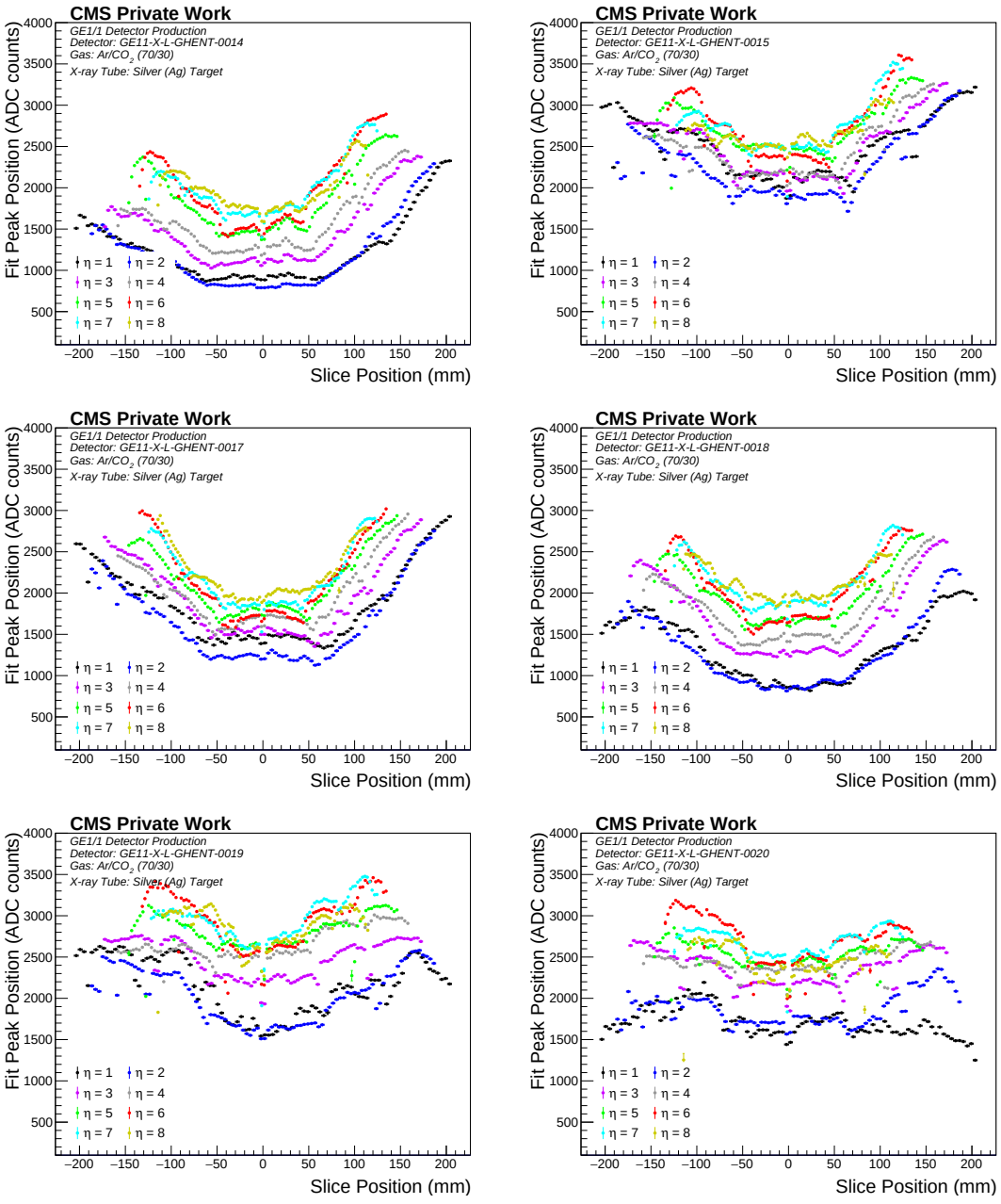

Figure A.12: Collection of the results from the gain uniformity tests performed for the GE1/1 quality control procedure (see caption of Fig. 5.30 for more information).

B Glossary

List of acronyms:

- ALICE = A Large Ion Collider Experiment
- AMORE = Automatic MOnitoRing Environment
- AOD = Analysis Object Data
- APV = Analogue Pipeline Voltage
- ASIC = Application-Specific Integrated Circuit
- ATLAS = A Toroidal LHC ApparatuS
- BSM = Beyond the Standard Model
- BX = Bunch Crossing
- CERN = Conseil Européen pour la Recherche Nucléaire
- CL = Confidence Level
- CMS = Compact Muon Solenoid
- CMSSW = CMS SoftWare
- COMPASS = Common Muon Proton Apparatus for Structure and Spectroscopy
- CSC = Cathode Strip Chamber
- DAQ = Data AcQuisition
- DATE = Data Acquisition and Test Environment
- DQM = Data Quality Monitoring
- DSA = Displaced StandAlone reconstruction
- DSR = Dispersion Suppressor Region
- DT = Drift Tube
- DY = Drell-Yan
- ECAL = Electromagnetic CALorimeter
- EDM = Event Data Model
- EYETS = Extended Year End Technical Stop
- FCNC = Flavor-Changing Neutral Currents
- FEC = Front-End Concentrator
- FEM = Finite Element Method
- FPGA = Field-Programmable Gate Array
- GE1/1 = GEM Endcap Station 1 Ring 1
- GE2/1 = GEM Endcap Station 2 Ring 1
- GEB = GEM Electronics Board

- GEM = Gas Electron Multiplier
- GMSB = Gauge-Mediated Symmetry Breaking
- GUI = Graphical User Interface
- HB = Hadron Barrel calorimeter
- HCAL = Hadronic CALorimeter
- HDMI = High-Definition Multimedia Interface
- HE = Hadron Endcap calorimeter
- HF = Hadron Forward calorimeter
- HGCAL = High-Granularity CALorimeter
- HLT = High-Level Trigger
- HL-LHC = High-Luminosity Large Hadron Collider
- HO = Hadron Outer calorimeter
- HV = High Voltage
- IP = Interaction Point
- IR = Interaction Region
- L1 = Level-1 (trigger)
- LEP = Large Electron-Positron Collider
- LHC = Large Hadron Collider
- LHCb = Large Hadron Collider beauty
- LLP = Long-Lived Particle
- LSP = Lightest Supersymmetric Particle
- LV = Low Voltage
- MCMC = Markov-Chain Monte Carlo
- Micromegas = Micro-mesh gaseous structure
- MIP = Minimum Ionizing Particle
- MM = MicroMegas
- MPGD = Micro-Pattern Gaseous Detector
- MSGC = MicroStrip Gaseous Chamber
- MSSM = Minimal Supersymmetric extension of the Standard Model
- MWPC = Multi-Wire Proportional Chamber
- NLO = Next-to-Leading Order
- NLSP = Next-to Lightest Supersymmetric Particle
- NNLO = Next-to-Next-to-Leading Order
- OA = Orientation A (GEM hole geometry)

- OB = Orientation B (GEM hole geometry)
- OH = Opto-Hybrid
- PCB = Printed Circuit Board
- Phase-1 = Period of LHC running, including Run-1/2/3
- Phase-2 = Period of HL-LHC running
- PV = Primary Vertex
- QC = Quality Control
- QCD = Quantum Chromo Dynamics
- R&D = Research and Development
- RPC = Resistive Plate Chamber
- SC = SuperChamber
- SCL = SuperConducting Link
- SL = SuperLayer
- SM = Standard Model
- SRS = Scalable Readout System
- SUSY = SUperSYmmetry
- TDR = Technical Design Report
- TEC = Tracker EndCap
- TIB = Tracker Inner Barrel
- TID = Tracker Inner Disk
- TMB = Trigger Mother Board
- TOB = Tracker Outer Barrel
- VFAT = Very Forward ATLAS and TOTEM
- WIMP = Weakly-Interacting Massive Particle
- YETS = Year End Technical Stop
- ZS = Zero-Suppression

Bibliography

[1] **CMS** Collaboration, S. Chatrchyan *et al.*, "Observation of a new boson at a mass of 125 GeV with the CMS experiment at the LHC", *Phys. Lett.* **B716** (2012) 30–61, arXiv:1207.7235 [hep-ex]. CMS-HIG-12-028, CERN-PH-EP-2012-220.

[2] F. Sauli, "GEM: A new concept for electron amplification in gas detectors", *Nucl. Instrum. Meth.* **A386** (1997) 531–534.

[3] **COMPASS** Collaboration, P. Abbon *et al.*, "The COMPASS experiment at CERN", *Nucl. Instrum. Meth.* **A577** (2007) 455–518, arXiv:hep-ex/0703049 [hep-ex].

[4] W. Anderson *et al.*, "Design, Construction, Operation and Performance of a Hadron Blind Detector for the PHENIX Experiment", *Nucl. Instrum. Meth.* **A646** (2011) 35–58, arXiv:1103.4277 [physics.ins-det].

[5] B. Surrow, "The STAR forward GEM tracker", in *Frontier detectors for frontier physics. Proceedings, 11th Pisa Meeting on Advanced Detectors, La Biodola, Italy, May 24-30, 2009*, vol. A617, pp. 196–198. 2010.

[6] **TOTEM** Collaboration, G. Antchev *et al.*, "Performance of the TOTEM Detectors at the LHC", *Int. J. Mod. Phys.* **A28** (2013) 1330046, arXiv:1310.2908 [physics.ins-det].

[7] A. Cardini, G. Bencivenni, and P. De Simone, "The operational experience of the triple-GEM detectors of the LHCb muon system: Summary of 2 years of data taking", in *Proceedings, 2012 IEEE Nuclear Science Symposium and Medical Imaging Conference (NSS/MIC 2012): Anaheim, California, USA, October 29-November 3, 2012*, pp. 759–762. 2012.

[8] F. Sauli, "The gas electron multiplier (GEM): Operating principles and applications", *Nucl. Instrum. Meth.* **A805** (2016) 2–24.

[9] **CMS Muon Group** Collaboration, Y. H. Lee and F. Fallavollita, "Aging studies of the triple-GEM detectors for future upgrades of the CMS muon high rate region at the HL-LHC", in *Proceedings, 39th International Conference on High Energy Physics (ICHEP2018): Seoul, Korea, July 4-11, 2018*, vol. ICHEP2018, p. 909. 2019.

[10] A. Colaleo, A. Safonov, A. Sharma, and M. Tytgat, "CMS Technical Design Report for the Muon Endcap GEM Upgrade", Tech. Rep. CERN-LHCC-2015-012. CMS-TDR-013, Jun, 2015.

[11] **CMS** Collaboration, "The Phase-2 Upgrade of the CMS Muon Detectors", Tech. Rep. CERN-LHCC-2017-012. CMS-TDR-016, CERN, Geneva, Sep, 2017.

[12] D. Abbaneo *et al.*, "Performance of a Large-Area GEM Detector Prototype for the Upgrade of the CMS Muon Endcap System", in *Proceedings, 21st Symposium on Room-Temperature Semiconductor X-ray and Gamma-ray Detectors (RTSD 2014): Seattle, WA, USA, November 8-15, 2014*, pp. 1–8. 2016. arXiv:1412.0228 [physics.ins-det].

[13] J. A. Merlin, "Study of long-term sustained operation of gaseous detectors for the high rate environment in CMS", Apr, 2016. CERN-THESIS-2016-041.

[14] **CMS** Collaboration, S. Chatrchyan *et al.*, "Search for Light Resonances Decaying into Pairs of Muons as a Signal of New Physics", *JHEP* **07** (2011) 098, arXiv:1106.2375 [hep-ex].

[15] **ATLAS** Collaboration, G. Aad *et al.*, "Search for long-lived neutral particles decaying into lepton jets in proton-proton collisions at $\sqrt{s} = 8$ TeV with the ATLAS detector", *JHEP* **11** (2014) 088, arXiv:1409.0746 [hep-ex].

[16] **PHENIX** Collaboration, A. Adare *et al.*, "Search for dark photons from neutral meson decays in $p + p$ and d + Au collisions at $\sqrt{s_{NN}} = 200$ GeV", *Phys. Rev. C* **91** no. 3, (2015) 031901, arXiv:1409.0851 [nucl-ex].

[17] J. B. Dent, F. Ferrer, and L. M. Krauss, "Constraints on Light Hidden Sector Gauge Bosons from Supernova Cooling", arXiv:1201.2683 [astro-ph.CO].

[18] **KLOE-2** Collaboration, D. Babusci *et al.*, "Search for light vector boson production in $e^+e^- \to \mu^+\mu^-\gamma$ interactions with the KLOE experiment", *Phys. Lett. B* **736** (2014) 459–464, arXiv:1404.7772 [hep-ex].

[19] **BaBar** Collaboration, J. P. Lees *et al.*, "Search for a Dark Photon in e^+e^- Collisions at BaBar", *Phys. Rev. Lett.* **113** no. 20, (2014) 201801, arXiv:1406.2980 [hep-ex].

[20] **CMS** Collaboration, "Search sensitivity for dark photons decaying to displaced muons with CMS at the high-luminosity LHC", CMS Physics Analysis Summary CMS-PAS-FTR-18-002, 2018.

[21] X. C. Vidal, M. D'Onofrio, P. J. Fox, R. Torre, and K. A. Ulmer, "Beyond the Standard Model physics at the HL-LHC and HE-LHC", *CERN Yellow Reports: Monographs* **7** no. 0, (2019) .

[22] J. Alimena *et al.*, "Searching for Long-Lived Particles beyond the Standard Model at the Large Hadron Collider", arXiv:1903.04497 [hep-ex].

[23] M. E. Peskin and D. V. Schroeder, "An introduction to quantum field theory." Westview Press Reading (Mass.), 1995.

[24] D. Griffiths, "Introduction to Elementary Particles." Wiley, Physics textbook, 2008.

[25] M. Czakon, "Quantum Field Theory: Lecture Notes." RWTH Aachen University, July, 2015.

[26] M. Erdmann, "Particle Physics I and II: Lecture Notes." RWTH Aachen University, 2014/2015.

[27] C. Berger, "Elementarteilchenphysik: Von den Grundlagen zu den modernen Experimenten." Springer-Verlag, 2014.

[28] D. H. Perkins, "Introduction to High Energy Physics." University of Oxford, 2000.

[29] "Standard Model of Elementary Particles", 2013. https://en.wikipedia.org/wiki/File:Standard_Model_of_Elementary_Particles.svg.

[30] S. Weinberg, "A Model of Leptons", *Phys. Rev. Lett.* **19** (Nov, 1967) 1264–1266.

[31] A. Salam, "Renormalizability of Gauge Theories", *Phys. Rev.* **127** (Jul, 1962) 331–334.

[32] P. W. Higgs, "Spontaneous Symmetry Breakdown without Massless Bosons", *Phys. Rev.* **145** (May, 1966) 1156–1163.

[33] F. Englert and R. Brout, "Broken Symmetry and the Mass of Gauge Vector Mesons", *Phys. Rev. Lett.* **13** (Aug, 1964) 321–323.

[34] **CMS** Collaboration, "Combination of standard model Higgs boson searches and measurements of the properties of the new boson with a mass near 125 GeV", CMS Physics Analysis Summary CMS-PAS-HIG-13-005, 2013.

[35] **CMS** Collaboration, "Standard Model Physics Publication", July, 2015. http://cms-results.web.cern.ch/cms-results/public-results/publications/SMP/index.html.

[36] G. F. Giudice, "Naturalness after LHC8", in *Proceedings, 2013 European Physical Society Conference on High Energy Physics (EPS-HEP 2013)*, vol. EPS-HEP2013, p. 163. 2013. arXiv:1307.7879 [hep-ph]. CERN-PH-TH-2013-180.

[37] G. Bertone, D. Hooper, and J. Silk, "Particle dark matter: Evidence, candidates and constraints", *Physics Reports* **405** (2005) 279–390, arXiv:hep-ph/0404175 [hep-ph].

[38] **CMS** Collaboration, "CMS Exotica Public Physics Results", 2019. https://twiki.cern.ch/twiki/bin/view/CMSPublic/PhysicsResultsEXO.

[39] C. Wiebusch, "Astroteilchenphysik: Skript SS 2010." RWTH Aachen University, 2010.

[40] D. Clowe, M. Bradač, A. H. Gonzalez, M. Markevitch, S. W. Randall, C. Jones, and D. Zaritsky, "A direct empirical proof of the existence of dark matter", *Astrophys. J.* **648** (2006) L109–L113, arXiv:astro-ph/0608407 [astro-ph].

[41] A. D. Sakharov, "Violation of CP Invariance, C asymmetry, and baryon asymmetry of the universe", *Pisma Zh. Eksp. Teor. Fiz.* **5** (1967) 32–35.

[42] **Particle Data Group** Collaboration, M. Tanabashi *et al.*, "Review of Particle Physics", *Phys. Rev. D* **98** (Aug, 2018) 030001.

[43] B. Shuve, "Theory overview of long-lived particles", LHC LLP workshop, CERN, Geneva, 2017. https://indico.cern.ch/event/607314/contributions/2542308/attachments/1447888/2231430/LHC-LLP_Shuve.pdf.

[44] C. Grupen and B. Shwartz, "Particle Detectors." *Cambridge monographs on particle physics, nuclear physics and cosmology*, Cambridge Univ. Press, 2008.

[45] H. Kolanoski and N. Wermes, "Teilchendetektoren." Springer Berlin, 2016.

[46] F. Sauli, "Gaseous radiation detectors: fundamentals and applications." *Cambridge monographs on particle physics, nuclear physics and cosmology*, Cambridge Univ. Press, 2014.

[47] C. Leroy and P.-G. Rancoita, "Principles of radiation interaction in matter and detection." World Scientific, Singapore, 2011.

[48] K. Kleinknecht, "Detectors for Particle Radiation." Cambridge Univ. Press, 1998.

[49] D. E. Groom, N. V. Mokhov, and S. I. Striganov, "Muon stopping power and range tables 10 MeV - 100 TeV", *Atomic Data and Nuclear Data Table* **78** no. 2, (2001) 183 – 356.

[50] H. A. Bethe, "Molière's Theory of Multiple Scattering", *Phys. Rev.* **89** (Mar, 1953) 1256–1266.

[51] E. B. Podgorsak, "Radiation Physics for Medical Physicists." Springer-Verlag Berlin Heidelberg, 2006.

[52] G. Knoll, "Radiation Detection and Measurement." John Wiley & Sons, New York, 1979.

[53] F. Sauli, "Principles of Operation of Multiwire Proportional and Drift Chambers." Lectures given in the Academic Training Programme of CERN 1975-1976, CERN-77-09, 1977.

[54] R. Veenhof, "Garfield, a drift chamber simulation program", in *Programming and mathematical techniques in physics. Proceedings, International Conference on programming and mathematical methods for solving physical problems, Dubna, Russia, June 14-19, 1993*, vol. C9306149, pp. 66–71. 1993.

[55] W. Price, "Nuclear Radiation Detection." McGraw-Hill, New York, 1958.

[56] W. Shockley, "Currents to Conductors Induced by a Moving Point Charge", *Journal of Applied Physics* **9** no. 10, (1938) 635–636.

[57] S. Ramo, "Currents induced by electron motion", *Proc. Ire.* **27** (1939) 584–585.

[58] E. Rutherford and H. Geiger, "An electrical method of counting the number of α-particles from radio-active substances", *Proceedings of the Royal Society of London. Series A, Containing Papers of a Mathematical and Physical Character* **81** no. 546, (1908) 141–161.

[59] G. Charpak, R. Bouclier, T. Bressani, J. Favier, and C. Zupančič, "Some read-out systems for proportional multiwire chambers", *Nucl. Instrum. Meth.* **65** (1968) 217–220.

[60] A. Oed, "Position Sensitive Detector with Microstrip Anode for electron Multiplication with Gases", *Nucl. Instrum. Meth.* **A263** (1988) 351–359. [,124(1988)].

[61] A. Bressan *et al.*, "High rate behavior and discharge limits in micropattern detectors", *Nucl. Instrum. Meth.* **A424** (1999) 321–342.

[62] T. Kawamoto *et al.*, "New Small Wheel Technical Design Report", Tech. Rep. CERN-LHCC-2013-006. ATLAS-TDR-020, Jun, 2013.

[63] Y. Giomataris, P. Rebourgeard, J. P. Robert, and G. Charpak, "MICROMEGAS: A High granularity position sensitive gaseous detector for high particle flux environments", *Nucl. Instrum. Meth.* **A376** (1996) 29–35.

[64] **MAMMA** Collaboration, Y. Kataoka, S. Leontsinis, and K. Ntekas, "Performance Studies of a Micromegas Chamber in the ATLAS Environment", *JINST* **9** (2014) C03016, arXiv:1310.8603 [physics.ins-det].

[65] G. Charpak, J. Derre, Y. Giomataris, and P. Rebourgeard, "MICROMEGAS, a multipurpose gaseous detector", *Nucl. Instrum. Meth.* **A478** (2002) 26–36.

[66] R. Chechik, A. Breskin, C. Shalem, and D. Mormann, "Thick GEM-like hole multipliers: Properties and possible applications", *Nucl. Instrum. Meth.* **A535** (2004) 303–308, arXiv:physics/0404119 [physics.ins-det].

[67] G. Bencivenni *et al.*, "The μ-RWELL layouts for high particle rate", *JINST* **14** no. 05, (2019) P05014, arXiv:1903.11017 [physics.ins-det].

[68] S. Bachmann *et al.*, "Discharge mechanisms and their prevention in the gas electron multiplier (GEM)", *Nucl. Instrum. Meth.* **A479** (2002) 294–308.

[69] **CMS** Collaboration, I. Yoon, "Results of quality control of large size GEM detectors based on the Korean GEM foil for the future upgrades of the CMS muon system", in *Proceedings, 39th International Conference on High Energy Physics (ICHEP2018)*, vol. ICHEP2018. Oct, 2018. CMS-CR-2018-235.

[70] **ATLAS** Collaboration, G. Aad *et al.*, "The ATLAS Experiment at the CERN Large Hadron Collider", *JINST* **3** (2008) S08003.

[71] **ALICE** Collaboration, K. Aamodt *et al.*, "The ALICE experiment at the CERN LHC", *JINST* **3** (2008) S08002.

[72] **CMS** Collaboration, S. Chatrchyan *et al.*, "The CMS Experiment at the CERN LHC", *JINST* **3** (2008) S08004.

[73] **LHCb** Collaboration, A. A. Alves, Jr. *et al.*, "The LHCb Detector at the LHC", *JINST* **3** (2008) S08005.

[74] K. Schindl, "The injector chain for the LHC", in *LEP performance. Proceedings, 9th Workshop, Chamonix, France, January 26-29, 1999*, pp. 47–52. 1999.

[75] L. Evans and P. Bryant, "LHC Machine", *JINST* **3** (2008) S08001.

[76] G. Apollinari, I. Béjar Alonso, O. Brüning, P. Fessia, M. Lamont, L. Rossi, and L. Tavian, "High-Luminosity Large Hadron Collider (HL-LHC)", *CERN Yellow Rep. Monogr.* **4** (2017) 1–516.

[77] **Particle Data Group** Collaboration, K. A. Olive *et al.*, "Review of Particle Physics", *Chin. Phys.* **C38** (2014) 090001.

[78] **CMS** Collaboration, "CMS Luminosity - Public Results", 2019. https://twiki.cern.ch/twiki/bin/view/CMSPublic/LumiPublicResults.

[79] **ATLAS** Collaboration, "LuminosityPublicResultsRun2", 2019. https://twiki.cern.ch/twiki/bin/view/AtlasPublic/LuminosityPublicResultsRun2.

[80] O. S. Brüning, P. Collier, P. Lebrun, S. Myers, R. Ostojic, J. Poole, and P. Proudlock, "LHC Design Report", *CERN Yellow Reports: Monographs* (2004) .

[81] J. Wenninger, "Operation and Configuration of the LHC in Run 2", Mar, 2019. CERN-ACC-NOTE-2019-0007.

[82] W. J. Stirling, "PARTON LUMINOSITY AND CROSS SECTION PLOTS", 2019. private communication.

[83] L. Rossi, "The LHC superconducting magnets", in *Particle accelerator. Proceedings, Conference, PAC 2003, Portland, USA, May 12-16, 2003*, vol. C030512, p. 141. 2003.

[84] **CMS** Collaboration, "The CMS magnet project: Technical Design Report", Tech. Rep. CERN-LHCC-97-010, CMS-TDR-1, 1997.

[85] F. Kircher *et al.*, "Final design of the CMS solenoid cold mass", *IEEE Transactions on Applied Superconductivity* **10** no. 1, (March, 2000) 407–410.

[86] Y.-S. Tsai, "Pair Production and Bremsstrahlung of Charged Leptons", *Rev. Mod. Phys.* **46** (Oct, 1974) 815–851.

[87] **CMS** Collaboration, S. Chatrchyan *et al.*, "Precise Mapping of the Magnetic Field in the CMS Barrel Yoke using Cosmic Rays", *JINST* **5** (2010) T03021, arXiv:0910.5530 [physics.ins-det].

[88] **CMS** Collaboration, V. Karimäki *et al.*, "The CMS tracker system project: Technical Design Report", Tech. Rep. CERN-LHCC-98-006, CMS-TDR-5, 1997.

[89] **CMS** Collaboration, "The CMS tracker: addendum to the Technical Design Report", Tech. Rep. CERN-LHCC-2000-016, CMS-TDR-5-add-1, 2000.

[90] **CMS** Collaboration, S. Chatrchyan *et al.*, "Description and performance of track and primary-vertex reconstruction with the CMS tracker", *JINST* **9** no. 10, (2014) P10009, arXiv:1405.6569 [physics.ins-det].

[91] **CMS** Collaboration, "The CMS electromagnetic calorimeter project: Technical Design Report", Tech. Rep. CERN-LHCC-97-033, CMS-TDR-4, 1997.

[92] A. A. Annenkov, M. V. Korzhik, and P. Lecoq, "Lead tungstate scintillation material", *Nucl. Instrum. Meth.* **A490** (2002) 30–50.

[93] X. D. Qu, L. Y. Zhang, and R. Y. Zhu, "Radiation induced color centers and light monitoring for lead tungstate crystals", *IEEE Trans. Nucl. Sci.* **47** (2000) 1741–1747.

[94] I. Dafinei, E. Auffray, P. Lecoq, and M. Schneegans, "Lead Tungstate For High Energy Calorimetry", *MRS Proceedings* **348** (1994) 99.

[95] P. Adzic *et al.*, "Energy resolution of the barrel of the CMS electromagnetic calorimeter", *JINST* **2** (2007) P04004.

[96] **CMS** Collaboration, "The CMS hadron calorimeter project: Technical Design Report", Tech. Rep. CERN-LHCC-97-031, CMS-TDR-2, 1997.

[97] **CMS HCAL** Collaboration, V. V. Abramov *et al.*, "Studies of the response of the prototype CMS hadron calorimeter, including magnetic field effects, to pion, electron, and muon beams", *Nucl. Instrum. Meth.* **A457** (2001) 75–100, arXiv:hep-ex/0007045 [hep-ex].

[98] **CMS** Collaboration, "The CMS muon project: Technical Design Report", Tech. Rep. CERN-LHCC-97-032, CMS-TDR-3, 1997.

[99] **CMS** Collaboration, G. Abbiendi, "The CMS muon system in Run2: preparation, status and first results", *PoS* **EPS-HEP2015** (2015) 237, arXiv:1510.05424 [physics.ins-det].

[100] **CMS** Collaboration, S. Chatrchyan *et al.*, "The Performance of the CMS Muon Detector in Proton-Proton Collisions at $\sqrt{s}$ = 7 TeV at the LHC", *JINST* **8** (2013) P11002, arXiv:1306.6905 [physics.ins-det].

[101] M. Abbrescia *et al.*, "The simulation of resistive plate chambers in avalanche mode: Charge spectra and efficiency", *Nucl. Instrum. Meth.* **A431** (1999) 413–427.

[102] M. Abbrescia *et al.*, "Local and global performance of double-gap resistive plate chambers operated in avalanche mode", *Nucl. Instrum. Meth.* **A434** (1999) 244–253.

[103] **CMS** Collaboration, "Endcap HV Cable Reshuffling", 2015. https://twiki.cern.ch/twiki/bin/view/Main/EndcapReshufflingRpc.

[104] **CMS** Collaboration, V. Khachatryan *et al.*, "The CMS trigger system", *JINST* **12** no. 01, (2017) P01020, arXiv:1609.02366 [physics.ins-det].

[105] **CMS** Collaboration, "CMSSW Application Framework", 2019. https://twiki.cern.ch/twiki/bin/view/CMSPublic/WorkBookCMSSWFramework.

[106] **CMS** Collaboration, G. L. Bayatian *et al.*, "CMS Physics", Tech. Rep. CERN-LHCC-2006-001, CMS-TDR-8-1, 2006.

[107] R. Frühwirth, "Application of Kalman filtering to track and vertex fitting", *Nucl. Instrum. Meth. A* **262** (1987) 444 – 450.

[108] **CMS** Collaboration, D. Contardo, M. Klute, J. Mans, L. Silvestris, and J. Butler, "Technical Proposal for the Phase-II Upgrade of the CMS Detector", Tech. Rep. CERN-LHCC-2015-010. LHCC-P-008. CMS-TDR-15-02, Geneva, Jun, 2015. https://cds.cern.ch/record/2020886.

[109] T. Mc Cauley, "Collision events recorded by CMS in 2016." CMS Collection, Jan, 2017.

[110] **CMS** Collaboration, J. Butler, D. Contardo, M. Klute, J. Mans, and L. Silvestris, "CMS Phase II Upgrade Scope Document", Tech. Rep. CERN-LHCC-2015-019. LHCC-G-165, CERN, Geneva, Sep, 2015.

[111] **CMS** Collaboration, "The Phase-2 Upgrade of the CMS Tracker", Tech. Rep. CERN-LHCC-2017-009. CMS-TDR-014, CERN, Geneva, Jun, 2017.

[112] **CMS** Collaboration, "The Phase-2 Upgrade of the CMS Barrel Calorimeters", Tech. Rep. CERN-LHCC-2017-011. CMS-TDR-015, CERN, Geneva, Sep, 2017.

[113] **CMS** Collaboration, "The Phase-2 Upgrade of the CMS Endcap Calorimeter", Tech. Rep. CERN-LHCC-2017-023. CMS-TDR-019, CERN, Geneva, Nov, 2017.

[114] **CMS** Collaboration, "The Phase-2 Upgrade of the CMS L1 Trigger Interim Technical Design Report", Tech. Rep. CERN-LHCC-2017-013. CMS-TDR-017, CERN, Geneva, Sep, 2017.

[115] **CMS Muon Group** Collaboration, D. Abbaneo *et al.*, "Layout and Assembly Technique of the GEM Chambers for the Upgrade of the CMS First Muon Endcap Station", *Nucl. Instrum. Meth.* **A918** (2019) 67–75, arXiv:1812.00411 [physics.ins-det].

[116] P. Aspell, "VFAT2: A front-end system on chip providing fast trigger information, digitized data storage and formatting for the charge sensitive readout of multi-channel silicon and gas particle detectors", in *Electronics for particle physics. Proceedings, Topical Workshop, TWEPP-07, Prague, Czech Republic, September 3-7, 2007*, p. 63. 2007.

[117] **CMS** Collaboration, M. Bianco *et al.*, "GE1/1 Quality Control: instructions." CMS GEM Internal Note, 2016.

[118] **CMS** Collaboration, "GEM DPG Public Page", 2019. https://twiki.cern.ch/twiki/bin/view/CMSPublic/GEMDPGPublic.

[119] Amptek, "Mini-X X-Ray Tube." https://usermanual.wiki/Document/MiniX20User20Manual20Rev20D2.2073057834.pdf.

[120] S. Martoiu, H. Muller, A. Tarazona, and J. Toledo, "Development of the scalable readout system for micro-pattern gas detectors and other applications", *JINST* **8** (2013) C03015.

[121] S. D. Pinto, "Micropattern gas detector technologies and applications the work of the RD51 collaboration", in *IEEE Nuclear Science Symposuim Medical Imaging Conference*, pp. 802–807. Oct, 2010.

[122] L. Jones, "APV25-S1: User guide version 2.2", 2001. https://cds.cern.ch/record/1069892.

[123] M. Raymond *et al.*, "The APV25 0.25 μm CMOS readout chip for the CMS tracker", in *2000 IEEE Nuclear Science Symposium. Conference Record (Cat. No.00CH37149)*, vol. 2, pp. 9/113–9/118. Oct, 2000.

[124] A. Sharma and F. Sauli, "A Measurement of the first Townsend coefficient in argon based mixtures at high fields", *Nucl. Instrum. Meth.* **A323** (1992) 280–283.

[125] F. Fallavollita, "Upgrade of the CMS Muon System with GEM Detectors: recent progress on construction, certification, Slice Test, and Long-term Operation." presented at VCI 2019, 2019.

[126] W. Carena *et al.*, "ALICE DAQ and ECS User's Guide." ALICE Internal note: CERN-ALICE-INT-2005-015, 2005.

[127] S. Chapeland and F. Roukoutakis, "The ALICE-LHC online Data Quality Monitoring framework", in *Proceedings, 2007 IEEE Nuclear Science Symposium and Medical Imaging Conference (NSS/MIC 2007): Honolulu, Hawaii, October 28-November 3, 2007*, pp. 213–218. 2007.

[128] B. L. Dorney, "CMS GEM Analysis Framework", 2018. https://github.com/bdorney/CMS_GEM_Analysis_Framework.

[129] **CERN** Collaboration, "FEAST: ASIC Information and Datasheets", 2019. http://project-dcdc.web.cern.ch/project-DCDC/public/ASICDatasheet.html.

[130] EXTECH, "RHT35: USB Humidity/Temperature/Barometric Pressure Datalogger." http://www.extech.com/products/RHT35.

[131] S. Glantz and B. Slinker, "Primer of Applied Regression and Analysis of Variance." McGraw-Hill Professional, 1990.

[132] M. Seidel, "Microscopic Simulation of GEM Signals." Bachelor thesis, RWTH Aachen University, 08/2018.

[133] R. Veenhof *et al.*, "Garfield++", 2018. http://garfieldpp.web.cern.ch/garfieldpp/.

[134] ANSYS, "Ansys Academic Research Mechanical, Release 16.1", 2019. https://www.ansys.com/.

[135] S. F. Biagi, "Monte Carlo simulation of electron drift and diffusion in counting gases under the influence of electric and magnetic fields", *Nucl. Instrum. Meth.* **A421** no. 1-2, (1999) 234–240.

[136] I. B. Smirnov, "Modeling of ionization produced by fast charged particles in gases", *Nucl. Instrum. Meth.* **A554** (2005) 474–493.

[137] **RD51** Collaboration, "RD51 Simulation School", Jan, 2011. https://indico.cern.ch/event/110634/overview.

[138] Ö. Şahin, I. Tapan, E. Özmutlu, and R. Veenhof, "Penning transfer in argon-based gas mixtures", *JINST* **5** no. 05, (2010) P05002.

[139] D. Janssens, R. Veenhof and E. Oliveri, "A better understanding of the gas gain in GEM detectors." RD51 collaboration meeting, CERN, Geneva, 2019.

[140] E. Cisbani and V. Brio, "GEM simulations: a flexible and efficient microscopic model based on Garfield++." RD51 collaboration meeting, CERN, Geneva, 2019.

[141] C. Geuzaine and J.-F. Remacle, "Gmsh: A 3-D finite element mesh generator with built-in pre- and post-processing facilities", *International Journal for Numerical Methods in Engineering* **79** no. 11, (2009) 1309–1331.

[142] **CMS Muon Group** Collaboration, A. Shah, A. Sharma, A. Kumar, J. A. Merlin, and M. Naimuddin, "Impact of Single-Mask Hole Asymmetry on the Properties of GEM Detectors", *Nucl. Instrum. Meth.* **A936** (2019) 459–461, arXiv:1811.04439 [physics.ins-det].

[143] J. Hegeman *et al.*, "CMS Luminosity DAQ Synchronization", 2019. https://twiki.cern.ch/twiki/pub/CMS/TcdsForBrilDaq/tcds_for_cms_luminosity_daq.pdf.

[144] S. P. Martin, "A Supersymmetry primer", arXiv:hep-ph/9709356 [hep-ph]. [Adv. Ser. Direct. High Energy Phys.18,1(1998)].

[145] M. Drees, "An Introduction to supersymmetry", in *Current topics in physics. Proceedings, Inauguration Conference of the Asia-Pacific Center for Theoretical Physics (APCTP), Seoul, Korea, June 4-10, 1996. Vol. 1, 2*. 1996. arXiv:hep-ph/9611409 [hep-ph].

[146] M. Baumgart, C. Cheung, J. T. Ruderman, L.-T. Wang, and I. Yavin, "Non-Abelian Dark Sectors and Their Collider Signatures", *JHEP* **04** (2009) 014, arXiv:0901.0283 [hep-ph].

[147] A. Falkowski, J. T. Ruderman, T. Volansky, and J. Zupan, "Hidden Higgs Decaying to Lepton Jets", *JHEP* **05** (2010) 077, arXiv:1002.2952 [hep-ph].

[148] B. Batell, M. Pospelov, and A. Ritz, "Probing a Secluded U(1) at B-factories", *Phys. Rev.* **D79** (2009) 115008, arXiv:0903.0363 [hep-ph].

[149] V. V. Ezhela, S. B. Lugovsky, and O. V. Zenin, "Hadronic part of the muon g-2 estimated on the σ^{2003}_{total}(e+ e- $\rightarrow$ hadrons) Evaluated Data Compilation", arXiv:hep-ph/0312114 [hep-ph].

[150] **CMS** Collaboration, "A search for pair production of new light bosons decaying into muons at $\sqrt{s} = 13$ TeV", CMS Physics Analysis Summary CMS-PAS-HIG-18-003, 2018.

[151] **CMS** Collaboration, V. Khachatryan *et al.*, "Searches for invisible decays of the Higgs boson in pp collisions at $\sqrt{s}$ = 7, 8, and 13 TeV", *JHEP* **02** (2017) 135, arXiv:1610.09218 [hep-ex].

[152] **LHC Higgs Cross Section Working Group** Collaboration, S. Dittmaier *et al.*, "Handbook of LHC Higgs Cross Sections: 1. Inclusive Observables", arXiv:1101.0593 [hep-ph].

[153] S. Ambrosanio, G. D. Kribs, and S. P. Martin, "Signals for gauge mediated supersymmetry breaking models at the CERN LEP-2 collider", *Phys. Rev.* **D56** (1997) 1761–1777, arXiv:hep-ph/9703211 [hep-ph].

[154] L. Calibbi and G. Signorelli, "Charged Lepton Flavour Violation: An Experimental and Theoretical Introduction", *Riv. Nuovo Cim.* **41** no. 2, (2018) 71–174, arXiv:1709.00294 [hep-ph].

[155] S. Dimopoulos, M. Dine, S. Raby, and S. D. Thomas, "Experimental signatures of low-energy gauge mediated supersymmetry breaking", *Phys. Rev. Lett.* **76** (1996) 3494–3497, arXiv:hep-ph/9601367 [hep-ph].

[156] J. D'Hondt, K. De Causmaecker, B. Fuks, A. Mariotti, K. Mawatari, C. Petersson, and D. Redigolo, "Multilepton signals of gauge mediated supersymmetry breaking at the LHC", *Phys. Lett.* **B731** (2014) 7–12, arXiv:1310.0018 [hep-ph].

[157] "Quantum effects in the minimal supersymmetric standard model. Proceedings, International Workshop, MSSM, Barcelona, Spain, September 9-13, 1997", *Singapore, Singapore: World Scientific (1998) 450 p* (1998) .

[158] G. Arcadi, L. Covi, and M. Nardecchia, "Gravitino Dark Matter and low-scale Baryogenesis", *Phys. Rev.* **D92** no. 11, (2015) 115006, arXiv:1507.05584 [hep-ph].

[159] J. Alwall, M. Herquet, F. Maltoni, O. Mattelaer, and T. Stelzer, "MadGraph 5 : Going Beyond", *JHEP* **06** (2011) 128, arXiv:1106.0522 [hep-ph].

[160] **CMS** Collaboration, "Muon Reconstruction and Identification Improvements for Run-2 and First Results with 2015 Run Data", CMS Detector Performance Note CMS-DP-2015-015, Jul, 2015. http://cds.cern.ch/record/2037372.

[161] C. Liu *et al.*, "Reconstruction of cosmic and beam-halo muons with the CMS detector", *Eur. Phys. J. C* **56** no. 3, (Aug, 2008) , arXiv:0810.3726 [physics.ins-det].

[162] T. Sjöstrand, S. Mrenna, and P. Z. Skands, "A Brief Introduction to PYTHIA 8.1", *Comp. Phys. Comm.* **178** (2008) 852–867, arXiv:0710.3820 [hep-ph].

[163] T. Sjöstrand, S. Ask, J. R. Christiansen, R. Corke, N. Desai, P. Ilten, S. Mrenna, S. Prestel, C. O. Rasmussen, and P. Z. Skands, "An introduction to PYTHIA 8.2", *Comp. Phys. Comm.* **191** (2015) 159, arXiv:1410.3012 [hep-ph].

[164] J. Alwall, R. Frederix, S. Frixione, V. Hirschi, F. Maltoni, O. Mattelaer, H. S. Shao, T. Stelzer, P. Torrielli, and M. Zaro, "The automated computation of tree-level and next-to-leading order differential cross sections, and their matching to parton shower simulations", *JHEP* **07** (2014) 079, arXiv:1405.0301 [hep-ph].

[165] P. Nason, "A new method for combining NLO QCD with shower Monte Carlo algorithms", *JHEP* **11** (2004) 040, arXiv:hep-ph/0409146 [hep-ph].

[166] S. Frixione, P. Nason, and C. Oleari, "Matching NLO QCD computations with parton shower simulations: the POWHEG method", *JHEP* **11** (2007) 070, arXiv:0709.2092 [hep-ph].

[167] S. Alioli, P. Nason, C. Oleari, and E. Re, "A general framework for implementing NLO calculations in shower Monte Carlo programs: the POWHEG BOX", *JHEP* **06** (2010) 043, arXiv:1002.2581 [hep-ph].

[168] **CMS** Collaboration, V. Khachatryan *et al.*, "Event generator tunes obtained from underlying event and multiparton scattering measurements", *Eur. Phys. J. C* **76** (2016) 155, arXiv:1512.00815 [hep-ex].

[169] **GEANT4** Collaboration, S. Agostinelli *et al.*, "GEANT4: A Simulation toolkit", *Nucl. Instrum. Meth. A* **506** (2003) 250–303.

[170] **CMS** Collaboration, "Search for displaced leptons in the e-mu channel", CMS Physics Analysis Summary CMS-PAS-EXO-16-022, 2016.

[171] **CMS** Collaboration, "Projected performance of Higgs analyses at the HL-LHC for ECFA 2016", CMS Physics Analysis Summary CMS-PAS-FTR-16-002, 2017.

[172] W. Beenakker, M. Klasen, M. Kramer, T. Plehn, M. Spira, and P. M. Zerwas, "The Production of charginos / neutralinos and sleptons at hadron colliders", *Phys. Rev. Lett.* **83** (1999) 3780–3783, arXiv:hep-ph/9906298 [hep-ph]. [Erratum: Phys. Rev. Lett.100,029901(2008)].

[173] G. Bozzi, B. Fuks, and M. Klasen, "Threshold Resummation for Slepton-Pair Production at Hadron Colliders", *Nucl. Phys.* **B777** (2007) 157–181, arXiv:hep-ph/0701202 [hep-ph].

[174] J. Fiaschi and M. Klasen, "Slepton pair production at the LHC in NLO+NLL with resummation-improved parton densities", *JHEP* **03** (2018) 094, arXiv:1801.10357 [hep-ph].

[175] **CMS** Collaboration, A. M. Sirunyan *et al.*, "Search for lepton-flavor violating decays of heavy resonances and quantum black holes to $e\mu$ final states in proton-proton collisions at $\sqrt{s} = 13$ TeV", *JHEP* **04** (2018) 073, arXiv:1802.01122 [hep-ex].

[176] **CMS** Collaboration, "Search for a high-mass resonance decaying into a dilepton final state in 13 fb^{-1} of pp collisions at $\sqrt{s} = 13$ TeV", CMS Physics Analysis Summary CMS-PAS-EXO-16-031, 2016.

[177] **CMS** Collaboration, "Updates on Search Sensitivity for New particles at HL-LHC", CMS Physics Analysis Summary CMS-PAS-FTR-16-005, 2017.

[178] G. Cowan, "Statistical data analysis." Oxford University Press, 1998.

[179] **CMS** Collaboration, "Documentation of the RooStats-based statistics tools for Higgs PAG", 2016. https://twiki.cern.ch/twiki/bin/viewauth/CMS/SWGuideHiggsAnalysisCombinedLimit#MarkovChainMC_algorithm.

[180] **RooStats** Collaboration, "RooStats page in CMS, Twiki", 2012. https://twiki.cern.ch/twiki/bin/view/CMS/RooStats.

[181] J. S. Conway, "Incorporating Nuisance Parameters in Likelihoods for Multisource Spectra", in *Proceedings, PHYSTAT 2011 Workshop on Statistical Issues Related to Discovery Claims in Search Experiments and Unfolding, CERN,Geneva, Switzerland 17-20 January 2011*, pp. 115–120. 2011. arXiv:1103.0354 [physics.data-an].

[182] C. Andrieu, N. De Freitas, A. Doucet, and M. I. Jordan, "An Introduction to MCMC for Machine Learning", Kluwer Academic Publishers, 2003. https://www.cs.ubc.ca/~arnaud/andrieu_defreitas_doucet_jordan_intromontecarlomachinelearning.pdf.

[183] S. S. Wilks, "The large-sample distribution of the likelihood ratio for testing composite hypotheses", *Ann. Math. Statist.* **9** no. 1, (03, 1938) 60–62.

[184] **CMS** Collaboration, M. M. Gruchala, "Upgrade of the CMS muon spectrometer in the forward region with the GEM technology", CMS Note CMS-CR-2018-325, CERN, Geneva, Oct, 2018.

Eidesstattliche Erklärung

I, Henning Christoph Keller
erklärt hiermit, dass diese Dissertation und die darin dargelegten Inhalte die eigenen sind und selbstständig, als Ergebnis der eigenen originären Forschung, generiert wurden.
Hiermit erkläre ich an Eides statt

1. Diese Arbeit wurde vollständig oder größtenteils in der Phase als Doktorand dieser Fakultät und Universität angefertigt;
2. Sofern irgendein Bestandteil dieser Dissertation zuvor für einen akademischen Abschluss oder eine andere Qualifikation an dieser oder einer anderen Institution verwendet wurde, wurde dies klar angezeigt;
3. Wenn immer andere eigene- oder Veröffentlichungen Dritter herangezogen wurden, wurden diese klar benannt;
4. Wenn aus anderen eigenen- oder Veröffentlichungen Dritter zitiert wurde, wurde stets die Quelle hierfür angegeben. Diese Dissertation ist vollständig meine eigene Arbeit, mit der Ausnahme solcher Zitate;
5. Alle wesentlichen Quellen von Unterstützung wurden benannt;
6. Wenn immer ein Teil dieser Dissertation auf der Zusammenarbeit mit anderen basiert, wurde von mir klar gekennzeichnet, was von anderen und was von mir selbst erarbeitet wurde;
7. Ein Teil oder Teile dieser Arbeit wurden zuvor veröffentlicht und zwar in:
    - CMS collaboration, *Search sensitivity for dark photons decaying to displaced muons with CMS at the high-luminosity LHC*, CMS-PAS-FTR-18-002, 2018.

Datum, Unterschrift